Copyright

by

Chadwick Hayward Young

2005

The Dissertation Committee for Chadwick Hayward Young
certifies that this is the approved version of the following dissertation:

Evolution of Low-Mass Protostars

Committee:

Neal J. Evans, II, Supervisor

Paul M. Harvey

Daniel T. Jaffe

John H. Lacy

Charles J. Lada

John M. Scalo

Evolution of Low-Mass Protostars

by

Chadwick Hayward Young, B.S., M.A.

Dissertation

Presented to the Faculty of the Graduate School of

The University of Texas at Austin

in Partial Fulfillment

of the Requirements

for the Degree of

Doctor of Philosophy

The University of Texas at Austin

August 2005

To Kaisa, my love.

Acknowledgments

While the completion of this work has only taken five years, I find the list of those I should acknowledge has grown to grand proportions. It is with their help that this project has been completed, and, undoubtedly, I will call on them again in the coming years. I can only hope that they will not be offended by the humble acknowledgements given here—wholly inadequate and certainly not commensurate with their contributions.

No person has offered me such a reward as that offered by my parents. Truly, their love and support have carried me through many trials and lifted me from many stumbles. Often, I think of their contribution, and, while knowing little about star formation, they have taught me those things that are the most important. I love them dearly and hope to honor them with this work.

Neal has provided the mechanics for this work, but his contribution quickly soars over mere machinery. Knowledge is easily gained, but wisdom is a gift from God. In both of these, Neal is well-gifted, showing wisdom in his daily life that is reminiscent of Solomon himself. How could I assume anything less from him? His patience with me has been neverending, and his grace towards me will linger for many years.

Grace Covenant Christian Church has been my home now for five years, and I thank these people for their love of Christ. Jason Matocha has listened to my woes on many a Wednesday morning and has offered well-placed encouragement

and exhortation. Joel Hock and Paul Hvass have unknowingly contributed to this dissertation as well; I sought their advice on numerous occasions, usually while rounding the last corner of an 800-meter sprint. Greg Herring has mentored me for the past two years, and, while I've groaned and complained, he has helped me to grow in my stature with men and God.

There is no human that I love more than Kaisa. With her, there is nothing of value that I lack; indeed, she is worth far more than rubies. Her intellect, patience, and diligence have provided for much of this work, but, most of all, her love for me has fueled these efforts. There are many good and noble wives in this world, but Kaisa surpasses them all.

Finally, no acknowledgement would be complete without thanking Him responsible for the very creation of the star-forming regions discussed herein. Our world, while certainly not comparable to His kingdom, is quite fascinating, and I am thankful that He has offered to us—and, indeed, me—the opportunity to study this physical universe.

CHADWICK HAYWARD YOUNG

The University of Texas at Austin
August 2005

Evolution of Low-Mass Protostars

Publication No. _____

Chadwick Hayward Young, Ph.D.
The University of Texas at Austin, 2005

Supervisor: Neal J. Evans, II

In this dissertation, I focus on the formation of low-mass stars, those stars with masses comparable to our own Sun. Mostly, my efforts center around the analysis of data from submillimeter and infrared telescopes, but I also consider an evolutionary picture of a forming star.

In Chapter 2, I present submillimeter continuum observations of 17 Class I protostars. These data were obtained with the James Clerk Maxwell Telescope's Submillimetre Common User's Bolometer Array (SCUBA) and the work has been completed with the collaboration of Yancy Shirley, Neal Evans, and Jonathan Rawlings. I analyze the data and present my results in this chapter (also in Young et al. 2003, ApJS, 145, 111).

Chapter 3 is a description of Spitzer Space Telescope observations of a "starless core," Lynds 1014. L1014 was part of the validation observations for the Legacy Program, From Molecular Cores to Planet-Forming Disks (c2d), and was the first star-forming core with no IRAS detection to be observed by Spitzer. In these observations, we detected a protostar embedded within the L1014 dark cloud. Chapter 3

offers a description of the multi-wavelength continuum and spectral line observations and is also in Young et al. (2004, ApJS, 154, 396).

I present an analysis of evolutionary signatures for an evolving protostar in Chapter 4. I have considered the inside-out collapse scenario of Shu (1977) and adapt it to include a disk and first hydrostatic core, which both affect the protostar's evolution. Then, I provide observational tools that will hopefully prove useful in scrutinizing this theory of protostar formation. This work is also presented in Young & Evans (2005, ApJ, 627; astro-ph/0503456).

Finally, in Chapter 5, I report on SCUBA observations for 38 star-forming cores at different stages of evolution. These data were collected as a complement to the c2d program and cover some of the same areas observed by the Spitzer Space Telescope. In this chapter, I present the data, some basic analysis, and comparisons of the SCUBA data for a few sources with Spitzer observations.

Contents

Acknowledgments v

Abstract vii

Chapter 1 Introduction 1

Chapter 2 Tracing the Mass during Low-Mass Star Formation: Observations and Modeling of the Submillimeter Continuum Emission from Class I Protostars 3

2.1 Abstract . . . 3

2.2 Introduction . . . 4

2.3 SCUBA Observations . . . 7

2.3.1 Sample . . . 7

2.3.2 Observations . . . 8

2.3.3 Image Reduction & Calibration . . . 10

2.3.4 Photometry . . . 15

2.3.5 Morphology . . . 18

2.4 Models . . . 19

2.4.1 Power Law Models . . . 19

2.4.2 Top Hat Models . . . 32

2.4.3 Shu Collapse Models . . . 35

2.4.4 Simple Analysis 36
2.4.5 Disk Contribution 39
2.5 Individual Sources 44
2.5.1 CB230 44
2.5.2 IRAS 04295+2251 45
2.5.3 IRAS 04166+2706 45
2.5.4 IRAS 04248+2612 46
2.5.5 IRAS 03256+3055 47
2.5.6 IRAS 04016+2610, 04108+2803, 04361+2547, and 04385+2250 48
2.6 Discussion 49
2.6.1 Envelope Mass 49
2.6.2 Luminosity and Stellar Mass 53
2.6.3 Classification: L_{obs}, T_{bol}, and L_{smm} 55
2.6.4 Density Structure 58
2.6.5 Caveats 65
2.7 Conclusions 65

Chapter 3 A "Starless" Core that Isn't: Detection of a Source in the L1014 Dense Core with the Spitzer Space Telescope 88

3.1 Abstract 88
3.2 Introduction 89
3.3 Environment of L1014 89
3.4 Observations and Results 90
3.5 Models for the L1014 Core 95
3.6 Conclusions 100
3.7 Acknowledgements 100

Chapter 4 Evolutionary Signatures in the Formation of Low-Mass Protostars **102**

4.1 Abstract . . . 102
4.2 Introduction . . . 103
4.3 The Model . . . 106
4.3.1 Interstellar Radiation Field & Dust Properties . . . 106
4.3.2 Envelope . . . 107
4.3.3 Disk . . . 112
4.3.4 Star . . . 116
4.4 Signatures . . . 124
4.5 Radiative Transfer . . . 125
4.6 An Evolving Protostar . . . 127
4.7 Free Parameters . . . 127
4.7.1 η_D . . . 129
4.7.2 η_* . . . 129
4.7.3 τ_{max} . . . 133
4.8 Results . . . 137
4.8.1 T_{bol} and L_{bol}/L_{smm} . . . 137
4.8.2 Mass Ratio . . . 141
4.8.3 BLT Diagrams: A Comparison with M98 . . . 145
4.8.4 Infrared Color-Magnitude Diagrams . . . 149
4.9 Conclusions . . . 152
4.10 Acknowledgements . . . 153

Chapter 5 Submillimeter Observations of Low-Mass Protostars **155**

5.1 Abstract . . . 155
5.2 Introduction . . . 156
5.3 Observations and Data Reduction . . . 156

5.3.1 Sample 156
5.3.2 Observations 157
5.3.3 Data Reduction 158
5.3.4 Calibration 165
5.4 Results 165
5.4.1 Mass 165
5.4.2 Multiplicity 169
5.4.3 Comparison with Spitzer Observations 169
5.4.4 2MASS 0347392+311912 174
5.5 Conclusion 181
5.6 Acknowledgements 181

Chapter 6 Summary **187**
6.1 Chapter 2 187
6.2 Chapter 3 188
6.3 Chapter 4 189
6.4 Chapter 5 190

Bibliography **192**

Vita **202**

Chapter 1

Introduction

In the study of astronomy, important discoveries are often marked not by what we see but, rather, by what we do not see—so it is with star formation. Modern astronomers first recognized dark nebulae as regions of star formation in the late nineteenth century; one author, (Barnard 1919) described them as"drop[s] of black ink on the bright background of the Milky Way." Today, we still marvel over these dark clouds like awestruck and sleepless children looking for monsters in the dark spaces of their sleeping chamber. May we never lose our awe even as we reveal the monsters waiting within.

In this dissertation, I focus on the formation of low-mass stars, those stars with masses comparable to our own Sun. Mostly, my efforts center around the analysis of data from submillimeter and infrared telescopes, but I also consider an evolutionary picture of a forming star.

In Chapter 2, I present submillimeter continuum observations of 17 Class I protostars. These data were obtained with the James Clerk Maxwell Telescope's Submillimetre Common User's Bolometer Array (SCUBA) and the work has been completed with the collaboration of Yancy Shirley, Neal Evans, and Jonathan Rawlings. I analyze the data and present my results in this chapter (also in Young et al.

2003, ApJS, 145, 111).

Chapter 3 is a description of Spitzer Space Telescope observations of a "starless core," Lynds 1014. L1014 was part of the validation observations for the Legacy Program, From Molecular Cores to Planet-Forming Disks (c2d), and was the first star-forming core with no IRAS detection to be observed by Spitzer. In these observations, we detected a protostar embedded within the L1014 dark cloud. Chapter 3 offers a description of the multi-wavelength continuum and spectral line observations and is also in Young et al. (2004, ApJS, 154, 396).

I present an analysis of evolutionary signatures for an evolving protostar in Chapter 4. I have considered the inside-out collapse scenario of Shu (1977) and adapt it to include a disk and first hydrostatic core, which both affect the protostar's evolution. Then, I provide observational tools that will hopefully prove useful in scrutinizing this theory of protostar formation. This work is also presented in Young & Evans (2005, ApJ, 627; astro-ph/0503456).

Finally, in Chapter 5, I report on SCUBA observations for 38 star-forming cores at different stages of evolution. These data were collected as a complement to the c2d program and cover some of the same areas observed by the Spitzer Space Telescope. In this chapter, I present the data, some basic analysis, and comparisons of the SCUBA data for a few sources with Spitzer observations.

Chapter 2

Tracing the Mass during Low-Mass Star Formation: Observations and Modeling of the Submillimeter Continuum Emission from Class I Protostars

2.1 Abstract

We present results from the observations and modeling of seventeen Class I cores with the Submillimetre Common Users Bolometer Array (SCUBA) on the James Clerk Maxwell Telescope (JCMT). Our sample consists of cores with 64< T_{bol}(K)<270, 0.2 < $L_{obs}/\mathrm{L}_{\odot}$ < 12, and 50 < L_{obs}/L_{smm} < 1000. By modeling the transfer of ra-

diation through the envelope for nine cores, we find, for a power law distribution $n(r) = n_f(r/r_f)^{-p}$, the average and standard deviation $\langle p \rangle = 1.6 \pm 0.4$ and a median of $p = 1.8$. However, the inclusion of a disk or other point-like component can cause the derived p to be shallower by as much as 0.5. We discuss uncertainties due to the interstellar radiation field (ISRF), disks, dust opacity, and outer radii in our modeling results. We find no evidence for a truncated outer radius or radially variant dust properties in most sources. Uncertainty in the strength of the ISRF and possible existence of a disk contribute the greatest uncertainty in p. In addition, we test the Shu collapse model for our sources and discuss the application of simpler analyses that derive a density power law distribution directly from the slope of the intensity radial profile. The total mass of the envelope in our sample has a range of $0.04 < M_{env}/\mathrm{M}_\odot < 5.0$, but these masses disagree with the virial masses derived from molecular line observations, indicating that observations of molecular lines do not trace the mass in some Class I cores. We also discuss several sources individually. In particular, IRAS 03256+3055, with its unique morphology, is an ideal object for testing theories of fragmentation in the formation of low-mass protostars. Also, we note the possibility, through some simple calculations, that IRAS 04385+2550 is a young, forming substellar object. Finally, we discuss the nature of these sources in light of various evolutionary indicators and find that T_{bol} and L_{obs}/L_{smm} are often inconsistent in distinguishing Class 0 from Class I cores. We note that, in this sample, the L_{obs}/L_{smm} criterion redefines many of these Class I sources (by T_{bol}) as Class 0 sources.

2.2 Introduction

The formation of low-mass stars has received considerable attention, but the process by which material moves from the outer envelope to the central protostar is still debated. Theories differ, primarily, in their prediction of the density, $n(r)$, and

velocity, $\vec{v}(r)$, as a function of radius, r. Larson (1969) and Penston (1969) proposed a model with initial conditions of constant density and zero velocity. Their model encounters problems due to its prediction of supersonic infall velocities that are not observed in regions of low-mass star formation (Zhou 1992). Shu (1977) proposed a scenario where infall begins from the inside, i.e., inside-out collapse. The initial density configuration is a singular isothermal sphere (SIS) with $n(r) \propto r^{-2}$. Collapse begins at the center and propagates outward at the sound speed, a_{eff}, leaving behind a density distribution that approaches $n(r) \propto r^{-1.5}$. Some perturbations to the Shu model include rotation (Terebey, Shu, & Cassen 1984) and magnetic fields (Galli & Shu 1993). McLaughlin & Pudritz (1997) proposed a different model in which accretion increases with time. Their scenario was similar to Shu (1977)—a collapse front propagating into a static envelope—but, because of differing initial conditions and a polytropic equation of state, they predict a much shallower density profile in the static envelope ($n \propto r^{-1}$). Foster & Chevalier (1993) conducted hydrodynamical calculations of the collapse of a Bonnor-Ebert sphere and found the density approaches a r^{-2} distribution at small radii. Other models exist with various predictions in the density distribution, $n \propto r^{-p}$. Therefore, observational determinations of this density distribution can help us to discern the physical processes governing the formation of low-mass stars.

Classification of the stages in protostellar evolution has grown more detailed. Initially, Lada et al. (1987) used the infrared spectral index to define Classes I-III. Later, Myers & Ladd (1993) proposed a classification of these forming stars based on their bolometric temperature (T_{bol}); this classification scheme was further codified by Chen et al. (1995). André et al. (1993) defined a criterion to discern Class 0 from Class I cores: the ratio of the submillimeter to bolometric luminosity. In this paper, we refer to the inverse of this quantity (L_{bol}/L_{smm}), a quantity that presumably increases with time.

The luminosity of a low-mass core (protostar+envelope) is emitted mostly at infrared wavelengths due to the reprocessing of higher energy radiation from the central protostar by dust grains in the envelope. These heated grains also emit detectable radiation at submillimeter wavelengths. Because the cloud is optically thin to this radiation, a measure of this dust emission renders a sampling of the entire mass in the cloud. In the past, astronomers have used single bolometers to detect this emission, but resolution and sensitivity limited their progress. Submillimeter bolometer arrays, such as SCUBA, have allowed us to map this dust emission from the protostellar envelopes and, for the first time, draw conclusions about the nature and distribution of mass within these envelopes.

In this paper, we present the observations and modeling of Class I cores. We describe our sample selection, observations, data reduction, and some basic data analysis in Section 2. In Section 3, we discuss various aspects of modeling these sources. power law models were the primary focus, but we also present simpler top hat models of the density distribution. Also, we report on Shu collapse models for nine sources. Additionally, in this third section, we compare the application of simpler analyses to our more detailed models. Also, we evaluate some possible scenarios where a disk is present and how the disk affects the modeled density profile. In Section 4, we discuss some individual sources. Section 5 holds a discussion of masses, classification, and the density structure of Class I protostars. Finally, in Section 6, we summarize our conclusions. The frugal reader, who wishes only for our major conclusions, can focus primarily on Sections 3, 5, and 6.

2.3 SCUBA Observations

2.3.1 Sample

In Shirley et al. (2000, hereafter, Paper I), we presented the results from observations of a sample ranging from Class −1 to Class I cores. In that sample, the presence of multiple sources within the observed field was common for the Class I sources but uncommon for the Class 0 objects. Therefore, Shirley et al. suggested that many Class I sources might appear as such because of the existence of multiple sources within the IRAS beam. This suggestion was one motivation for observing this sample of Class I objects: to determine the existence and effect of multiplicity. In addition, we hoped to present a similar treatment and analysis as in Papers I-III (Shirley et al., 2000; Evans et al. 2001; Shirley et al. 2002)—i.e., determining source characteristics and proposing possible density and temperature profiles through simulations with a one-dimensional radiative transfer code.

We have selected a sample of sixteen sources; these are listed in Table 1 with their positions in B1950.0 and J2000.0 coordinates. The positions were obtained, mostly, from the IRAS PSC as well as from 2 μm observations pursued by Tamura et al. (1991) and Moriarty-Schieven et al. (1994).

The distances to these sources range from 140 to 450 parsecs (pc), but most of the objects (13) are in the nearby Taurus star-forming region at 140 pc (Elias 1978). We adopt a distance of 450 pc for CB230 (Launhardt & Henning 1997), 300 pc for L1251B (Kun & Prusti 1993), and 320 pc for IRAS 03256+3055 in Perseus (de Zeeuw 1999). The distance for Perseus is based on recent Hipparcos observations and differs from that used in Papers I & III (220 pc).

We classify the cores in our sample by their bolometric temperature ($T_{bol} >$ 70 K for Class I). Therefore, two objects, L1251B and IRAS 03256+3055 (with $T_{bol} <$ 70 K), are not included in the average values for various parameters describing Class I cores.

2.3.2 Observations

We observed this sample of Class I sources with SCUBA, the Submillimeter Continuum Users Bolometer Array (Holland et al. 1999), on the James Clerk Maxwell Telescope (JCMT) atop Mauna Kea, Hawaii. Over four nights in November 1999 and February 2000, we mapped each of these cores at 850 and 450 μm by the 64-point jiggle map method that fully samples a field of 2.3'. Since we expected to see very extended emission, we adopted a five-point mapping technique with 30$''$ spacings between each of the five 64-point jiggle maps. By this method, we removed the effects of bad bolometers and integrated for a longer time on the central 2$'$ of the map. In some sources, we increased the coverage of our maps to include extended emission.

We performed pointing and skydip measurements between each five-point map. The average pointing RMS, over the four nights of observations, was $\pm$2.0$''$. We measured the sky opacity via the skydip method at 450 and 850 μm ($\langle\tau_{450}\rangle$ = 1.07 and $\langle\tau_{850}\rangle$ = 0.21) while also recording the opacity as measured by the CSO radiometer at 225 GHz ($\langle\tau_{CSO}\rangle$ = 0.05). In our calculation of τ_{850} and τ_{450}, we used the updated hot and cold load temperatures as given by Archibald et al. (2000). In addition, we find a relationship between τ_{850} and τ_{CSO} that is in agreement with that presented by Archibald et al. (2000). We list all opacity measurements in Table 2.7.

Observations of Uranus (November 1999) and AFGL 618 (February 2000) were used to determine the beam profile of the JCMT. In Figure 2.1, we show the radial intensity profiles of these point sources for various times during the night—our observing shift was from about 1730-0130, Hawaii-Aleutian Standard Time (HST). Two points should be considered in regard to these beam profiles: the significant and variable nature of the sidelobes and the changing FWHM size of the beam (θ_{mb}). First, Mueller et al. (2002) noted the significance of sidelobes in their treat-

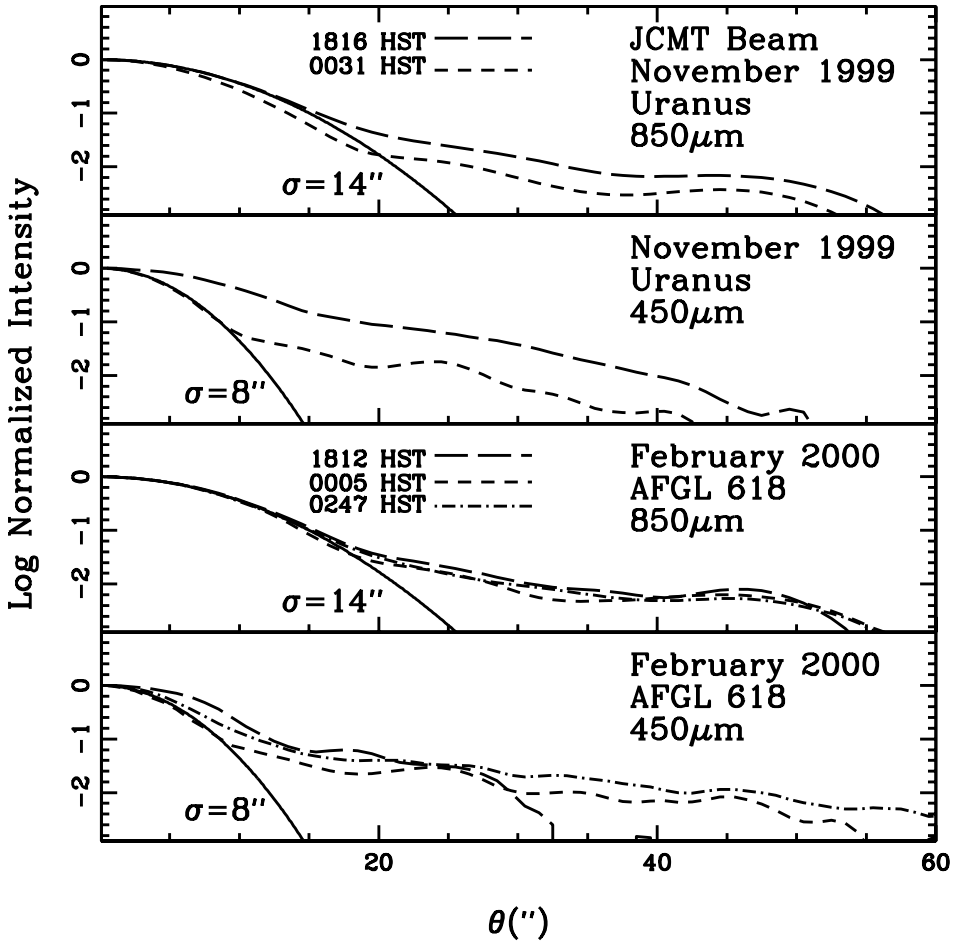

Figure 2.1: The observed JCMT beam profiles were obtained through observations of Uranus or AFGL618 and are shown by the squares. The solid lines are Gaussian functions with a FWHM of 15″ and 11″ for 850 and 450μm, respectively, and represent the resolution at these wavelengths.

ment of dust continuum emission from massive star-forming regions. They find that disregard of these sidelobes and the assumption of a Gaussian beam can cause the derived density power law index to be shallower by ∼0.4. Indeed, the beam profiles in Figure 2.1 show considerable power (about 1/10 of the maximum) in the second and, sometimes, third sidelobes. Additionally, we find the sidelobes become smaller as the night progresses and the dish cools. Second, for both nights, the 450 μm beam profile has a large FWHM ($\sim 11''$) at about 1800 HST, but the beamsize decreases to $\theta_{mb} \sim 8''$ at about midnight (HST). For November 1999, as shown in Figure 2.1, the 450 μm FWHM decreased by $3''$ as the night progressed. However, because the S/N is much better and the beam more stable at 850 μm, we relied more heavily on it in the determination of certain source properties (e.g., the deconvolved FWHM size). The 850 μm beam profile is also variable ($\delta FWHM \sim 1 - 2''$), however, and we propagate this variability as an uncertainty in the measured properties dependent on the beamshape. Additionally, in our modeling, we used the observed beam profile that is closest in time to the source observation. In one case (CB230), where there were no beam profiles within one hour in time, we took the time-weighted average of two neighboring beam profiles; in all other cases, the beam profiles were taken from observations of Uranus or AFGL 618 that were within one-half hour of the source observation. While the existence of and variations in the sidelobes *significantly affect* the analysis of radial intensity profiles, we have taken great care to remove uncertainties due to these imperfections.

2.3.3 Image Reduction & Calibration

We analyzed and reduced our data with the SCUBA User's Reduction Facility (SURF) (Jenness & Lightfoot 1997). The first-order effects of chopping had already been removed from the raw data, so our reduction entailed flatfielding, extinction correction, removal of sky variations, and the coadding and rebinning of the maps.

This process of data reduction is described in Paper I. The contour maps (with greyscale) for 850 and 450 μm are in Figures 2.2-2.6.

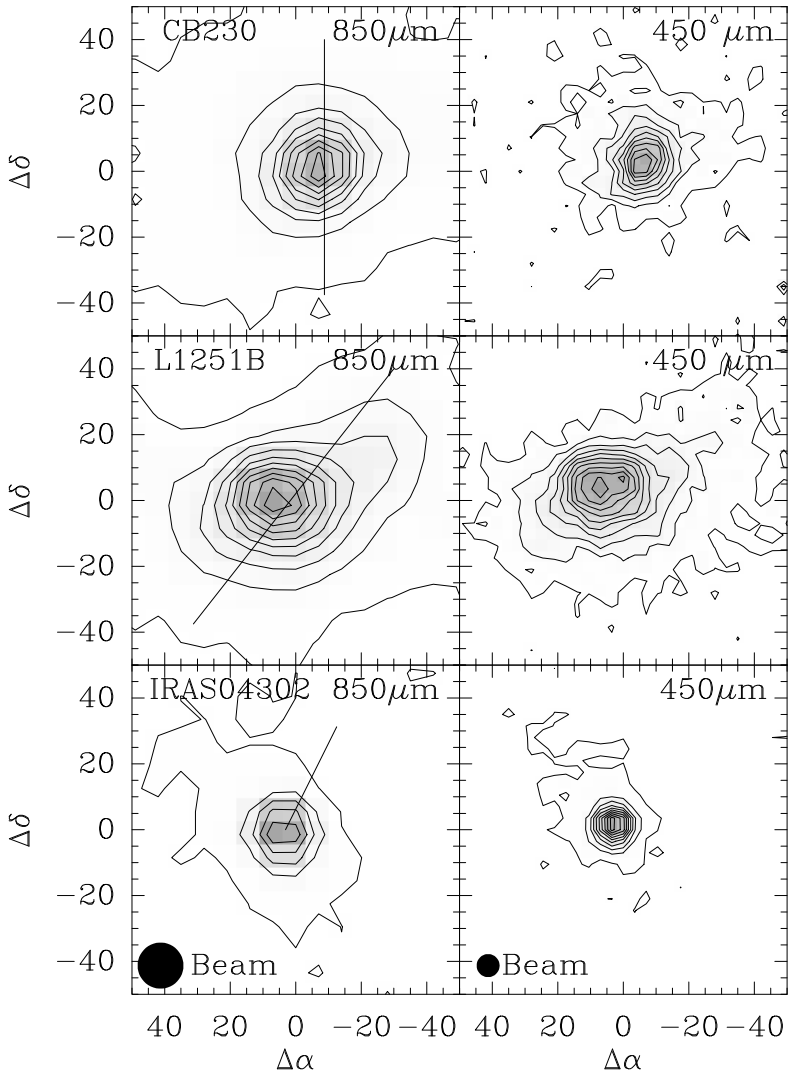

Figure 2.2: Maps of emission at 850 and 450μm. For all the maps, the lowest contour is at the 2-σ level. The contours increase by intervals of ten percent of the peak for CB230 (10-σ and 2-σ for 850μm and 450μm) and L1251B (6-σ and 2-σ for 850μm and 450μm). The contours of IRAS 04302+2247 are shown in increments of twenty percent (10-σ) for the 850μm map and ten percent (4-σ) for the 450μm map. Greyscale is from a level of -1σ to the peak flux. Central positions are in Table 1. References for outflows are as follows: CB230, Yun & Clemens, 1994.; L1251B, Sato et al., 1994; IRAS 04302+2247, Bontemps, et al. 1996.

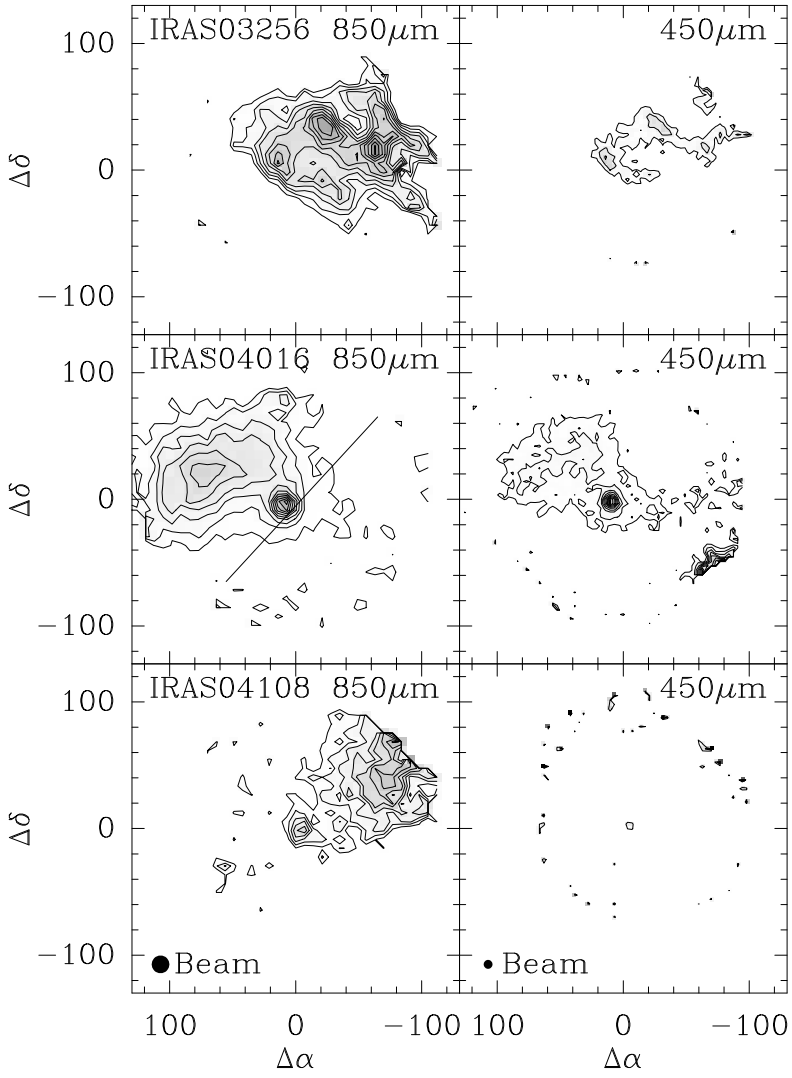

Figure 2.3: Maps of emission at 850 and 450μm. For all the maps, the lowest contour is at the 2-σ level. The 850μm contours increase by intervals of ten percent of the peak for IRAS 03256+3055 (1-σ), IRAS 04016+2610 (4-σ), and and IRAS 04108+2803 (2-σ). Contours for IRAS 04016+2610 at 450μm are drawn at levels of 10 percent (2-σ) The 450μm maps for IRAS 03256+3055 and IRAS 04108+2803 have contours at 1-σ intervals. Central positions are in Table 1. Outflow directions are labeled with bold lines; references for outflows are as follows: IRAS 04016+2610, Hogerheijde, et al. 1998.

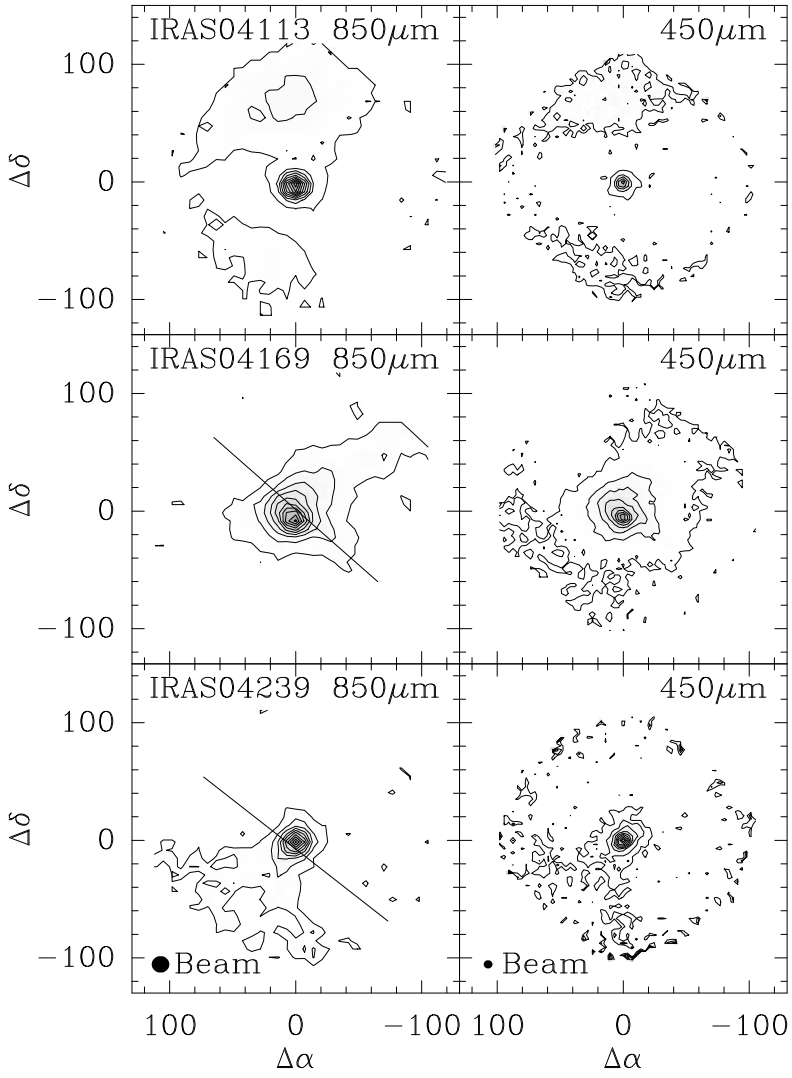

Figure 2.4: Maps of emission at 850 and 450μm. For all the maps, the lowest contour is at the 2-σ level. The 850μm contours increase by ten percent of the peak (IRAS 04113+2758, 6-σ; IRAS 04169+2702, 3-σ; IRAS 04239+2436, 2-σ). The 450μm contours for IRAS 04113+2758 and IRAS 04169+2702 increase by twenty percent (4- and 6σ, respectively) and by ten percent (2-σ) for IRAS 04239+2436. Central positions are in Table 1. Outflow directions are labeled with bold lines;r eferences for outflows are as follows: IRAS 04169+2702, Bontemps et al, 1996.; IRAS 04239+2436, Saito et al., 2001. IRAS 04113+2758 shows no detectable outflow activity (Saito et al., 2001).

We calibrated our flux measurements through observations of Uranus and AFGL 618, a primary and secondary calibrator, respectively. We measured total voltages within 40″ and 120″ apertures. By dividing these values into the expected flux from each of these sources[1], we obtained the nightly calibration factors. For each night, we average the calibration factors and report this average in Table 2.7. In February, we observed AFGL618 seven times and found significant variations ($\sim$40%) in our measurement of its flux at 450 μm. These variations are reflected in the large standard deviation reported as uncertainties ($\delta(C_{40}^{450})$ and $\delta(C_{120}^{450})$) in Table 2.7. To account for uncertainty in the flux calibration, we take the average of the calibration factors as determined from the observations from all three nights in February and propagate the standard deviation as uncertainty in the flux measurement. This final average was used in the voltage-to-flux conversion for data obtained in February, 2000, and is reported in Table 2.7.

2.3.4 Photometry

We find the flux for each of our images by first measuring the total voltage within 40″ and 120″ apertures. Then, we use the calibration factors given in Table 2.7 to convert these values to flux measurements. The fluxes at 450 and 850 μm are given in Table 2.7. Statistical and calibration errors dominate our uncertainty (calculated as in Paper I, Equation 2). In the modeling of these sources, we use the *normalized* intensity ($I_\nu^{norm}(\theta)$), so uncertainty in calibration has no effect on analysis of the radial profile.

In our February 2000 observations, we had maps with a high signal-to-noise ratio, but the calibration errors approach 100% at 450 μm (e.g., L1251B). In Ta-

[1]We use the *fluxes* package in SURF to obtain the expected fluxes for Uranus. In November 1999, these were: $S_{850} = 65.63$ Jy and $S_{450} = 173.37$ Jy. The fluxes for AFGL 618 were $S_{850} = 4.56$ Jy and $S_{450} = 11.2$ Jy as reported on the SCUBA secondary calibrator web page. These fluxes for AFGL 618 are comparable (within uncertainty) to the fluxes given, recently, by Jenness et al. (2002).

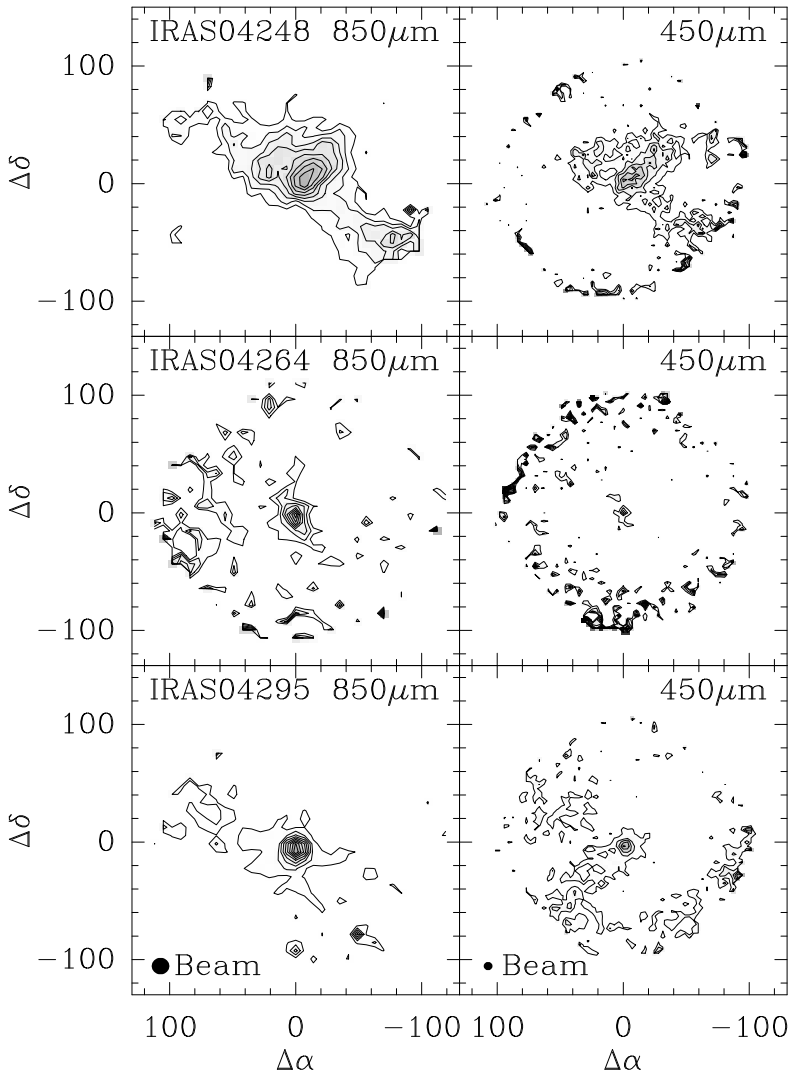

Figure 2.5: Maps of emission at 850 and 450μm. For all the maps, the lowest contour is at the 2-σ level. For IRAS 04248+2612 and IRAS 04264+2433, the 850 and 450μm contours increase by 1-σ intervals. IRAS 04295+2251 has contours that increase by ten percent of the peak (2-σ) at 850μm and twenty percent (3-σ) at 450μm. Central positions are in Table 1.

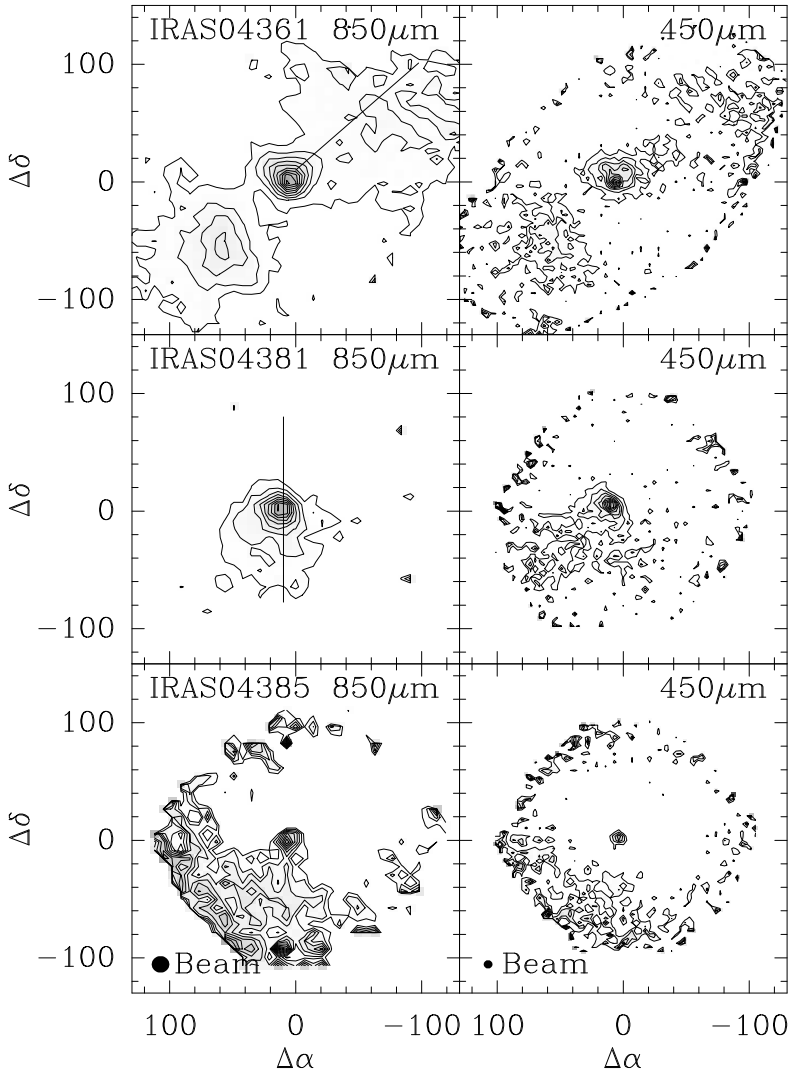

Figure 2.6: Maps of emission at 850 and 450μm. For all the maps, the lowest contour is at the 2-σ level. The 850 and 450μm contours increase by ten percentof the peak for IRAS 04361+2547 and IRAS 04381+2540 corresponding to 5- and 2-σ for IRAS 04361+2547 (850 and 450μm, respectively) and 1-σ for IRAS 04381+2540 (both maps). The contours for IRAS 04385+2550 are drawn at the 1-σ level. Central positions are in Table 1. Outflow directions are labeled with bold lines; references for outflows are as follows: IRAS 04361+2547 and IRAS 04381+2540, Bontemps et al. 1996.

ble 2.7, we include the S/N ratio to give an indication of the quality of our maps. Additional photometry information is given in Table 4.8. The peak intensity centroids are given in Table 2.7. In addition, for IRAS 04016+2610 and 04361+2547, we give the flux and centroid for neighboring condensations. In Table 2.7, we give the calculated values for T_{bol}, L_{obs}, and L_{obs}/L_{smm}.

2.3.5 Morphology

We define an aspect ratio for each of the sources by dividing the major and minor axis lengths as measured at the 2-σ contour. These values are reported in Table 2.7. For some cores (e.g., IRAS 03256+3055, 04016+2610 and 04108+2803), the major and minor axes were not discernable. In some cases, the cores are not ellipsoidal but, instead, have extensions in different directions. Also, the aspect ratio defined by the outer contours does not always reflect the morphology of the inner contours. The average aspect ratio was 1.3±0.4 with the most aspherical source being IRAS 04248+2612 with an aspect ratio of 2.3.

For each modeled source, we determine the deconvolved source size (θ_{dec}) from the FWHM size of the beam (θ_{mb}) and source (θ_{src}) intensity profiles: $\theta_{dec} = \sqrt{\theta_{src}^2 - \theta_{mb}^2}$. The values for θ_{dec}/θ_{mb} are in Table 2.7; the reported uncertainties are based on the variability of θ_{mb} ($\delta\theta_{mb}$ = 1-3″). In most cases (∼70%) , we resolve the emission, but the observed source size is sometimes comparable to the FWHM of the beam. For example, IRAS 04295+2251, with $\theta_{dec}/\theta_{mb} = 0.7$, has an observed intensity profile that, at the FWHM, is only 1.3 times the FWHM of the beam (i.e., $\theta_{src} = 20''$ and $\theta_{mb} = 16''$). In Figure 2.1, we showed that the FWHM beamwidth does change slightly as the telescope cools. However, this mostly affects the 450 μm beam, and we derive our deconvolved source sizes from the 850 μm profiles. Any source with $\theta_{dec}/\theta_{mb} > 1$ is definitely resolved. Of course, those sources with $\theta_{dec}/\theta_{mb} = 0$ are clearly unresolved. For those sources with $0 < \theta_{dec}/\theta_{mb} < 1$,

we have more closely analyzed their profiles. IRAS 04113+2758 was observed in November 1999 when the FWHM of the beam was quite variable ($\pm 3''$), so we do not consider this a resolved source. IRAS 04016+2610, 04239+2436, and 04295+2251 were all observed in February 2000, when the 850 μm beam was fairly stable. We consider each of these sources to be resolved. Further, we determine θ_{dec}/θ_{mb} from the FWHM of the intensity profiles, but our data is sensitive out to 3-5 beamwidths for most sources—i.e. we do resolve the outer envelope emission from these cores. As we will show in Section 3.1, the real discerning power of our observations is not in the inner regions but in the observations of emission from the outer regions of the envelope.

Also, several sources showed additional emission within the maps. For example, IRAS 04016+2610, 04108+2803, and 04361+2547 show sources of continuum emission that have comparable (or even greater) fluxes than the observed Class I protostar. Statistically, however, distinct, neighboring condensations of dust are not common in our sample—only about 20%. In Paper I, we suggested Class I cores might be classified as such because of multiple sources within a beamwidth; in that sample, multiple sources were found in 9/16 of the observed Class 0 and Class I cores. However, the occurrence of multiplicity is much less (3/16) in this sample of Class I cores.

2.4 Models

2.4.1 Power Law Models

As in Paper III, we have modeled the dust emission from a subset of these Class I cores. We have selected the following sources for modeling based on their symmetric morphology and quality of data: CB230, L1251B, IRAS 04166+2706, IRAS 04169+2702, IRAS 04239+2436, IRAS 04248+2612, IRAS 04295+2251, IRAS 04361+2547,

and IRAS 04381+2540. We use a modification of the radiative transfer package by Egan, Leung, & Spagna (1988), *CSdust3* —a ray-tracing, 1-dimensional radiative transfer code. This program has several input parameters: luminosity of the central source, opacity of the dust grains as a function of wavelength, strength of the interstellar radiation field (ISRF), and the density distribution of material surrounding the source.

Primarily, we test power law density distributions, i.e.,

$$n(r) = n_f \left(\frac{r}{r_f} \right)^{-p} ; r \in [r_i, r_o] \tag{2.1}$$

where n_f is the density at a fiducial radius, $r_f = 1000$ AU. The density has a lower limit of 1000 cm^{-3}, roughly simulating the ambient molecular cloud. We choose these models because they are simple and, a priori, make no assumptions about the theory incorporated by the collapse of material. In a later section, we do discuss the Shu collapse model (Shu 1977) because it has only one free parameter and is easily tested. Other theories of low-mass star formation (e.g., Larson (1969), McLaughlin & Pudritz (1997); Foster & Chevalier (1993); Henriksen, André, & Bontemps (1997); Whitworth & Ward-Thompson (2001); etc.) often differ primarily in the value of p.

For each of the model parameters, we have tested a reasonable range on two test cases: CB230 and IRAS 04295+2251. We selected these sources as test cases because of their high S/N maps and azimuthally symmetric morphology. The results from these tests are in Tables 2.7 and 2.7. From these two test cases, we have also determined the uncertainty in p caused by the uncertainty in other parameters (see Table 2.7).

The luminosity of the central source (L_{int}) is determined by matching the modeled (L_{mod}) to the observed bolometric luminosity (L_{obs}). At short wavelengths ($\lambda \leq 60 \mu m$), the cloud becomes optically thick, and the SED becomes more sensitive to opacity and geometry. Therefore, for L_{mod} and L_{obs} we use only those flux points with $\lambda > 60$ μm. For a given mass distribution (constrained by the intensity profile),

we are able to determine the internal luminosity, L_{int}, required to produce L_{obs}. This luminosity, L_{int}, may include both the luminosity of the protostar as well as accretion luminosity—basically, any source of luminosity within the inner radius. In most cases, L_{int} is less than L_{obs} because the interstellar radiation field contributes a portion of the observed bolometric luminosity, $\sim$0.2 $L_\odot$. This is in accord with our results in Papers II and III.

We use dust opacities given by Ossenkopf & Henning (1994) for protostellar cores. They simulated the coagulation of dust grains (with an initial standard MRN size distribution) over 10^5 yr and calculated the opacities for different initial gas densities. For the modeling of our sample, we compare two "types" of dust from Table 1 of Ossenkopf & Henning. In Papers II & III, we have shown that the dust with thin ice mantles provides the best-fit models for preprotostellar and Class 0 sources. The opacities for this dust are given in the fifth column of Table 1 in Ossenkopf & Henning (1994) and, hence, it is named "OH5" dust. In addition, we model sources with the opacities from column 2 of Table 1 (OH2 dust), representing dust grains without ice mantles. In the two test cases, we find that OH5 dust fits the SED best, but the choice of dust type introduces a negligible source of uncertainty in p (see Table 2.7).

We use the interstellar radiation field, given in Paper II, based on Black (1994) and Draine (1978). For ultraviolet to far-infrared wavelengths, we introduce a factor, s_{ISRF}, to scale the ISRF. For the two test cases, $s_{ISRF} = 0.3$ fits the data best, in accord with the ISRF found to fit Class -1 and 0 cores in Papers II & III. For this sample, uncertainty in the ISRF contributes a large source of uncertainty in p: $\delta p \sim 0.4$ (see Table 2.7).

CSdust3 requires the input of an inner and outer radius as boundary conditions to be used in solving the radiative transfer. We have developed some practical criteria in determining these radii. We set the inner radius to 100 AU for all

sources—this corresponds to 0.7″ for the Taurus sources, 0.2″ for CB230, and 0.3″ for L1251B. The outer radius should be, at least, the sum of the chop throw (120″) and the radius of the model. For example, with CB230 (at 450 pc), we used an outer radius of 100,000 AU which accounts for the 120″ chop (54,000 AU) and for modeling out to 100″ (45,000 AU). The outer radius for L1251B is 72,000 AU; for Taurus sources, 33,000 AU. We do choose a lower limit for the density ($n = 10^3$ cm^{-3}), but, for most cores, the outer radius lies within this limit. In Table 2.7, we show the effect of varying the inner and outer radii on the derived value of p. Changes in the inner radius cause a negligible change in p; uncertainty in the outer radius causes an uncertainty $\delta p = 0.3$ in the modeling of CB230 and $\delta p = 0.2$ for IRAS 04295+2251.

By assigning values to these various parameters and simulating the transfer of radiation in the envelope, we calculate the temperature for the assumed density distribution. Then, as described in Paper III, we simulate the observations including the effects of chopping and convolution of the data with the observed beam profile. The selection of this beam profile was discussed in Section 2.2; we took great care in using the appropriate beam since it does vary with time. While a Gaussian beam will cause the derived value of p to be steeper by ∼0.4, using an obseved beam profile from a different night causes negligible uncertainty (see Table 8). We attempted modeling of IRAS 04302+2247, a source that was obviously unresolved. In this case, we were only able to determine that $p > 3.5$, which, of course, we expect in the modeling of a point source.

We constrain the total amount of mass in the envelope by normalizing the modeled SED to the observed 850 μm flux, and the luminosity of the internal source is constrained by the observed luminosity, L_{obs}. Then, we find the best-fit value for p, which we select by the lowest $\Sigma\chi^2$—the sum of the χ^2 values for the 450 and 850 μm profiles (see Equation 4 in Paper III for the definition of χ^2_λ). In most cases, the

best-fit model based on $\Sigma\chi^2$ is identical to that selected by χ^2_{850} (cf. L1251B, IRAS 04361, and IRAS 04381 in Table 2.7); because the uncertainty is much smaller for the 850 μm data, χ^2_{850} is much larger than χ^2_{450} and, hence, dominates the sum. Even though the intensity profiles show Nyquist sampled data, we use, as in Papers II and III, only points spaced by a full beam to calculate χ^2_λ. The derived value of p is virtually unaffected by the envelope mass or the luminosity of the internal source. We list the best-fit models in Table 2.7 along with those models where $p = \pm 0.1$ and $p = \pm 0.5$. In Figures 2.7-2.15, we show the modeled and observed SEDs, radial profiles, and temperature distributions for each of our modeled sources.

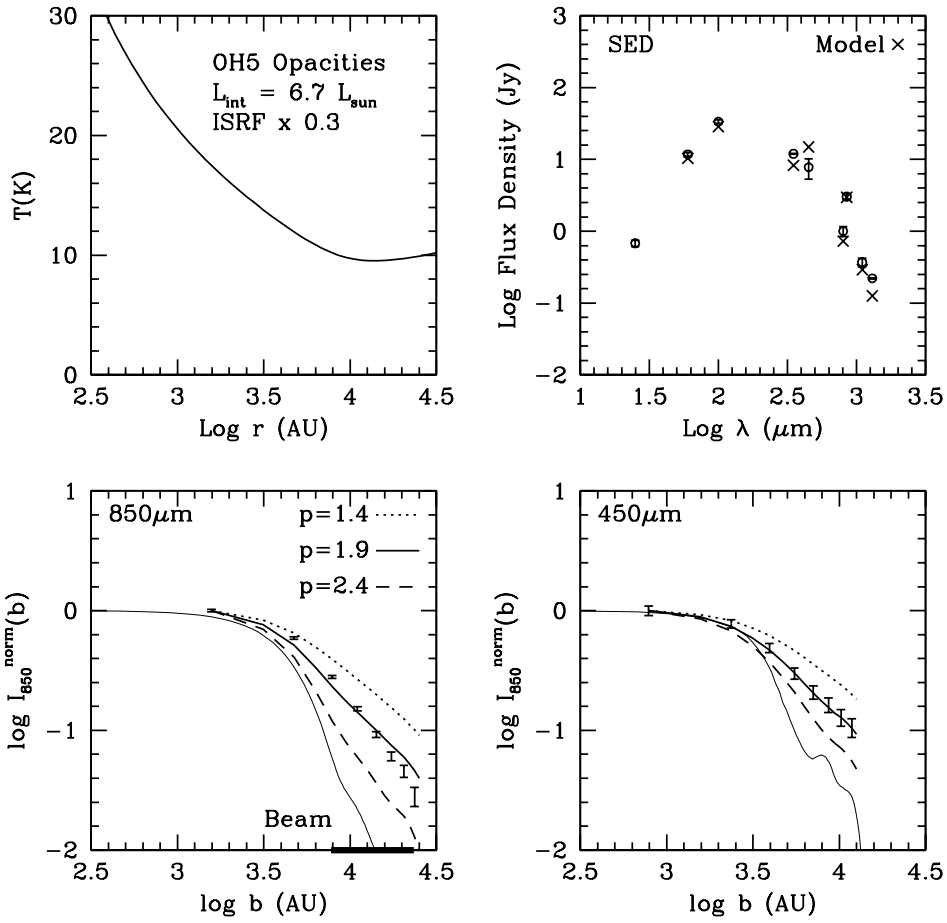

Figure 2.7: Model of CB230. In the upper left panel, we show the modeled temperature profile. The modeled spectral energy distribution is marked by crosses in the upper right panel, the observed fluxes are circles. The two bottom plots have the modeled and observed radial profiles— the best-fit model is a solid dark line. Also shown in these plots are the beam profiles used in the beam convolution. The range of fit for m (in the calculation of p_m) is shown by the bold line on the x-axis.

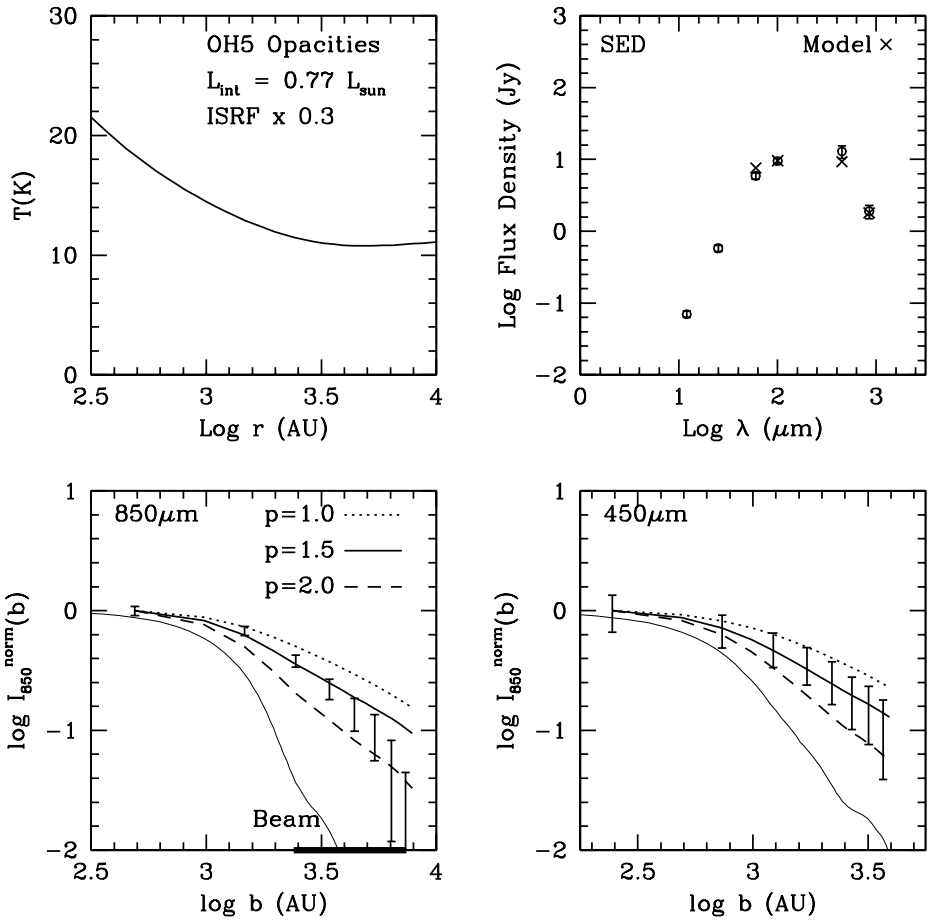

Figure 2.8: Model of L1251B. In the upper left panel, we show the modeled temperature profile. The modeled spectral energy distribution is marked by crosses in the upper right panel, the observed fluxes are circles. The two bottom plots have the modeled and observed radial profiles— the best-fit model is a solid dark line. Also shown in these plots are the beam profiles used in the beam convolution. The range of fit for m (in the calculation of p_m) is shown by the bold line on the x-axis.

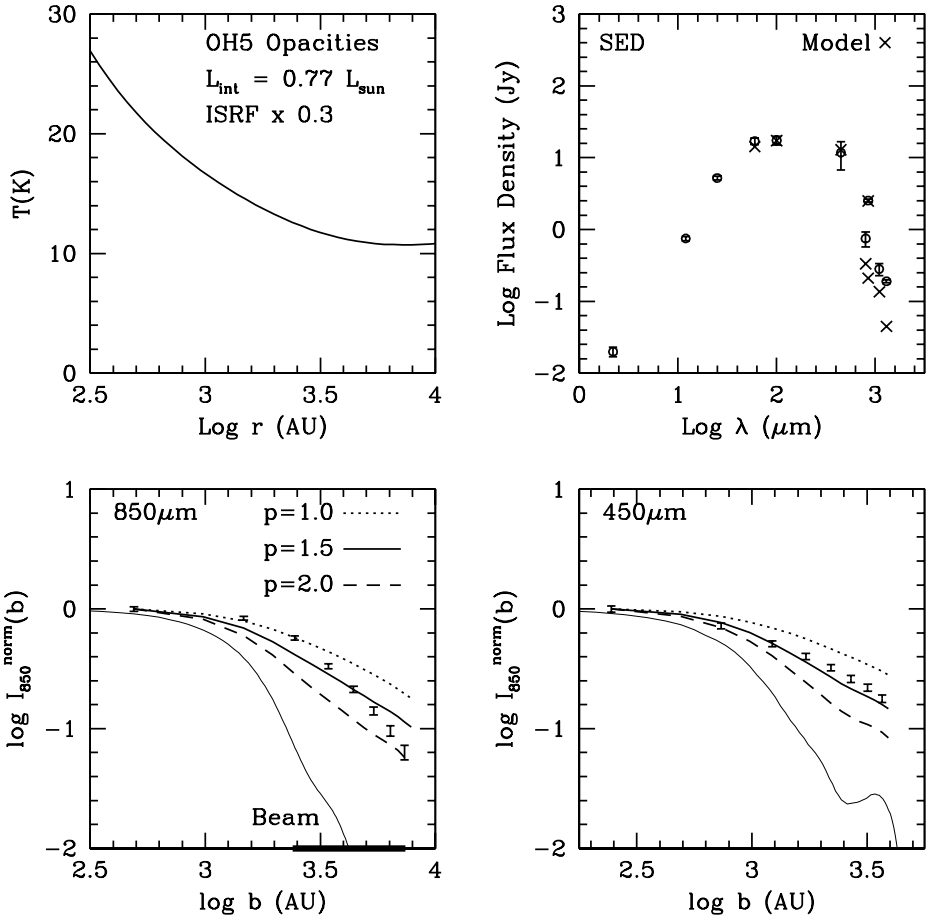

Figure 2.9: Model of IRAS 04166+2706. In the upper left panel, we show the modeled temperature profile. The modeled spectral energy distribution is marked by crosses in the upper right panel, the observed fluxes are circles. The two bottom plots have the modeled and observed radial profiles— the best-fit model is a solid dark line. Also shown in these plots are the beam profiles used in the beam convolution. The range of fit for m (in the calculation of p_m) is shown by the bold line on the x-axis.

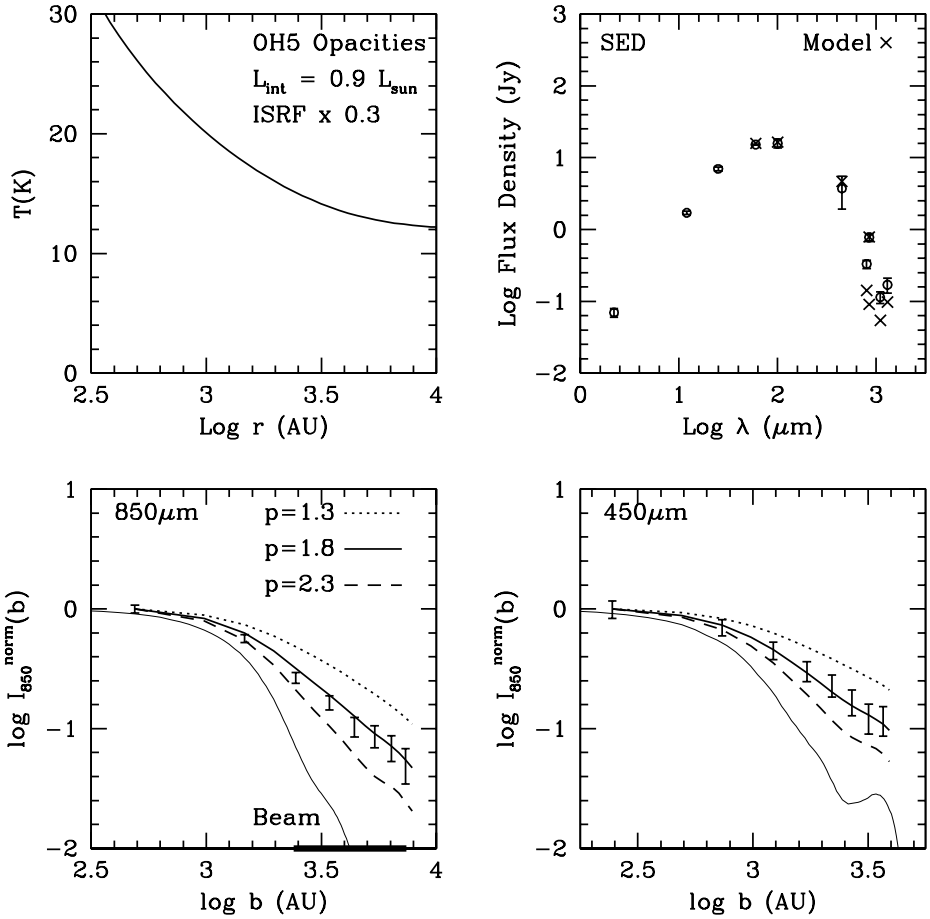

Figure 2.10: Model of IRAS 04169+2702. In the upper left panel, we show the modeled temperature profile. The modeled spectral energy distribution is marked by crosses in the upper right panel, the observed fluxes are circles. The two bottom plots have the modeled and observed radial profiles— the best-fit model is a solid dark line. Also shown in these plots are the beam profiles used in the beam convolution. The range of fit for m (in the calculation of p_m) is shown by the bold line on the x-axis.

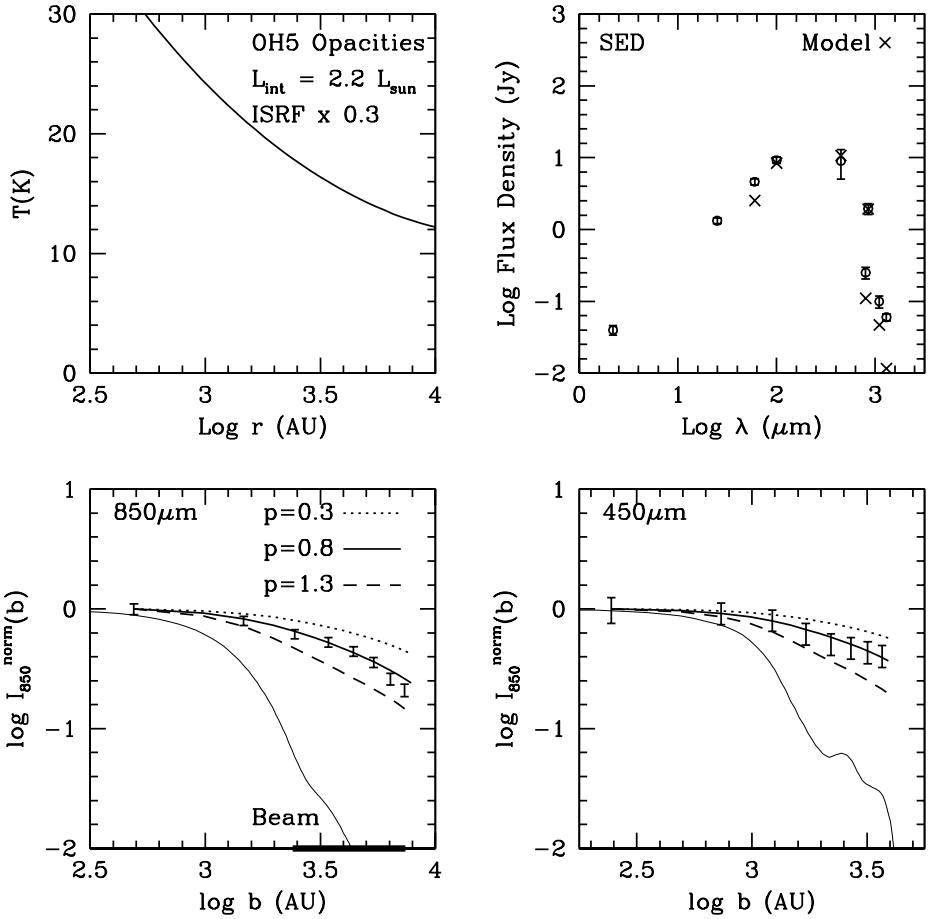

Figure 2.11: Model of IRAS 04239+2436. In the upper left panel, we show the modeled temperature profile. The modeled spectral energy distribution is marked by crosses in the upper right panel, the observed fluxes are circles. The two bottom plots have the modeled and observed radial profiles— the best-fit model is a solid dark line. Also shown in these plots are the beam profiles used in the beam convolution. The range of fit for m (in the calculation of p_m) is shown by the bold line on the x-axis.

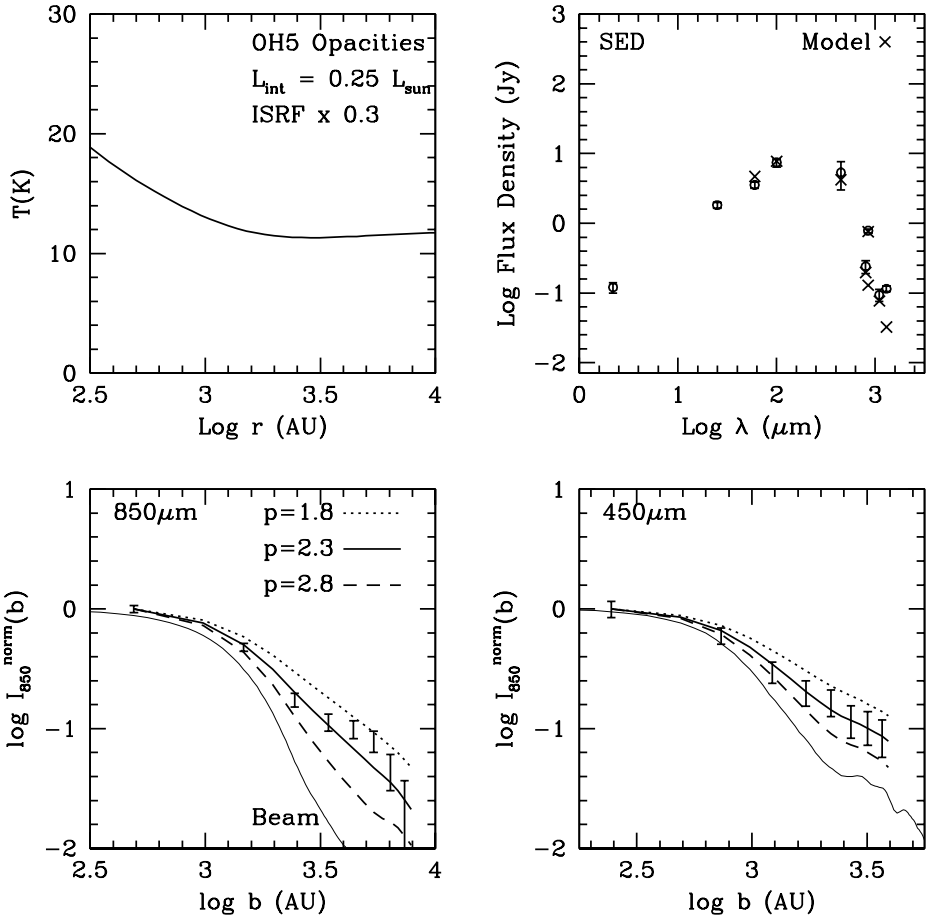

Figure 2.12: Model of IRAS 04248+2612. In the upper left panel, we show the modeled temperature profile. The modeled spectral energy distribution is marked by crosses in the upper right panel, the observed fluxes are circles. The two bottom plots have the modeled and observed radial profiles— the best-fit model is a solid dark line. Also shown in these plots are the beam profiles used in the beam convolution. The range of fit for m (in the calculation of p_m) is shown by the bold line on the x-axis.

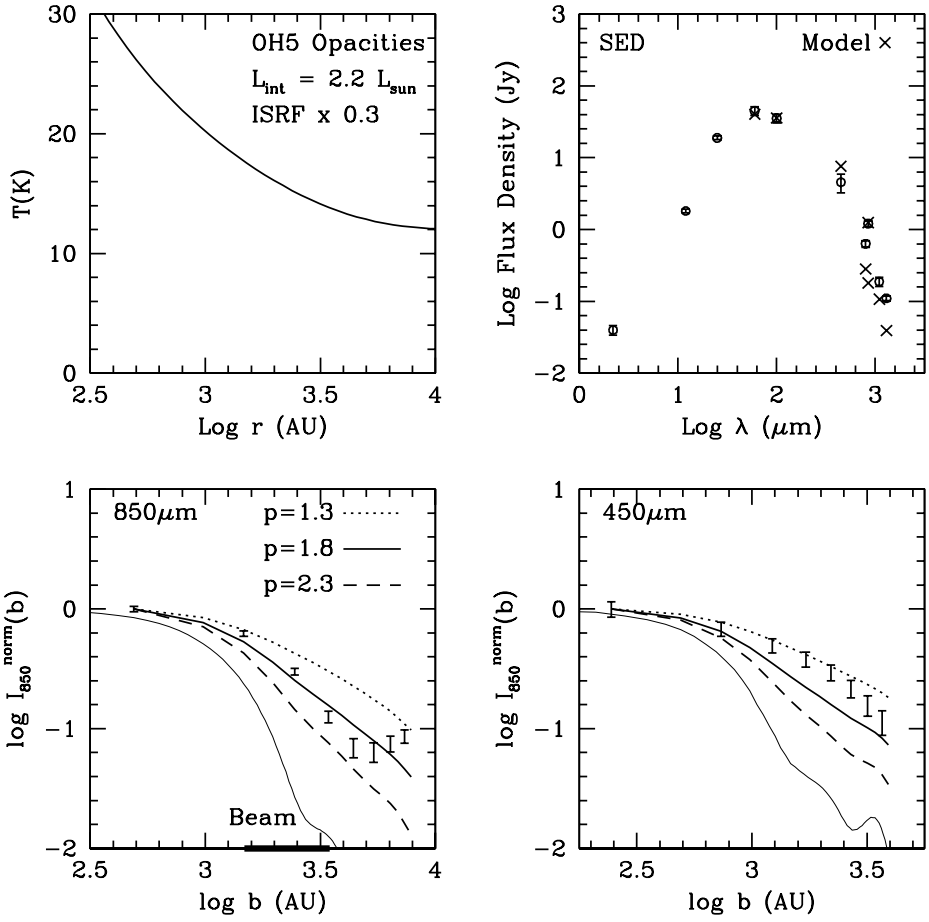

Figure 2.13: Model of IRAS 04295+2251. In the upper left panel, we show the modeled temperature profile. The modeled spectral energy distribution is marked by crosses in the upper right panel, the observed fluxes are circles. The two bottom plots have the modeled and observed radial profiles— the best-fit model is a solid dark line. Also shown in these plots are the beam profiles used in the beam convolution. The range of fit for m (in the calculation of p_m) is shown by the bold line on the x-axis.

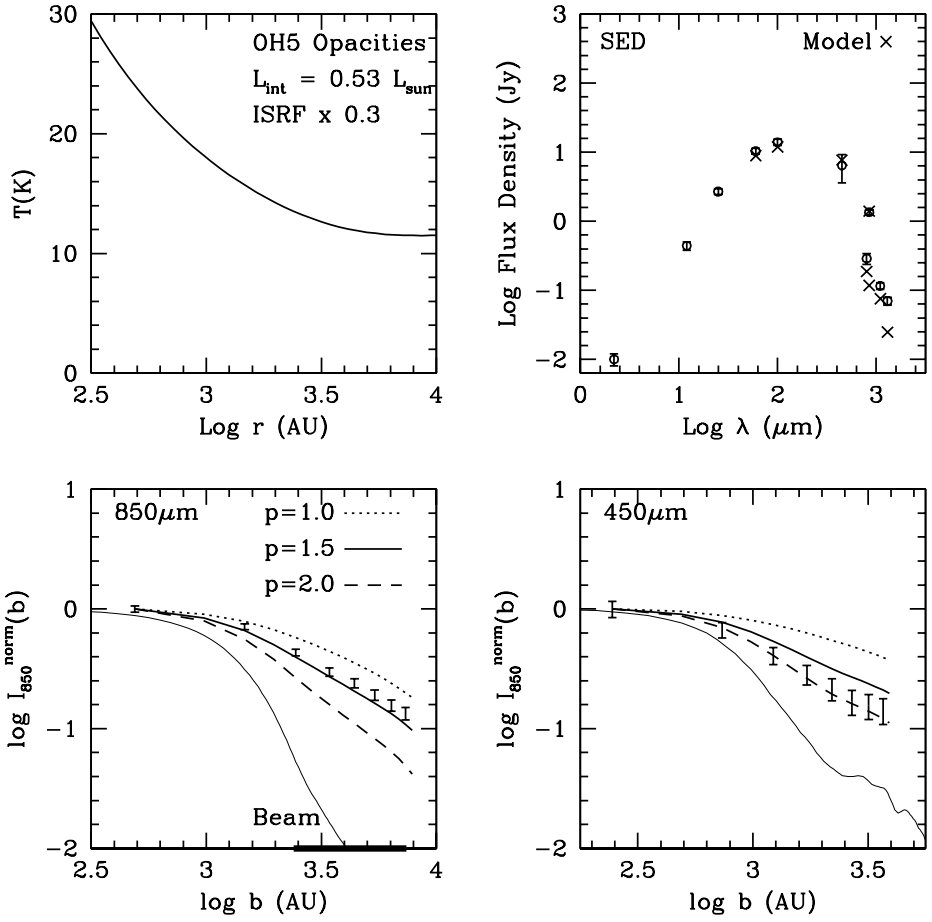

Figure 2.14: Model of IRAS 04361+2547. In the upper left panel, we show the modeled temperature profile. The modeled spectral energy distribution is marked by crosses in the upper right panel, the observed fluxes are circles. The two bottom plots have the modeled and observed radial profiles— the best-fit model is a solid dark line. Also shown in these plots are the beam profiles used in the beam convolution. The range of fit for m (in the calculation of p_m) is shown by the bold line on the x-axis.

2.4.2 Top Hat Models

We consider simple models of the density distribution in order to investigate the discerning capabilities of our methods—i.e. are we able to discern a power law distribution in the density from a top hat distribution? We define a top hat density distribution as an envelope model where the density is constant from the inner radius to some "break" radius; then, the density drops to 10^3 cm^{-3} in the region from this break radius to the outer radius. It should be most difficult to discern a power law from top hat distribution with the source for which we derive the steepest power law, $p = 2.3$ for IRAS 04295+2251. In Figure 2.16, we show the modeled intensity profiles for three top hat distributions with breaks in the density at 5", 15", and 25" (corresponding to 700, 2100, and 3500 AU). The maximum density in the top hat functions is set so that the total mass is equal to that in the derived power law distribution. Also, in this figure, we show the best-fit power law model along with the observed intensity profile for IRAS 04295+2251. This intensity profile shows a "bump" at about 5000 AU (or 35") that is coincident with additional emission within the field-of-view. We find the 5" and 15" top hat functions do not have enough emission at large radii to reproduce the 850 μm profile. The 25" top hat has emission in the outer regions that is not seen in either the 850 or 450 μm observed profile. Likewise, the intensity profiles of other sources in our sample are not easily reproduced by simple top hat functions. Indeed, power law models, in contrast to the top hat functions, match the shape of the observed intensity profiles quite well.

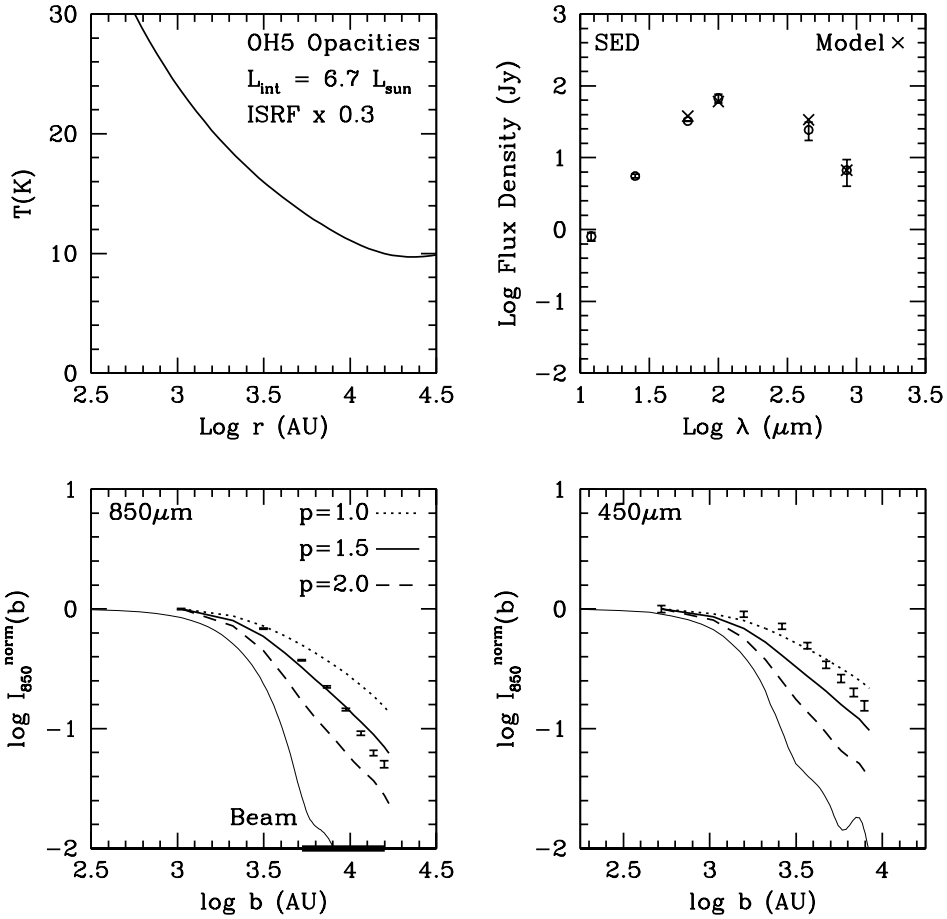

Figure 2.15: Model of IRAS 04381+2540. In the upper left panel, we show the modeled temperature profile. The modeled spectral energy distribution is marked by crosses in the upper right panel, the observed fluxes are circles. The two bottom plots have the modeled and observed radial profiles— the best-fit model is a solid dark line. Also shown in these plots are the beam profiles used in the beam convolution. The range of fit for m (in the calculation of p_m) is shown by the bold line on the x-axis.

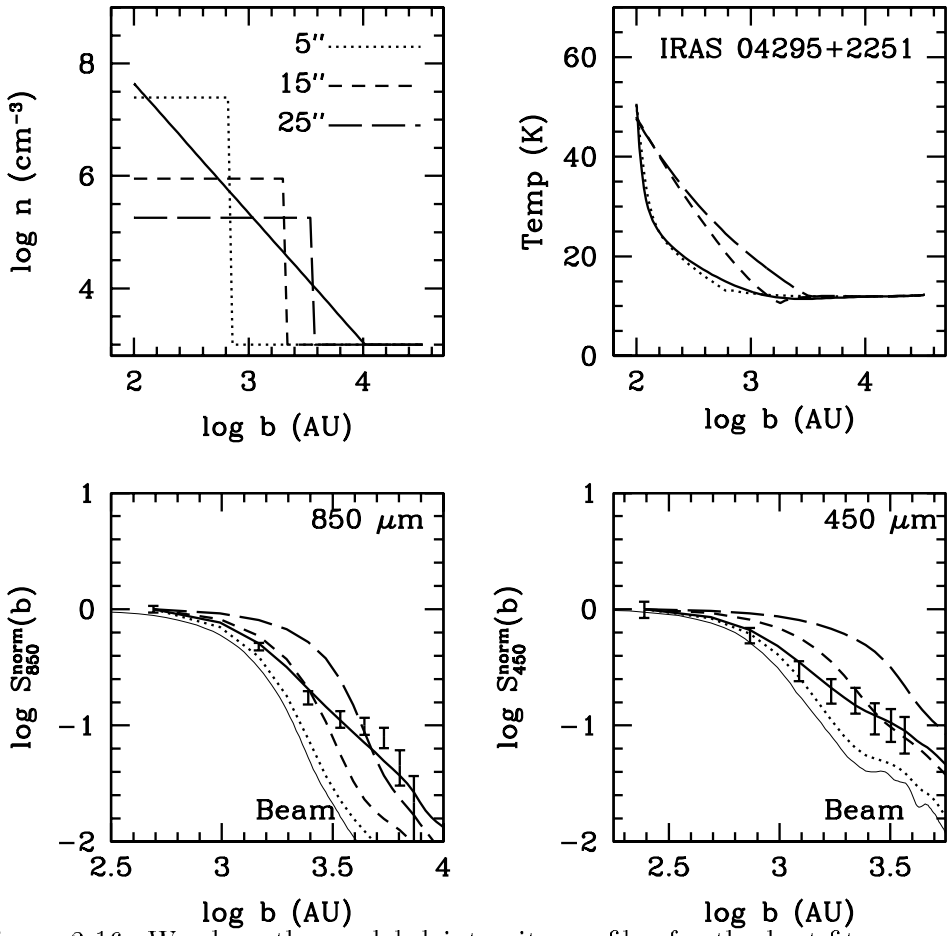

Figure 2.16: We show the modeled intensity profiles for the best-fit power law of IRAS 04295+2251 ($p = 2.3$, solid line) along with a series of top hat functions. The top hat functions (dashed and dotted lines) have steps at 5", 15", and 25" where the density drops to 10^3 cm^{-3}. The bottom panels also have the observed beam profile shown by the light, solid line.

2.4.3 Shu Collapse Models

In addition to modeling power law density distributions for our sample of nine cores, we have modeled these sources with the Shu inside-out collapse model (Shu 1977). This model begins with a singular isothermal sphere with a density distribution that is proportional to r^{-2}. Through some perturbation, collapse begins inside the cloud and proceeds outward at the sound speed (a_{eff}). As collapse ensues, the cloud's density distribution is described by an outer, static region with $n \propto r^{-2}$ and a region within the front of collapse (or infall radius, r_{inf}) whose density approaches $n \propto r^{-1.5}$ (indicative of freefall). The beauty of this theory is that there is only one free parameter: time. As time progresses, the front of collapse (or infall radius, r_{inf}) propagates outward at a_{eff}.

We determine a_{eff} from the observed linewidths in Table 4.2. Assuming a gas temperature of 10K, we are able to separate the turbulent and thermal components (a_{turb} and a_{th}) of these linewidths and determine the effective sound speed ($a_{eff} = \sqrt{a_{th}^2 + a_{turb}^2}$). For each source, a_{eff} is in Table 4.2.

We list the parameters for our Shu collapse models in Table 2.7. For all modeled sources, the spectral energy distribution is not fitted well by the Shu model. The Shu model overestimates all fluxes with $\lambda > 100$ μm, indicating this model predicts too much mass within the cores. We may have overestimated the sound speed in these cores and, hence, also the mass (see Section 6.1). Also, variations in dust opacity and geometry can greatly affect the SED (e.g., Moore & Doty 2002). Consequently, in choosing the best-fit Shu models, we give little regard to the values for χ^2_{SED}. Instead, we focus on the nature of the intensity profiles wherein lies the strength of our analysis.

The beam at 850 μm ($\theta_{mb} = 15''$) corresponds to 2100, 4500, and 6800 AU for Taurus, L1251B, and CB230, respectively. For all but two sources (IRAS 04169+2702 and 04381+2540), the infall radius of the best-fit Shu model falls within

these radii. Basically, then, we are fitting straight power laws with an index of $p = 2$. In Figure 2.17, we show the results of two models for IRAS 04295+2251. The best-fit model is with $r_{infall} = 500$ AU, but we include a model with $r_{infall} = 3000$ AU. The larger infall radius causes the modeled profile to flatten.

For IRAS 04169+2702, the best-fit infall radius is slightly larger than the JCMT beamwidth ($r_{infall} = 3000$ AU), and the best-fit Shu model has improved χ^2 values over the power law model ($p = 1.5$). In Figure 2.18, we show the results of this model. IRAS 04169+2702 was fitted with a power law of $p = 1.5$, so one might conclude that the Shu model should fit with an infall radius outside our modeling range. However, the Shu model predicts an inner region that *approaches* $n \propto r^{-1.5}$. The density distribution just within the infall radius is actually significantly shallower than $r^{-1.5}$, so the steep outer region is required to fit the data.

Our basic conclusion for these Shu collapse models is that most sources in this sample exhibit no evidence for a break in the power law density distribution on the scales we can probe with SCUBA ($\sim 1000 - 8000$ AU).

2.4.4 Simple Analysis

As in Paper I, we offer the results of a simple analysis involving the slope, m, of the outer part of the intensity profile (Adams 1991). Assuming the temperature distribution in the envelope to be described by a power law, $T_d(r) = T_d(r_f)(r/r_f)^{-q}$ where r_f is a fiducial radius, one can determine the density power law index, which we call p_m, by the following relation: $p_m = m - q + 1$ (see Equations 5-8 in Paper I; assume $q = 0.4$). In Paper I, we argued that this method is of dubious validity for two reasons: failure of the Rayleigh-Jeans approximation and deviation of the temperature profile from a power law due to heating from the ISRF and the central source. In order to compare with our more detailed modeling, we have performed such an analysis here to determine p_m.

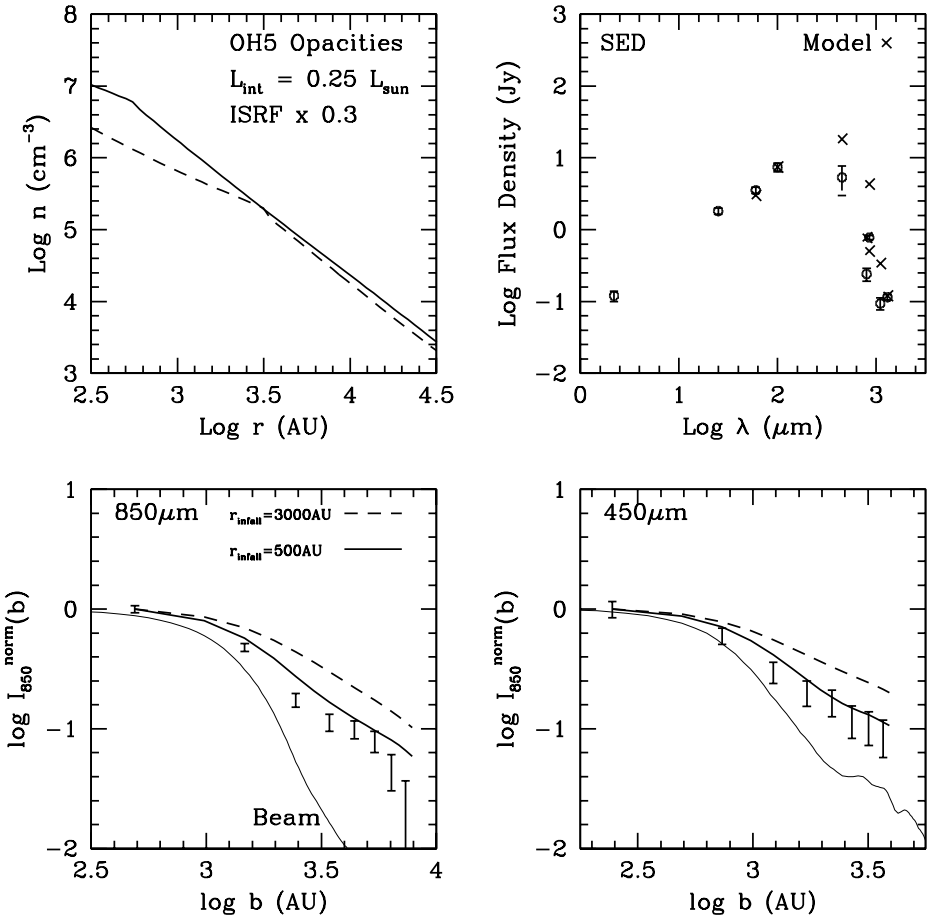

Figure 2.17: Shu collapse models for IRAS 04295+2251 with two different infall radii, 500 (solid) and 3000 AU (dashed). In the upper left panel, we show the modeled density profile. The modeled spectral energy distribution is marked by crosses in the upper right panel, the observed fluxes are circles with errorbars. The two bottom plots have the modeled and observed radial profiles—the best-fit model is a solid dark line. Also shown in these plots are the beam profiles used in the beam convolution (solid light line).

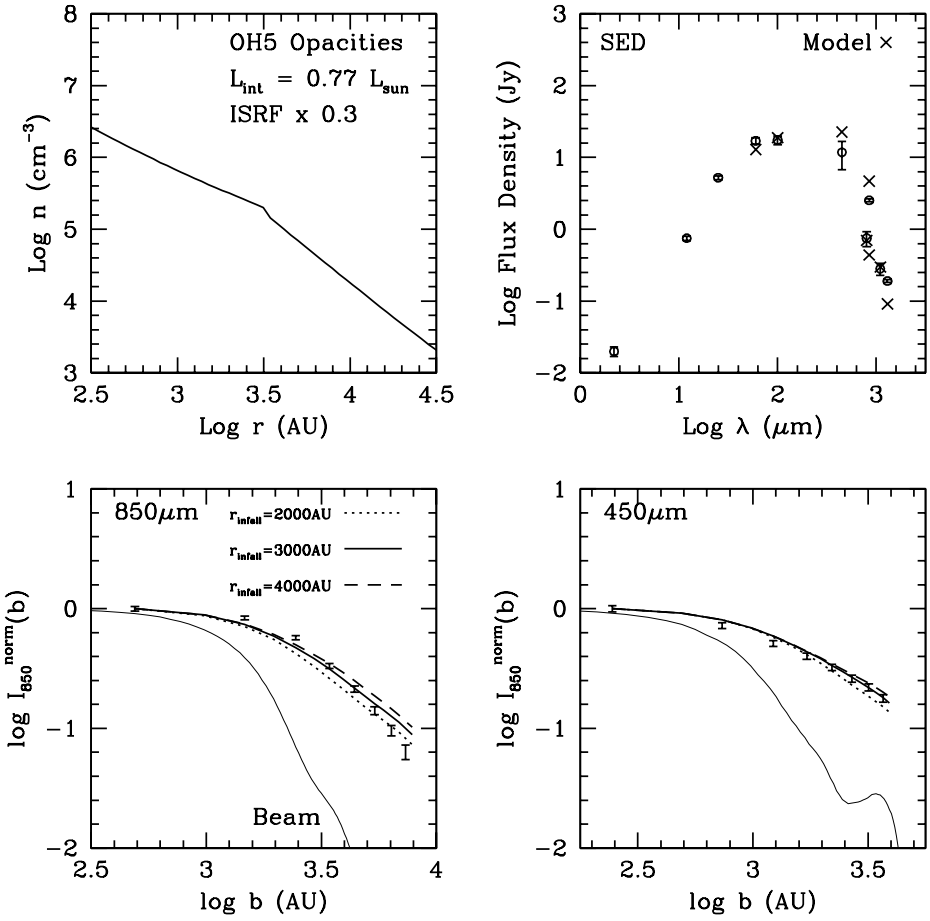

Figure 2.18: Shu collapse model for IRAS 04169+2702. In the upper left panel, we show the modeled density profile. The modeled spectral energy distribution is marked by crosses in the upper right panel, the observed fluxes are circles. The two bottom plots have the modeled and observed radial profiles—the best-fit model is a solid dark line. Also shown in these plots are the beam profiles used in the beam convolution (solid light line).

In Figures 2.7-2.15, we show the range over which we fit for m by the bold line on the x-axis of the 850 μm intensity profile. The derived values of p_m from the linear fits to the 850 μm profiles are in Table 2.7; we did not calculate m for the 450 μm data. The average difference between p_m and p is $\langle p_m - p \rangle = 0.6 \pm 0.3$; i.e., the simple analysis tends to predict a much steeper density profile. This discrepancy is discussed in greater detail in Paper I (Section 4.2), but, in short, the failure of Rayleigh-Jeans approximation causes p_m to be steeper than the actual distribution; exclusion of the ISRF causes p_m to be shallower than the actual distribution.

If we apply this correction to the sources analyzed in Paper I by this method, we find $\langle p_m^{cor} \rangle = 1.5 \pm 0.5$ (compared to $\langle p \rangle = 1.6 \pm 0.4$ reported in this paper).

Additionally, we apply the correction to the results of the large 1.3 mm survey by Motte & André (2001). At this wavelength, $h\nu/k$ =11 K, so the Rayleigh-Jeans approximation (where $h\nu/kT \ll 1$) is better, but still not completely valid. Also, Motte & André chose values for q that ranged from -0.2 to 0.4 for their sample of Class 0 and I cores. From Figures 2.7-2.15, it is clear that a negative power law (indicative of external heating) does not describe the temperature profiles for these evolved protostars, and $q = 0$ can be ruled out for all but one source, IRAS 04295+2251. Therefore, we assume $q = 0.4$ and calculate p_m from their values for m: $\langle p_m \rangle = 1.8 \pm 0.4$, and, with our rough correction, $\langle p_m^{cor} \rangle = 1.2 \pm 0.5$. However, because the Rayleigh-Jeans approximation is less invalid at these longer wavelengths, this correction factor is probably too large and, hence, p_m^{cor} should be slightly larger.

2.4.5 Disk Contribution

We provide a simple analysis to determine the effect of the dust emission from a disk on our models. We assume the emission from a disk to be included only in the central beam of our observations. Mundy et al. (1996) found the disk for HL Tau to be <180 AU, and, since our beam subtends 2000-7000 AU, this assumption is

reasonable. For the two test cases, CB230 and IRAS 04295+2210, we determine the effects of including a point source within the central beam that contributes one-half of the measured flux. In Figure 2.19, we show the results of adding this point source to the modeled intensity profile. The addition of this point source causes the modeled intensity profile to steepen—hence, the best-fit intensity profile, when a point source is considered, can be matched by a *shallower* density profile. We find the best-fit density power law to be shallower by $p = 0.5$ when an unresolved component contributes one-half the flux measured within the central JCMT beamwidth. Therefore, until the submillimeter emission from disks is better constrained, we attribute an additional source of uncertainty in our calculation of p: $\delta p = -0.5$. However, this effect could be much more important for Class I cores, where the envelope is less substantial, than for Class 0 cores.

Observing submillimeter emission from disks requires submillimeter interferometers (e.g., SMA, ALMA), but we make some simple estimates of the disk emission for one source, IRAS 04361+2547. This source was observed in detail by Terebey et al. (1990, 1993) at near-infrared and millimeter wavelengths from which they suggest the existence of a $\sim$1000 AU disk or, at least, some dense component near the central position of this protostar. At $\lambda = 2.6$ mm, they report $S_\nu = 21 \pm 7$ mJy (1993)—observations at the Owens Valley Radio Observatory (OVRO) with a synthesized beam of $7.7'' \times 6.6''$. Further, they claim that these flux measurements are dominated by the emission from dust and not free-free emission. With our power law model for this source, we predict $S_\nu \sim 2$ mJy (at $\lambda = 2.7$ mm); i.e., the observed flux does require the existence of an additional source of flux other than the envelope. Indeed, we consistently underestimate the long-wavelength flux ($\lambda > 1$ mm) with our model of the envelope for all sources, further suggesting the existence of some unresolved component in these cores.

We adopt a simple disk model (Butner et al. 1994) in order to estimate the

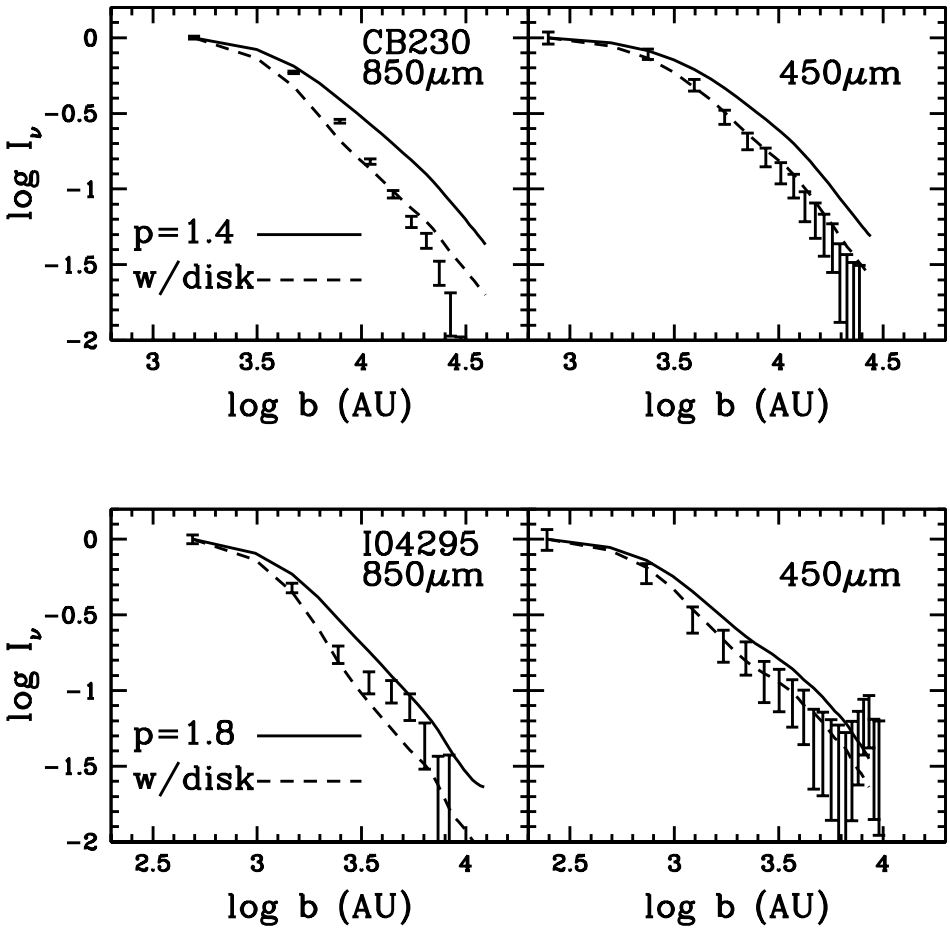

Figure 2.19: The observed radial intensity profiles are shown as error bars for CB230 and IRAS 04285+2251. The best-fit models, assuming all emission originates in only the envelope, are $p = 1.9$ and $p = 2.3$ for CB230 and IRAS 04295+2251, respectively. The solid line represents a model of the envelope that has a shallower density profile by 0.5 ($p = 1.4$ and $p = 1.8$). The dashed line results from adding a point source to this modeled envelope emission. This point source can cause the modeled intensity profile from the envelope+disk to be considerably steeper, and, hence, the derived density power law for the envelope is shallower. We assume moderate fluxes for the disk and find the effect to be a decrease in p by 0.5, but the effect could possibly be much more significant.

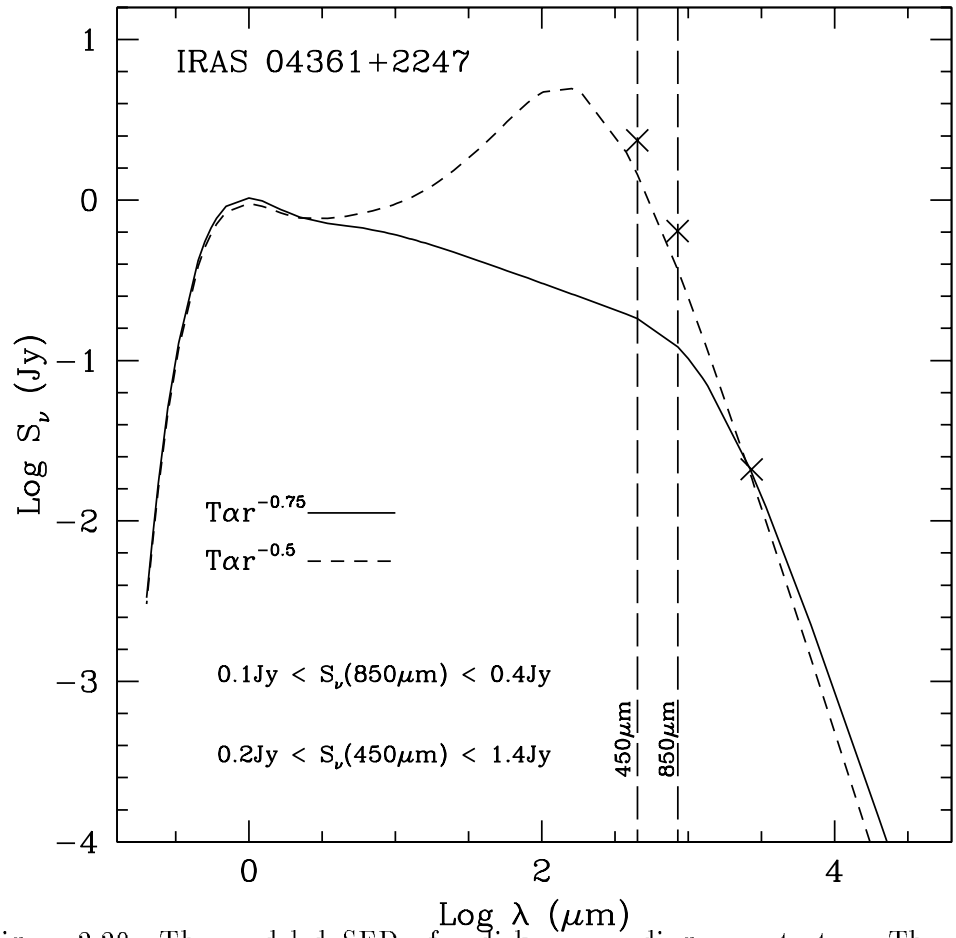

Figure 2.20: The modeled SED of a disk surrounding a protostar. The surface density profile of the dust within this disk is a power law ($\Sigma \propto r^{-1.5}$). The solid line shows a model where the temperature power law is steep ($T \propto r^{-0.75}$) while the dashed line model has a shallower profile ($T \propto r^{-0.5}$). The latter is intended to simulate the effects of flaring. The crosses are observed 2.6 mm flux density from Terebey et al. (1993) and the submillimeter fluxes in this paper (for 40″ aperture). The ranges for S_ν at 850 and 450 μm as derived from the two models are given—these ranges are reasonable upper and lower limits on the dust emission from the disk at these wavelengths.

850 and 450 μm flux for IRAS 04361+2547. The model consists of a central protostar surrounded by a disk whose surface density is described by a power law ($\Sigma \propto r^{-1.5}$). We assume a dust opacity of $\kappa_\nu \propto \nu^\beta$ where $\beta = 1$ and $\kappa(850\ \mu\mathrm{m}) = 0.018\ \mathrm{cm^2 gm^{-1}}$. In Figure 2.20, we show the results of two calculations. The solid line represents a temperature profile in the disk that follows a power law, $T \propto r^{-0.75}$. The dashed line shows a disk with $T \propto r^{-0.5}$; the outer edges of the disk are hotter and, thus, crudely simulate a flared disk. From the model of the "flared" disk, we set reasonable limits for the flux at 850 and 450 μm: $S_\nu(850\ \mu\mathrm{m}) < 0.4$ Jy and $S_\nu(450\ \mu\mathrm{m}) < 1.4$ Jy. For each wavelength, these upper limits are 60% of the observed flux in a 40″ aperture.

We have completed a similar analysis for IRAS 04108+2803. Terebey et al. (1993) found $S_\nu(2.6\ \mathrm{mm}) = 15$ mJy ($\theta_{mb} = 8.5'' \times 7.4''$) for this Class I source. Through the simple disk model, we set the following upper limits: $S_\nu(850\ \mu\mathrm{m}) < 0.24$ Jy and $S_\nu(450\ \mu\mathrm{m}) < 0.84$ Jy. These upper limits correspond to 30% more than the observed 850 μm flux (within errors) and 74% of the observed 450 μm flux. IRAS 04108+2803 is not resolved by our observations, so it is conceivable that all of our observed flux is from a cental point source. Likewise, the observed 2.7 mm flux for IRAS 04016+2610 (6.8 mJy)(Hogerheijde et al. 1997) sets an upper limit on the submillimeter fluxes originating from the presumed disk: $S_\nu(850\ \mu\mathrm{m}) < 0.15$ Jy and $S_\nu(450\ \mu\mathrm{m}) < 0.73$ Jy, 25% and 94% of the observed 850 and 450 μm fluxes (40″ aperture), respectively. The central component of IRAS 04016+2610 (L1489) was not resolved by our observations, so, again, it is possible that all of the submillimeter flux is from an unresolved central component. Indeed, since the nearby condensation to IRAS 04016+2610 lies partially within the 40″ aperture, our reported flux values probably overestimate the flux of this Class I protostar.

Chandler & Richer (2000) investigated the problem of disk contribution to the submillimeter continuum flux and concluded that the existence of a disk in Class 0 sources, where the envelope is more substantial, has little effect on the derived

value for p. Further, they claim the disk does become a significant contributor in Class I objects. The envelope is less prominent in these cores, and a higher fraction of flux coming from the disk (i.e., by their formalism, decreased f_{env}) causes a lower value for p. We conclude similarly, claiming that the inclusion of a disk causes the value for p to be decreased by 0.5; however, this effect could be significantly greater. Firmer conclusions await constraints from submillimeter interferometric observations.

2.5 Individual Sources

2.5.1 CB230

CB230 (also IRAS 21169+6804) is the most luminous source we observed. It is also the most distant at 450 pc (Launhardt & Henning 1997). Yun & Clemens (1994) observed a molecular outflow in the ^{12}CO 2-1 line for which the direction is shown on the 850 μm contour map in Figure 2.2.

The submillimeter dust emission from CB230 is quite round with an aspect ratio of about 1. There does, however, appear to be a slight extension in the direction perpendicular to the outflow axis (oriented N-S). Due to the observed symmetry, we chose this source to model as a test case (see Table 2.7). The best-fit power law for CB230 is $p = 1.9$. We find good fits for both the 850 and 450 μm radial profiles, and the spectral energy distribution is matched well except for the 450 μm flux. This discrepancy is probably due to poor calibration at 450 μm, but, since the focus of our modeling (i.e., the radial distribution) is independent of the absolute flux, we have not pursued this in great detail.

2.5.2 IRAS 04295+2251

IRAS 04295+2251 is the least luminous source we have modeled, with L_{obs} = 0.6 $L_\odot$ and L_{int} = 0.3 $L_\odot$. It is clearly a Class I core by the bolometric temperature criterion with T_{bol} = 270 K, but it is Class 0 by its submillimeter luminosity—L_{obs}/L_{smm} = 50. The core is resolved at 850 μm, but its deconvolved size is the least of any of our modeled sources (θ_{dec}/θ_{mb} = 0.8). This source also has the highest derived value for p (2.3). We discuss the correlation between p and θ_{dec}/θ_{mb} in a later section. From the modeled density profile, we found the envelope mass to be 0.10 $M_\odot$. We chose this source as one of our test cases (see Table 2.7) because of its symmetric morphology (aspect ratio = 1) and high quality data (S/N=40 at 850 μm).

IRAS 04295+2251 is the only object in our sample that was detected by the NRAO VLA Sky Survey (NVSS) at 21 cm (Condon et al. 1998). While it is not uncommon to find continuum radio emission ($\lambda > 3$ cm) from Class I cores (Lucas et al. 2001), reports of strong emission at such a long wavelength are rare (cf. Skinner 1993).

2.5.3 IRAS 04166+2706

IRAS 04166+2706 is a protostar associated with the B213 dark cloud in Taurus with a well-detected outflow in the northeast to southwest direction (Bontemps et al. 1996). The observations of IRAS04166+2706 were originally presented in Paper I; but, since the core was classified as a Class I source (using the T_{bol} criterion), we model it here. The submillimeter emission is characterized by circularly symmetric contours except for an extension perpendicular (southeast) to the outflow direction in the lowest contour interval (10% of the peak or 3σ; Paper I). We report the fluxes in a 120″ aperture here: S_{850} = 1.9±0.6 Jy and S_{450} = 12.9±3.9 Jy. The bolometric luminosity is 0.5 $L_\odot$ and the bolometric temperature is 75 K.

2.5.4 IRAS 04248+2612

IRAS 04248+2612 is about one arcminute north of the starless core Barnard 217 (B217) and is coincident with HH31 IRS2. Padgett et al. (1999) observed IRAS 04248+2612 with HST/NICMOS in the near-infrared bands. Their images showed a clear bipolar structure, oriented NW-SE, that they claim is a reflection nebulosity, near-infrared light escaping by way of an outflow cavity. In addition, they observe a dark lane aligned perpendicular to this nebulosity. Our submillimeter maps (which exclude B217), show two sets of extensions: 1) on a small scale of $\sim 50''$, in the direction of the bipolar nebulosity (NW-SE) and 2) on a larger scale ($\sim 200''$), aligned with the dark lanes observed by Padgett et al. (1999) in a NE-SW direction. This large-scale structure is probably indicative of a filamentary-like distribution of mass in the cloud. The small-scale structure (within the central $30''$) is probably due to heating of the dust caused, in some way, by an outflow.

Myers et al. (1988) report no outflow activity in their ^{12}CO 2-1 observations, for which the noise in one channel was $\sim$0.2 K, but Moriarty-Schieven et al. (1992) find that the ^{12}CO 3-2 line observed at the central position shows low velocity line wings ($\Delta v \sim 4.5$ km s^{-1}). Unfortunately, no molecular maps clarifying this outflow question have been published.

Despite the asymmetric morphology of this source, we have attempted to model the dust emission. The best-fit power law is the lowest of any source, $p = 0.8$, and renders quite a good fit (see Figure 2.11). Of course, the extended emission is included in the azimuthal radial average, so one might argue that this is the source of the modeled, flattened density distribution. However, we excluded the emission from the large-scale, NE-SW extensions and found that the best-fit power law distribution is still very low: $p = 1.0$. IRAS 04248+2612 is clearly different from all of our other sources, both in morphology and modeled density distribution. Its aspect ratio (see Table 2.7) is 2.3, the highest of any source. In Paper III,

we showed that there does seem to be some correlation between aspect ratio and density distribution—i.e., those sources with a high aspect ratio tend to have flatter density distributions. It is possible that, in IRAS 04248+2612, we are observing the formation of a star under different physical processes and initial conditions than with the other cores.

2.5.5 IRAS 03256+3055

IRAS 03256+3055 is at 320 pc in the Perseus star-forming region. Unfortunately, this object has received little attention observationally, but we offer the first map of its dust emission (Figure 2.3). Ladd, Myers, & Goodman (1994) reported undetectable NH_3 emission towards this object, but other reports of molecular line emission are found in the literature (Mardones et al. 1997, Gregersen et al. 2000). We give its SED information in Table 4.8; this consists of a 60 μm flux and our submillimeter fluxes. Dent, Matthews, & Ward-Thompson (1998) report a very low 800 μm flux—0.125 Jy as compared to the 2.45 Jy we measure at 850 μm. However, their observations were with a single bolometer with a beamsize of $\sim 16''$ while the emission from IRAS 03256+3055 spans $\sim 100''$.

The luminosity of this object is 0.7 $L_\odot$, and, from its poorly sampled SED, we also derive a bolometric temperature of 16 K. This bolometric temperature is much lower than that reported by Jennings et al. (1987)(74 K) and, subsequently, Mardones et al. (1997), but they used IRAS upper limits on the flux at 12, 25, and 100 μm in their calculations. The envelope mass of IRAS 03256+3055 is 1.7 $M_\odot$ and is shared between, at least, three distinct dust condensations and significant extended emission.

Nakamura & Li (2002) have conducted axisymmetric calculations concerning the formation of stellar groups via fragmentation. At least, in morphology, their results are strikingly similar to what we see in IRAS 03256+3055—a ring-like

structure with multiple condensations of dust. IRAS 03256+3055 provides an ideal laboratory in which to test the feasibility of such calculations as that presented by Nakamura & Li (2002) and, similarly, Boss (1993).

2.5.6 IRAS 04016+2610, 04108+2803, 04361+2547, and 04385+2250

These four cores are located in Taurus and associated with L1489, L1495, TMR1, and TMC1. (respectively, for IRAS 04016+2610, 04108+2803, 04361+2547, and 04385+2250). They are all Class I cores by their bolometric temperatures (i.e., $T_{bol} > 70$ K), but the submillimeter luminosity of IRAS 04108+2803 ($L_{obs}/L_{smm} = 111$) identifies it as a Class 0 core.

Each of these cores has a neighboring condensation as shown in Figures 2.3 & 2.6. The flux condensation associated with IRAS 04016+2610 has been noted as a Class -1 core by some (e.g., Hogerheijde & Sandell 2000), and we agree with this classification. Hogerheijde et al. (1998) observed an outflow associated with this Class I core that is not coincident with the flux condensation.

IRAS 04361+2547 does exhibit a peak of submillimeter flux that is coincident with the outflow direction (outflow observed by Bontemps et al. 1996). Motte & André observed this source at 1.3 mm, but the condensation is not obvious at this longer wavelength indicative of the dust in this area being somewhat warmer than, for example, the Class -1 core associated with IRAS 04016+2610, which was detected by Motte & André (2000). Perhaps, the dust is heated directly by the outflow, or it is swept up and then heated by radiation from the central protostar that escapes by way of the outflow cavity. Regardless, IRAS 04361+2547 is probably not a Class -1 core.

IRAS 04108+2803 and 04385+2250 are both surrounded by significant extended emission, but, in contrast to 04361+2547 and 04016+2610, this emission is not distinct from the central core. It could be that these cores have evolved by some

asymmetrical collapse or that they are part of some larger star-forming complex. In the next section, we discuss IRAS 04385+2250 in the context of forming substellar objects.

2.6 Discussion

2.6.1 Envelope Mass

For the modeled sources, we have calculated the envelope mass by integrating the best-fit power law density distribution to an outer radius of 60″ (M_{env} per Equation 6 in Paper III). Because the cloud is optically thin to submillimeter wavelength radiation, the following expression is is often used to estimate the envelope mass (Hildebrand 1983):

$$M_{env}^{iso} = \frac{S_\nu D^2}{B_\nu(T_{iso})\kappa_\nu}; \tag{2.2}$$

where S_ν is the flux density at 850 μm in a 120″ beam (Table 2.7), B_ν is the Planck function, κ_ν is the opacity per gram of gas and dust at 850 μm ($\kappa_\nu = 1.8 \times 10^{-2}$ cm^{-2}gm^{-1} for OH5 dust), T_{iso} is the isothermal dust temperature, and D is the distance to the source. Of course, the dust is not isothermal, but we use our models to estimate the isothermal temperature (T_{iso}) that makes Equation 2 agree with the masses derived from the more detailed models (see Equation 7, Paper III). We use the resulting average T_{iso} (16±4 K) for the modeled sources to calculate the isothermal envelope mass (M_{env}^{iso}) for the unmodeled sources. The values for M_{env} and M_{env}^{iso} are in Table 4.2. In Figure 2.21, we show a histogram of these calculated masses for the Class I sources in this paper and the Class 0 cores in Papers I and IV. The envelopes of Class I cores are clearly less massive than Class 0 sources. Only CB230, of the Class I cores, has $M > 0.5$ M$_\odot$, and it is very close to the Class 0 boundary with $T_{bol} = 74$ K. The remaining cores have $M < 0.5$ M$_\odot$ and are in Taurus.

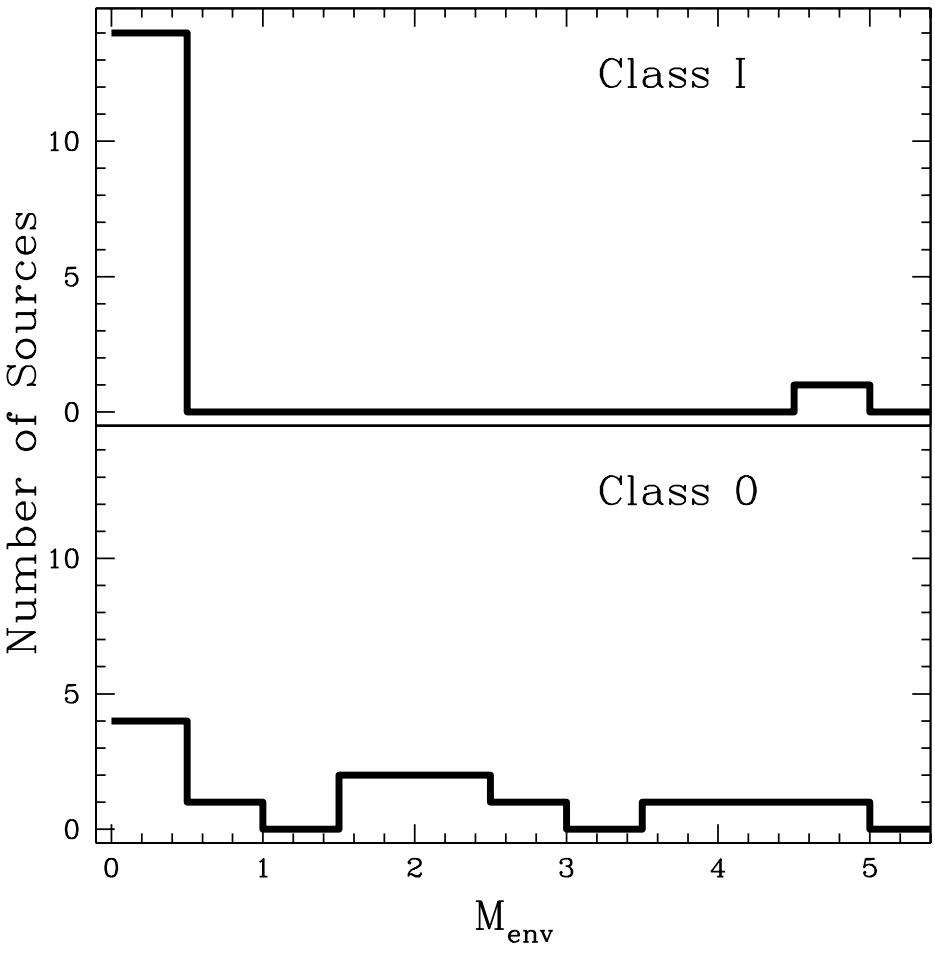

Figure 2.21: The histogram of envelope masses for Class I and Class 0 cores from this paper and Paper III. We show the mass derived from the modeled density profile for the modeled sources and the isothermal mass (assuming 100:1 gas-to-dust ratio) as discussed in the text. All Taurus cores in this sample have $M_{env} < 0.5$ M$_\odot$. Those sources with $M_{env} > 0.5$ M$_\odot$ have $T_{bol} < 75$ K.

In Table 4.2, we also give the FWHM linewidth, associated reference, and the calculated virial mass. The virial mass, $M_{vir}^{\theta_{ap}}$, is corrected for the best-fit power law density distribution as in Paper III (Equations 8 & 9). For those sources not modeled, we adopt the average p (1.6) to calculate the virial mass. To be consistent with our dust mass calculations, we adopt an aperture of $\theta_{ap} = 120''$, which corresponds, in Taurus, to 16,800 AU. We plot the ratio of virial to dust mass (M_{vir}/M_{dust}) against M_{dust} and T_{bol} in Figure 2.22. For $T_{bol} > 70$ K, these two calculations of the envelope mass begin to diverge. Reasonable variations in the dust opacity can introduce a factor of ten uncertainty (Ossenkopf & Henning 1994), but these variations cannot account for values of $M_{vir}/M_{dust} \sim 60$. One scenario is that the molecular tracers used, mostly N_2H^+, do not trace the material surrounding Class I cores. Caselli et al. (2002) mapped two Class I cores coincident with our sample: IRAS 04016+2610 and IRAS 04248+2612 (listed as L1498 and B217, respectively, by Caselli et al.). In both cases, the nearby preprotostellar core is observed to have strong emission in these tracers, but the tracer shows no peak on the Class I core. Simply, observations of N_2H^+ do not trace the mass in these Class I cores.

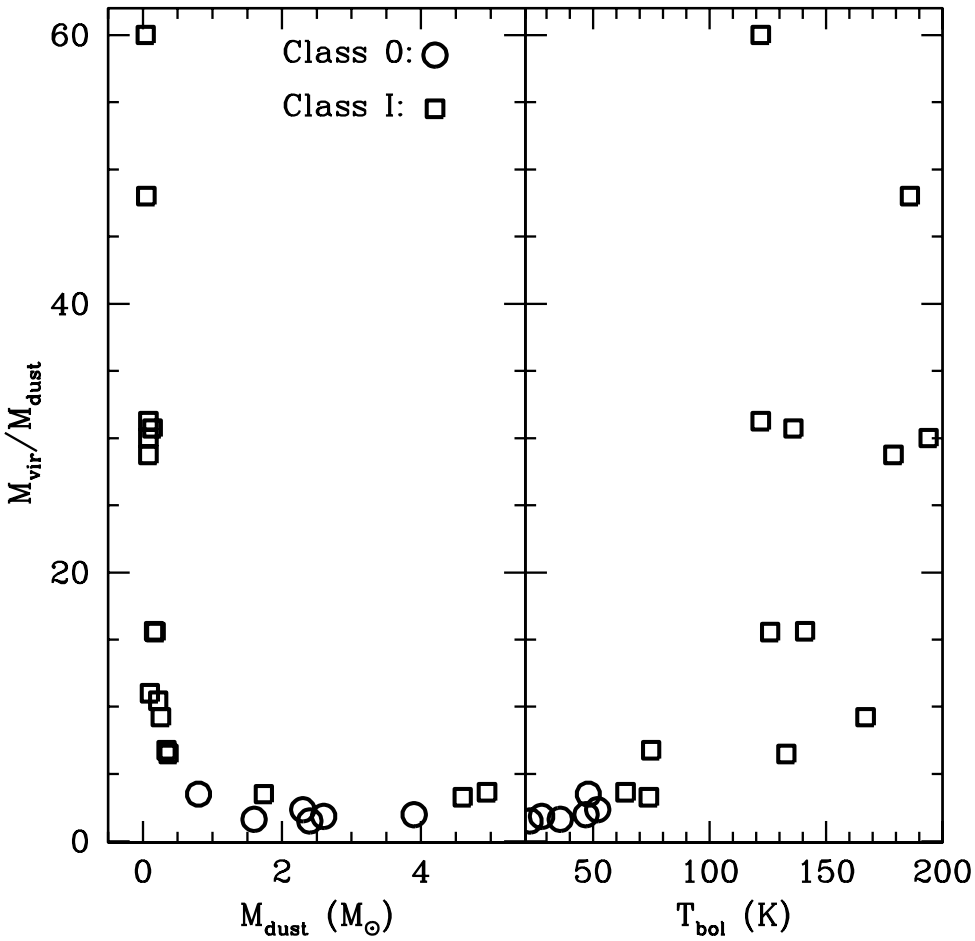

Figure 2.22: We plot the ratio of virial to dust mass (M_{vir}/M_{dust}) against M_{dust} and T_{bol}. Class I cores are represented by squares; Class 0 cores (from Paper III) are circles.

2.6.2 Luminosity and Stellar Mass

As discussed in the previous section, the masses for the envelopes of these cores are very low. Likewise, the observed luminosities are very low. For those cores in Taurus, we find a range of bolometric luminosities from 0.2 to 4.6 $L_\odot$ with an average of 1.4±1.3 $L_\odot$. These luminosities are upper limits on the luminosity of the central protostellar system because of the ISRF contribution. For the most luminous sources, L1251B and CB230, the ISRF contributes negligibly to the bolometric luminosity, but, for those cores in Taurus, the ISRF accounts for a considerable fraction of L_{obs}. We estimate the total contribution of the ISRF to the observed luminosity to be about 0.2 $L_\odot$.

Based on the standard picture of a Class I protostar in which the observed luminosity results from accretion, we can calculate the mass of this protostar by a simple relationship (e.g., Stahler 1994):

$$M_* = \frac{L_{acc} R_*}{G\dot{M}}. \tag{2.3}$$

Here, M_* is the stellar mass, L_{acc} is the luminosity due to accretion, G is the gravitational constant, R_* is the stellar radius, and $\dot{M}$ is the accretion rate given as $\dot{M} = n_o a_T^3/G$, where a_T is the isothermal sound speed and n_o is a numerical constant of order unity (Stahler 1994). Assuming a minimum isothermal sound speed of 0.2 km s^{-1}, we calculate $\dot{M} = 2 \times 10^{-6}$ $M_\odot yr^{-1}$. Then assuming $R_* = 3$ $R_\odot$, an overestimate of the stellar radius based on the models of Stahler (1988), we can calculate an upper limit on the stellar mass from this relationship. For the least luminous of the cores in this sample (IRAS 04385+2250; $L_{obs} = 0.2$ $L_\odot$), the mass, based on Equation 3, is $M_* = 0.01$ $M_\odot$ or, since this in the substellar realm, $M_* = 10$ M_{Jup}. The envelope mass for this core is 0.04 $M_\odot$, and, assuming a star formation efficiency of 25% (Wilking et al. 1989), the final mass of this object would be $M_* = 0.02$ $M_\odot$ (or 20 M_{Jup}) in about 10^4 yr (assuming constant $\dot{M} = 2 \times 10^{-6}$ $M_\odot yr^{-1}$).

This analysis holds many shortcomings and uncertainties. The mass accretion rate ($\dot{M}$) is highly uncertain, possibly episodic, and perhaps $1-2$ orders of magnitude smaller than that used in this calculation (e.g., Muzerolle et al. 1998). Such an accretion rate would increase M_* by a factor of $10-100$. On the other hand, the observed luminosity is probably some combination of the disk accretion luminosity and luminosity of the central protostar. Indeed, Muzerolle et al. (1998) find, in some cases, the accretion luminosities contribute $\sim 10\%$ to the total observed luminosity. If only 10% of the total luminosity results from accretion (as estimated by Muzerolle et al. 1998), the calculated stellar mass is a factor of 10 smaller.

We can also estimate the stellar mass by other means. If we assume an age (τ), we can place IRAS 04385+2250 on calculated isochrones. The models of Siess et al. (2000), with $\tau = 10^6$ yr, predict $M_* \sim 0.1$ M$_\odot$. Burrows et al. (2001) give $M_* \sim 0.2$ M$_\odot$ for $\tau = 10^6$ yr. These models probably overestimate M_*, however, because they assume no accretion and have not considered the initial conditions governed by infall and collapse of the protostellar envelope. Also, the age of embedded Class I cores has been estimated to be $\sim 10^5$ yr (e.g., Myers et al. 1987, Kenyon et al. 1990); most stellar evolution models begin at $\tau = 10^6$ yr and are highly uncertain for ages less than 10^6 yr. Siess et al. (1999) included accretion ($\dot{M} = 10^{-7}$ M$_\odot$yr^{-1}) in their calculations of pre-main sequence evolutionary tracks, and, for $\tau = 4.5 \times 10^6$ yr, their models would indicate $M_* < 0.1$ M$_\odot$; unfortunately, these models do not include objects with masses lower than 0.1 M$_\odot$ as required to accomodate IRAS 04385+2250. Additionally, the application of these models to Class I cores is quite precarious; these models are intended for T Tauri stars.

Observations of young, forming (Class 0/I) brown dwarfs have yet to be firmly established, but the existence of older substellar objects with disks (e.g. Natta & Testi 2001) suggest that brown dwarfs do form by similar mechanisms as T Tauri stars. If so, we, indeed, probably have observed brown dwarfs within their natal

envelopes. Then, it should not be surprising that, in this sample of low-luminosity Class I cores, a fraction are substellar. Indeed, Kenyon & Hartmann (1995) concluded similarly, i.e. the "luminosity problem" for Class I objects is solved if such objects are substellar. Of course, these authors also present another viable solution, that the accretion radius is larger in these young objects than we expect.

2.6.3 Classification: $\mathbf{L}_{obs}$, $\mathbf{T}_{bol}$, and $\mathbf{L}_{smm}$

Currently, the class system (Class -1—III) implies a sequence of stages that are occupied at some point by all evolving protostars (e.g., André & Montmerle 1994). Hence, statistical arguments have been constructed by comparing the numbers of sources in each stage to establish the relative time spent in each epoch (e.g., André & Montmerle 1994). As discussed previously, three criteria for classification have been put forth: α_{NIR} (Lada et al. 1987), T_{bol} (Myers & Ladd 1993), and L_{obs}/L_{smm} (André et al. 1993). These values are given in Table 2.7 for our sample of sources.

For the selection of the SED points from which these values were calculated (see Table 4.8), we required that the aperture be large enough to include all emission: $\theta_{mb} > 20''$. This restriction causes the exclusion of the near-infrared (NIR) fluxes, but we also calculate T_{bol} with the NIR data because the bolometric temperature is most affected by the NIR data. The NIR flux, no matter how weak, causes this mean frequency to be skewed to higher values. Indeed, if we do not include the NIR flux in our calculation of T_{bol}, 35% of our Class I sources become Class 0 by the T_{bol} criterion. Of course, Class I sources are identified by their NIR emission and are even called, by some, NIR protostars. However, detection of the NIR light is often dependent on orientation and, hence, could feasibly be obscured in an otherwise Class I object.

An additional complication in distinguishing between Class I and 0 cores is found in the luminosity scheme developed by André et al. (1993). They define a

Class I source as one for which $L_{obs}/L_{smm} > 200$, assuming that, as a protostar evolves, the envelope should be cleared away and, hence, this ratio should increase. Originally, this indicator was based on measurements within a small aperture ($20''$) because of nearby sources. However, for our isolated cores, it is clear that such a small aperture does not sample the total submillimeter flux emitted by the object. Therefore, we use only large aperture measurements ($> 20''$) in the calculation of these values (Table 2.7); for our submillimeter fluxes, we used the $40''$ aperture fluxes in the calculation of L_{obs}/L_{smm} so that nearby condensations would not contribute to the submillimeter flux.

In Figure 2.23, we show a plot of T_{bol} versus L_{obs}/L_{smm} that includes all sources from Paper I and this paper. Class I cores are characterized by $T_{bol} > 70K$ (Myers & Ladd 1993, Chen et al. 1995) or $L_{obs}/L_{smm} > 200$ (André et al. 1993). We have subdivided the plot into four regions based on these boundaries. Class I cores should be found only in the upper right-hand portion of the plot, and Class 0 cores should be in the lower left-hand portion. This is clearly not the case. While there is a noticeable correlation between the two evolutionary indicators, the divisions between the classes are not so obvious. Indeed, all of the cores in this paper's sample are Class I by the T_{bol} criteria (except for L1251B and IRAS 03256+3055); half of these Class I cores, however, are Class 0 by the L_{obs}/L_{smm} criterion. The problem arises in that the T_{bol} observable is greatly affected by geometry whereas L_{obs}/L_{smm} is not so affected. Visser, Richer, & Chandler (2002) also found such a discrepancy between these classification criteria. They find that the submillimeter luminosity criterion ($L_{obs}/L_{smm} > 200$) renders far fewer Class I cores than does the bolometric temperature. Further, they infer lifetimes for the evolutionary stages based on the numbers of Class 0 and I cores. In order to create such statistical arguments concerning the lifetimes of Class $-$1-III objects, one must recognize that different numbers of Class 0 or I objects will be found depending on the system of

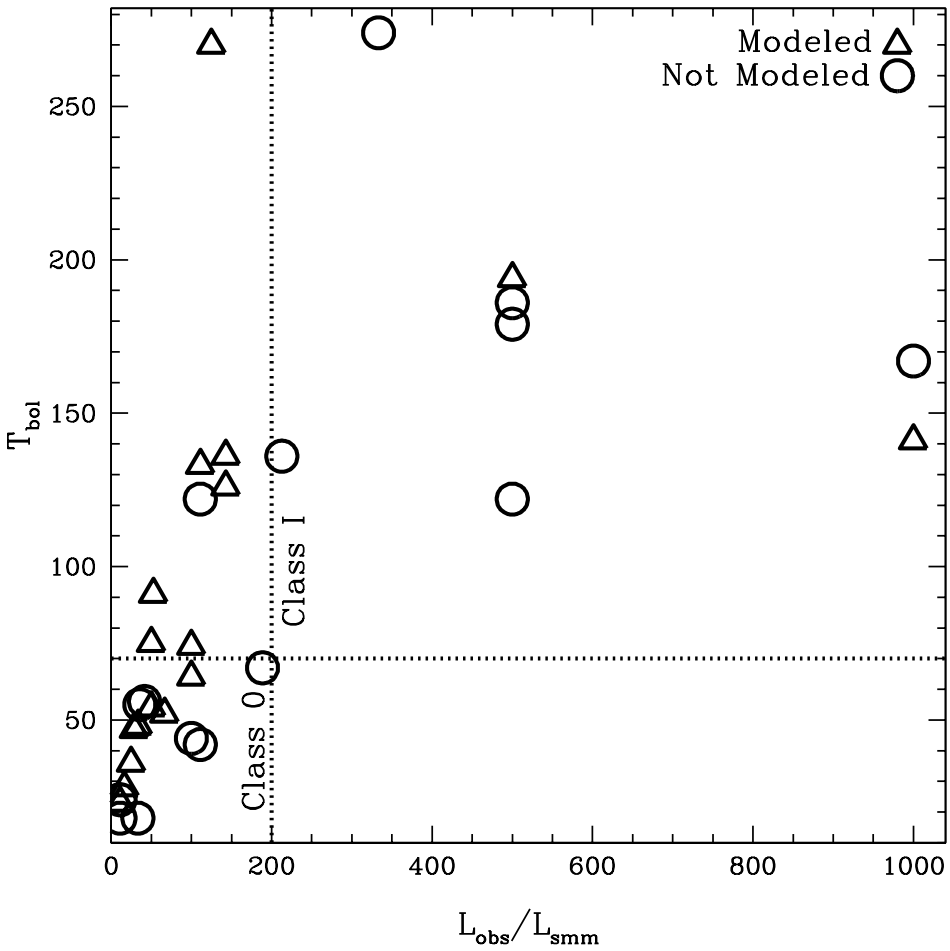

Figure 2.23: The bolometric temperature (T_{bol}) is plotted against L_{obs}/L_{smm}. The dashed lines represent the boundary between Class 0 and I. Class I objects have $T_{bol} > 70$ K (Myers & Ladd 1983) and $L_{obs}/L_{smm} > 200$ (André et al. 1993).

classification employed.

2.6.4 Density Structure

The primary purpose of our modeling is to derive the actual distribution of matter in the envelopes of these forming protostars. For the Class I cores in this paper, we find the density power law exponent $\langle p \rangle = 1.6 \pm 0.4$ (mean $\pm$ the standard deviation of the sample); however, the presence of a disk or point-like component could cause p to decrease by as much as 0.5. The median for this sample of Class I cores is $p = 1.8$. In Paper III, we reported $\langle p \rangle = 1.6 \pm 0.3$ for the Class 0 sources. For the Class 0 and I objects in Papers III and IV, we find $\langle p \rangle = 1.6 \pm 0.4$, and the median is $p = 1.8$. If we leave out those Class 0 or I sources with aspect ratios > 1.5, a total of four sources from Papers III and IV, we find $\langle p \rangle = 1.8 \pm 0.2$, and the median is also $p = 1.8$. We include these modeled sources in a histogram (Figure 2.24) both separately and together. The value for p is clearly peaked between 1.5-2.0, seemingly inconsistent with models that predict very shallow distributions—e.g., McLaughlin & Pudritz (1997). However, these models should not be excluded altogether, for we do see evidence, in some sources, of a shallower profile, and the inclusion of a disk allows for significantly shallower density profiles.

In Figure 2.25, for all modeled sources (from Paper III and IV), we show the aspect ratio as a function of p. A clear correlation exists between these two values such that the more aspherical sources exhibit shallower profiles. Of course, the azimuthal averaging of an aspherical object could result in a shallow intensity profile (and, hence, shallower density profile), but we claim this is a small effect. In Section 4.4, we discussed the modeling of IRAS 04248+2612 and how the derived density power law changes negligibly with exclusion of the extended emission in the NE-SW extensions. We also found this to be true in aspherical, Class 0 sources—see Paper III.

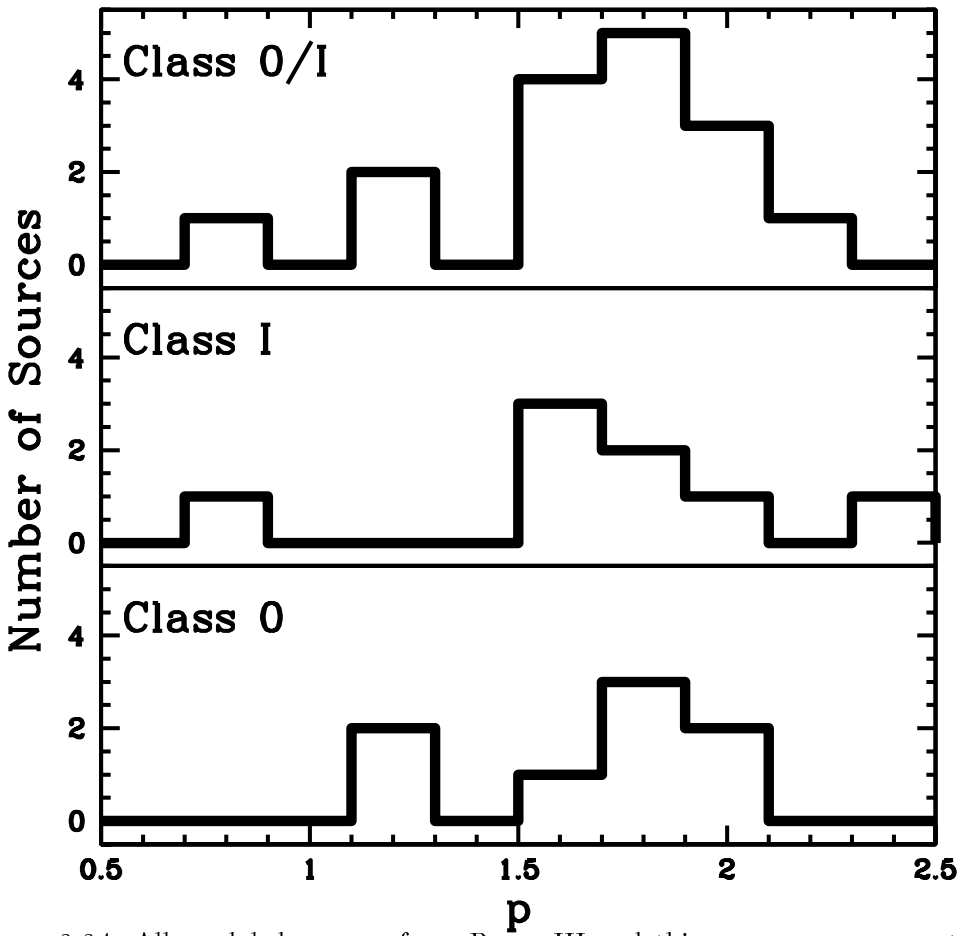

Figure 2.24: All modeled sources from Paper III and this paper are represented in the top histogram. Class 0 and I (from Paper III and this paper) sources are shown in the bottom and middle histograms, respectively.

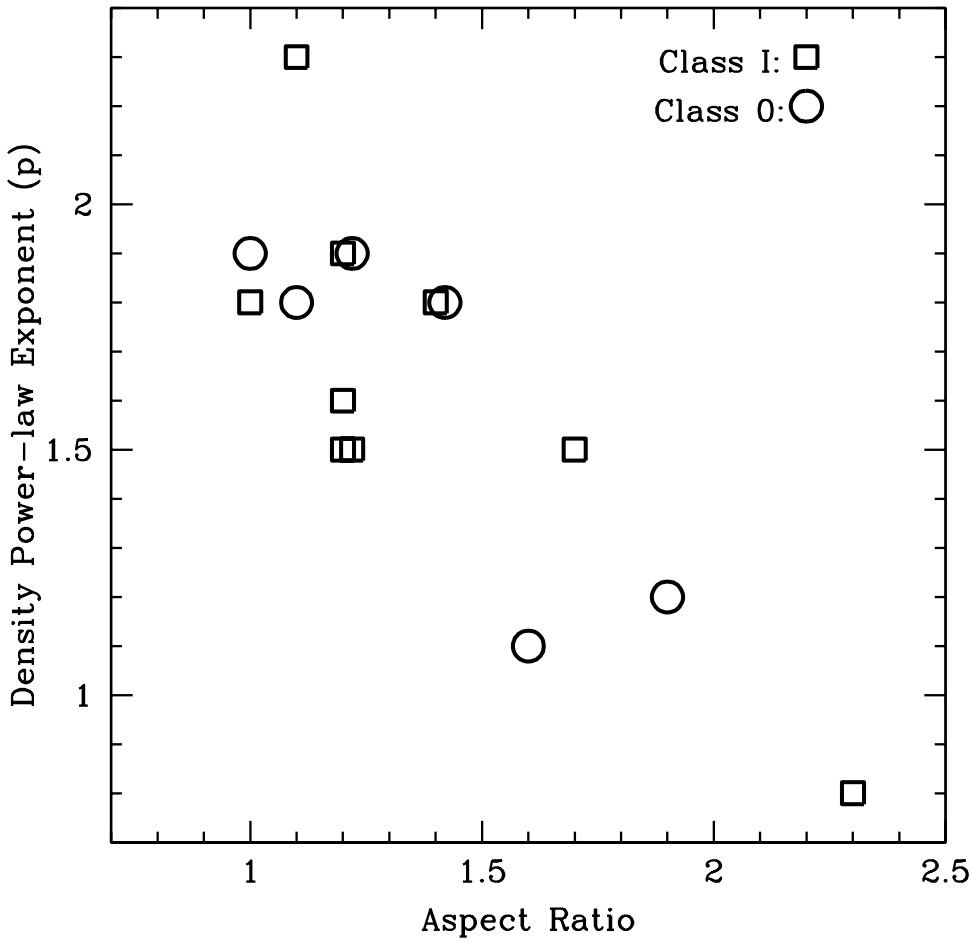

Figure 2.25: The aspect ratio (given in Table 2.7) is on the horizontal axis and the modeled density power law exponent (p) is on the vertical axis. More aspherical objects are best modeled with shallow density profiles—an effect that is possibly real and not just an artifact of our one-dimensional model.

As in Paper III, we find little evidence for variation of dust properties within the envelope. We compare the normalized intensity ratios ($I^{norm}_{450\mu m}/I^{norm}_{850\mu m}$) in Figure 2.26 and conclude that, for most sources, the observed variations in this ratio are well-fitted by including the effects of external heating by the ISRF and convolution of the actual beam. For L1251B, IRAS 04361+2547, and IRAS 04381+2540, we are unable to simultaneously match the observed 850 and 450 μm intensity profiles. The dust opacity may vary with radius in these sources, but it could also be that we have not appropriately modeled the temperature in these cores, perhaps, due to asymmetric heating, externally, by the ISRF or, internally, by a disk+protostar or binary central source.

While power law density distributions do not have a physical size, we define an observational size from the deconvolved FWHM of our modeled sources (Table 2.7). In Figure 2.27, we show the derived value for p plotted against the effective size (θ_{dec}/θ_{mb}) for the modeled Class 0 and I cores (from Papers III & IV). Additionally, the solid line shows a series of models for $0.5 < p < 2.5$ for which the deconvolved model size is measured with the $15''$ beam. The models show that steeper power laws are clearly less well-resolved in agreement with the observed trend.

The trend in Figure 2.27, while not surprising, is quite striking; smaller sources exhibit a larger value for p. We stress this point for three reasons. First, Terebey, Chandler, & André (1993) addressed this resolution issue—that steeper power law density distributions are less well-resolved. However, one must be very careful when analyzing the intensity profiles of marginally resolved sources because uncertainty in the beamshape can be $\sim 1 - 3''$ (see Section 3.2). Indeed, there are examples of marginally resolved sources for which the authors have derived very steep density power laws ($p > 2.5$), density distributions that have little theoretical basis.

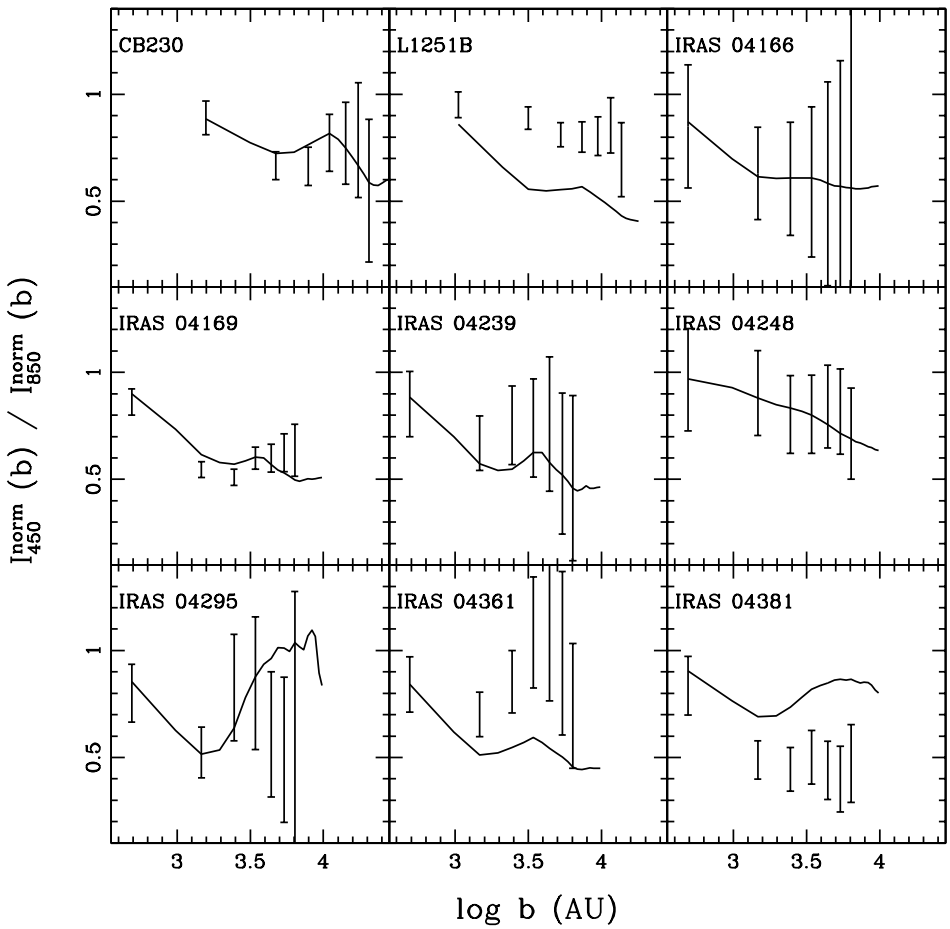

Figure 2.26: The error bars represent the observed ratio of 450 to 850 μm flux. The solid line represents the modeled value.

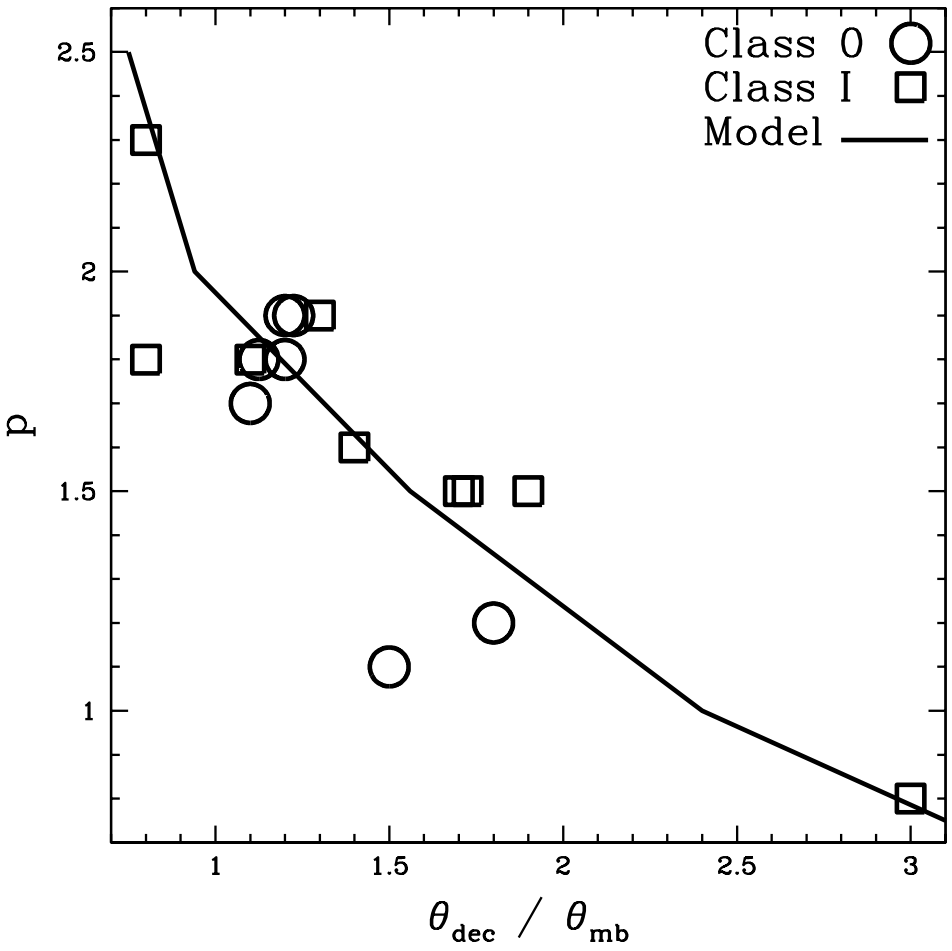

Figure 2.27: The derived value for p is plotted against the ratio of deconvolved source size and beam size (at FWHM). The solid line represents models of the dust emission with $0.5 < p < 2.5$. We note an obvious trend of increasing p for the less well-resolved sources. This trend is possibly an effect due to the cores compact nature, but we also note the possibility that we are observing the outer parts of the envelope in these "smaller" cores.

Also, we propose an intriguing possibility implying this trend is not entirely systematic and might be indicative of some physical quality. Perhaps, we are observing only the outer envelope of these less well-resolved cores. That is, these "smaller" sources are not small because they are more evolved and have collapsed over time, but they are small because they began with an initial preprotostellar core that was lower in mass and, hence, has a smaller outer radius than the other cores in our sample. In the Shu collapse model, we would expect a steeper density profile in the outer, static envelope, and it might be that, indeed, we are seeing just that.

A third scenario is also possible. Perhaps, the "smaller" cores, which we interpret to have steeper density profiles, have a greater disk contribution. This point source of emission, as shown in a previous section, results in the derivation of a steeper power law distribution in the density. In this case, the envelope mass distribution could be considerably shallower that we predict here. Indeed, if the disk contribution is more significant as the core size decreases, the trend for the envelope density distribution shown in Figure 2.27 could be shifted such all cores harbor an envelope described by $1.0 < p < 1.5$, a possibility that would suggest the validity of the theory presented by McLaughlin & Pudritz (1997).

We compare these results to those recently presented by Jørgensen, Schöier, and van Dishoeck (2002) (hereafter, JSD) and find that we reach similar conclusions. These authors model two sources coincident with our sample: IRAS 04361+2547 and IRAS 04381+2540, which they call TMR1 and TMC1, respectively. Our derived values of the density power law exponent for these two sources are consistent with those of JSD. However, their modeling differs from ours in the assigning of two parameters: the ISRF and outer radius; additionally, they do not simulate the effects of chopping. Exclusion of the ISRF should cause JSD to derive a shallower power law exponent to fit the observed data. Also, JSD adopt much smaller outer radii than we do in this paper—in some cases, a factor of four smaller. By assigning a

small outer radius and excluding the effects of chopping, these authors should derive a somewhat steeper power law for the density distribution than that presented here. The combination of these two effects (i.e., exclusion of the ISRF and truncated outer radius) seem to cancel in their analysis, rendering similar results to our own.

2.6.5 Caveats

As presented in the previous sections, we have discussed several caveats that hinder direct interpretation of the dust continuum emission: beam convolution of our model, complex temperature distributions due to external heating, different assumed dust opacities, contribution to the observed flux from a disk component, and the inner and outer radii assumed in the model. We do not analyze the effects of outflows because, for most of our sources, the outflows are either very weak or undetected (e.g., Bontemps et al. 1997). Our modeling is also limited by its one-dimensional nature, but we point out objects for which three-dimensional modeling will prove fruitful (e.g., IRAS 04248+2612). Our assertion that asymmetric sources exhibit shallower density distributions suggests that these objects are forming in truly different environments. However, this issue will not be fully resolved until models of radiative transfer for three dimensions are completed.

2.7 Conclusions

Our conclusions are as follows:

1) We find that 3/16 (20%) of the sources in this sample have distinct, neighboring condensations (IRAS 03256+3055, 04016+2610 and 04361+2547). These condensations could be the result of complex structure (03256+3055), neighboring preprotostellar cores (04016+2610), or the heating due to outflows (04361+2547).

2) We have fit power law models for the density distribution in the outer envelopes of nine Class I cores and find $\langle p \rangle = 1.6 \pm 0.4$ and a median of $p = 1.8$. The

existence of a disk or point-like component could cause p to be much *shallower*—by about 0.5. Table 2.7 has a summary of parameters for the best-fit models.

3) We test the Shu inside-out collapse model and find that, in most cases, this model provides a good fit for the intensity profile but with an infall radius that is within the central resolution element of our observations. Most sources in this sample exhibit no evidence for a break in the power law density distribution on the scales we can probe with SCUBA ($\sim 1000 - 8000$ AU).

4) We compare our analysis with a simpler analysis put forth by Adams (1991) and as used in Paper I. This method assumes a temperature power law (with index $q = 0.4$) and $h\nu/kT \ll 1$. These assumptions are invalid for these low luminosity sources, and this simple analysis overestimates p by $\sim$0.6.

5) In modeling the density distribution, we have determined several sources of uncertainty: possible existence of a disk ($\delta(p) = -0.5$), variations in the ISRF ($\delta(p) = \pm 0.4$), and uncertainty in the outer radius ($\delta(p) = \pm 0.3$). Contributions by the disk to the observed submillimeter flux will be addressed by such instruments as SMA and ALMA while the ISRF may be constrained by future observations in the mid- to far-infrared (e.g., SIRTF). We find no evidence for a truncated outer radius in models completed over a wide range of radii.

6) For our modeled sources, we have calculated the mass of the envelope surrounding the protostar: $\langle M_{env} \rangle = 6.6 \pm 2.4$ M$_\odot$ for the two most luminous sources and $\langle M_{env} \rangle = 0.2 \pm 0.1$ M$_\odot$ for those modeled sources in Taurus. We find that these masses are clearly less than those found for Class 0 cores (Paper III) and, further, contradict the virial masses predicted by N_2H^+ linewidths. Molecular line tracers such as N_2H^+ simply do not trace the mass in these Class I cores.

7) The standard classification criteria, T_{bol} and L_{obs}/L_{smm}, are sometimes inconsistent for Class 0 and I cores. The mode of classification is important for studies that attempt to estimate core lifetimes based on the Class 0 and Class I

source counts (e.g. Visser, Richer, & Chandler 2002).

8) Sources with higher aspect ratios are better fitted with shallower density power laws. While this effect is partially due to our one-dimensional models, we propose that, indeed, these sources are forming in physically different initial conditions. Three-dimensional modeling will help to unravel this question.

9) We note a trend between deconvolved FWHM source size and p—smaller cores have higher values for p. This trend is expected since steeper density power law distributions produce less well-resolved intensity profiles. It is also possible that we are observing the outer portions of the envelope in these less well-resolved sources.

10) We have also discussed several sources individually. In particular, IRAS 03256+3055, with its unique morphology, is an ideal object on which to test theories of fragmentation in the formation of low-mass protostars. Also, we note the possibility, through some simple calculations, that IRAS 04385+2550 is a young, forming substellar object with a mass of ~ 10 M_{Jup}.

Table 2.1: Observed Sources

Source	α (B1950.0) (^{h} ^{m} ^{s})	δ (B1950.0) (^{o} ' ")	Date	Source environment
CB230	21 16 55.0	68 04 52	11/19/99	IRAS 21169+6804
L1251B	22 37 40.8	74 55 50	11/19/99	IRAS 22376+7455
IRAS 03256+3055	03 25 39.2	30 55 20	02/02/00	Per
IRAS 04016+2610	04 01 40.0	26 10 49	02/03/00	L1489
IRAS 04108+2803	04 10 49.3	28 03 57	02/03/00	L1495
IRAS 04113+2758	04 11 20.9	27 58 30	11/19/99	L1495
IRAS 04166+2706	04 16 37.8	27 06 29	08/30/98	
IRAS 04169+2702	04 16 54.0	27 02 52	02/03/00	B213
IRAS 04239+2436	04 23 54.5	24 36 54	02/02/00	L1524
IRAS 04248+2612	04 24 53.2	26 12 39	02/01/00	HH31 IRS/B217
IRAS 04264+2433	04 26 28.1	24 33 24	02/03/00	L1524
IRAS 04295+2251	04 29 32.2	22 51 11	02/01/00	L1536
IRAS 04302+2247	04 30 16.6	22 47 05	02/02/00	L1536
IRAS 04361+2547	04 36 09.4	25 47 27	11/19/99	TMR1
IRAS 04381+2540	04 38 07.6	25 40 48	02/01/00	TMC1
IRAS 04385+2550	04 38 34.2	25 50 43	02/03/00	TMC1

Table 2.2: Observing and Performance Summary

Date	τ_{850}	τ_{450}	τ_{cso}	C_{120}^{850} Jy/V	C_{120}^{450} Jy/V
November					
11/19/99	0.27 (0.08)	1.24(0.09)	0.061(0.006)	0.78 (0.03)	2.73 (0.78)
February					
02/01/00	0.23 (0.03)	1.23(0.18)	0.048(0.007)	0.68 (0.03)	1.87(0.63)
02/02/00	0.17 (0.03)	0.79(0.27)	0.044(0.002)	0.67 (0.01)	2.54(0.26)
02/03/00	0.21 (0.02)	1.02(0.16)	0.050(0.006)	0.69 (0.03)	2.88(0.09)
				February Average	
				0.68(0.03)	2.35(0.61)

Table 2.3: Observed Flux Densities

Source	Centroid ($\Delta\alpha''$,$\Delta\delta''$)	S_ν (Jy) 850 μm	S_ν (Jy) 450 μm	$\alpha_{450/850}$	$\alpha_{450/850}$	S/N
CB230	(-8,2)	3.03(0.28)	7.76(2.44)	1.0	1.5	110
L1251B	(4,3)	6.69(2.70)	24.34(7.07)	2.2	2.0	70
IRAS 03256+3055	...	2.45(0.29)	8.08(3.89)	2.3	1.9	30
IRAS 04016+2610	(10,0)	1.92(0.10)	11.13(6.65)	3.1	2.8	40
	(74,16)	...	...	2.4	...	...
IRAS 04108+2803	(-3,-9)	0.61(0.06)	5.38(2.31)	2.9	3.4	14
IRAS 04113+2758	(0,-1)	1.65(0.15)	4.36(1.27)	0.9	1.5	180
IRAS 04166+2706	(1,-4)	1.9(1.0)	12.9(6.0)	2.1	3.0	18
IRAS 04169+2702	(4,2)	2.53(0.12)	11.75(5.05)	2.6	2.4	60
IRAS 04239+2436	(2,-2)	0.78(0.10)	3.72(1.79)	2.6	2.5	50
IRAS 04248+2612	(-2,1)	1.95(0.33)	8.97(3.93)	2.6	2.4	20
IRAS 04264+2433	(3,-3)	0.37(0.04)	1.32(0.57)	2.5	2.0	10
IRAS 04295+2251	(1,-6)	0.78(0.05)	5.34(2.34)	2.9	3.0	40
IRAS 04302+2247	(5,1)	0.62(0.08)	1.88(0.91)	2.0	1.8	90
IRAS 04361+2547	(5,4)	1.21(0.11)	4.55(1.32)	2.1	2.1	60
	(63,-57)	...	...	2.0	...	...
IRAS 04381+2540	(15,6)	1.35(0.11)	6.41(2.80)	2.5	2.5	40
IRAS 04385+2550	(6,1.7)	0.29(0.04)	0.37(0.16)	0.8	0.4	10

Fluxes for 120" aperture.

Table 2.4: Spectral Energy Distributions of Sources

Source	λ (μm)	S_ν (Jy)	θ_{mb} (")	Ref.
CB230	2.2	0.005(0.001)	6.3	8[a]
	12	<0.25	300×45	10
	25	0.68(0.07)	300×45	10[a]
	60	11.75(0.71)	90×300	10[a]
	100	33.53(2.01)	180×300	10[a]
	350	12.0(0.2)	19.5	5
	450	4.4(0.5)	18.5	5
	450	7.76(2.44)	120	11[a]
	450	7.0(...)	...	6
	800	1.00(0.16)	16.5	5
	850	3.03(0.28)	120	11[a]
	850	1.2(...)	...	6
	1100	0.37(0.05)	18.5	5
	1300	0.23(0.01)	16.5	5
	1300	0.221(0.005)	12	12
	36000	0.2	11.1×8.6	7
	60000	0.1	90×300cm	7
L1251B	12	0.80(0.11)	300×45	10[a]
	25	5.55(0.33)	300×45	10[a]
	60	32.34(0.32)	90×300	10[a]
	100	66.84(9.36)	180×300	10[a]
	450	24.34(7.07)	120	11[a]
	850	6.69(2.70)	120	11[a]
IRAS 03256+3055	60	1.43(0.14)	90×300	10[a]
	450	8.08(3.89)	120	11[a]
	850	2.45(0.29)	120	11[a]

[a] Flux value used in the calculation of T_{bol} and L_{obs}.

References: 1. Myers et al. 1987;2. Moriarty-Scheiven et al. 1994;
3. Tamura et al. 1991;4. Kenyon et al. 1990;5. Launhardt et al. 1997;
6. Huard et al. 1999; 7.Moreira et al. 1997;8. Yun et al. 1995;
9.Kun & Prusti 1993; 10. IRAS PSC, 1988; 11. this paper;
12. Launhardt & Henning, 1997; 13. Barsony & Kenyon, 1992;
14. Motte & André, 2000;15. Hogerheijde & Sandell, 2000;
16. Padgett et al., 1999; 17. Saito et al., 2001;18. Dent et al., 1998.

SED Table Continued...

Source	λ (μm)	S_ν (Jy)	θ_{mb} (")	Ref.
IRAS 04016+2610	2.2	0.13(0.02)	10.7	3[a]
	2.2	0.12	3.8	16
	7.8	2.8(0.3)	12	1
	8.7	2.1(0.1)	12	1
	9.5	1.7(0.1)	12	1
	10.3	2.5(0.1)	12	1
	11.6	3.4(0.1)	12	1
	12	3.64(0.07)	300×45	10[a]
	12.5	4.9(0.2)	12	1
	25	15.81(0.95)	300×45	10[a]
	60	48.79(4.9)	90×300	10[a]
	100	55.69(7.8)	180×300	10[a]
	450	11.13(6.65)	120	11[a]
	450	3.25(0.46)	17.5	13
	450	23.3()	...	15
	800	0.29(0.042)	13.5	13
	800	0.31(0.061)	16.8	13
	800	0.582(0.079)	16.8	2
	850	1.92(0.10)	120	11[a]
	850	5.78()	...	15
	1100	0.055(0.016)	18.5	13
	1100	0.180(0.021)	18.5	2
	1300	0.130(0.005)	11	14
	1300	0.150(...)	60	14[a]

[a] Flux value used in the calculation of T_{bol} and L_{obs}.

References: 1. Myers et al. 1987;2. Moriarty-Scheiven et al. 1994;
3. Tamura et al. 1991;4. Kenyon et al. 1990;5. Launhardt et al. 1997;
6. Huard et al. 1999; 7.Moreira et al. 1997;8. Yun et al. 1995;
9.Kun & Prusti 1993; 10. IRAS PSC, 1988; 11. this paper;
12. Launhardt & Henning, 1997; 13. Barsony & Kenyon, 1992;
14. Motte & André, 2000;15. Hogerheijde & Sandell, 2000;
16. Padgett et al., 1999; 17. Saito et al., 2001;18. Dent et al., 1998.

SED Table Continued...

Source	λ (μm)	S_ν (Jy)	θ_{mb} (")	Ref.
IRAS 04108+2803	2.2	0.029(0.004)	10.7	3[a]
	7.8	0.31(0.06)	12	1
	8.7	0.50(0.08)	12	1
	9.5	0.49(0.09)	12	1
	10.3	0.57(0.09)	12	1
	11.6	0.44(0.09)	12	1
	12.5	1.3(0.2)	12	1
	12	0.87(0.05)	300×45	10[a]
	25	3.88(0.39)	300×45	10[a]
	60	7.49(0.75)	90×300	10[a]
	100	10.86(0.11)	180×300	10[a]
	450	5.38(2.31)	120	11[a]
	800	0.085(0.033)	16.8	2
	850	0.61(0.06)	120	11[a]
	1100	<0.1	18.5	2
	1300	<0.02	60	14

[a] Flux value used in the calculation of T_{bol} and L_{obs}.

References: 1. Myers et al. 1987;2. Moriarty-Scheiven et al. 1994;
3. Tamura et al. 1991;4. Kenyon et al. 1990;5. Launhardt et al. 1997;
6. Huard et al. 1999; 7.Moreira et al. 1997;8. Yun et al. 1995;
9.Kun & Prusti 1993; 10. IRAS PSC, 1988; 11. this paper;
12. Launhardt & Henning, 1997; 13. Barsony & Kenyon, 1992;
14. Motte & André, 2000;15. Hogerheijde & Sandell, 2000;
16. Padgett et al., 1999; 17. Saito et al., 2001;18. Dent et al., 1998.

SED Table Continued...

Source	λ (μm)	S_ν (Jy)	θ_{mb} (")	Ref.
IRAS 04113+2758	2.2	0.32 (0.05)	10.7	3[a]
	2.2	0.66(0.02)	9	13
	12	2.03 (0.28)	300×45	10[a]
	60	12.75 (0.13)	90×300	10[a]
	100	15.82 (2.21)	180×300	10[a]
	450	4.36(1.27)	120	11[a]
	800	0.98(0.12)	16.8	2
	850	1.65(0.15)	120	11[a]
	1100	0.461(0.053)	18.5	2
	1300	0.410(0.040)	11	14
	1300	0.750(...)	60	14[a]
	3400	0.052(0.006)	8	17
IRAS 04166+2706	1.6	0.00010(0.00002)	10	4
	2.2	0.00019(0.00009)	10	4
	12	0.07(0.007)	300×45	10[a]
	25	0.58(0.058)	300×45	10[a]
	60	5.9(0.59)	90×300	10[a]
	100	9.5(0.95)	180×300	10[a]
	450	12.9(6.0)	120	11[a]
	850	1.9(1.0)	120	11[a]

[a] Flux value used in the calculation of T_{bol} and L_{obs}.

References: 1. Myers et al. 1987;2. Moriarty-Scheiven et al. 1994;
3. Tamura et al. 1991;4. Kenyon et al. 1990;5. Launhardt et al. 1997;
6. Huard et al. 1999; 7.Moreira et al. 1997;8. Yun et al. 1995;
9.Kun & Prusti 1993; 10. IRAS PSC, 1988; 11. this paper;
12. Launhardt & Henning, 1997; 13. Barsony & Kenyon, 1992;
14. Motte & André, 2000;15. Hogerheijde & Sandell, 2000;
16. Padgett et al., 1999; 17. Saito et al., 2001;18. Dent et al., 1998.

SED Table Continued...

Source	λ (μm)	S_ν (Jy)	θ_{mb} (")	Ref.
IRAS 04169+2702	2.2	0.02(0.003)	10.7	3[a]
	2.2	0.02(0.004)	9	13
	12	0.75(0.05)	300×45	10[a]
	25	5.21(0.31)	300×45	10[a]
	60	17.00(1.7)	90×300	10[a]
	100	17.46(2.4)	180×300	10[a]
	450	11.75(5.05)	120	11[a]
	800	0.75(0.18)	16.8	2
	800	0.52(0.069)	13.5	13
	800	0.73(0.051)	16.8	13
	850	2.53(0.12)	120	11[a]
	1100	0.280(0.025)	18.5	13
	1100	0.281(0.053)	18.5	2
	1300	0.190(0.009)	11	14
	1300	0.730(...)	60	14[a]
	3400	<0.026	8	17
IRAS 04239+2436	2.2	0.07 (0.01)	10.7	3[a]
	12	1.71(0.1)	300×45	10[a]
	25	6.98(0.42)	300×45	10[a]
	60	15.24(0.15)	90×300	10[a]
	100	15.88(2.22)	180×300	10[a]
	450	3.72(1.79)	120	11[a]
	800	0.333(0.043)	16.8	2
	800	0.23(0.025)	13.5	13
	850	0.78(0.10)	120	11[a]
	1100	0.077(0.023)	18.5	13[b]
	1100	0.114(0.021)	18.5	2
	1300	0.080(0.01)	11	14
	1300	0.170	60	14[a]
	3400	<0.024	8	17

[a] Flux value used in the calculation of T_{bol} and L_{obs}.

References: 1. Myers et al. 1987;2. Moriarty-Scheiven et al. 1994;
3. Tamura et al. 1991;4. Kenyon et al. 1990;5. Launhardt et al. 1997;
6. Huard et al. 1999; 7.Moreira et al. 1997;8. Yun et al. 1995;
9.Kun & Prusti 1993; 10. IRAS PSC, 1988; 11. this paper;
12. Launhardt & Henning, 1997; 13. Barsony & Kenyon, 1992;
14. Motte & André, 2000;15. Hogerheijde & Sandell, 2000;
16. Padgett et al., 1999; 17. Saito et al., 2001;18. Dent et al., 1998.

SED Table Continued...

Source	λ (μm)	S_ν (Jy)	θ_{mb} (")	Ref.
IRAS 04248+2612	2.2	0.04(0.006)	10.7	3[a]
	2.2	0.04()	3.8	16
	25	1.33(0.13)	300×45	10[a]
	60	4.62(0.46)	90×300	10[a]
	100	9.26(0.93)	180×300	10[a]
	450	8.97(3.93)	120	11[a]
	800	0.252(0.046)	16.8	2
	800	0.12(0.033)	13.5	13
	800	0.21(0.039)	16.8	13
	850	1.95(0.33)	120	11[a]
	1100	0.100(0.019)	18.5	13
	1100	0.099(0.015)	18.5	2
	1100	0.15(0.045)	...	18
	1300	0.060(0.007)	11	14
	1300	0.450	60	14[a]
IRAS 04264+2433	2.2	0.026(0.001)	9	13[a]
	12	0.39(0.02)	300×45	10[a]
	25	2.94(0.18)	300×45	10[a]
	60	5.21(0.52)	90×300	10[a]
	450	1.32(0.57)	120	11[a]
	850	0.37(0.04)	120	11[a]
	1300	0.031(0.008)	11	14
	1300	0.031(...)	60	14[a]

[a] Flux value used in the calculation of T_{bol} and L_{obs}.

References: 1. Myers et al. 1987;2. Moriarty-Scheiven et al. 1994;
3. Tamura et al. 1991;4. Kenyon et al. 1990;5. Launhardt et al. 1997;
6. Huard et al. 1999; 7.Moreira et al. 1997;8. Yun et al. 1995;
9.Kun & Prusti 1993; 10. IRAS PSC, 1988; 11. this paper;
12. Launhardt & Henning, 1997; 13. Barsony & Kenyon, 1992;
14. Motte & André, 2000;15. Hogerheijde & Sandell, 2000;
16. Padgett et al., 1999; 17. Saito et al., 2001;18. Dent et al., 1998.

SED Table Continued...

Source	λ (μm)	S_ν (Jy)	θ_{mb} (")	Ref.
IRAS 04295+2251	2.2	0.12 (0.02)	10.7	3[a]
	12	0.60(0.11)	300×45	10[a]
	25	1.82(0.18)	300×45	10[a]
	60	3.53(0.35)	90×300	10[a]
	100	7.41(1.04)	180×300	10[a]
	450	5.34(2.34)	120	11[a]
	800	0.241(0.050)	16.8	2
	850	0.78(0.05)	120	11[a]
	1100	0.094(0.018)	18.5	2
	1300	0.115(0.010)	11	14
	1300	0.115(...)	60	14[a]
IRAS 04302+2247	2.2	0.03(0.005)	10.7	3[a]
	2.2	0.025(0.001)	9	13
	2.2	0.025(...)	3.8	16
	25	0.44(0.06)	300×45	10[a]
	60	6.40(0.13)	90×300	10[a]
	100	9.43(0.19)	180×300	10[a]
	450	1.88(0.91)	120	11[a]
	800	0.342(0.057)	16.8	2
	850	0.62(0.08)	120	11[a]
	1100	0.149(0.019)	18.5	2
	1300	0.180(0.010)	11	14
	1300	0.180(...)	60	14[a]

[a] Flux value used in the calculation of T_{bol} and L_{obs}.

References: 1. Myers et al. 1987;2. Moriarty-Scheiven et al. 1994;
3. Tamura et al. 1991;4. Kenyon et al. 1990;5. Launhardt et al. 1997;
6. Huard et al. 1999; 7.Moreira et al. 1997;8. Yun et al. 1995;
9.Kun & Prusti 1993; 10. IRAS PSC, 1988; 11. this paper;
12. Launhardt & Henning, 1997; 13. Barsony & Kenyon, 1992;
14. Motte & André, 2000;15. Hogerheijde & Sandell, 2000;
16. Padgett et al., 1999; 17. Saito et al., 2001;18. Dent et al., 1998.

SED Table Continued...

Source	λ (μm)	S_ν (Jy)	θ_{mb} (")	Ref.
IRAS 04361+2547	2.2	0.04(0.006)	10.7	3[a]
	2.2	0.04(0.001)	9	13
	12	1.81(0.11)	300×45	10[a]
	25	18.87(1.13)	300×45	10[a]
	60	44.75(6.27)	90×300	10[a]
	100	35.43(4.96)	180×300	10[a]
	450	4.55(1.32)	120	11[a]
	800	0.634(0.067)	16.8	2
	850	1.21(0.11)	120	11[a]
	1100	0.188(0.027)	18.5	2
	1300	0.110(0.008)	11	14
	1300	0.440(...)	60	14[a]
IRAS 04381+2540	2.2	0.01 (0.002)	10.7	3[a]
	12	0.44(0.06)	300×45	10[a]
	25	2.69(0.27)	300×45	10[a]
	60	10.29(1.0)	90×300	10[a]
	100	13.91(1.4)	180×300	10[a]
	450	6.41(2.80)	120	11[a]
	450	12.5()	...	15
	800	0.289(0.053)	16.8	2
	850	1.35(0.11)	120	11[a]
	850	2.60()	...	15
	1100	0.116(0.013)	18.5	2
	1300	0.070(0.009)	11	14
	1300	0.300(...)	60	14[a]

[a] Flux value used in the calculation of T_{bol} and L_{obs}.

References: 1. Myers et al. 1987;2. Moriarty-Scheiven et al. 1994;
3. Tamura et al. 1991;4. Kenyon et al. 1990;5. Launhardt et al. 1997;
6. Huard et al. 1999; 7.Moreira et al. 1997;8. Yun et al. 1995;
9.Kun & Prusti 1993; 10. IRAS PSC, 1988; 11. this paper;
12. Launhardt & Henning, 1997; 13. Barsony & Kenyon, 1992;
14. Motte & André, 2000;15. Hogerheijde & Sandell, 2000;
16. Padgett et al., 1999; 17. Saito et al., 2001;18. Dent et al., 1998.

SED Table Continued...

Source	λ (μm)	S_ν (Jy)	θ_{mb} (")	Ref.
IRAS 04385+2550	12	0.54(0.03)	300×45	10[a]
	25	1.55(0.16)	300×45	10[a]
	60	2.88(0.29)	90×300	10[a]
	450	0.37(0.16)	120	11[a]
	850	0.29(0.04)	120	11[a]
	1300	0.030(0.005)	11	14
	1300	0.030(...)	60	14[a]

[a] Flux value used in the calculation of T_{bol} and L_{obs}.

References: 1. Myers et al. 1987;2. Moriarty-Scheiven et al. 1994;
3. Tamura et al. 1991;4. Kenyon et al. 1990;5. Launhardt et al. 1997;
6. Huard et al. 1999; 7.Moreira et al. 1997;8. Yun et al. 1995;
9.Kun & Prusti 1993; 10. IRAS PSC, 1988; 11. this paper;
12. Launhardt & Henning, 1997; 13. Barsony & Kenyon, 1992;
14. Motte & André, 2000;15. Hogerheijde & Sandell, 2000;
16. Padgett et al., 1999; 17. Saito et al., 2001;18. Dent et al., 1998.

Table 2.5: Observed Source Properties

Source	T_{bol}[a] K	T_{bol} K	L_{obs} $L_\odot$	$\frac{L_{smm}}{L}$	Aspect Ratio $\frac{a}{b}$	θ_{dec}/θ_{mb}
CB230	47	74	11.5	50	1.2	1.3
L1251B[b]	64	...	10.8	50	1.7	1.7
IRAS 03256+3055[b]	16	...	0.3	...	...	...
IRAS 04016+2610	92	167	4.6	200	...	...
IRAS 04108+2803	98	179	1.0	111	...	...
IRAS 04113+2758	82	274	2.0	200	...	...
IRAS 04166+2706	50	75	0.5	25	1.2	1.4
IRAS 04169+2702	83	133	1.4	50	1.2	1.9
IRAS 04239+2436	103	194	1.8	250	1.4	0.8
IRAS 04248+2612	49	136	0.9	50	2.3	3.0
IRAS 04264+2433	109	186	0.5	200	...	...
IRAS 04295+2251	91	270	0.6	50	1.1	0.8
IRAS 04302+2247	53	122	0.5	125	...	...
IRAS 04361+2547	98	141	3.6	333	1.0	1.1
IRAS 04381+2540	78	126	0.9	100	1.2	1.7
IRAS 04385+2550[b]	122	...	0.2	200	...	...

[a]Near-infrared data is not included in the calculation of this value.
[b]No near-infrared data has been detected towards these objects.

Table 2.6: Derived Masses & Velocities

Source	Δv	a_{eff}	$M_v^{\theta_{ap}}$	M_{env}	M_{env}^{iso}	T_{iso}	Δv
	km/s	km/s	$M_\odot$	$M_\odot$	$M_\odot$	K	Ref.
CB230	0.8	0.39	15	4.60	...	11	2
L1251B	1.00	0.46	18	4.95	...	14	1
IRAS 03256+3055	0.34	0.23	6.1	...	1.74	16	1
IRAS 04016+2610	0.23	0.21	2.4	...	0.26	16	3
IRAS 04108+2803	0.22	0.20	2.3	...	0.08	16	4
IRAS 04113+2758	0.22	0.20	2.3	...	0.22	16	4
IRAS 04166+2706	0.34	0.23	2.3	0.34	...	13	1
IRAS 04169+2702	0.29	0.22	2.4	0.37	...	15	1
IRAS 04239+2436	0.26	0.21	2.4	0.08	...	19	4
IRAS 04248+2612	0.34	0.23	4.3	0.14	...	23	4
IRAS 04264+2433	0.26	0.21	2.4	...	0.05	16	4
IRAS 04295+2251	0.3	0.22	1.1	0.10	...	16	4
IRAS 04302+2247	0.3	0.22	2.5	...	0.08	16	4
IRAS 04361+2547	0.36	0.24	2.5	0.16	...	16	4
IRAS 04381+2540	0.36	0.24	2.8	0.18	...	15	4
IRAS 04385+2550	0.27	0.22	2.4	...	0.04	16	4

References: 1. Mardones et al. 1997 (N_2H^+); 2. Wang et al. 1995 ($C^{18}O$); 3. Fuller & Myers 1993 (HC_3N); 4. Caselli et al. 2002 (N_2H^+).

Table 2.7: Test Case, CB230

p	n_f ($\times 10^5 cm^{-3}$)	r_i (AU)	r_o (AU)	κ_ν	L_{int} $L_\odot$	s_{ISRF}	χ^2_{450}	χ^2_{850}	χ^2_{SED}
ISRF									
1.9	22	100	1	OH5	6.7	**0.3**	0.4	28	91
2.0	22.5	100	1	OH5	5.8	**0.6**	0.9	31	105
2.2	25	100	1	OH5	4.5	**1**	0.6	53	113
2.2	< 25	100	1	OH5	...	**3**	...	...	...
Inner Radius									
2.2	30	**50**	1	OH5	4.5	1	0.6	53	113
2.2	25	**100**	1	OH5	4.5	1	0.6	53	113
2.2	25	**200**	1	OH5	4.75	1	0.5	49	120
2.2	25	**400**	1	OH5	6.75	1	0.3	43	117
2.2	25	**800**	1	OH5	6.8	1	1	38	200
Outer Radius									
1.9	35	100	**0.25**	OH5	4.8	1	1.6	33	32
2.1	33	100	**0.5**	OH5	4.7	1	1.9	50	28
2.1	27	100	**0.75**	OH5	4.4	1	2.9	48	88
2.2	25	100	**1**	OH5	4.5	1	0.6	53	113
2.2	0.5	100	**2**	OH5	6.0	1	33	560	591
Dust Type									
2.2	25	100	1	**OH5**	4.5	1	0.6	53	113
2.2	...	100	...	**OH2**	...	1	...	...	...
Beam									
2.2	25	100	1	OH5	4.5	1	2	20	113

Table 2.8: Test Case, IRAS 04295+2251

p	n_f ($\times 10^5 cm^{-3}$)	r_i (AU)	r_o (AU)	κ_ν	L_{int} $L_\odot$	s_{ISRF}	χ^2_{450}	χ^2_{850}	χ^2_{SED}
ISRF									
2.3	2	100	3.3	OH5	0.25	**0.3**	0.3	2	12
2.5	1.5	100	3.3	OH5	0.19	**0.6**	0.3	4	12
2.7	0.8	100	3.3	OH5	0.1	**1**	0.3	5	18
2.7	< 0.8	100	3.3	OH5	0.1	**3**	...	...	...
Inner Radius									
2.7	1	**50**	3.3	OH5	0.06	1	0.3	5	20
2.7	0.8	**100**	3.3	OH5	0.1	1	0.4	4	23
2.6	1	**200**	3.3	OH5	0.1	1	0.6	3	21
2.6	1	**400**	3.3	OH5	0.4	1	0.6	4	25
Outer Radius									
2.5	3.6	100	**1.1**	OH5	0.19	1	0.4	2	16
2.5	2.2	100	**2.2**	OH5	0.12	1	0.9	2	16
2.3	0.8	100	**3.3**	OH5	0.1	1	3.3	3.5	21
2.3	...	100	**6.6**	OH5	...	1	...	...	...
Dust Type									
2.3	0.9	100	3.3	**OH2**	0.05	1	6	5	24
2.3	0.8	100	3.3	**OH5**	0.1	1	3.3	3.5	21
Beam									
2.7	0.8	100	3.3	OH5	0.1	1	2	5	19

Table 2.9: Modeling Uncertainty Analysis

Variable	Range	Δp	ΔL_{int}
ISRF	0.3-3[a]	± 0.3	2.2
	0.3-3[b]	± 0.4	0.15
Inner Radius	50-400AU[a]	< 0.1	2.3
	50-400AU[b]	< 0.1	0.3
Outer Radius	25,000-200,000AU[a]	± 0.3	1.2
	11,000-66,000AU[b]	± 0.2	0.1
Dust Type	OH2-OH5	< 0.1	...
Disk	20-80% of total flux	-0.5	...
Beam	Nov99-Feb00	< 0.1	...
	Total uncertainty[a]:	$^{+0.4}_{-0.7}$	$\pm 3.4 L_{\odot}$
	Total uncertainty[b]:	$^{+0.4}_{-0.7}$	$\pm 0.4 L_{\odot}$

[a]For CB230.

[b]For IRAS 04295+2251.

Table 2.10: Power Law Models

Source	p	n_f ($\times 10^5 cm^{-3}$)	L_{int} $L_\odot$	χ^2_{450} [b]	χ^2_{850}	χ^2_{SED}
CB230	2.0	30	6.6	1	45	37
	1.9	22	6.7	0.4	28	91
	1.8	18	7.2	1	37	119
	2.4	55	6.8	10	242	169
	1.4	6.0	12	34	455	251
IRAS04166+2706	1.7	3.2	0.4	0.2	3	64
	1.6	3.0	0.4	0.2	2	72
	1.5	2.4	0.4	0.3	3	92
	2.1	6.6	0.2	2	16	57
	1.1	1.0	0.4	6	26	28
IRAS 04169+2702	1.6	3.5	0.73	11	50	35
	1.5	2.8	0.77	10	57	39
	1.4	2.5	0.80	10	71	40
	2.0	7.0	0.55	50	94	18
	1.0	0.8	0.9	155	308	57
IRAS 04239+2436	2.0	1.0	1.0	1.7	1.6	94
	1.9	1.0	1.0	0.8	0.7	18
	1.8	0.9	0.9	0.1	2	6
	1.7	0.75	0.9	0.2	5	12
	2.3	1.5	0.75	5	9	3
	1.3	0.3	1.7	18	66	150
IRAS 04248+2612	0.9	0.5	0.5	0.7	1	11
	0.8	0.35	0.6	0.5	2	12
	0.7	0.25	0.95	1.4	6	13
	1.3	1.5	0.4	7	20	5
	0.3	0.09	1.0	15	67	22
	1.0[a]	1.0	0.5	1	3	8

[a] We set an inner radius of 100AU for all sources. The outer radius is assigned as follows: CB230, 100,000AU;L1251B, 72,000AU; Taurus sources, 33,000AU. The ISRF is 0.3 times the standard as discussed in the text.
[b] We excluded the extended emission for this model.

Power-Law Models, continued.

Source	p	n_f ($\times 10^5 cm^{-3}$)	L_{int} $L_\odot$	χ^2_{450} [b]	χ^2_{850}	χ^2_{SED}
IRAS 04295+2251	2.4	2.0	0.25	0.3	4	11
	2.3	2.0	0.25	0.3	2	12
	2.2	2.0	0.25	0.9	2	12
	2.8	2.0	0.2	2	13	7
	1.8	0.9	0.4	9	14	29
IRAS 04361+2547	1.9	1.9	2.2	9	17	16
	1.8	1.8	2.2	6	14	17
	1.7	1.5	2.2	4	16	20
	2.3	3.0	1.5	17	49	6
	1.3	0.5	3.0	8	125	33
IRAS 04381+2540	1.7	2.0	0.53	2	17	4
	1.6	1.8	0.53	4	9	4
	1.5	1.4	0.53	7	4	6
	1.4	1.0	0.6	12	1	8
	1.3	0.8	0.7	22	1	9
	2.0	3.2	0.6	1	54	1
	1.0	0.35	1.1	78	42	15
L1251B	1.4	8.3	13	22	183	646
	1.5	12	10	41	111	73
	1.6	16	10	61	172	82
	2.0	44	7.5	138	1050	1261
	1.0	2.3	14.0	36	2033	570

[a] We set an inner radius of 100AU for all sources. The outer radius is assigned as follows: CB230, 100,000AU;L1251B, 72,000AU; Taurus sources, 33,000AU. The ISRF is 0.3 times the standard as discussed in the text.
[b] We excluded the extended emission for this model.

Table 2.11: Shu Collapse Models

Source	r_{infall} (AU)	a_{eff} km/s	L_{int} $L_\odot$	χ^2_{450}	χ^2_{850}	χ^2_{SED}
CB230	1000	0.39	6.7	2	21	4600
	2000	0.39	6.7	0.8	18	2089
	3000	0.39	6.7	0.7	78	1251
	4000	0.39	6.7	1	170	880
IRAS 04166+2706	1000	0.23	0.4	0.3	3	43
	2000	0.23	0.4	0.2	0.8	36
	3000	0.23	0.4	0.8	4	33
IRAS 04169+2702	1000	0.22	0.8	23	58	92
	2000	0.22	0.8	6	29	72
	3000	0.22	0.8	6	29	64
	4000	0.22	0.8	12	49	60
IRAS 04239+2436	500	0.21	0.9	0.5	1	682
	1000	0.21	0.9	0.3	5	488
	2000	0.21	0.9	3	20	328
IRAS 04248+2612	10,000	0.23	0.6	6	13	146
	15,000	0.23	0.6	7	17	140
IRAS 04295+2251	500	0.22	0.25	3	12	928
	1000	0.22	0.25	10	23	759
IRAS 04361+2547	500	0.24	2.2	8	14	359
	1000	0.24	2.2	4	12	655
	1500	0.24	2.2	2	18	546
IRAS 04381+2540	3000	0.24	0.5	10	3	187
	4000	0.24	0.5	14	2	152
	5000	0.24	0.5	17	4	131
L1251B	2000	0.46	10	52	161	2316
	3000	0.46	10	36	23	1989
	4000	0.46	10	28	40	1678

Table 2.12: Power-Law Models: Best-Fit Summary

Source	p	n_f ($\times 10^5 cm^{-3}$)	r_i (AU)	r_o ($\times 10^4$AU)	κ_ν	L_{int} $L_\odot$	s_{ISRF}	p_m
CB230	1.9	22	100	10	OH5	6.7	0.3	2.5
IRAS 04166+2706	1.6	3.0	100	3.3	OH5	0.4	0.3	2.4
IRAS 04169+2702	1.5	2.8	100	3.3	OH5	0.77	0.3	2.4
IRAS 04239+2436	1.8	0.9	100	3.3	OH5	0.9	0.3	2.1
IRAS 04248+2612	0.8	0.35	100	3.3	OH5	0.6	0.3	1.5
IRAS 04295+2251	2.3	2.0	100	3.3	OH5	0.25	0.3	...
IRAS 04361+2547	1.8	1.8	100	3.3	OH5	2.2	0.3	2.3
IRAS 04381+2540	1.6	1.8	100	3.3	OH5	0.53	0.3	1.7
L1251B	1.5	12	100	7.2	OH5	10	0.3	2.3

Chapter 3

A "Starless" Core that Isn't: Detection of a Source in the L1014 Dense Core with the Spitzer Space Telescope

3.1 Abstract

We present observations of L1014, a dense core in the Cygnus region previously thought to be starless, but data from the Spitzer Space Telescope shows the presence of an embedded source. We propose a model for this source that includes a cold core, heated by the interstellar radiation field, and a low-luminosity internal source. The low luminosity of the internal source suggests a substellar object. If L1014 is representative, other "starless" cores may turn out to harbor central sources.

3.2 Introduction

Modern astronomers first recognized dark nebulae as regions of star formation in the late nineteenth century. Molecular line studies (e.g., Myers & Benson 1983) showed that these dark nebulae contained copious amounts of cold material. Of these molecular cores, some were detected by the InfraRed Astronomical Satellite (IRAS) and others, so-called starless cores, were not. With the Infrared Space Observatory (ISO), Ward-Thompson et al. (2002) observed 18 starless cores at 90, 170, and 200 μm. While they mapped the emission at 170 and 200 μm, only one core was detected at 90 μm, consistent with the idea that most of these starless cores have no associated star more luminous than $\sim$0.1 $L_{\odot}$. The Spitzer Space Telescope (Werner et al. 2004) offers unprecedented sensitivity and resolution at wavelengths relevant to understanding the emission from luminous objects in dense cores. The Cores to Disks Legacy team (*c2d*, Evans et al. 2003) will observe over fifteen square degrees of large molecular clouds and over 120 star-forming cores, of which about 75 are considered to be starless. The only starless core observed so far is L1014, which presented a surprise. Spitzer's observations reveal an infrared point source in this supposedly "starless" core.

3.3 Environment of L1014

L1014 is a Lynds opacity class 6 dark cloud (Lynds 1962) that was undetected by both IRAS and MSX. Visser et al. (2002) observed this core with the Submillimetre Common Users Bolometer Array (SCUBA), and concluded that L1014 is a starless core based on two criteria: 1) it was not detected by IRAS and 2) they could not find evidence for an outflow.

While most authors have assumed a distance of 200 pc to L1014, there is no firm evidence for this distance. The lack of foreground stars indicates that it must

be closer than 1 kpc. Because it lies in the plane ($b = -025°$) near the Cygnus arm, distance estimates to these sources are unreliable. We adopt a distance of 200 pc for L1014, but we discuss the consequences of larger distances.

3.4 Observations and Results

For L1014, we present several new observations. First, we used Spitzer's InfraRed Array Camera (IRAC) and Multiband Imaging Photometer for Spitzer (MIPS) to observe this core at wavelengths from 3.6 to 70 μm (Fazio et al. 2004, Rieke et al. 2004). We also present new data from the Max-Planck Millimeter Bolometer (MAMBO) instrument on the IRAM 30-meter telescope and briefly discuss new molecular line observations with the Five College Radio Astronomy Observatory (FCRAO) and Seoul Radio Astronomy Observatory (SRAO). Finally, we include data from the 2 Micron All-Sky Survey (2MASS) and submillimeter observations from Visser et al. (2002).

The core of L1014 was observed with Spitzer on 2 Dec 2003 in all four IRAC bands (PROGID=139, AORKEY=5163776). The observations in each band consisted of two 30-second images, dithered by ~10", resulting in a generally uniform sensitivity across the 5'×5' field. Using a modified version of *dophot* (Schechter et al. 1993), we identified over 2900 different sources in the IRAC images, all but one of which are consistent with being reddened background stars. This one source was distinct from the other objects by its IRAC colors ([3.6] – [4.5] = 1.65, [5.8] – [8.0] = 1.65); see Allen et al. (2004) and Whitney et al. (2003) for a more detailed discussion of IRAC colors. The observed fluxes were obtained by fitting interpolated, real point spread functions (PSFs) to the detected sources. IRAC fluxes for the one source that is not consistent with being a reddened background star, SSTc2d 2124075+495909, at RA=$21^h24^m07.51^s$ and Dec=+49°59'09.0" (J2000.0), are listed in Table 1. We refer to this source as L1014-IRS and give all positions

relative to these coordinates.

MIPS 24 and 70 μm large field photometry of L1014-IRS was done on 10 Dec 2003 (PROGID=139, AORKEY=5164032). The 24 and 70 μm integration times were 36 and 100 seconds,respectively. The sky offset position was 300" in the scan direction (PA$\sim$ 45°). The 24 μm source is shifted from the IRAC position for L1014-IRS by (ΔRA, ΔDec)=($-$0.5", 0.7"). The 70 μm source is shifted by (1.8", 1"). The fluxes at 24 and 70 μm are in Table 1, listed with 20% uncertainty based on the calibration uncertainty as given by the SSC. We show a 3-color image, including the 3.6, 8.0, and 24 μm emission, in Figure 3.1. L1014-IRS stands out as the large red source at the center. The two closest, bright, bluer sources are seen in 2MASS; the brighter of the two is saturated in some of the IRAC bands. The available data for both sources are consistent with the idea that they are heavily reddened background stars, while the colors of L1014-IRS are inconsistent with those of a reddened background star.

The 2MASS point source catalog does not offer measured JHK fluxes for L1014-IRS. However, inspection of the K-band "Quicklook" image suggests the presence of faint, extended emission coincident with the central position of L1014-IRS. We have obtained the uncompressed 2MASS image and derived a K-band flux, in Table 1, for an 8" aperture. This aperture includes all of the extended emission that is visible in the 2MASS image.

We observed the 1.2 mm continuum emission, shown overlaid on the 8.0 μm data in Figure 3.2, in October 2002 using the 37-channel MAMBO array (Kreysa et al. 1999) at the IRAM 30-meter telescope on Pico Veleta (Spain). The beam size on the sky was 10.7". The source was observed on-the-fly, with the telescope secondary chopping in azimuth by 60" at a rate of 2 Hz; the total on-target observing time was 85 minutes. Zenith optical depth was 0.2. The data were reconstructed and analyzed using iterative methods (Kauffmann et al., in prep.). The map was

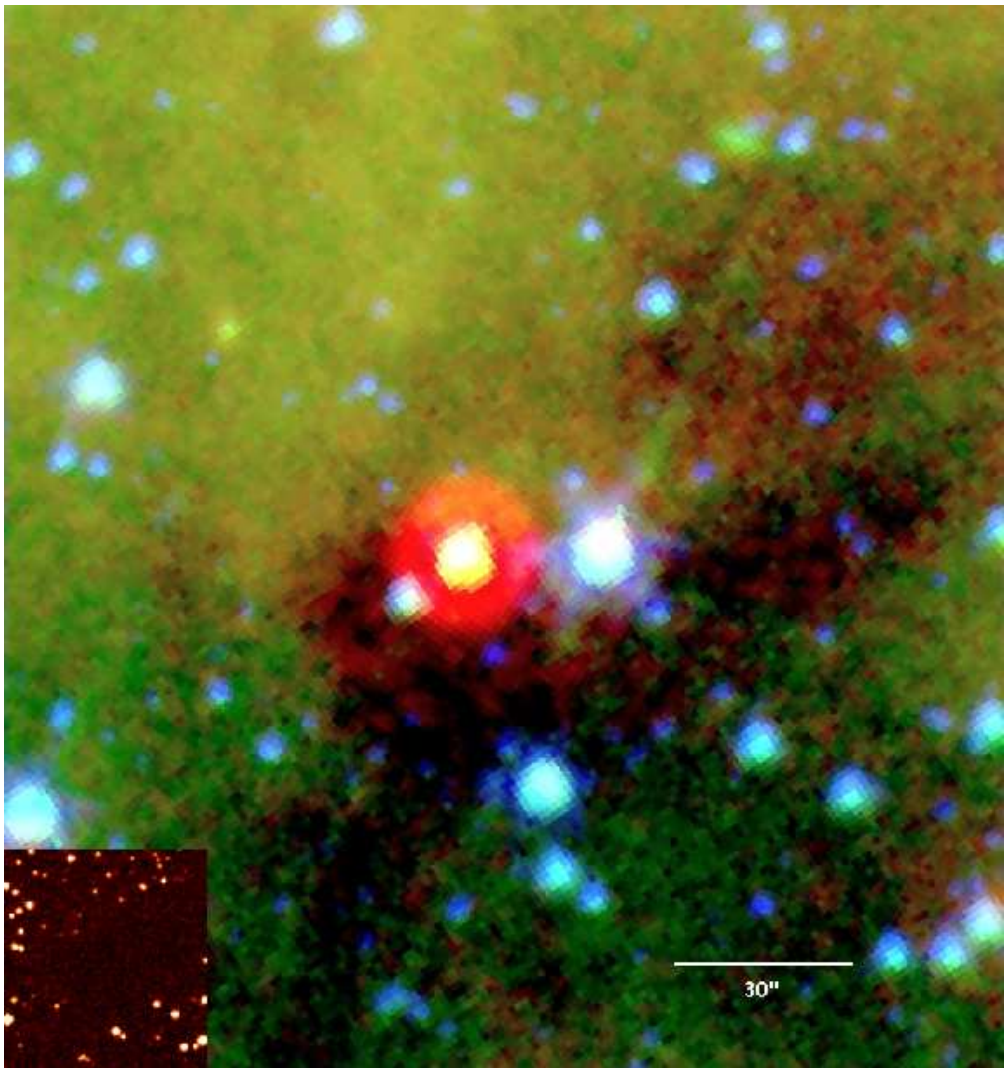

Figure 3.1: Three-color composite image of L1014-IRS. The IRAC 3.6 and 8.0 μm data are represented here as blue and green while the MIPS 24 μm data, with resolution more than three times worse than that of the IRAC bands, are shown in red. The R-band image, at lower left, is of the same field from the Digitized Sky Survey (DSS-2). The scale and orientation are the same as in Figure 3.2.

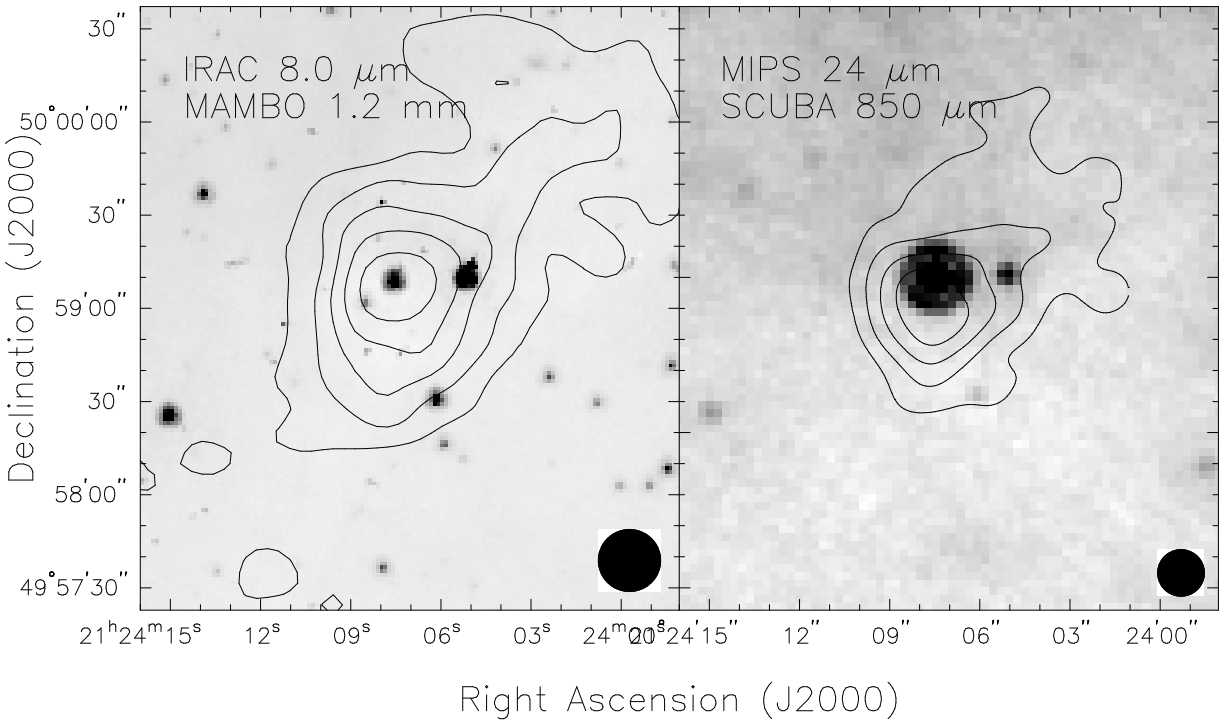

Figure 3.2: The 8.0 μm data from IRAC are shown in greyscale with the MAMBO 1.2 mm data as contours. The contours begin at 3-σ (3-σ =3.9 mJy beam^{-1}) and increase by 3-σ. The white cross marks the position of L1014-IRS (21h24m07.51s, +49d59m09.0s J2000). The data has been smoothed by 20", as shown by the black circle. The 24 μm data from MIPS are shown in greyscale with the SCUBA 850 μm data as contours. The contours begin at 3-σ and increase by 3-σ. The black circle shows the resolution of the James Clerk Maxwell Telescope at 850 μm, 15". The white cross marks the position of L1014-IRS (21h24m07.51s, +49d59m09.0s J2000). Additionally, 2MASS 21240852+4959021, as discussed in the text, is marked by a white square.

smoothed to 20". The observed flux for L1014, in Table 1, is calculated within a 120" aperture centered on the position of a Gaussian fit to the data. The center of the Gaussian is shifted from the IRAC position for L1014-IRS by (−1.5", −5.4").

Finally, we have collected the SCUBA data (850 and 450 μm) of Visser et al. (2002) from the telescope's archive; the 850 μm data are shown as contours overlaid on the MIPS 24 μm image in Figure 3.2. To provide consistency with our measured flux from MAMBO, we have taken the SCUBA fluxes with a 120" aperture centered on the position of a Gaussian fit to the data. The 850 and 450 μm peaks are shifted from the IRAC position by (−1.5", −8″) and (0" , −6.9"), respectively. With these continuum data (from λ = 3.6 to 1200 μm), we calculate T_{bol} = 50 K (Myers & Ladd 1993) and L_{bol}/L_{smm} = 20 (André et al. 1993), classifying L1014-IRS as a Class 0 core.

We observed the emission from various molecular transitions with the SRAO 6-m telescope at Seoul National University (Koo et al. 2003), with a beam size of $\sim 100''$. Our CO (1→0) maps covered 480"×480" with a 4' grid spacing; the ^{13}CO (1→0) map covered 120" by 120" on a 2' grid. We also made single pointing observations toward the center of L1014 in CS (2→1) and HCN (1→0). The observations of CO show that there are two different velocity components at about 4 and −40 km s^{-1} towards L1014 (σ = 0.05 K). The 4 km s^{-1} component was detected in CS (2→1) (T_A^* ∼0.22 K) and marginally in HCN (1→0) (0.09 K). The −40 km s^{-1} component was not detected in either CS or HCN (σ = 0.03 K).

We also mapped L1014 in CO and C^{18}O (1→0) using the SEQUOIA 32-pixel, focal-plane array mounted on the 14-m FCRAO, with a beamsize of $\sim 40''$. The spectra were taken in a 800"×800" region centered at the 1.2 mm emission peak in on-the-fly mode. We detected strong emission of CO (1→0) (σ = 0.100 K; Δv = 0.127 km s^{-1}) and C^{18}O (1→0) (σ = 0.022 K; Δv = 0.133 km s^{-1}) at L1014's velocity (4.2 km s^{-1}); this emission extended across our entire map. The

spectra were highly non-Gaussian and showed a blue wing-like emission throughout the map. The CO emission also has an additional overlapping component redward of the $C^{18}O$ line center position (at 5 km s^{-1}) that peaks at (−200", −200") and is elongated in the SW-NE direction. The $C^{18}O$ (1→0) integrated intensity peaks at (−27", 26") from the reference position; the emission is elongated in the SE-NW direction and is approximately 200" wide. The component at $v_{LSR} = -40$ km s^{-1} peaks at (32", −73") relative to our reference position. From the FCRAO and SRAO molecular line observations, we make two conclusions: 1) while the CO line profiles are non-Guassian, the region is too complicated to either confirm or deny the existence of an outflow, and 2) we see a second velocity component in the CO and $C^{18}O$ spectra at about −40 km s^{-1}.

Brand & Blitz (1993) assigned a distance of 2.6 kpc to an HII region, S124, whose associated molecular cloud has $v_{lsr} = -40$ km s^{-1}; S124 is offset from L1014-IRS by (3.5°, −0.5°). This velocity component was not seen in our observations of HCN (1→0) and CS (2→1). Because no foreground stars are observed within ∼1' of the core's center, the dark cloud as seen in the DSS image cannot be at 2.6 kpc, so it must be associated with the 4 km s^{-1} component. We believe that the infrared source is also associated with the 4 km s^{-1} component, but we will consider the alternative possibility.

3.5 Models for the L1014 Core

In an attempt to understand the physical state of L1014, we have used the data to create a working model. We used the SCUBA 850 μm data to determine the density profile by matching our models with the observed intensity profile at 850 μm. We have used a 1-dimensional radiative transfer package, *Dusty* (Ivezić et al. 1999), to calculate the temperature profile and the observed SED; *ObsSphere* (Shirley et al. 2002) was used to simulate the SCUBA observations, including the

effects of chopping. We used the dust opacities of Ossenkopf & Henning (1994), which represent grains with thin ice mantles (OH5 dust) and are appropriate for cold, dense cores (e.g., Evans et al. 2001).

The core is heated internally by a protostar and externally by the interstellar radiation field (ISRF). The ISRF has been attenuated with dust whose properties are given by Draine & Lee (1984) with A_V=0.5. Both a shallow power-law ($n(r) \propto r^{-1.0}$) and a Bonnor-Ebert (BE) sphere were found to provide good fits to the observed 850 μm brightness profile, in agreement with results from other "starless" cores (e.g., Evans et al. 2001). Because it offers a good fit to the density structure, we use the analytical approximation given by Tafalla et al. (2002) for an isothermal BE sphere, $n(r) = \frac{n_c}{1+\left(\frac{r}{r_0}\right)^{\alpha}}$ and found a good fit for $n_c = 1.5 \times 10^5$ cm^{-3}; for this central density, a BE sphere is approximated with $r_0 = 4090$ AU and $\alpha = 2.32$. We used inner and outer radii of 50 and 15000 AU, respectively, but these are poorly constrained. This core has a mass of 1.7 $M_\odot$.

The long-wavelength dust continuum emission shows that a cold, dense core is present and external heating can explain the emission longward of 70 μm. The bolometric luminosity for L1014-IRS is 0.3 $L_\odot$, typical of starless cores heated only by the ISRF (Evans et al. 2001). In these respects, L1014 looks like a core with no significant internal heating.

The IRAC and MIPS data trace the SED of a considerably warmer source. The starless core model underestimates the 70 μm flux by a factor of 50 and cannot begin to explain the data at shorter wavelengths. Given the parameters above, we find that a source with luminosity of 0.025 $L_\odot$ and $T_{eff} = 700 \pm 300$ K best fits the IRAC data (as seen in Figure 4.8).

To match the 24 and 70 μm points, a cooler component with substantially more surface area, such as a disk, is required. We use a simple model (Butner et al. 1994; Adams et al 1988) to simulate the disk emission. The disk has a total mass

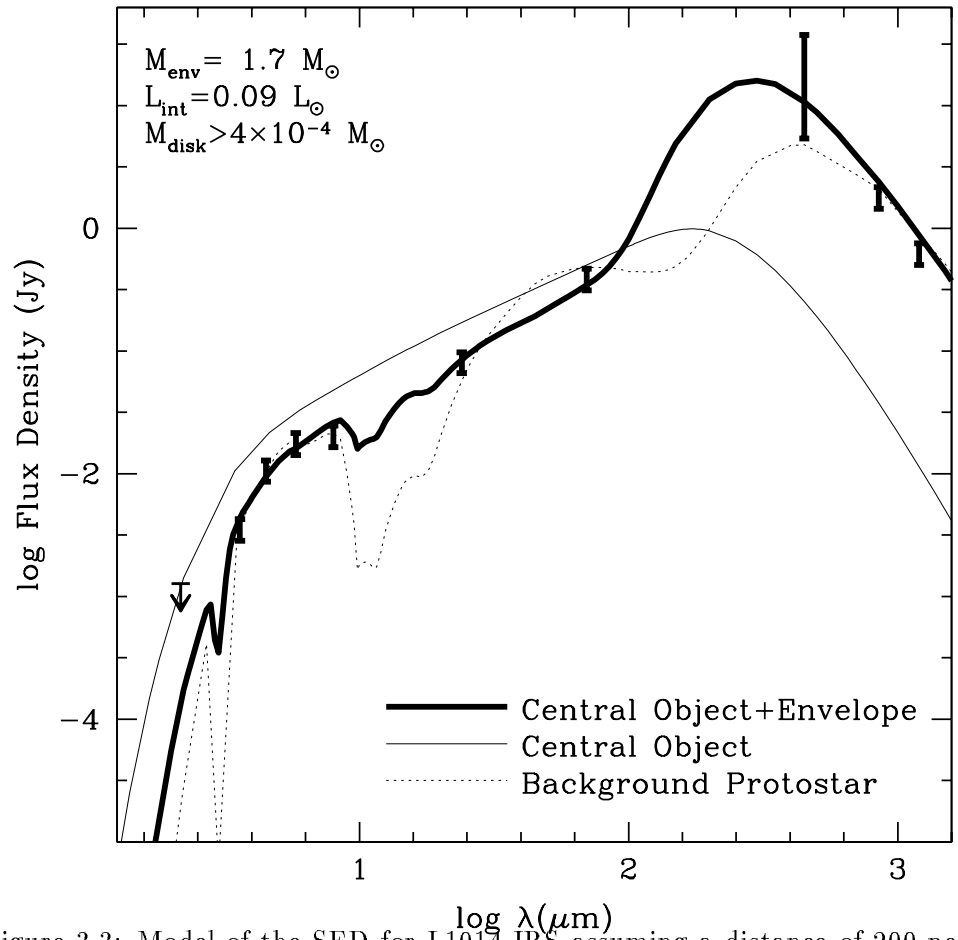

Figure 3.3: Model of the SED for L1014-IRS assuming a distance of 200 pc. This model shows the emission from a Bonnor-Ebert sphere heated externally by the interstellar radiation field and internally by a star and disk. The star has a luminosity of 0.025 $L_\odot$ and effective temperature of 700 K. The disk is made to simulate flaring, has a mass of 4×10^{-4} $M_\odot$, and has an intrinsic luminosity of 0.065 $L_\odot$. The spectrum for the internal source is drawn by the thin, solid line; this is the input spectrum for *Dusty*. The emergent SED is represented with the thicker line. The thin, dotted line shows the model for a background protostar, as discussed in the text.

(gas & dust) of $4 \times 10^{-4} (R_D/50\mathrm{AU})^{0.5}$ $\mathrm{M}_\odot$, and a temperature profile, $T(r) \propto r^{-0.5}$, simulating the effects of accretion onto the disk surface. R_D, the outer radius of the disk, is set to 50 AU, the smallest disk that matches the 70 μm data; larger values for R_D and the mass are possible.

The disk model that fits is passively heated by the central protostar and is itself luminous, possibly from accretion directly onto the disk. The partition of luminosity between the star and disk is not well constrained, so we use 0.09 $\mathrm{L}_\odot$ for the total luminosity of a central source in further discussion. Future observations with millimeter and submillimeter interferometers are needed to constrain the value of R_D and hence mass; this model, with $R_D = 50$ AU, predicts a flux of 4.3 mJy at 850 μm.

If this model is correct, we are observing a very low-mass protostar (or proto-brown dwarf). Assuming spherical accretion at a rate of 2×10^{-6} $\mathrm{M}_\odot$ yr^{-1} (as expected for a 10 K collapsing, isothermal sphere) onto a star with a radius of 3 $\mathrm{R}_\odot$ and a mass of 0.1 $\mathrm{M}_\odot$, the luminosity would be 1.8 $\mathrm{L}_\odot$, 20 times what the observations permit. If we consider accretion rates appropriate for the BE or "Plummer-like" sphere (e.g., 3×10^{-5} $\mathrm{M}_\odot$ yr^{-1}) as in Whitworth & Ward-Thompson (2001), the disparity between the predicted and observed luminosity is greatly amplified. Kenyon and Hartmann (1995) suggested that protostars may appear sub-luminous if accretion occurs toward the edge of a circumstellar disk. As the disk becomes too massive, the system will undergo an FU Ori-type event where material accretes onto the star in a short burst. Maybe, we see L1014-IRS during a quiescent time when material is accreting and collecting in the disk. Nonetheless, this is not an ordinary, accreting pre-main-sequence star. Unless accretion is much less or the radius much larger, the mass of the central object is possibly substellar.

These conclusions depend on the distance, which is uncertain. Roughly, the core mass and central luminosity scale as d^2. For 400 pc, the values would be 6.8

$M_\odot$ and 0.36 $L_\odot$. Furthermore, the geometry might vary from the 1-dimensional core model studied in this paper. We have created a simple 2-dimensional model that includes a completely evacuated outflow cavity with a 30° opening angle and an internal source as already described. Using *Radmc* (Dullemond & Dominik, 2004), we have calculated the SED for this model and found that, unless you look into the outflow cavity, the SED does not change by more than 10%.

Another possible alternative is that L1014-IRS is a background protostar in the -40 km s^{-1} cloud at 2.6 kpc. Models were calculated for an embedded protostar at this distance obscured by a foreground cloud; the emergent SED for this model is shown in Figure 4.8. This was calculated in two steps in *Dusty*, first calculating the emerging spectrum of the protostar and then illuminating a 10 K planar slab of an $A_V = 10$ with this spectrum. The protostellar envelope was assumed to be free-falling ($n = n_0(r/r_0)^{-3/2}$), and the ISRF was ignored. The modeled protostar had $L = 16$ $L_\odot$ and was surrounded by a 0.6 $M_\odot$ envelope but no disk. The infrared source could be a typical protostar at a larger distance. We find this scenario to be statistically unlikely for several reasons. First, the lack of CS and HCN emission from the -40 km s^{-1} component and the fact that the CO and ^{13}CO emission do not peak at this position argue against this scenario. Second, a map of CS (2→1) at FCRAO with a 50" beam shows that the 4 km s^{-1} component has peak emission within one beam of L1014-IRS, further supporting our nearby distance (de Vries et al. in prep.). Finally, at 70 μm, L1014-IRS was the only source of emission within our field; the 24 μm flux for this source was the largest within the MIPS field for L1014. Such bright, infrared objects are uncommon, so a chance alignment between a background protostar and a foreground starless core is unlikely.

3.6 Conclusions

We have presented one of the most comprehensive sets of continuum data for a "starless" core since their discovery. These data span wavelengths from 2.17 to 1200 μm and include spatially resolved maps of the millimeter emission from L1014-IRS. From these data, we conclude that this core, previously thought to be starless, does harbor a central object. Assuming a distance of 200 pc, we have created a model for this object that includes a 1.7 $M_\odot$ envelope heated externally by the ISRF. This core contains a central object with low luminosity ($\sim$ 0.09 $L_\odot$). This central source must have "stellar" and disk-like components in order to match the 3.6 to 70 μm photometry. This object appears to be substellar, though there is enough envelope mass to grow a star if a substantial fraction accretes. We have considered an alternate scenario, in which a distant, more luminous, but less embedded, protostar lies behind the core of the L1014 dark cloud. This scenario is unlikely but cannot be ruled out conclusively without further observations.

Assuming that the infrared source lies in the L1014 cloud, there are two significant conclusions. First, cores thought to be starless may harbor central objects. If this phenomenon is common, estimates for timescales for the evolution of starless cores will need revision. Second, for plausible distances, this source has a very low luminosity. The usual assumptions about accretion rates and pre-main-sequence masses and radii produce far more luminosity than is seen. This object currently appears to be substellar, though it is likely to accrete more mass.

3.7 Acknowledgements

Support for this work, part of the Spitzer Legacy Science Program, was provided by NASA through Contracts Number 1224608 and 1230780 issued by the Jet Propulsion Laboratory, California Institute of Technology under NASA contract 1407. The

Table 3.1: Photometry of L1014-IRS

Source	λ (μm)	$S_\nu(\lambda)$ (mJy)	σ (mJy)	θ_{ap} (")
L1014-IRS	2.17	1.3	0.2	8
α=21^h 24^m 07.51"	3.6	3.6	0.7	1.7[1]
δ=+49° 59'09.0"	4.5	10.7	2.1	1.5[1]
	5.8	17.8	3.6	1.7[1]
	8.0	20.6	4.1	2.0[1]
	24	81.8	16.0	5.7[1]
	70	390	40	17[1]
	450	21500	16100	120
	450	1070	230	Peak (mJy/beam)
	850	1800	400	120
	850	160	30	Peak (mJy/beam)
	1200	630	126	120
	1200	23	5	Peak (mJy/beam)

[1]FWHM of the Spitzer point spread profile.

Leiden *c2d* legacy team is supported by a Spinoza grant from the Netherlands Foundation for Scientific Research (NWO) and by a grant from the Netherlands Research School for Astronomy (NOVA). Observations at the SRAO were supported by the KOSEF R01-2003-000-10513-0 program. The SCUBA data were provided to us as a guest user, Canadian Astronomy Data Centre, which is operated by the Dominion Astrophysical Observatory for the National Research Council of Canada's Herzberg Institute of Astrophysics. This publication makes use of data products from the Two Micron All Sky Survey, which is a joint project of the University of Massachusetts and the Infrared Processing and Analysis Center/California Institute of Technology, funded by NASA and the NSF. Finally, we thank our anonymous referee for insightful and useful comments.

Chapter 4

Evolutionary Signatures in the Formation of Low-Mass Protostars

4.1 Abstract

We present an evolutionary picture of a forming star. We assume a singular, isothermal sphere as the initial state of the core that undergoes collapse as described by Shu (1977). We include the evolution of a first hydrostatic core at early times and allow a disk to grow as predicted by Adams & Shu (1986). We use a 1-dimensional radiative transfer code to calculate the spectral energy distribution for the evolving protostar from the beginning of collapse to the point when all envelope material has accreted onto the star+disk system. Then, we calculate various observational signatures (T_{bol}, L_{bol}/L_{smm}, and infrared colors) as a function of time.

As defined by the bolometric temperature criterion, the Class 0 stage should be very short, while the Class I stage persists for much of the protostar's early life. We present physical distinctions among the classes of forming stars and calculate

the observational signatures for these classes. Finally, we present models of infrared color-magnitude diagrams, as observed by the Spitzer Space Telescope, that should be strong discriminators in determining the stage of evolution for a protostar.

4.2 Introduction

In 1977, Shu presented seminal work in the theory of low-mass, isolated star formation (Shu 1977, hereafter Shu77). He presented the idea that stars could form from inside-out collapse. This model is still important today because it is simple, yet it predicts so many observables in the process of star formation. It prescribes the evolution of inflow, the velocity structure of the envelope, and the particular shape of the envelope's density distribution. Motte & André (2001) found that the inside-out collapse model fit millimeter observations of protostars in Taurus and various Bok globules. However, these authors also found Class 0 sources in Perseus, a less quiescent region of star formation, that had central densities and accretion rates that were too high to be accounted for by the Shu77 model. Molecular line observations have also been used to compare the predicted densities and velocities with the actual conditions in star-forming cores. Hogerheijde & Sandell (2000) and Zhou et al. (1993) presented evidence that the envelopes of some protostars are undergoing inside-out collapse. Others have presented evidence against inside-out collapse. For example, Tafalla et al. (1998) suggested that L1544, a starless core, exhibits infall motions across the entire core. Nonetheless, it is still not clear whether the Shu77 inside-out collapse scenario or its variants can be ruled out.

Therefore, we have calculated the observational signatures of a star, which is forming through inside-out collapse, so that astronomers can test this theory in a well-defined way. The most relevant aspects of the Shu77 inside-out collapse model are a constant accretion rate of material from the envelope onto the star+disk system and an envelope density that is initially described by a singular, isothermal sphere

(SIS).

The constant accretion rate in this model has given rise to the so-called "luminosity problem": the luminosities that result when material accretes onto a central object with a small radius and increasing mass exceed those seen for most young, low-mass stars (Kenyon & Hartmann, 1995). The presence of a disk can help by increasing the accretion radius and acting as a reservoir where matter is stored and then episodically accreted. However, a disk does not completely eliminate the "luminosity problem" in these models.

A constant accretion rate in star-forming cores should be evident when comparing populations in the different stages of star formation. The transition from Class 0 to Class I object is thought to occur when the mass of the star and disk is equal to the envelope mass. Therefore, we should observe equal numbers of Class 0 and I objects if they form with constant accretion rates. André & Montmerle (1994) found about a 10:1 ratio for Class I and 0 sources in Ophiuchus, suggesting the Class 0 stage is very short. However, Visser et al.(2002), in an unbiased survey of dark clouds, found a 1:1 ratio. These authors suggested that Ophiuchus has experienced a burst of star formation in the past, resulting in the 10:1 ratio. Future and ongoing surveys of nearby star-forming regions will certainly offer more information regarding the relative populations of Class 0 and Class I sources (Evans et al. 2003;Benjamin et al. 2003).

The initial density configuration for the Shu77 model is that of a SIS, which has $n(r) \propto r^{-2}$. One-dimensional modelling of the submillimeter emission from starless cores has shown that their density distributions are well-fitted by Bonnor-Ebert spheres, but power-law density profiles are not conclusively ruled out (Ward-Thompson et al. 1994; Evans et al. 2001). Indeed, some starless cores have a density structure that seems to be approaching the SIS. For example, three-dimensional modelling of L1544 shows a power-law density distribution with $n(r) \propto r^{-2}$ (Doty

et al. 2005). Other studies of the density distribution in more evolved star-forming cores were unable to rule out the Shu77 predictions (Young et al. 2003); in fact, one-third of the sources in Young et al. (2003) were well-fitted by the inside-out collapse model. For this paper, we assume that starless cores must evolve into an SIS. At this point, collapse ensues, and we begin modeling the evolution of the protostar. This work has been expanded by Lee et al. (2004) to model the chemical evolution of these star-forming cores.

Other authors have predicted the observed signatures of a forming star. Myers et al. (1998), hereafter M98, developed a framework on which to calculate various signatures of star formation. Our work has been prompted by their efforts. However, the methods and models employed in this work are quite different from those of M98; as a result, our conclusions are different. We discuss these differences in this paper.

Because these models are 1-dimensional, we do not consider the role of outflows, flattened envelopes, or asymmetric disks; therefore, we probably underestimate the amount of short-wavelength radiation. Whitney et al. (2003, hereafter W03) have included some of these complications. However, W03 did not create a consistent evolutionary model but, instead, considered "typical" protostellar objects of different observational classes. Fortunately, these authors were able to explore the impact of 3-dimensional effects, which we are unable to model. In this way, we consider this effort to be complementary to the work of W03 and compare our results to theirs.

The advent of large surveys such as 2MASS and the Spitzer Space Telescope's Legacy programs (Evans et al. 2003; Benjamin et al. 2003) provide vast sets of data through which theories of star formation may be vigorously tested. In this work, we hope to provide some tangible means to study the validity of the inside-out collapse model in the role of forming stars.

4.3 The Model

First, we define the framework through which we have created this evolutionary sequence. In this section, we discuss what has been assumed for the dust opacity, interstellar radiation field, envelope structure and dynamics, and the evolution of the star and disk components of the system.

4.3.1 Interstellar Radiation Field & Dust Properties

Evans et al. (2001) showed that, for starless cores, the interstellar radiation field (ISRF) significantly affects both the total observed luminosity and the shape of the observed submillimeter intensity profile; even objects with a luminous, internal source might attribute most of their luminosity to the ISRF (Young et al. 2004a). Evans et al. (2001) scaled the ISRF by a constant, but we have used the opacity of Draine & Lee (1984) dust to attenuate the ISRF with $A_V = 0.5$ (see Figure 8 in Young et al. 2004b). This method simulates the effects of low density material in the environs of a star-forming core.

These authors (Evans et al. 2001; Shirley et al. 2002; Young et al. 2003) also found that the multi-wavelength observations were best matched by using the opacities of the dust modeled by Ossenkopf & Henning (1994). In particular, they concluded that "OH5" dust, found in the fifth column of Table 1 in Ossenkopf & Henning (1994), was optimal for star-forming cores. Unfortunately, the modeled data for OH5 dust does not include wavelengths shortward of 1.25 μm. Ossenkopf & Henning (1994) calculated only the values for the dust opacity (κ) and not the scattering and absorption cross-sections (σ_{abs} and σ_{scat}) as needed by DUSTY, the radiative transfer program we have used (Ivezić et al. 1999; Ivezić et al. 1997). Therefore, we have obtained data from Pollack et al. (1994), which includes the scattering and absorption cross-sections for wavelengths as short as 0.091 μm. In Figure 4.1, we show the opacities for OH5 dust and the opacity calculated by Pollack

et al. (1994) for dust grains with a radius of 0.1 μm at a temperature of 10 K (hereafter, P1 dust); we have assumed a gas-to-dust ratio of 100 and give the opacity of the gas in this figure. At short wavelengths, these two types of opacities are in fairly good agreement; unless τ is low, however, the short-wavelength opacity is not relevant. We used the opacity given for OH5 and σ_{scat} for the P1 dust to calculate the absorption coefficient for the OH5 dust. Further, we used the albedo values given by Pendleton et al. (1990, Figure 4b) to apportion the opacity due to scattering and absorption from the 3 μm ice feature. Finally, we have extrapolated the cross-sections out to 3.6 cm, as required by DUSTY. For σ_{scat}, we extrapolate by a λ^{-4} power-law as expected for Rayleigh scattering. We fit the last several data points of the OH5 absorption coefficients to determine the $\lambda^{-1.8}$ power-law used to extrapolate σ_{abs} out to $\lambda = 3.6$ cm. We show the scattering and absorption coefficients in Figure 4.1.

4.3.2 Envelope

For the density structure in the envelope, we adopt the inside-out collapse scenario (Shu 1977). This model begins with an SIS with a density distribution that is proportional to r^{-2}. Through some perturbation, collapse begins inside the cloud and proceeds outward. As collapse ensues, the cloud's density distribution can be approximately described by a broken power law: the inner collapsing portion, $n \propto r^{-3/2}$ (indicative of freefall), and the outer static envelope, $n \propto r^{-2}$. However, there is a transition region just within the infall radius where the density profile is significantly flatter than the $r^{-3/2}$ power law. Therefore, we use the actual solutions to Equations 11 and 12 in Shu (1977).

When the infall radius exceeds the outer radius, the Shu77 solution is no longer valid. Therefore, we adopt a density profile with $n \propto r^{-3/2}$ and let the mass of the envelope (and, hence, the fiducial density) decrease as mass is accreted onto

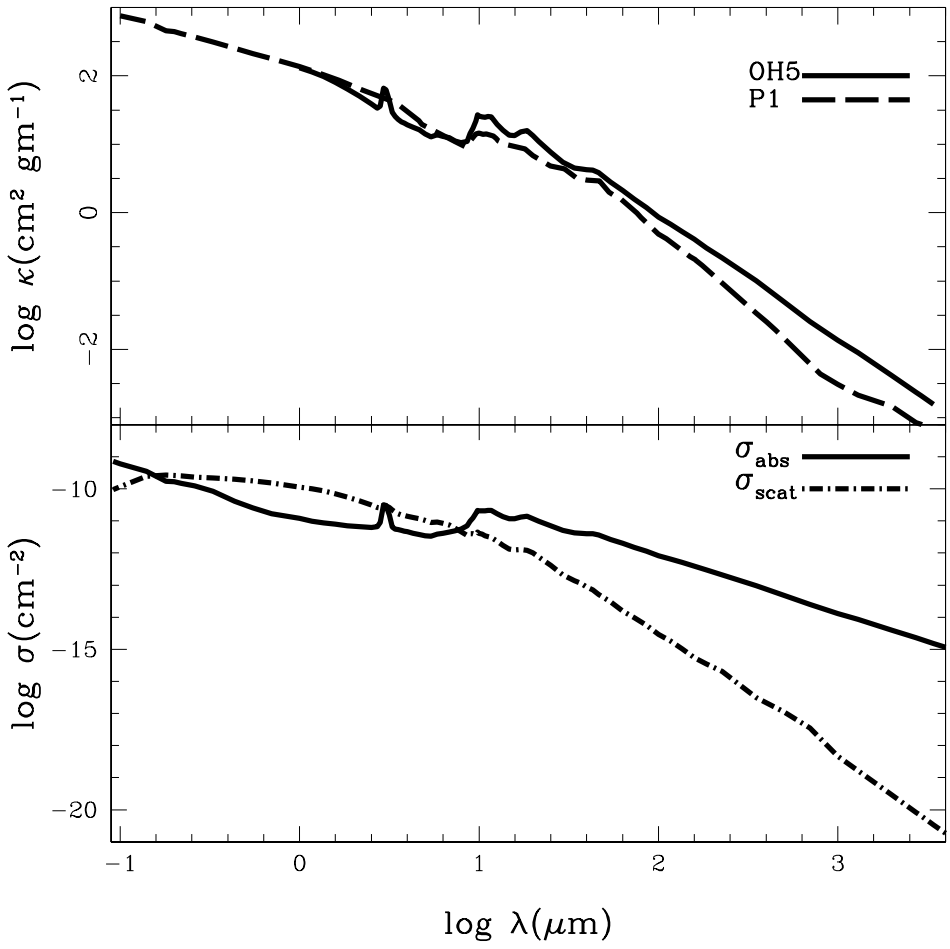

Figure 4.1: The top plot shows the opacity of the gas with OH5 and P1 dust (assuming a gas-to-dust ratio of 100). We have used the OH5 dust for our models. However, we used the P1 opacities for wavelengths shortward of 1 μm. The bottom plot shows the absorption and scattering cross-sections for OH5 dust.

the protostar and disk.

The total amount of mass is constrained by the effective sound speed (c_s) and the envelope's outer radius (r_o). The models presented herein all begin with cores whose initial masses are different. We calculate this mass from the following expression:

$$M_{env}^{t=0} = \frac{2c_s^2 r_o}{G}, \tag{4.1}$$

where G is the gravitational constant, and c_s is the effective sound speed,

$$c_s = \left(\frac{kT}{\mu m_H} + \frac{1}{2}v_{turb}^2\right)^{1/2}, \tag{4.2}$$

where k is Boltzmann's constant, T is the isothermal temperature, μ is the mean molecular mass ($\mu = 2.29$), and m_H is the mass of the hydrogen atom ($m_H = 1.6733 \times 10^{-24}$g) and v_{turb} is the turbulent velocity (1/e Doppler width). We choose $T = 10$ K and the value for v_{turb} such that the turbulent contribution to the sound speed is equal to the thermal component ($v_{turb} = 0.268$ km s^{-1}); $c_s = 0.268$ km s^{-1}.

We calculate the total envelope mass as follows,

$$M_{env} = \mu m_H \int_{r_i}^{r_o} 4\pi r^2 n(r) dr, \tag{4.3}$$

where r_i and r_o are the inner and outer radii of the envelope. In this paper, radii pertaining to the envelope are denoted by the lower-case "r" (r_i, r_{inf}, and r_o) while the radii of the star and disk are denoted by the upper-case "R" (R_*, R_i, R_D).

Even though the Shu77 model has no specific mass scale, we assume that the model is applicable to the formation of stars with different masses. In order to define the mass of the core, we truncate the outer radius of the envelope, using Equation 4.1. Such truncated envelopes are not unheard of; Motte et al. (1998) found evidence for truncated outer radii for cores in Ophiuchus. In this paper, we consider cores with three initial masses: 0.3, 1.0, and 3.0 $M_\odot$. With our assumed sound speed, these masses correspond to outer radii of 1767, 5889, and 17667 AU.

We end our modeling when all envelope material has accreted onto the star-disk system. In these three scenarios, this event occurs at 62500, 210000, and 625000 years, respectively. The time for collapse varies significantly among the three models, but this variation is inherent within the inside-out collapse model, assuming similar initial conditions. With constant and identical accretion rates, lower-mass objects simply form more quickly than higher-mass objects. We show the mass evolution for each of these cases in Figure 4.2.

It is not clear whether this model is realistic for cores with masses as low as 0.3 $M_\odot$. The Jean's mass for a core with $T = 10$ K and density of 10^6 cm^{-3} is $\sim$0.6 $M_\odot$ ($M_J = 18 M_\odot T_K^{1.5} n^{-0.5}$). However, if the cloud is cooler, it could be unstable to collapse (e.g., if $T = 5$ K and $n = 10^6$, $M_J = 0.2$ $M_\odot$). In fact, much smaller mass cores can be created through turbulent fragmentation (Boyd & Whitworth 2005), so the 0.3 $M_\odot$ is probably not so absurd. Considering that some evolved protostars are thought to be substellar (White & Hillenbrand 2004), we must consider how these objects are formed.

Defining the envelope's inner radius is an issue. One choice is that the envelope's inner radius could be equal to the outer radius of the disk. However, this disk radius, which is defined as the centrifugal radius (Section 4.3.3), is very small at early times. With a small inner radius, the density in the inner region is unrealistically large (e.g., $n \sim 10^{10}$ cm^{-3}). These dense regions cause the opacity to become very high. Further, a rotating envelope becomes flattened and aspherical at these small radii (Terebey et al. 1984), so a spherical model is not appropriate to these regions. Therefore, we set a maximum value for $\tau(100\ \mu\mathrm{m})$ and calculate the inner radius of the SIS (at $t = 0$) so that $\tau_\nu(100\mu\mathrm{m})$ is equal to τ_{max}.

$$r_i = \left[\frac{\tau_{max} G 2\pi}{\kappa_\nu c_s^2} + \frac{1}{r_o} \right]^{-1} \tag{4.4}$$

We choose $\tau_{max} = 10$ and discuss the impact of varying this in section 4.7.3. The envelope's inner radius follows this formula until it is exceeded by the disk radius.

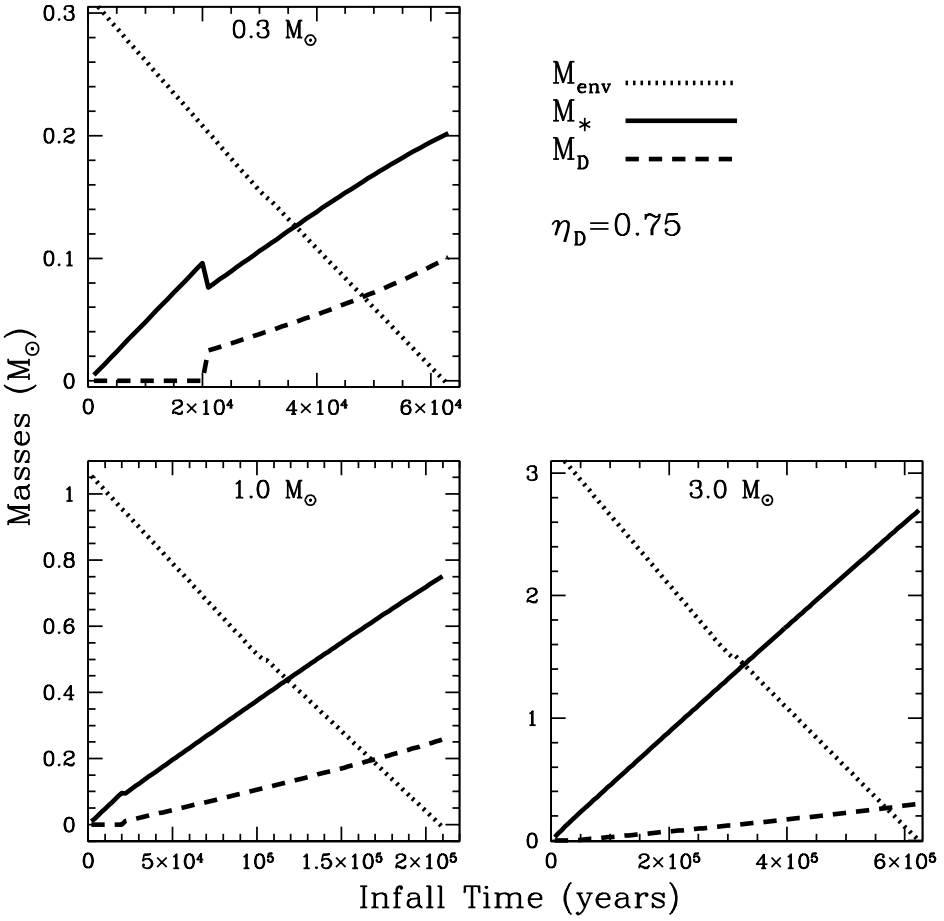

Figure 4.2: The mass of the star and disk increase as mass from the envelope is accreted by the protostellar system as shown here for the three mass scenarios considered.

For the three cores, the envelope's inner radius is 100 AU at the end of collapse (see Section 4.3.3).

We define the infall rate for the case of a non-magnetic, centrally peaked envelope density distribution as described in the Shu (1977) scenario. The rate of constant accretion is calculated as follows:

$$\dot{M} = m_o \frac{c_s^3}{G}, \tag{4.5}$$

where m_o is a dimensionless constant of order unity. Since $c_s = 0.268$ km s^{-1}, the accretion rate, $\dot{M}$, is 4.8×10^{-6} M$_\odot$ yr^{-1}.

We adopt the prescription of Adams & Shu (1986) for the infall rate onto the disk and star. These authors assume that all mass is accreted onto either the disk or star such that $\dot{M} = \dot{M}_* + \dot{M}_D$ where $\dot{M}_*$ is the accretion rate of envelope material directly onto the star and $\dot{M}_D$ is the accretion rate onto the disk. These values are calculated as follows:

$$\dot{M}_* = \dot{M}[1 - (1 - u_*)^{1/2}], \tag{4.6}$$

$$\dot{M}_D = \dot{M}(1 - u_*)^{1/2}, \tag{4.7}$$

where u_* is the ratio of the star and disk radii, R_*/R_D. In almost all cases, u_* becomes very small in a short time and, hence, $\dot{M}_*$ also approaches zero. However, material also accretes from the disk onto the star; this process is not included in these equations. Adams & Shu (1986) defined an efficiency factor—η_D, the fraction of material in the disk that will accrete onto the star—so that the star could gain mass and be a source of accretion luminosity. We discuss the implementation of this accretion process in the next section.

4.3.3 Disk

Evidence in the form of near- and mid-infrared (Padgett et al. 1999) and millimeter (Mundy et al. 1996; Kitamura et al. 2002) observations of disks surrounding stellar

and substellar objects has recently become more convincing. Also, the inclusion of a disk in various models has a significant effect on the interpretations of those models. Therefore, to not include a disk in this evolutionary scheme is wholly unrealistic.

We adopt the disk model developed, in theory, by Adams et al. (1988), and, in practice, by Butner et al. (1994). The density distribution for the dust and gas (assuming homogeneous mixing) is defined as

$$\Sigma(R) = \Sigma_\circ \left(\frac{R}{R_f}\right)^{-p}, \tag{4.8}$$

where $\Sigma_\circ$ is the surface density (in gm/cm^2) at R_f, a fiducial radius. We choose $p = 1.5$ in accordance with the density structure for vertical hydrostatic equilibrium (Chiang & Goldreich 1997). The mass of the disk, given this power law distribution is given by:

$$M_D = \int_{R_i}^{R_D} 2\pi\Sigma R dR = \frac{2\pi\Sigma_\circ R_f^p}{2-p}(R_D^{2-p} - R_i^{2-p}), p < 2, \tag{4.9}$$

where R_i, R_D, and R_f are the inner, outer, and fiducial radii of the disk.

Radius of the Disk

The inner radius of the disk is the dust destruction radius defined as:

$$R_i = \sqrt{\frac{L_*}{4\pi\sigma T_{dust}^4}}, \tag{4.10}$$

where we define the dust destruction temperature, $T_{dust} = 2000$ K, and L_* is the luminosity of the star.

For the disk outer radius, R_D, we adopt the centrifugal radius that evolves with time as follows (Terebey et al. 1984),

$$R_D(t) = \frac{m_\circ^3}{16} c_s t^3 \Omega_\circ^2, \tag{4.11}$$

where t is the time and $\Omega_\circ$ is the angular velocity of the cloud prior to collapse; other variables are as already defined. We set $\Omega_\circ$ so that, at the end of the Class I

stage, the disk radius is 100 AU. These angular velocities are 1×10^{-14}, 5.5×10^{-14}, and 3.4×10^{-13} s^{-1} for the 3, 1, and 0.3 M$_\odot$ models, respectively. Goodman et al. (1993) found a range for $\Omega_\circ$ from 9.7×10^{-15} to 1.3×10^{-13} s^{-1}. The upper end of this range is about one-third of $\Omega_\circ$ for the 0.3 M$_\odot$ model, but the least massive of the cores in Goodman et al. (1993) was 0.6 M$_\odot$. We assume that less massive and smaller cores have higher angular velocities.

Mass of the Disk

We evolve the mass of the disk via the expression given by Adams & Shu (1986):

$$M_D = (1 - \eta_D) \int_{t_o}^{t} \dot{M}_D dt = (1 - \eta_D) \mathcal{M}_\mathcal{D} M, \tag{4.12}$$

where t_o is the time when $u_* = 1$ (i.e., $R_D = R_*$). We assume $t_o = 0$. Further, Adams & Shu (1986) defines $\mathcal{M}_\mathcal{D}$ as follows:

$$\mathcal{M}_\mathcal{D} = \frac{1}{3} u_* \int_{u_*}^{1} (1 - u_*)^{1/2} u^{-4/3} du. \tag{4.13}$$

We evaluate this expression numerically as suggested by Adams & Shu (1986). Finally, M is the total mass accreted (i.e. $M = \dot{M}t$). Adams & Shu (1986) give η_D as a free parameter; η_D is the fraction of material accreted onto the disk that will eventually accrete onto the star. To determine a value for η_D, we assume that the ratio of star to disk mass must be $\sim 1/4$, which is in accord with theoretical work (Li 2002). In Figure 4.3, we show this ratio for several values of η_D. We choose $\eta_D = 0.75$ so that $M_D/M_* \sim 1/4$ for the 1 M$_\odot$ model. We apply the same criterion for the 0.3 and 3 M$_\odot$ models and set $\eta_D = 0.7$ and $\eta_D = 0.9$, respectively. In section 4.7, we explore the effects of allowing it to vary.

Luminosity of the Disk

The temperature distribution for the disk is defined by the following,

$$T(R) = T_\circ \left(\frac{R}{R_f} \right)^{-q} (K), \tag{4.14}$$

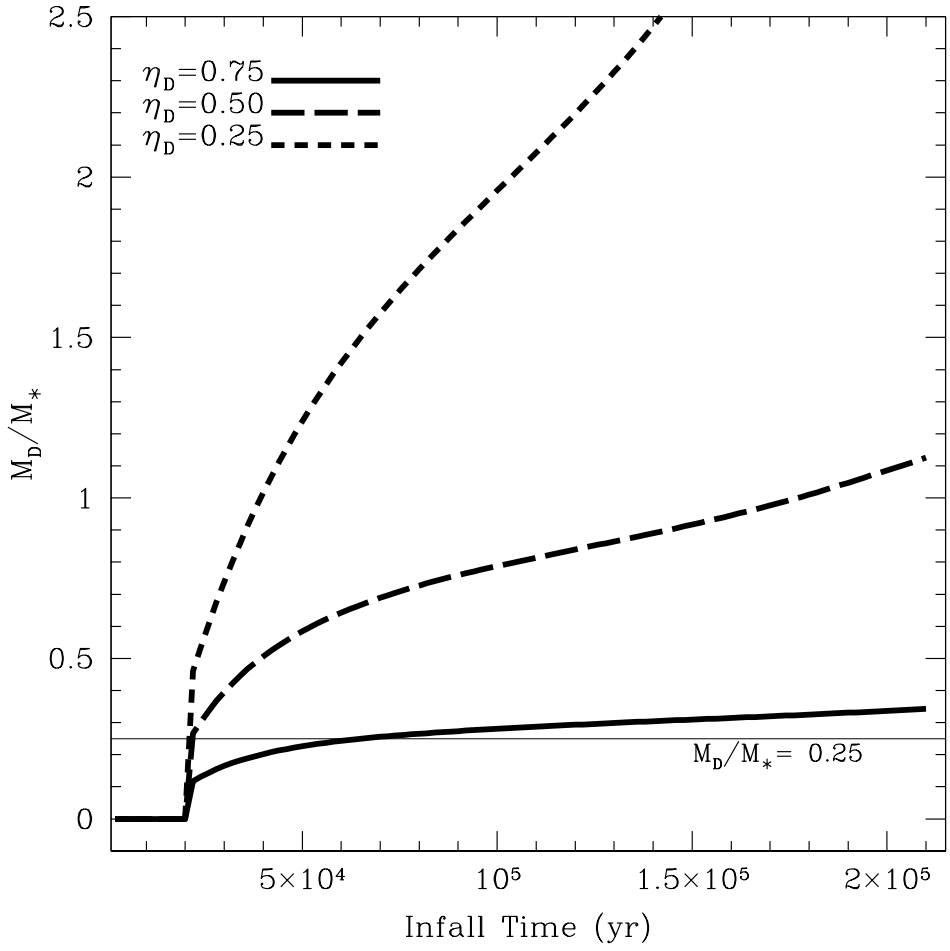

Figure 4.3: We show the ratio of disk to stellar mass for the 1 $M_\odot$ model as it evolves with time. We have chosen $\eta_D = 0.75$ so that this ratio approaches 0.25. For the 0.3 and 3.0 $M_\odot$ models, we use $\eta_D = 0.7$ and $\eta_D = 0.9$, respectively.

where $T_\circ$ is the temperature at the fiducial radius, R_f. We set $q = 0.5$, a temperature distribution that decreases more slowly with radius than expected for a flat disk, to simulate flaring and disk accretion (Butner et al. 1994; Kenyon & Hartmann 1987).

The luminosity of the disk has several components as given by Adams & Shu (1986). First, envelope material falling onto the disk will act as a source of luminosity. Then, there is a source of "mixing luminosity" that arises, basically, from the mixing of newly accreted material and that material already in orbit around the star. Finally, Adams & Shu (1986) assumed that some fraction (η_D) of the disk material will frictionally dissipate its remaining orbital energy and fall onto the star. Adams & Shu (1986) give the expression for L^D_{acc} in equation 33b of their work; we use this equation for L^D_{acc}, which includes all three of these components, in the evolutionary model. As the disk radius grows larger with time and $u_* \rightarrow 0$, their expression for L^D_{acc} simplifies to (Adams et al. 1987)

$$L^D_{acc} \approx \frac{1}{2}\eta_D L_\circ, \tag{4.15}$$

where $L_\circ \equiv \frac{GM_*\dot{M}_*}{R_*}$.

4.3.4 Star

For the star, we define several parameters: mass (M_*), luminosity (L_*), radius (R_*), and effective temperature (T_{eff}). Each of these quantities evolve over time, and they are generally interdependent.

Mass of the Star

For the stellar mass, we subtract the disk mass from the total accreted mass as in Adams & Shu (1986):

$$M_* = M - M_D = [1 - (1 - \eta_D)\mathcal{M}_\mathcal{D}]M. \tag{4.16}$$

All variables are as previously defined. Included in this equation are two means by which the star gains mass. Material accretes directly from the envelope onto the star until the disk grows in size and accretes most of the infalling envelope mass. Then, the star mostly gains material that has accreted onto and is processed through the disk.

Luminosity of the Star

The luminosity of the star has two components: that arising from accretion (L^*_{acc}), the dominant source of luminosity at early times, and the luminosity due to gravitational contraction and deuterium burning (L_{phot}). Simply, $L_* = L^*_{acc} + L_{phot}$.

Adams & Shu (1986) calculate the accretion luminosity from material accreting onto the star. Their calculations include the luminosity from material that falls onto the star and the energy released due to differential rotation of the protostar. Adams & Shu (1986) give an expression for L^*_{acc} in equation 33a of their work; we use this prescription for L^*_{acc}. As the disk radius grows larger with time and $u_* \rightarrow 0$, this simplifies to (Adams et al. 1987)

$$L^*_{acc} \approx \frac{1}{2}\eta_D^2 \eta_* L_\circ. \tag{4.17}$$

Adams & Shu (1986) define η_* as an "efficiency factor" that dictates how the star dissipates the energy due to differential rotation. Adams et al. (1987) considered this value to be a free parameter but chose $\eta_* = 0.5$ for their standard model, which we use as well. In section 4.7, we discuss the effects of varying η_*.

L_{phot} was calculated by D'Antona & Mazzitelli (1994, hereafter DM). We have made linear fits to their pre-main sequence tracks with opacities from Alexander et al. (1989) (Tables 1 and 5 of DM). First, we have fit a power-law in the luminosity-time plane for each stellar mass given by DM. For masses less than 0.2 $M_\odot$, where a single power-law is not appropriate, we have fit two-piece power-laws to DM's data. For times earlier than those covered by DM's tracks, we have assumed a power-law

expression: $L_{phot} = L_{\circ}^{phot} \left(\frac{t}{t_{\circ}}\right)^5$, where $t_{\circ}$ is the earliest time in the calculations by DM, and $L_{\circ}^{phot}$ is the luminosity of the pre-main sequence star at time $t_{\circ}$. This equation is ad hoc and meant to smoothly bridge the transition from where there is no data for L_{phot} to the point where DM's evolutionary tracks begin. Finally, to obtain the appropriate value for L_{phot}, we linearly interpolate between masses for a given time in the star's evolution.

As noted in M98, the beginning of infall and accretion luminosity is not the same time as that for the onset of the luminosity represented by L_{phot}. We adopt, as M98 did, a difference in these two timescales of 10^5 years such that, for $L_{phot}(t)$, we take $t = t_{phot} + 10^5$ yr for particular values of t_{phot} as given by DM; this assumption is based on the theoretical work of Stahler (1983). After collapse begins, the forming star must wait 10^5 years before the luminosity due to contraction and deuterium burning (as described by DM) will begin. Further, the luminosity from DM's models does not become significant until $\sim 7 \times 10^4$ years. Therefore, L_{phot} is not relevant until $t \sim 1.7 \times 10^5$ years, which is greater than the time required for the 0.3 $M_{\odot}$ to collapse and only 4×10^4 years more than the collapse time for the 1 $M_{\odot}$ core.

With this final term, the total luminosity of the protostellar system is now made of three components: L_{acc}^{*}, the luminosity due to accretion and differential rotation of the protostar; L_{phot}, the luminosity arising from gravitational contraction and deuterium burning in the protostar, and L_{acc}^{D}, the luminosity from accretion onto the disk and dissipation of the orbital energy within the disk.

In addition, there is the luminosity that results from the ISRF, L_{ISRF}. We calculated L_{ISRF} by illuminating a core that has no internal source. However, the core does have an evolving density distribution identical to the three mass scenarios presented herein. Then, we calculate the luminosity that results from the dust grains, which are heated externally. At early times, the external radiation field contributes most of the luminosity. As the envelope mass decreases and the internal

source luminosity grows, L_{ISRF} becomes insignificant. We plot the evolution of L_{ISRF} in Figure 4.4.

In conclusion, the total luminosity is given as

$$L_{tot} = L^*_{acc} + L_{phot} + L^D_{acc} + L_{ISRF}. \tag{4.18}$$

For T_{eff}, we use the Stefan-Boltzmann Law,

$$T_{eff} = \left(\frac{L_*}{\sigma 4\pi R_*^2}\right)^{1/4}, \tag{4.19}$$

where $L_* = L^*_{acc} + L_{phot}$. At early times, the effective temperature is very low, $\sim$ 100 K because the radius of the first hydrostatic core (Section 4.3.4) is $\sim$5 AU. When the stellar radius approaches 2-5 $R_\odot$, T_{eff} becomes more stellar-like ($\sim$ 3000 K).

Radius of the Star - Simulating the FHC

We allow the radius of the star to evolve as suggested by Palla & Stahler (1991, see Figure 1 in their paper). In their calculations, they find that the radius of the star rises to about 2-5 solar radii; this result is in accord with the assumption of a constant radius at 3 $R_\odot$ by M98. However, the time at which to apply these calculations is not so clear.

In the evolution of a protostar, the early years are occupied by the first hydrostatic core. While not yet clearly observed, the first hydrostatic core has been predicted (Boss & Yorke 1995; Masunaga et al. 1998). Boss & Yorke (1995) concluded, based on some simple arguments, that the lifetime of this stage should be short, only about 20,000 years. Further, Masunaga et al. (1998) have determined that the average radius of this core should be about 5 AU. The transition between this very large core and the smaller core described by the calculations of Palla & Stahler (1991) is not well-understood. We have assumed the stellar radius evolves as shown in Figure 4.5. In the beginning, the radius of the first hydrostatic core is 5 AU. At t=20,000 years, we allow the radius to decrease from 5 AU to the

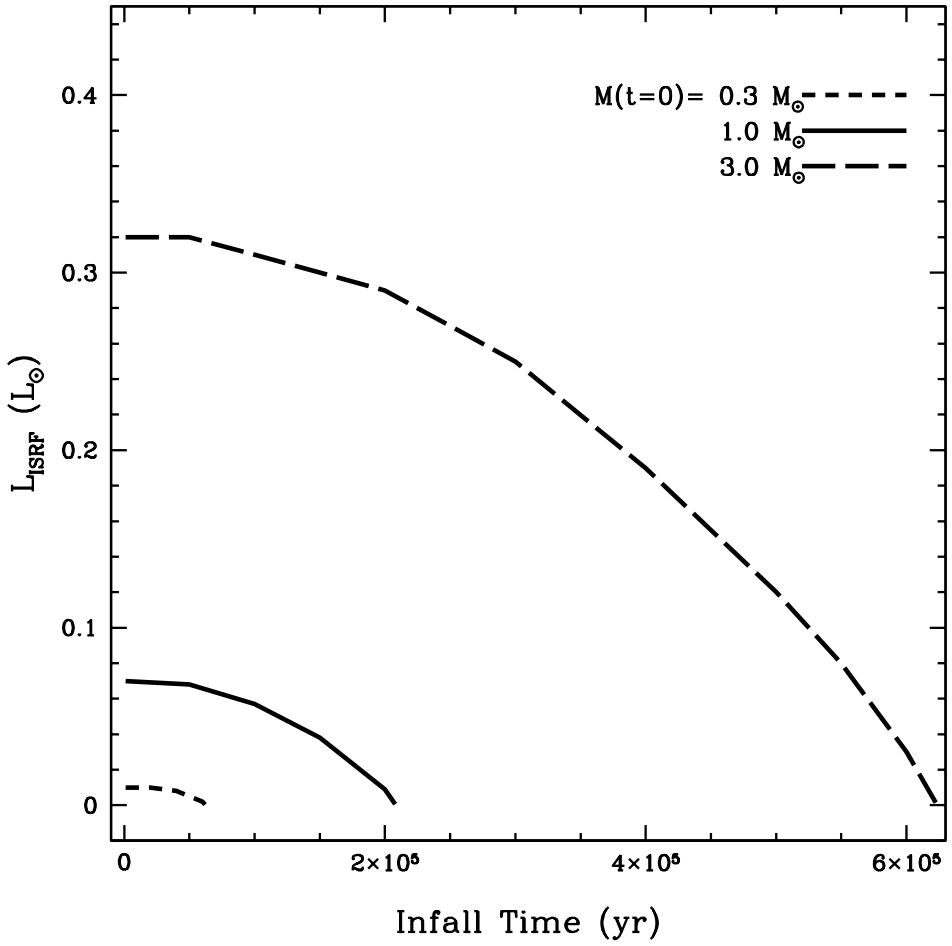

Figure 4.4: Evolution of the luminosity from the ISRF with time. Each line represents a core with a different initial mass.

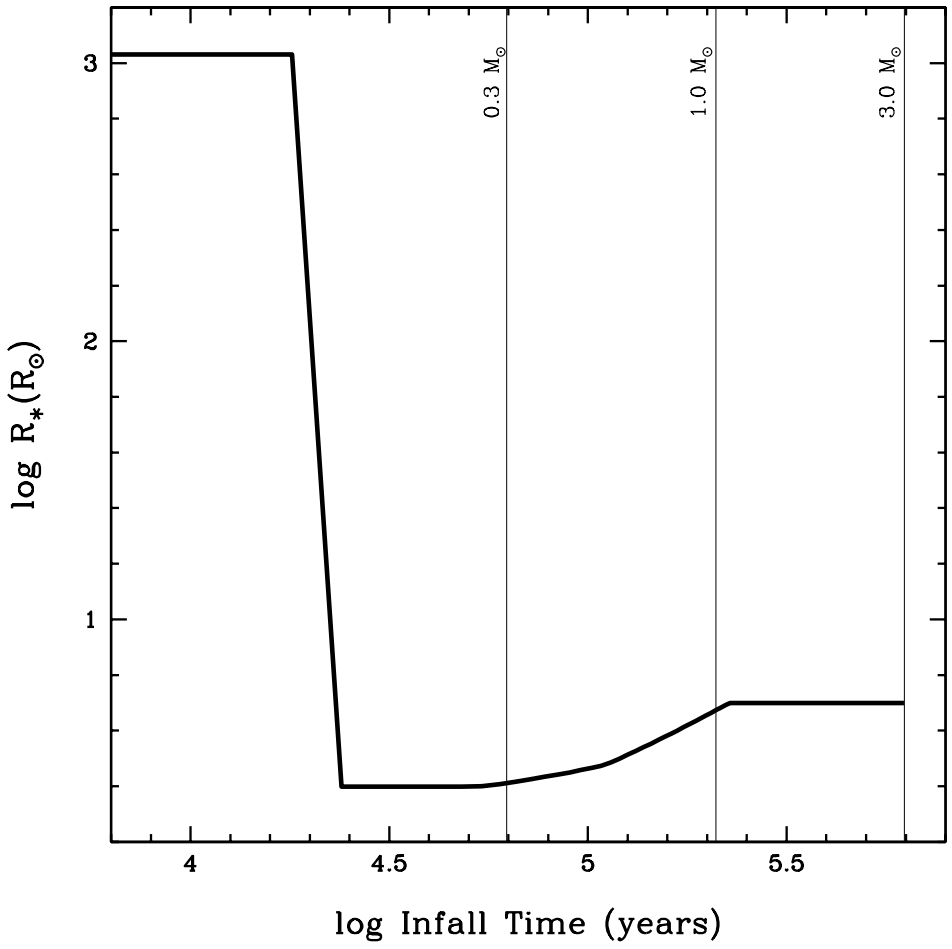

Figure 4.5: We show the data used for the radius of our evolving protostar. The radius in the first 20,000 years simulates the first hydrostatic core phase. The radius for the remaining time is from Figure 1 of Palla & Stahler (1991). The thin, vertical lines show where the evolution ends for the various masses modeled.

radius calculated by Palla & Stahler (1991). This transition lasts 100 years and is described, in our model, by:

$$R_*(AU) = 5\left[1 - \left(\frac{t - 20000}{100}\right)^{0.5}\right] + R_*^{PS}, \qquad (4.20)$$
$$20,000 < t < 20,100$$

where t is the time in years and R_*^{PS} is the value for the radius calculated by Palla & Stahler (1991). This equation is somewhat ad hoc and simply used to simulate the transition between the large radius as predicted by Masunaga et al. (1998) and the much smaller radius of the actual star as predicted by Palla & Stahler (1991).

There are consequences for including this large radius at early times. Because the centrifugal radius is very small and, hence, the disk has not formed, the luminosity at these early times is derived wholly from spherical accretion onto the central source. If this central source is small, the accretion luminosity can be very high. In Figure 4.6, we show the evolution of the accretion luminosity for two scenarios. In one case, we have included the FHC. We also plot L_{acc}^* when there is no FHC. In this case, the stellar radius evolves via the data of Palla & Stahler (1991) (i.e., between 2 and 5 $R_\odot$). Without a FHC, the accretion luminosity rises quickly because there is no disk and material is accreting directly onto the star. At about 2×10^4 years, the centrifugal radius has increased so that a disk can form. Then, the accreting material is processed by the disk causing L_{acc}^*, which arises from accretion onto the star, to decrease.

In summary, we let the mass of the star and the accretion luminosity evolve as defined by Adams & Shu (1986), the radius of the star change as predicted by Palla & Stahler (1991) (except at early times), and the luminosity due to deuterium burning and gravitational contraction of the PMS star evolve as calculated by DM. The effective temperature, given these other factors, is defined by the Stefan-Boltzmann Law.

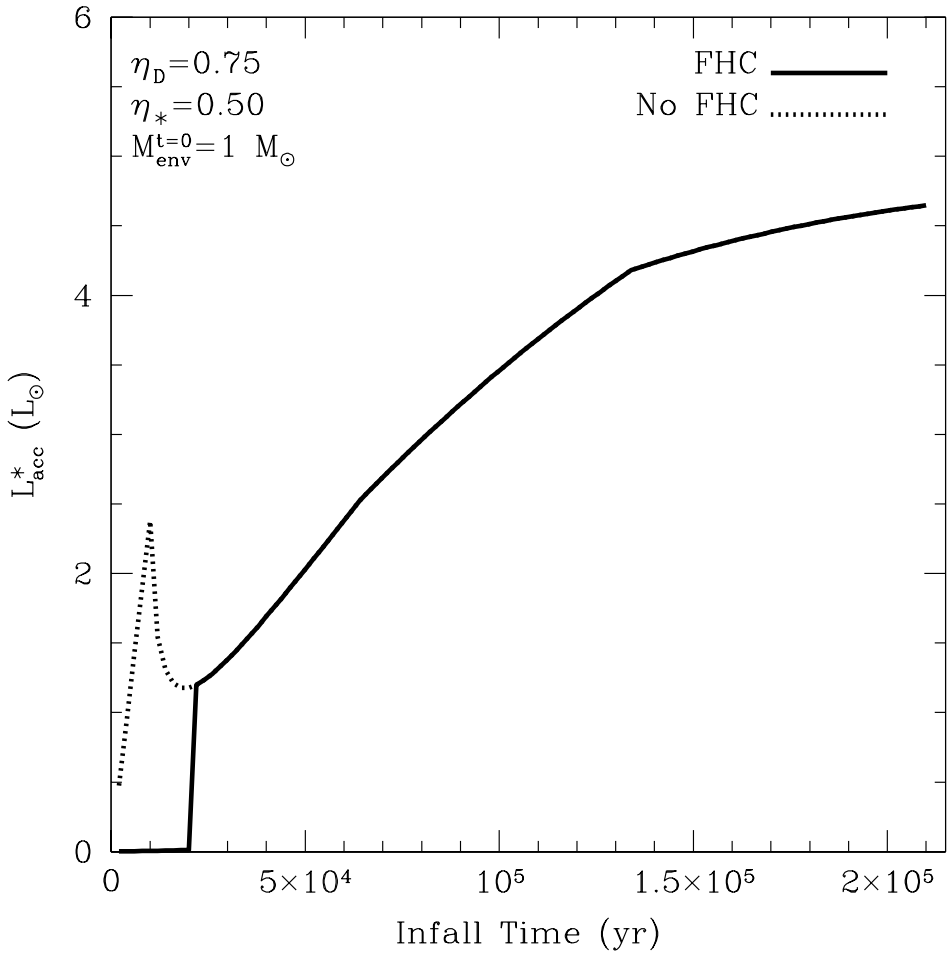

Figure 4.6: The solid line represents L_{acc} as it evolves with time; the first hydrostatic core (FHC) is included. Without the FHC, L_{acc} evolves as represented by the dotted line. For our models, we include the FHC.

4.4 Signatures

In this section, we discuss the various observational signatures in the evolution of protostellar systems.

We calculate the bolometric temperature by the prescription given in Myers et al. (1993),

$$T_{bol} \equiv [\zeta(4)/4\zeta(5)]h\bar{\nu}/k = 1.25 \times 10^{-11}\bar{\nu}, \tag{4.21}$$

where $\zeta(m)$ is the Riemann zeta function of argument m, h is Planck's constant, k is Boltzmann's constant, and the mean frequency, $\bar{\nu}$, is the ratio of the first and zeroth frequency moments:

$$\bar{\nu} \equiv I_1/I_0, I_m = \int_0^\infty \nu^m S_\nu d\nu. \tag{4.22}$$

In addition, we calculate the bolometric luminosity:

$$L_{bol} = \int_0^\infty 4\pi D^2 S_\nu d\nu \tag{4.23}$$

where S_ν is the flux density, and D is the distance. We set $D = 140$ pc, suitable for nearby star-forming regions. We also calculate L_{bol}/L_{smm} for our models (André et al. 1993). L_{smm} is found by integrating Equation 4.23 from 350 μm to ∞.

We also calculate the fluxes that would be seen by the photometric bands on the Spitzer Space Telescope by convolving the modeled spectral energy distribution (SED) with the bandpasses for the MIPS instruments. These fluxes do not vary substantially from the monochromatic fluxes for the central wavelength of each bandpass. To convert the fluxes to magnitudes, we use these zero-point fluxes for MIPS bands 1-3 (24, 70, and 160 μm), respectively: 7.2, 0.8, and 0.17 Jy (Young et al. 2005). We do not convolve the MIPS resolution element with the model but assume that all emission is included within this beam.

4.5 Radiative Transfer

We use the radiative transfer code, DUSTY, as developed by Ivezić et al. (1999), to calculate the temperature distribution in the envelope and the emergent SED of the star, disk and envelope. In this section, we discuss the effect and treatment of scattering by dust grains in these calculations.

DUSTY assumes that scattering from dust grains is isotropic. Longward of 10 μm, the SED is barely affected because the scattering cross-section (σ_{scat}) is significantly less than the absorption cross-section (σ_{abs}, see Figure 4.1). Further, the effect is also minimal at wavelengths shortward of 10 μm when the interstellar radiation field is not included.

Unfortunately, the assumption of isotropic scattering causes some problems when the interstellar radiation field is included. In Figure 4.7, we show the SED for a core with a mass of 1 $M_\odot$ (with $\tau_{100\mu m} = 1$). In these models, the only heating of the dust grains is externally from the ISRF. For the solid line, we include the effects of isotropic scattering by the dust grains while the dashed line shows the SED without scattering. Both SEDs have a peak at submillimeter wavelengths as is expected. However, the SED with scattering included also has a peak in the near-infrared. Of course, we do not observe strong near-infrared radiation from starless cores. At short wavelengths, these dust grains preferentially forward scatter light, so neglecting the anisotropic nature of the scattering causes this unrealistic flux in the near-infrared.

Our options are either a) neglect the effects of scattering in calculating the emergent SED or b) ignore the ISRF. The latter is not really feasible because, at early times, the ISRF provides the sole source of heating and, hence, ignoring it radically affects the temperature profile for the core. Therefore, we opt for the first alternative and ignore the effects of scattering.

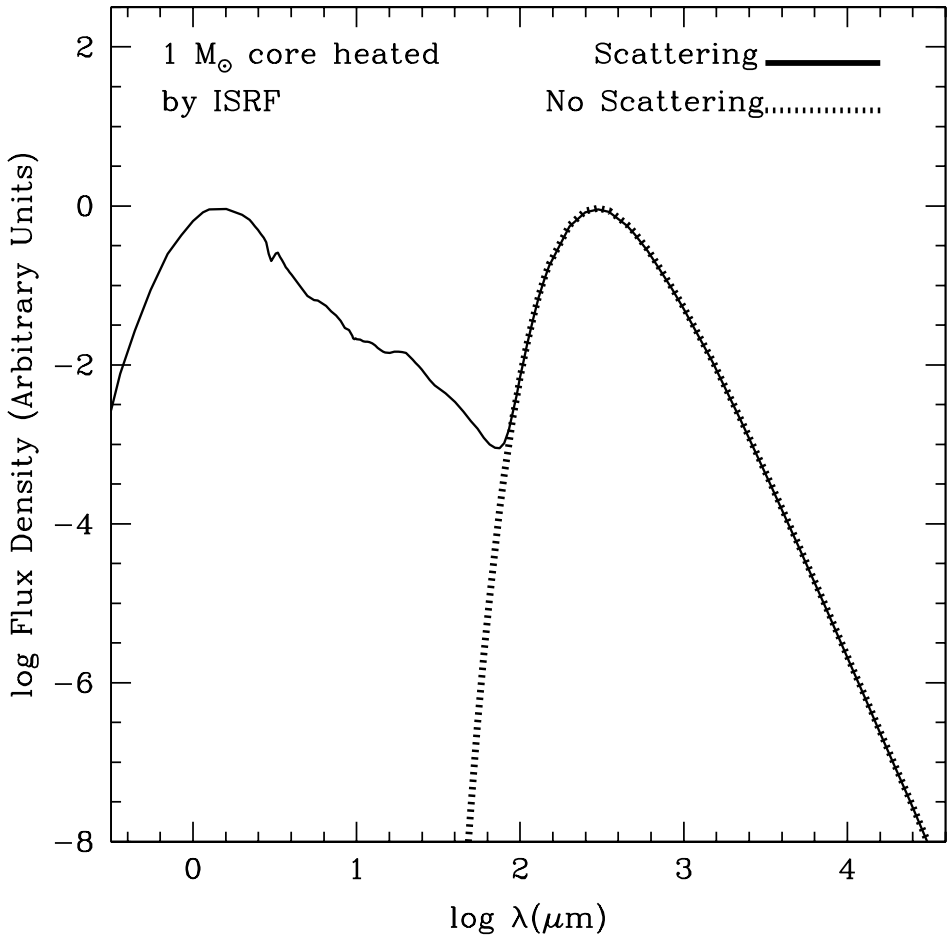

Figure 4.7: We plot the SED of a 1 $M_\odot$ core (with $\tau_{100\mu m} = 1$). This model does not include a central luminosity source; the heating is entirely due to the ISRF. The solid line includes the effects of isotropic scattering while the dotted line does not.

4.6 An Evolving Protostar

With these methods and assumptions, we have calculated the SED for an evolving protostar. In Figure 4.8, we show the SED for particular times in the evolution of the core that began with a pre-collapse mass of 1 $M_{\odot}$. We have also set $\tau_{max} = 10$, $\eta_D = 0.75$, and $\eta_* = 0.5$ (see sections 4.3.2, 4.3.3, and 4.3.4). The solid line is the emergent SED as observed at 140 pc, the distance to Taurus. The dashed line represents the star+disk SED; this spectrum is for the central source and is the input for DUSTY. The bars represent the sensitivity for the Spitzer Space Telescope c2d Legacy program (Evans et al. 2003); we have increased the 70 μm sensitivity by a factor of three based on in-flight performance. The asterisks in the second frame are IRAS sensitivities.

We calculate the observational signatures, described in Section 4.4, for models with different initial conditions and whose evolution proceeds in different ways. We use different timesteps for the models: $\Delta t = 1000$, 2000, and 6000 years for the 0.3, 1, and 3 $M_{\odot}$ models, respectively. These timesteps are each about 1% of the total infall time.

4.7 Free Parameters

In this section, we explore the effects of various parameters in these models. We show how the model changes when we use different values for η_D, η_*, and τ_{max}. We find that neither η_D or η_* have a large effect on the observational signatures of the SEDs, but the choice for τ_{max} can significantly affect the short-wavelength emission during all stages of evolution. We adopt these values: $\eta_D = 0.75$, $\eta_* = 0.5$, and $\tau_{max} = 10$.

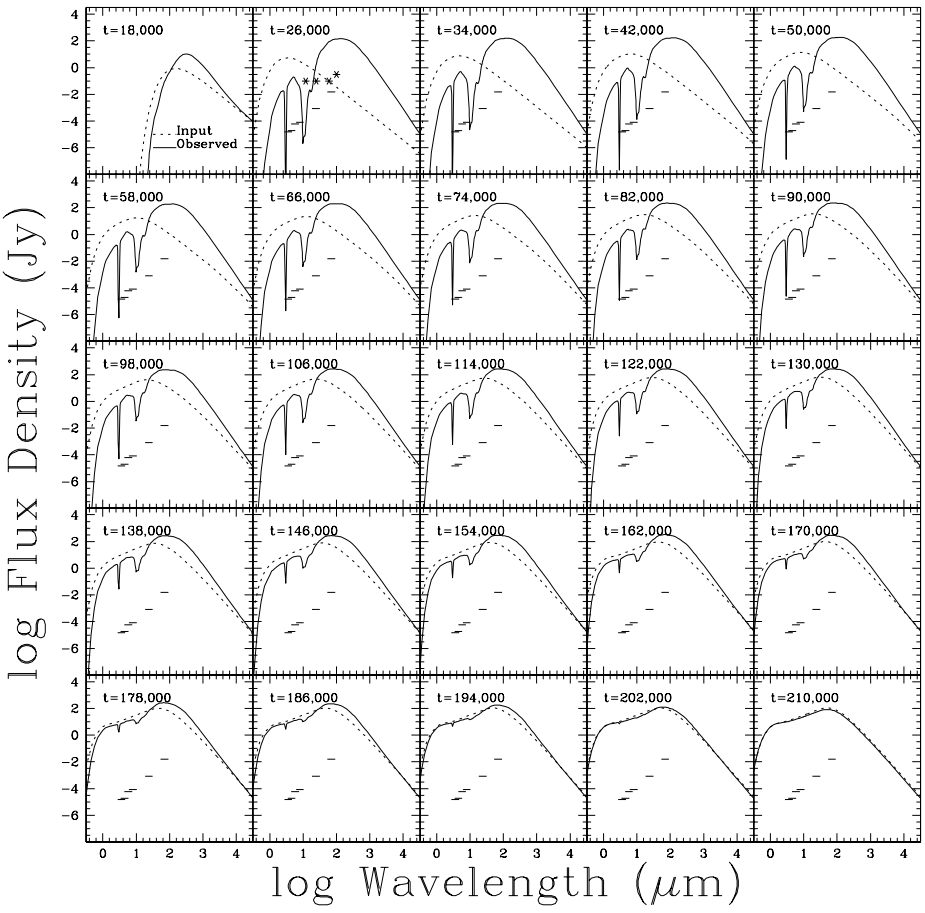

Figure 4.8: Each panel in the plot has the SED for a core with initial mass of 1 $M_\odot$, a temperature of 10 K, $\tau_{max} = 10$, $\eta_D = 0.75$, and $\eta_* = 0.5$. The age for the model is labeled in each panel. The dotted line is the input disk spectrum, and the solid line is the observed SED as calculated by DUSTY. Sensitivities for the Spitzer Cores to Disks Legacy program are shown as horizontal bars; IRAS sensitivities are in the second frame as asterisks. The distance is 140 pc.

4.7.1 η_D

This factor determines what fraction of the disk material will dissipate its energy and accrete onto the star. It is relevant in the calculation of the disk mass (M_D, equation 4.12), the disk accretion luminosity (L^D_{acc}, equation 4.15), the mass of the star (M_*, equation 4.16), and the stellar accretion luminosity (L^*_{acc}, equation 4.17).

We show the effects of changing η_D for the 1 $M_\odot$ core in Figure 4.9. Varying η_D alters the evolution of all components of the luminosity. Of course, this parameter is included directly in the equations for the disk and stellar accretion luminosities. Because η_D determines the stellar mass, it also affects the luminosity due to deuterium burning and contraction (L_{phot}). With $\eta_D = 0.75$, each of these are higher than in the other two scenarios ($\eta_D = 0.25$ & 0.5).

Finally, in the left panels of Figure 4.10, we show how changing η_D affects observational signatures. We plot T_{bol} and L_{bol}/L_{smm} versus time with $\eta_D = 0.25$, 0.5, and 0.75. Variations in η_D have almost no effect on the evolution of T_{bol}, and L_{bol}/L_{smm} only varies slightly for the different values of η_D.

4.7.2 η_*

This factor is a measure of how much of the total luminosity arises from the central star. In practice, it is only relevant for the accretion luminosity, L^*_{acc}, as in equation 4.17. In Figure 4.11, we plot the evolution of L^*_{acc} for different values of η_*. The value that we choose for this "efficiency factor" does considerably change the accretion luminosity. However, as shown by Figure 4.10, the value for η_* has very little effect on the observational signatures. For the standard model in this paper, we adopt $\eta_* = 0.5$.

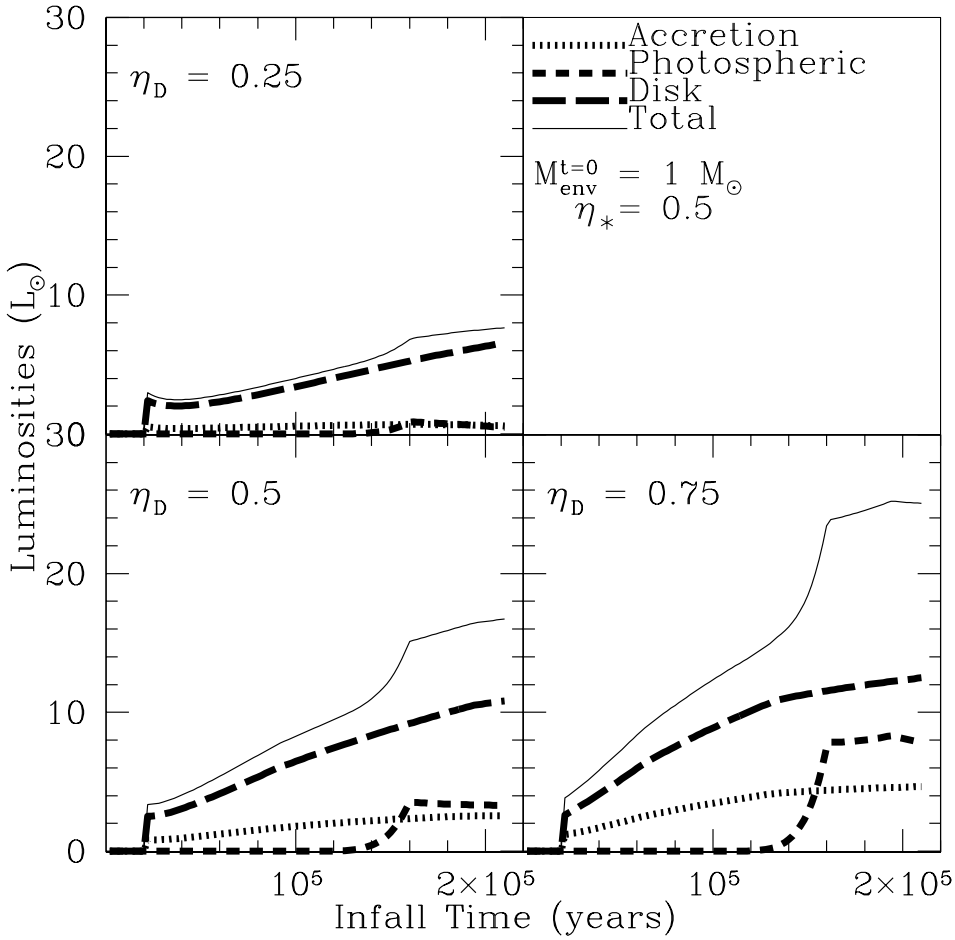

Figure 4.9: Contributing forms of luminosity are shown here for different values of η_D. The accretion luminosity (L_{acc}) is from material accreting onto the star. Photospheric luminosity (L_{phot}) is calculated by DM94 and due to contraction of the central star and deuterium burning. The disk luminosity (L_D) has several components, which are described in section 4.3.3. The sum of these luminosities is shown by the "Total."

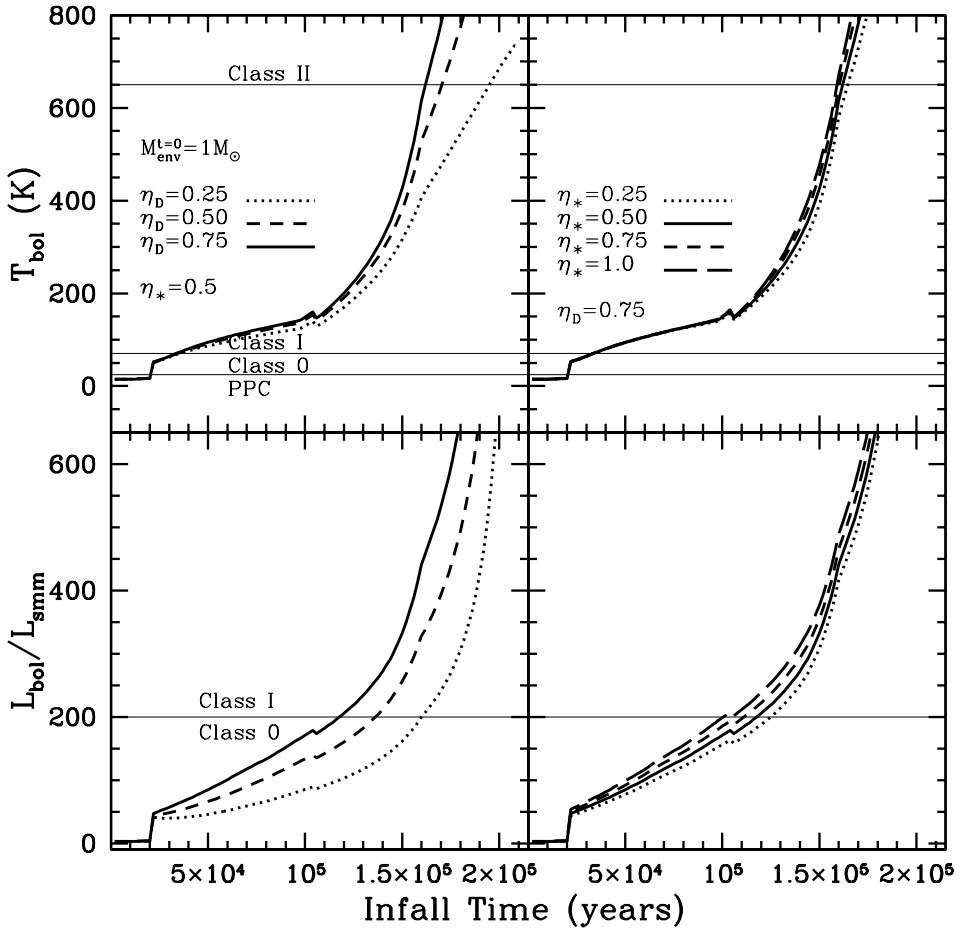

Figure 4.10: For the 1 $M_\odot$ core, we show T_{bol} and L_{bol}/L_{smm} with different values for η_D and η_*. The left panels show data where $\eta_* = 0.5$ and η_D is varied; data in the right panels have $\eta_D = 0.75$ and different values for η_*.

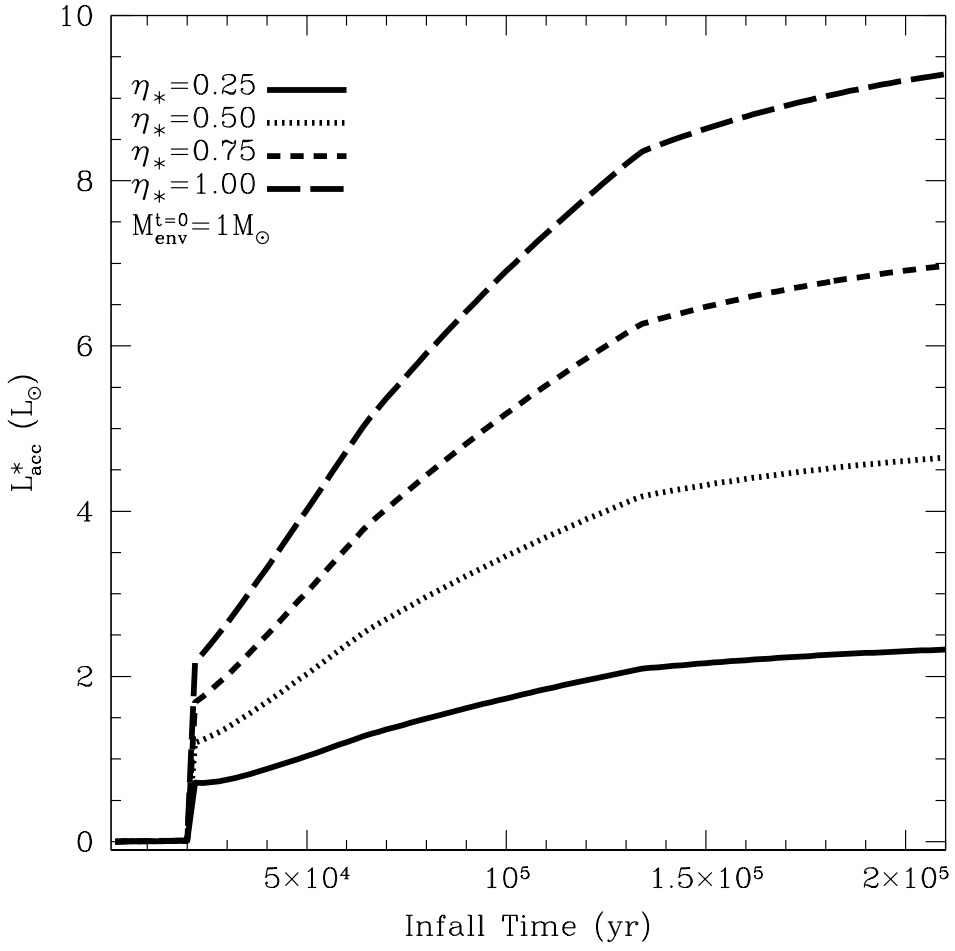

Figure 4.11: For the 1 $M_\odot$ core, we plot L_{acc} for various values of η_*. For our models, we choose $\eta_* = 0.5$ in accord with Adams et al. (1987).

4.7.3 τ_{max}

As discussed in section 4.3.2, the inner radius of the envelope is set so that $\tau(100\mu\text{m})$ does not exceed a certain value. Previously, some have proposed that the condition of isothermality is violated if $\tau(100\mu\text{m})> 1$ (Larson 1969). However, Masunaga et al. (1999) showed that $\tau(100\mu\text{m})$ could be significantly greater than 1 while the core still maintains isothermality.

In Figure 4.12, we plot the evolution of $\tau_\nu(100\ \mu\text{m})$ with $\tau_{max} = 1$, 5, 10, and 15. The density profile begins with a distribution of $n(r) \propto r^{-2}$, but, as collapse begins, the inner region drops to a considerably shallower profile. Because the inner density profile changes, τ drops considerably. In Figure 4.13, we show the SED of a 1 $M_\odot$ core at $t = 4 \times 10^4$ and 10^5 years with $\tau_{max} = 1$, 10, and 15. The model with $\tau_{max} = 1$ shows more emission at shorter wavelengths than those with higher τ_{max}. The SED with $\tau_{max} = 10$ is almost identical, at all times, to that with $\tau_{max} = 15$.

In Figure 4.12, there is a discontinuity at $\sim 1 \times 10^5$ years. This is the point where the infall radius exceeds the outer radius of the infalling envelope. At this point, we changed from the Shu (1977) solution to an envelope whose density is described by $n(r) \propto r^{-3/2}$. This is not a perfect transition, however, so the "kink" at $\sim 1 \times 10^5$ years is an artifact of the model.

We explore the effects of changing τ_{max} on the observational signatures of our evolving protostar. In Figure 4.14, we show the evolution of T_{bol} and L_{bol}/L_{smm} for the different values of τ_{max}. The bolometric temperature is most affected by varying τ_{max}; higher values for τ_{max} slow the transition from a Class I to a Class II protostar (as defined by T_{bol}). Simply, less short-wavelength radiation can escape the cloud when the opacity is higher. However, for those models with $\tau_{max} \geq 5$, the evolution of T_{bol} begins to converge. Finally, not surprisingly, L_{bol}/L_{smm} is unaffected by changing τ_{max}. We do not significantly alter the mass of the envelope, which dictates L_{smm}, nor the accretion processes, which are responsible for L_{bol}.

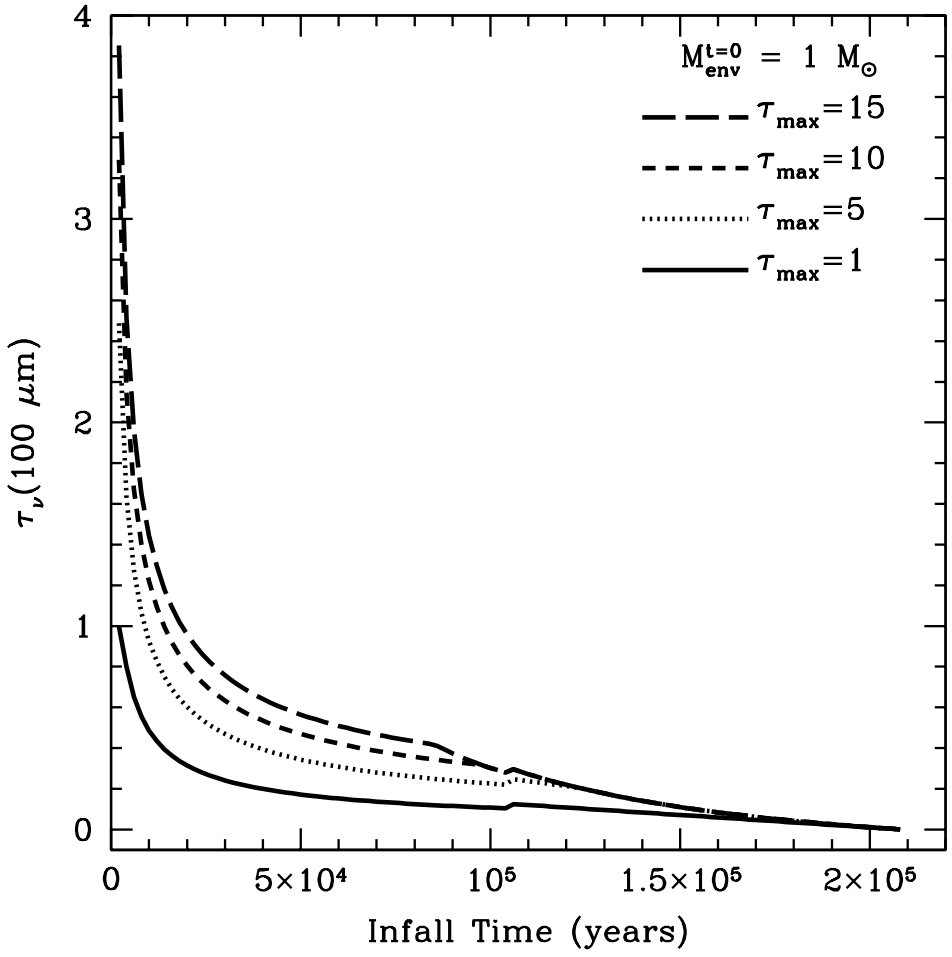

Figure 4.12: We set different initial conditions for the forming star by allowing $\tau_\nu(100\mu\mathrm{m})$ to range from 1 to 15. We vary τ_ν by changing the envelope's inner radius. There is a slight "kink" in the evolution of τ_ν around $t = 10^5$ years that is due to the shift from the Shu77 collapsing envelope to a free-falling envelope with $n(r) \propto r^{-3/2}$.

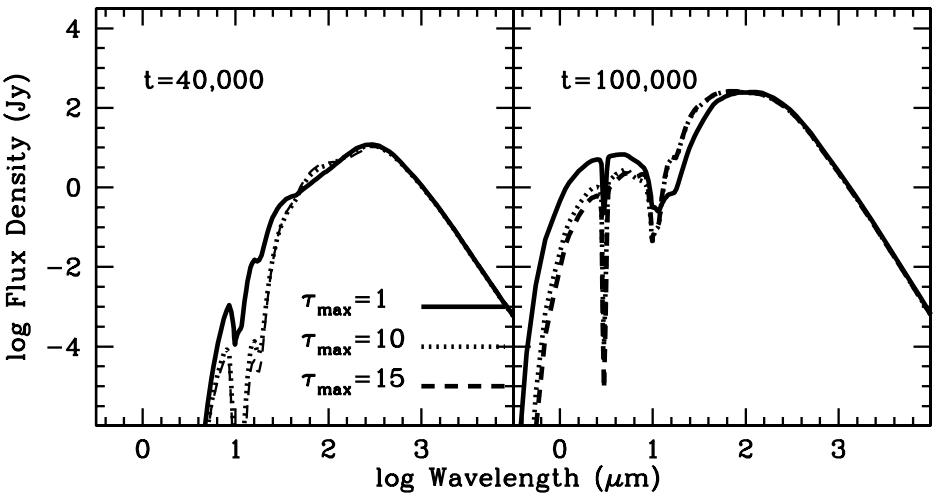

Figure 4.13: For the 1 $M_\odot$ core, we show the modeled SED with different values for τ_{max}. The model with $\tau_{max} = 1$ shows greater emission at short wavelengths than those with higher τ_{max}. We choose $\tau_{max} = 10$ for the models hereafter.

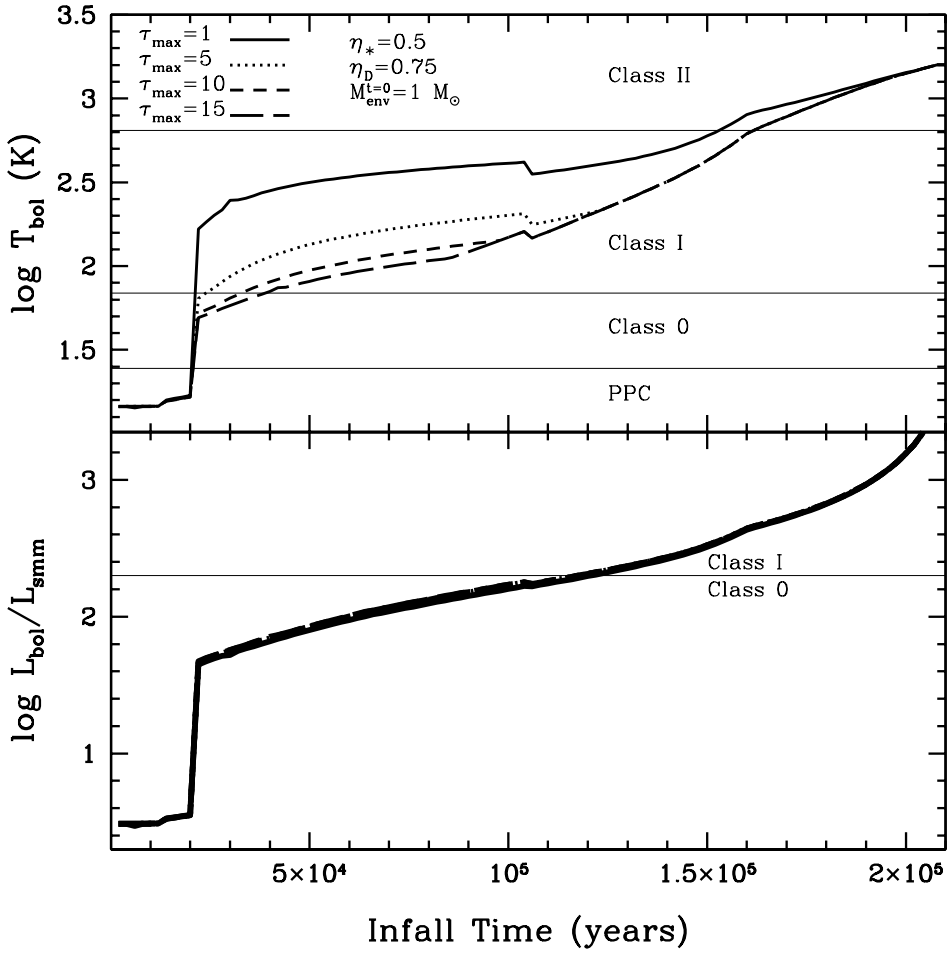

Figure 4.14: For the 1 $M_\odot$ core, we show T_{bol} and L_{bol}/L_{smm} with different values for τ_{max}.

The actual value for τ_{max} is highly uncertain. We do not fully understand the density structure in this transition area between the envelope and disk nor do we include the geometrical effects of a flattened envelope in this region. We assume that $\tau_{max} = 10$; higher values of τ_{max} have little effect on observed quantities (i.e., the SED and its derived signatures). The peak of a 10 K blackbody is 350 μm. Assuming $\kappa \propto \lambda^{-1.5}$, $\tau_{350\mu m} = 1.5$ when $\tau_{100\mu m} = 10$.

4.8 Results

With these free parameters set to the given values, we have run models with different initial masses: 0.3, 1.0, and 3.0 $M_\odot$. Then, we have calculated the various observational signatures.

4.8.1 T_{bol} and L_{bol}/L_{smm}

The bolometric temperature and the ratio of bolometric to submillimeter luminosity have emerged, in the past decade, as the two primary methods of classifying protostars. Because T_{bol} is a measure of the flux-weighted mean frequency of the protostar's SED, it is highly affected by the emergence of any short-wavelength radiation. The ratio of the bolometric to submillimeter luminosity, on the other hand, is virtually unaffected by the short-wavelength emission. Therefore, L_{bol}/L_{smm} is less susceptible to the effects of geometry, which can cause more or less NIR radiation to be observed. This ratio is a rough measure of the ratio of protostellar mass (including the disk and star) to the envelope mass.

In Figure 4.15, we plot the two signatures as they change for the evolving protostar. For the 0.3 $M_\odot$ core, each of the evolutionary indicators increase drastically at about 2.0×10^4 years, when the FHC contracts. All of the envelope material has accreted onto the star and disk by 6.3×10^4 years, shortly after the central star has contracted from the FHC stage. Therefore, as the central star becomes hotter

and more luminous, there is little material left in the envelope. Then, T_{bol} increases because more short-wavelength radiation is observed, and L_{bol}/L_{smm} increases because $L_{smm} \rightarrow 0$ as the envelope goes away. If this model is correct, these low-mass stars should proceed through the FHC stage and, almost immediately, be seen as Class II objects.

The 1.0 and 3.0 $M_\odot$ objects track one another fairly well, up to 10^5 years, in the T_{bol} plot (Figure 4.15) despite the fact that they form on different timescales. The 1.0 $M_\odot$ core requires 2.1×10^5 years for all envelope mass to accrete while the 3.0 $M_\odot$ core requires 6.24×10^5 years. However, both cores evolve from Class 0 to Class I at about 50,000 years, which is about 1/4 and 1/10 of the total infall time for the 1.0 and 3.0 $M_\odot$ cores, respectively.

This transition from Class 0 to I is partly due to the sudden "turning on" of the central source as it contracts to ~ 3 $R_\odot$, and accretion luminosity becomes relevant. There is, however, another reason for this sudden transition. As shown in Figure 4.12, the Shu77 model exhibits a drastic decrease in τ regardless of the adopted value for τ_{max}. Initially, the envelope is described by $n(r) \propto r^{-2}$, but, as collapse ensues, it changes to $r^{-3/2}$ and τ drops. Because τ is so low, any substantial source of stellar luminosity will cause observable short-wavelength radiation to emerge from the system.

These details are actually quite important if one uses these evolutionary signatures to derive relative lifetimes of the various classes as has been done in the past. If one calculates the bolometric temperature for a group of protostars (whose SEDs have been well sampled), there should be very few Class 0 cores—conservatively, about 1/10 to 1/4 of the Class I population, but most likely a much smaller fraction. Visser et al. (2002) presented their efforts to do such a study; they found approximately equal numbers of Class 0 and I objects. However, their data only included the far-infrared (IRAS) and submillimeter fluxes. Analysis of

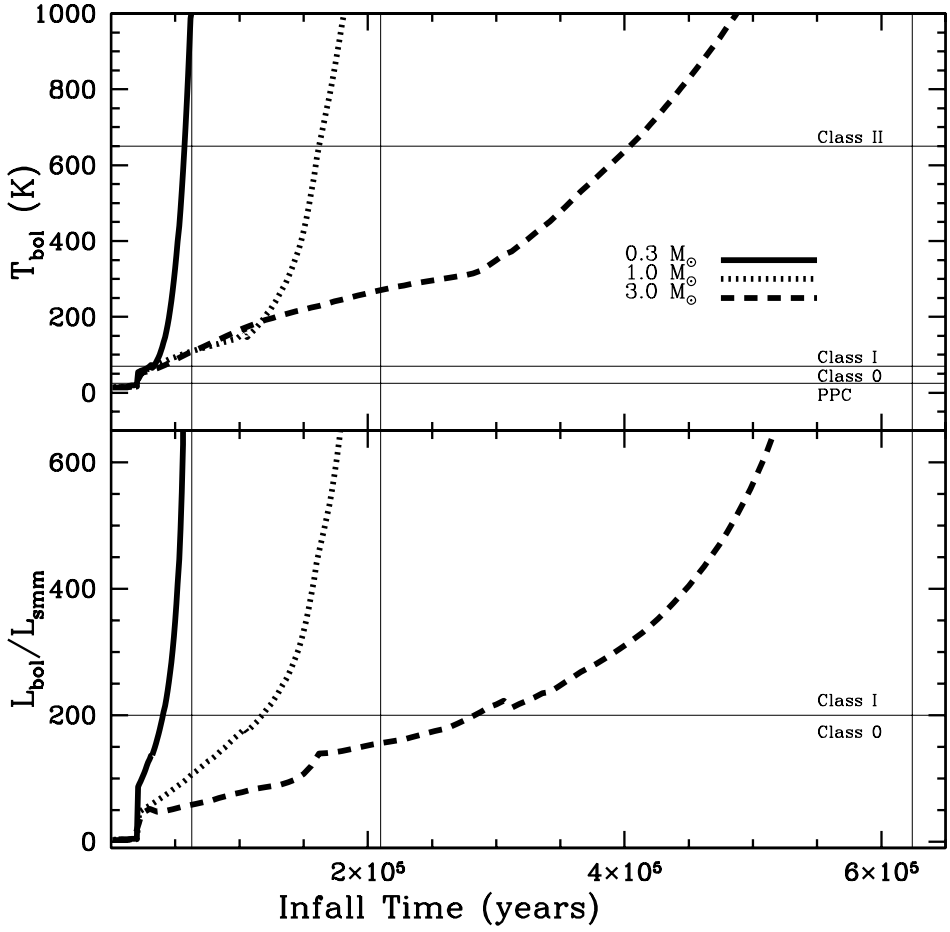

Figure 4.15: We plot T_{bol} and L_{bol}/L_{smm} as they evolve with time for each of the three models. The horizontal lines represent the boundaries for classes of protostars; vertical lines mark the point when all envelope material has accreted onto the star+disk system for each of the three modeled cores.

the mid- and near-infrared data from the Spitzer Legacy and 2MASS surveys along with far-infrared and millimeter observations will almost certainly produce different results. With more complete sampling of the protostars' SEDs, very few Class 0 cores, by the T_{bol} criterion, should remain if this picture of evolution is correct.

Finally, in the plot of T_{bol}, the 0.3, 1.0, and 3.0 $M_{\odot}$ data exhibit a "kink" at about 3×10^4, 10^5, and 3×10^5 years, respectively. This is the point where the envelope's density distribution is described by a power-law, $n(r) \propto r^{-3/2}$, instead of the Shu77 solution. The power-law distribution has a slightly higher τ that causes less short-wavelength radiation to be observed. As a result, T_{bol} decreases slightly at this point of transition, but this is an artifact of the model.

The ratio of bolometric to submillimeter luminosity seems to be much more consistent in describing the evolution of these protostars. Adopting $L_{bol}/L_{smm} = 200$ as the dividing line for Class 0 and I cores, we find that the 1 and 3 $M_{\odot}$ protostars become Class I objects after 1.18×10^5 and 3.6×10^5 years, respectively. These times correspond to slightly more than 1/2 of the total infall time for each core whereas the T_{bol} criterion showed that the cores became Class I after 1/4 and 1/10 of their total infall times.

Finally, in Figure 4.16, we show a plot of T_{bol} and L_{bol}/L_{smm} for the three models. The points represent data from Young et al. (2003), Shirley et al. (2000), and Froebrich (2005). In general, these models are consistent with the data. However, the 11 starless cores in the lower left-hand section of this plot show higher L_{bol}/L_{smm} than the model predicts. The definition of L_{bol}/L_{smm} includes data longward of 350 μm, but, for all of these cores, no 350 μm data exist. Therefore, the observed L_{smm} is lower than that which is modeled. Second, there is little near- or mid-infrared data available for many of the sources represented. With future observations, the bolometric temperature will almost certainly increase. For example, we consider the 1 $M_{\odot}$ model and calculate T_{bol} by including different fluxes. If we use

IRAS fluxes only, T_{bol} = 83 K for the core at 5×10^4 years while T_{bol}, calculated with just the Spitzer bands, is 92 K. At $t = 10^5$ years, T_{bol} is 88 and 151 K as measured with the IRAS and Spitzer fluxes, respectively.

4.8.2 Mass Ratio

We can look at classification from a different, more physical, perspective. In Figure 4.17, we plot the ratio of the stellar and disk mass to the envelope mass. Physically, we might consider a protostar to move from Class 0 to Class I when this ratio is 1 and there are equal amounts of mass in the protostellar system and the envelope surrounding this star+disk. This event occurs at $t = 3.1 \times 10^4$, 1.05×10^5, and 3.1×10^5 years for the 0.3, 1.0, and 3.0 $M_\odot$ cores. Of course, as defined by Shu77, this is also the time when the infall radius is equal to the outer radius.

In Figure 4.18, we plot T_{bol} and L_{bol}/L_{smm} as a function of $(M_* + M_D)/M_{env}$. In the T_{bol} plot, the 1 and 3 $M_\odot$ cores change from Class 0 to Class I while $(M_* + M_D)/M_{env} < 0.5$. With the presently defined boundaries, the bolometric temperature does not appropriately classify the stages of star formation. Only the 0.3 $M_\odot$ core changes from Class 0 to I when $(M_* + M_D)/M_{env} \sim 1$ as is appropriate for our understanding of these stages.

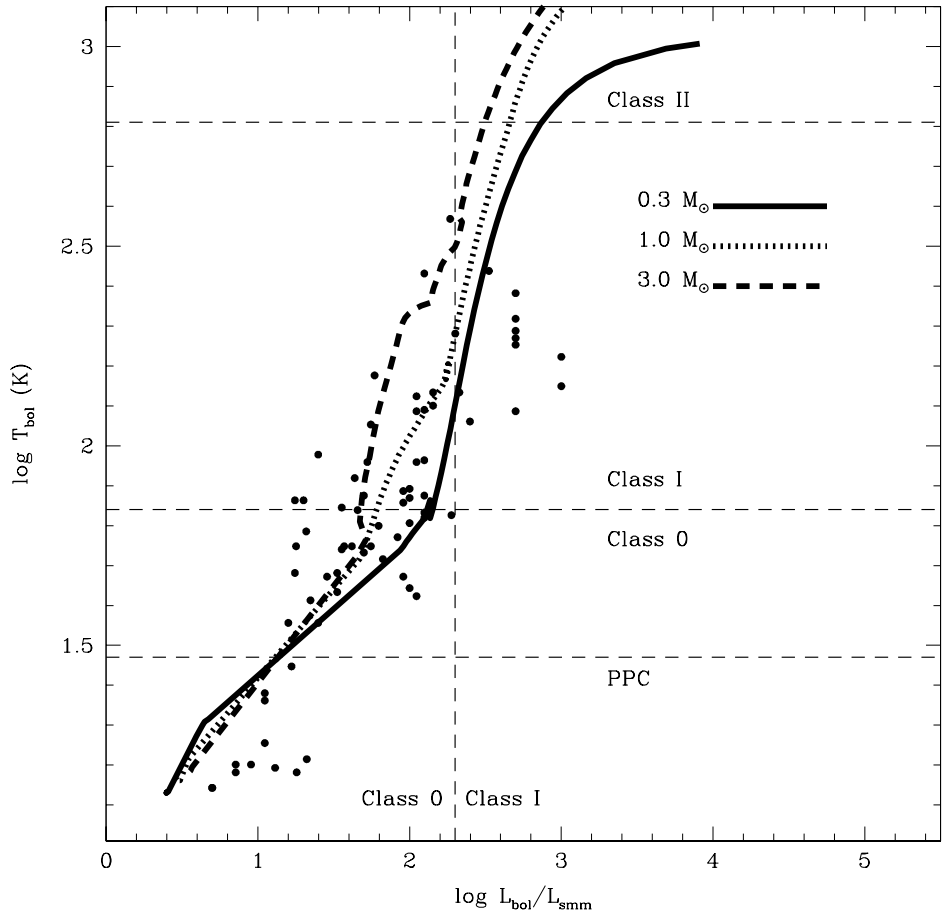

Figure 4.16: We plot T_{bol} and L_{bol}/L_{smm} for the three scenarios that we modeled. The points are data taken from Young et al. (2003), Shirley et al. (2002), Shirley et al. (2004), and Froebrich (2005).

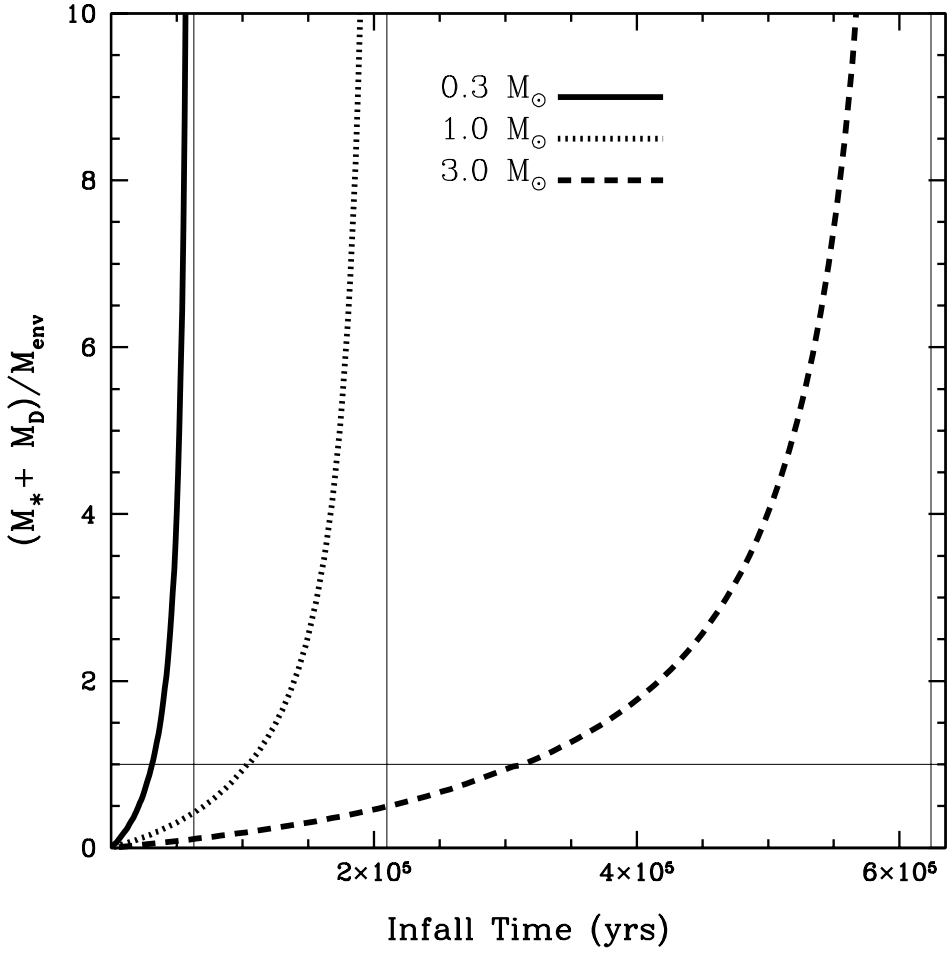

Figure 4.17: For the three models, we plot $(M_* + M_D)/M_{env}$. The thin, vertical lines mark the point when all of the envelope mass has accreted onto the star+disk system. The horizontal line shows where the envelope mass is equal to the accreted protostellar mass.

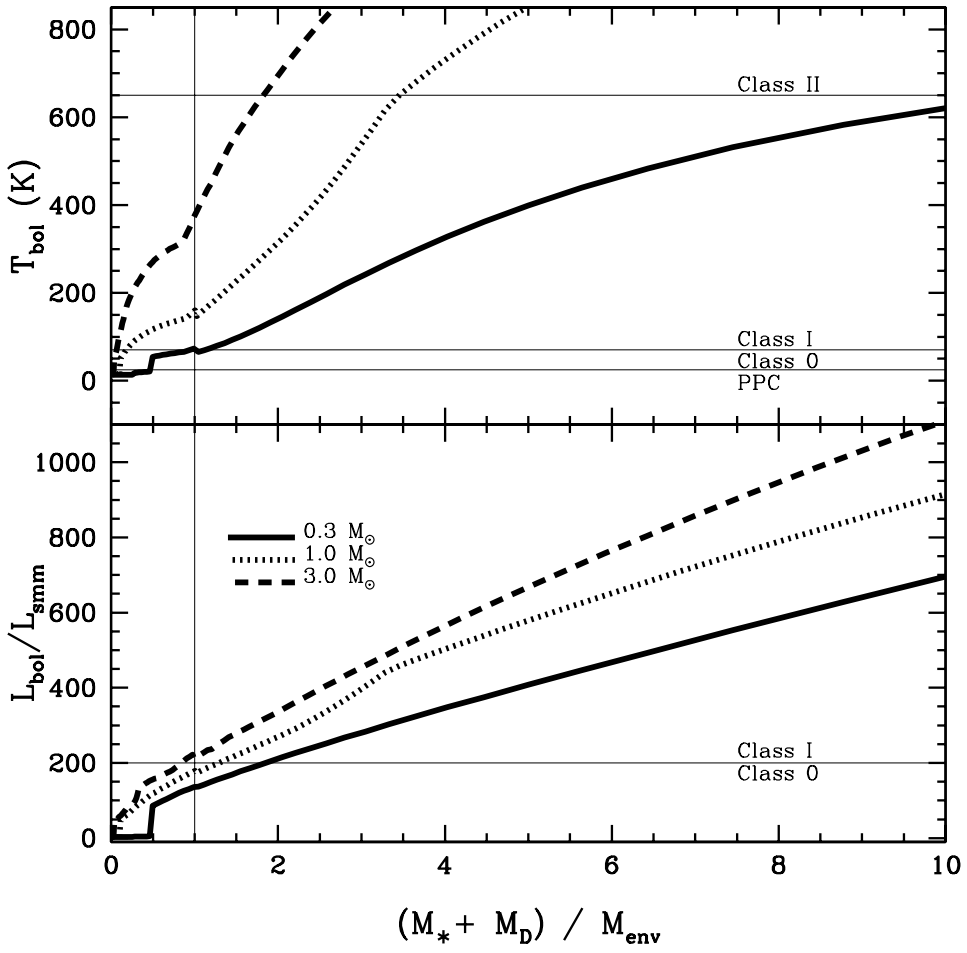

Figure 4.18: Two evolutionary signatures, T_{bol} and L_{bol}/L_{smm}, are plotted against the ratio $(M_* + M_D)/M_{env}$. The thin horizontal lines denote boundaries for the class transitions while vertical line marks where the star+disk mass equals the envelope mass.

However, with the L_{bol}/L_{smm} criterion, we find that the cross-over from Class 0 to I occurs approximately when $(M_* + M_D)/M_{env} = 1$, which is a more realistic view of these evolutionary stages. Indeed, this observational signature is also favored because it is not largely dependent on what is observed at short wavelengths where geometric effects play a big role (André et al. 1993).

Therefore, we set some physical divisions for the evolutionary transitions. First, we let the PPC/Class 0 transition occur when the FHC first collapses at $\sim 2.0 \times 10^4$ years. For all three cores, this occurs when $L_{bol}/L_{smm} \sim 35$. For the Class 0/I transition, we let $(M_* + M_D)/M_{env} = 1$; $L_{bol}/L_{smm} \sim 175$ when this criterion is met. Notice that this value is slightly less than the requirement given by André et al. (1993), i.e. $L_{bol}/L_{smm} = 200$. The Class II stage begins when all of the envelope material has been accreted. Our models are not reliable at these late times, and the L_{bol}/L_{smm} signature is not a very good indicator for this stage of evolution. Nonetheless, we find that L_{bol}/L_{smm} is approximately 2000 at this point, but this value is dependent on the adopted model for the disk.

4.8.3 BLT Diagrams: A Comparison with M98

In Figure 4.19, we show a plot of the bolometric luminosity and temperature, which M98 called a BLT diagram. The axes are laid out to mimic the Hertzsprung-Russell diagram with T_{bol} increasing right to left. In Figure 4.19, we have included M98's models from Figure 7 in their paper. Two of the thin lines in Figure 4.19 are their models for forming, 0.5 $M_\odot$ protostars whose initial envelope masses were 1 and 3 $M_\odot$. We also show their 0.3 $M_\odot$ model from Figure 9, but we label it here as 1.8 $M_\odot$ because this is the mass of the envelope before collapse begins while 0.3 $M_\odot$ is the mass of the star at t=∞. We also plot data from Young et al. (2003), Shirley et al. (2002), and Shirley et al. (2004) as crosses; the dots represent data from Chen et al. (1995) and Chen et al. (1997). Our tracks are markedly different

from any of those presented in M98, so a summary of the differences between two models is relevant here. Primarily, our methods differ in that M98 attempts to create a reasonable model that fits the data while we are simply determining the observational signatures of the Shu77 model.

The most significant difference between this work and that of M98 is the assumptions for infall evolution. M98 described the infall and accretion with an exponential decay function such that the accretion rates began at about 10^{-6} $M_\odot$ yr^{-1} and, as the star approached the main sequence, finished with 10^{-9} $M_\odot$ yr^{-1}. We assume constant accretion onto the star+disk system throughout the duration of the life of the envelope as predicted by the Shu77 collapse solution. However, in our model, the rate of accretion onto the star's surface does decrease with time as the disk forms and takes a more prominent role in processing material from the envelope to the star. Also, the modeled evolution is longer for M98 (10^6 years) than in our model ($2 - 6 \times 10^5$ years).

These different assumptions about infall have several implications. First, in our model, we form a more massive star from similar initial conditions in less time. For our 3 $M_\odot$ core, the star reaches 0.5 $M_\odot$ at $t = 132,000$ years. On the other hand, M98's models require, by design, about 10^6 years to create this 0.5 $M_\odot$ star from a 3 $M_\odot$ core. Of course, at the end of 10^6 years, the star created by M98 has completed its pre-main-sequence evolution, while our model still requires time to completely accrete the disk material.

This discrepancy in the star's final mass presents another difference between this work and that of M98. M98 included a dispersal timescale for the envelope that included an assumption of mass loss due to outflow from the central protostar. We do not include outflows in any way in these models. The lack of outflows in this work has two implications: 1) the mass evolution, as depicted in Figure 4.2, is incomplete and 2) we do not consider the effects of an evacuated outflow cavity. Fortunately,

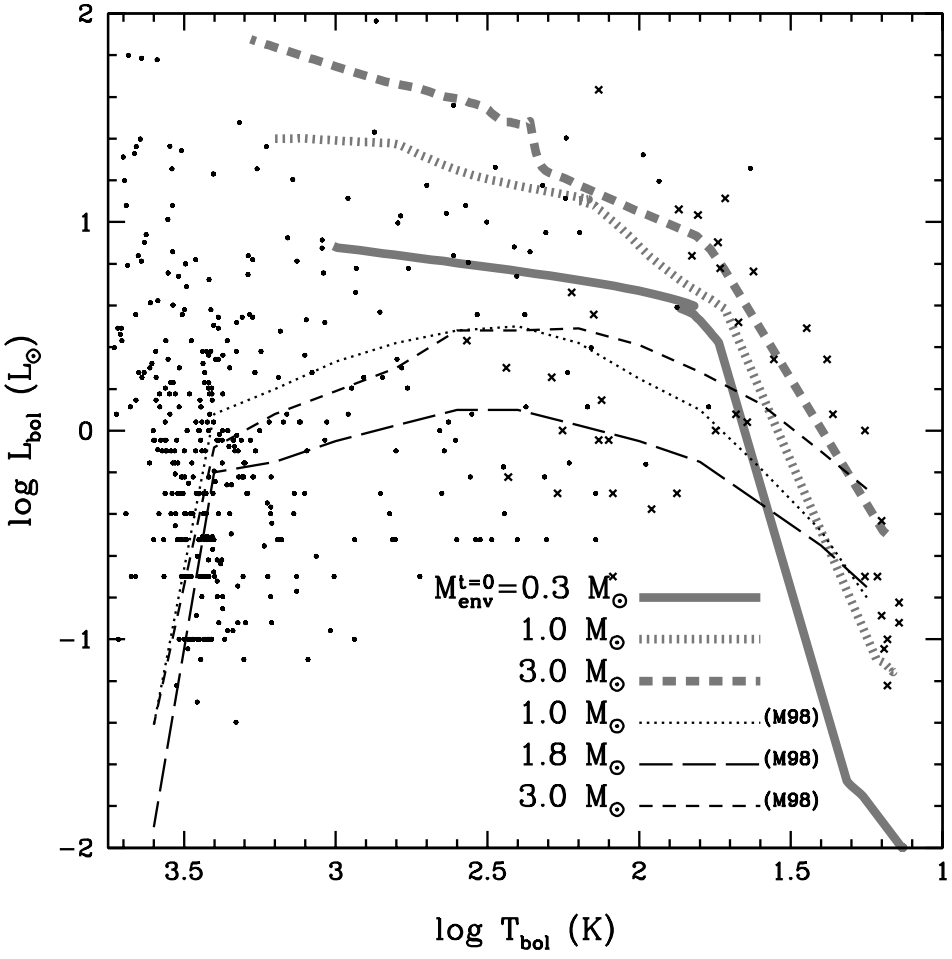

Figure 4.19: As seen in M98, this is a bolometric luminosity and temperature diagram. The thick lines are our models for three different initial masses. The thin lines are models from M98 with the initial envelope masses labeled. The 1.0 and 3.0 $M_\odot$ models are from figure 7 in M98. The 1.8 $M_\odot$ model is from figure 9 in M98. The crosses are from Young et al. (2003), Shirley et al. (2002), and Shirley et al. (2004). The dots are from Chen et al. (1995) and Chen et al. (1997).

the mass evolution is not considerably altered by the exclusion of outflows. Calvet (1998) found that the ratio of mass loss rate to mass accretion rate is ~ 0.1. We are unable to model the scattered light coming from the outflow cavity. Others have, however, and we discuss their work in Section 4.8.4.

M98 also assume the envelope to have a density profile with a free-falling structure, $n(r) \propto r^{-3/2}$. We use the Shu77 solution, which has an inner free-falling envelope surrounded by a static envelope with $n(r) \propto r^{-2}$. These differences in structure of the envelope cause great disparities in the opacity. For example, a core that has 0.8 $M_{\odot}$ of material with $n(r) \propto r^{-3/2}$ creates $\tau_{\nu}(100\mu m) = 0.26$. A core with the same amount of material but described by the Shu77 collapse solution, with an infall radius that is one-half of the outer radius, creates $\tau_{\nu}(100\mu m) = 0.17$. Such a disparity causes large changes in T_{bol}. For example, if we place a 0.7 $L_{\odot}$ star with T_{eff}=2000 K inside these two cores, the Shu77 core has $T_{bol} = 416$ K, and the free-falling core has a bolometric temperature that is half as high, $T_{bol} = 207$ K.

M98 do not calculate the full SED. Instead, they consider the optically thin and thick limits and calculate two moments of the protostellar spectrum: the bolometric temperature and luminosity. On the other hand, we use DUSTY to calculate the full radiative transfer in the protostellar system.

Finally, M98 use a single power-law to describe the dust emissivity, κ. In contrast, we use the dust properties calculated by Ossenkopf & Henning (1994). While the dust opacity is aptly described by a power-law at long wavelengths, the shorter wavelength opacities are clearly not properly represented in the same way (see Figure 4.1).

Interestingly, the data encompass both models, but M98's models obviously best cover the median range for the data. However, there are a substantial number of sources that have a lower bolometric luminosity than either model allows. Perhaps, these sources are in the quiescent stage of episodic accretion so that L_{acc} is very

low, or these low-luminosity objects could simply have a mass less than 0.3 $M_\odot$ and not be included in these models. Also, our models show higher luminosities at later times than most of the data, a result of the aforementioned "luminosity problem." Perhaps, accretion does occur episodically and only for short times, and we should expect only a few objects to be in the phase where material is accreting onto the star and, hence, have a high luminosity. Another explanation, of course, is that the assumption of constant accretion throughout the star's evolution is wrong.

4.8.4 Infrared Color-Magnitude Diagrams

In Figure 4.20, we show color-magnitude diagrams as would be observed with the Multiband Imaging Photometer for Spitzer (MIPS) on the Spitzer Space Telescope (SST). The three mass sequences (0.3, 1.0, and 3.0 $M_\odot$) are represented by the black lines in these figures. We show the magnitude at 24 μm ([24]) plotted against the [24] – [70] color; on the right of Figure 4.20, we plot [70] and [70] – [160].

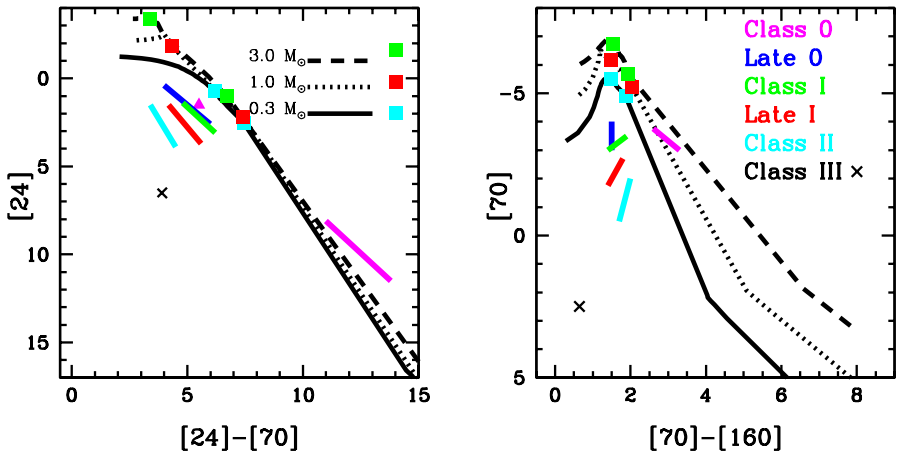

Figure 4.20: The black lines in this plot represent the SST MIPS colors as calculated for our models; [24], [70], and [160] are the magnitudes observed with MIPS. The colored lines are from Whitney et al. (2003) and extend over varying inclination angles. For the Class 0 models, the line represents most inclination angles except for the pole-on scenario, which is shown here as a magenta, filled triangle. Transitions, as discussed in Section 4.8.4, for the 1 $M_\odot$ models are shown as red squares while the green squares represent the transitions for the 3 $M_\odot$ model and cyan for the 0.3 $M_\odot$ core.

Also, we show the models of W03 from Figure 8a of their work. The colored lines show W03's calculations over varying angles of inclination. The magenta line represents almost all inclination angles for the Class 0 stage, and the magenta triangle is the Class 0 stage as viewed pole-on.

Many differences exist between these models and our work. For example, W03 describe the envelope as a rotating, freely falling envelope (Ulrich 1976); W03 also set the envelope's inner radius to be quite small ($\sim 10 R_{\odot}$) while we use a much larger inner radius. In addition, W03 have a number of "common" model parameters, which do not change for the different models. These parameters include the stellar radius, temperature, and mass as well as the overall source luminosity. In our model, we allow all of these to evolve with time. Finally, W03 included the effects of outflow cavities, 2-dimensional disks, and varying inclination angles. We are unable to account for these things.

Young objects in the PPC/Class 0 segment of their lifespan are very red in our calculations and occupy the lower, right-hand section of this plot. However, these models are bluer in this plane than the W03 models for a Class 0 source. Several factors probably contribute to this disparity. Most of the difference arises from the fact that W03's models have a considerably more luminous central source than our models. Thus, the envelope material is heated more and emits a greater 70 μm flux. Because W03 uses a very small inner radius, the optical depth is larger than for our models even though they may have similarly massive envelopes. Therefore, relative to the 24 μm flux, there is a higher 70 μm flux for W03's models, and their Class 0 stage appears redder (and, of course, more luminous). The effect is much less pronounced in the [70] – [160] plane because these longer wavelength fluxes are less affected by optical depth effects.

As with W03's models, our evolutionary tracks show that the objects become bluer in the [24] – [70] color as the source becomes more luminous and [24] increases.

We have marked the PPC/Class 0 and Class 0/I transitions (as determined by L_{bol}/L_{smm} as in section 4.8.2). The Class I/II transition occurs at the end of our modeling sequence when all envelope mass has accreted onto the star and disk. However, aspherical effects are most relevant with these later stages, so these models probably underestimate the 24 μm flux for the Class I/II transition. Transitions for the 0.3 $M_{\odot}$ models are shown as cyan squares, the red squares represent the transitions for the 1 $M_{\odot}$ model, and the green squares are for the 3.0 $M_{\odot}$ model.

The right panel of Figure 4.20 shows a simpler behavior for the evolution as seen at 70 and 160 μm. As an FHC, the protostar appears very red but becomes bluer as the core collapses to $\sim$3 $R_{\odot}$ and grows in luminosity. The 160 μm flux increases over time as the internal luminosity continues to grow. However, there is a point where the envelope contains so little material that the 160 μm flux drops despite the fact that the far-infrared emission of the internal star is growing. By the end of these tracks, the objects have reached the end of their Class I stage; they no longer have envelope material but do have an optically thick disk.

4.9 Conclusions

We have presented the results from modeling the evolution of protostars with 3 different masses: 0.3, 1.0, and 3.0 $M_{\odot}$. The framework for the evolution of these protostars was taken mostly from the work of Adams & Shu (1986) but also used the results from several other authors. These efforts were similar and complementary to the work of Myers et al. (1998) and Whitney et al. (2003) but employed different methods and theories and, hence, got different results.

We note that the evolution of these modeled protostars is significantly affected by the existence and lifetime of the first hydrostatic core. The work done heretofore is useful (Boss & Yorke 1995; Masunaga et al. 1998), but more detailed theoretical work is needed. As we begin to observe earlier stages of star formation

(Young et al. 2004a), the role of the FHC must be ascertained.

We find that the Class 0 stage, when determined by T_{bol}, should be short-lived, lasting only about 1/10 to 1/4 of the protostar's life. This result is somewhat model dependent, but it should also extend to other models of star formation. Therefore, the surveys being conducted with the Spitzer Space Telescope and 2MASS should reveal a small fraction of Class 0 to Class I objects. However, we suggest not using the T_{bol} criterion for classification.

We find that the bolometric temperature is a poor discriminator for protostars at early evolutionary stages. Instead, we suggest using the L_{bol}/L_{smm} signature proposed by André et al. (1993). Based on physical grounds, we suggest these boundaries for classifying protostars: $L_{bol}/L_{smm} = 35$ for PPC/Class 0, $L_{bol}/L_{smm} = 175$ for Class 0/I, and $L_{bol}/L_{smm} \sim 2000$ for the Class I/II transition. The latter is largely dependent on the adopted disk model. Also, L_{bol}/L_{smm} is not relevant after all envelope mass has been accreted (beyond the Class I stage) since it is a measure of the stellar to envelope mass ratio (André et al. 1993).

We have presented several observational tools by which the inside-out collapse model can be effectively tested: infrared color-magnitude diagrams, plots of the bolometric luminosity and temperature, and a plot of T_{bol} and L_{bol}/L_{smm}. Large surveys will produce these observable quantities for hundreds of young protostars and test the theory of inside-out collapse.

4.10 Acknowledgements

We thank Minho Choi for the use of his program to calculate the density profiles. Also, many thanks to Moshe Elitzur, Maia Nenkova, and Željko Ivezić for providing the modified version of DUSTY that allows heating by the ISRF and for much assistance in the use of DUSTY. Many thanks also to our anonymous referee whose thorough reading and thoughtful critique have made this a better paper. This work

Table 4.1: Model Parameters

	Symbol	Adopted Value
Envelope parameters		
Envelope inner radius	r_i	Equation 4.4
Envelope outer radius	r_o	Equation 4.1
Envelope dust opacity	κ_ν	Ossenkopf & Henning(1994)
Disk parameters		
Inner radius	R_i	Equation 4.10
Outer radius	R_o	Equation 4.11
Accretion luminosity	L_D	Equation 33b, Adams & Shu (1986)
Temperature power-law	T_D	Equation 4.14
Stellar parameters		
Accretion luminosity	L_{acc}	Equation 33a, Adams & Shu (1986)
Photospheric luminosity	L_{phot}	D'Antona & Mazzitelli (1994)
Effective temperature	T_{eff}	Equation 4.19
Radius	R_*	Palla & Stahler (1991)

is supported by NASA grants NAG5-10488 and NNG04GG24G.

Chapter 5

Submillimeter Observations of Low-Mass Protostars

5.1 Abstract

We present submillimeter observations of dark clouds that are part of the Spitzer Legacy Program, From Molecular Cores to Planet-Forming Disks (c2d). We used the Submillimetre Common User's Bolometer Array to map the regions observed by Spitzer by the c2d program so that we can create a census of star-forming cores including data from the infrared to the submillimeter. In this paper, we present the basic data from these observations: maps, fluxes, and source attributes. In addition, we make some comparisons with other studies of these regions. We also show data for an object just outside the Perseus cloud that was inadvertently observed in our program. We propose that this object is a newly discovered, evolved protostar. Finally, we compare the SCUBA data to Spitzer observations.

5.2 Introduction

In recent years, significant progress has been made toward a theory for the formation of low mass stars, which are the likely sites for the formation of planetary systems. Maps of submillimeter dust continuum emission are excellent tracers of the column density and mass, while infrared observations trace luminosity. The Spitzer Legacy program, From Molecular Cores to Planet-Forming Disks, has obtained extremely sensitive observations from 3.6 to 70 μm, yielding vital new information on low-mass protostars. In order to obtain the full benefit of this database, it is crucial to examine data at longer wavelengths where the dust emission is optically thin.

SCUBA is arguably the most powerful and efficient tool for mapping extended dust emission, critical information for studying star formation. We have mapped star-forming regions, which are already observed by the c2d program, with SCUBA in order to trace the flow of matter from cloud to disk. Together with other complementary data at optical and near-infrared wavelengths, our observations will give the most comprehensive catalog of multi-wavelength data for star-forming regions.

5.3 Observations and Data Reduction

5.3.1 Sample

We have observed 38 cores that were initially included in the c2d observation plan; 13 were not detected at 850 or 450 μm. The sources have been drawn from complete catalogs of nearby cores that have molecular line maps (Lee & Meyers 1999; Jijina et al. 1999; Lee et al. 2001). The gas in these cores in these cores is well-studied, mostly by mapping observations of the 1.3 cm line of NH_3 (Benson & Myers 1989) and the 3 mm line of N_2H^+ (Caselli et al 2002). These sources are all relatively nearby, within 450 pc, so their maps have good spatial resolution. A few sources have

been observed by others before, but not over a region as large as that mapped by the Spitzer Space Telescope. In these observations, we have matched the SCUBA maps to cover the same area as the Spitzer maps; in most cases, these maps are $5' \times 5'$, but they are sometimes larger.

In Table 5.6, we list the right ascension and declination for each source that we have detected. In cases where we have detected multiple sources in the same field, we have added a letter (a, b, or c) to distinguish the individual sources.

We had intended to observe Per9, whose position is in Caselli et al. (2002). However, we improperly entered the coordinates at the telescope and mistakenly observed a field that happens to be centered on 2MASS 0347392+311912. This field is about $30''$ from the edge of the c2d coverage for the Perseus cloud. We discuss the nature of this object in Section 5.4.4.

Finally, some cores in Table 5.6 were removed from the c2d observations plan in order to meet time constraints. These sources are presented in this paper but are not observed by the c2d Legacy Program: CB224, CB230, IRAS04361, L1082A, L1082C, L1157, Per4, Per5, Per6, Per9, RNO43, CB28, DC253, L77, and Per7.

5.3.2 Observations

We observed these sources with the James Clerk Maxwell Telescope (JCMT) beginning in January 2002 and ending February 2004. We were granted time during each semester between these dates. However, the data collected during the semester 02A and December 2002 to February 2003 were not usable because of technical problems with the JCMT.

We used the scan mapping technique (Holland et al. 1999), which is used to map regions much larger than SCUBA's field of view. Through this method, the telescope scans across the field while chopping at 30, 44, and 68 degrees from the scan direction. The chopping removes sky variations and DC offsets, but it creates

a difference map of the source, a positive and negative source separated by the chop throw.

During the course of observations, we measured τ_{850} and τ_{450} with frequent skydips, compared this data with τ_{CSO}, and found good agreement.

Finally, we observed several sources for flux calibration: CRL 618, Mars, Uranus, and IRC10216. We generally observed at least 2-3 calibrators during an observing shift.

5.3.3 Data Reduction

We analyzed and reduced our data with the SCUBA User's Reduction Facility (SURF) (Jenness et al. 1997); we also closely followed the reduction methods of Pierce-Price (2001). Our reduction entailed flatfielding, extinction correction, removal of bad pixels, removal of baselines, and the coadding and rebinning of the maps.

To correct the data for extinction, we measured τ_{850} and τ_{450} from skydips that were completed at the time of each map; these values for τ are listed in Table 5.6 and Table 5.6 for the sources and calibrators, respectively.

For the removal of bad pixels, we first used SURF's "despike2" tool, which removes spikes from scanmap observations. This package has 2 criteria for despiking. The first considers each data point and asks how disparate it is from the two adjacent data points. If this difference is greater than a certain number of standard deviations for the scan (NSIGMA), the data point is rejected. We use NSIGMA=4. The second criterion convolves the data with a three sample box and uses NSIGMA in the same way. In addition, we have used "sclean" to interactively search all of the data for bad pixels.

We use SURF's "scan_rlb" to remove the baselines from the extinction corrected and cleaned data. We assume there is no emission at the end of each scan,

which is generally true, and use the linear method of baseline removal. In this way, scan_rlb fits the baseline to the end of each scan and then applies it to the remaining scan.

Next, we rebin the data, with baselines removed, to create the dual-beam map. We used pixels appropriate for Nyquist sampling (3.5″ and 7.5″ for 450 and 850 μm, respectively) and do not smooth the maps. At this point, we examine each rebinned, dual-beam map to search for evidence of bad data, such as stripes or other artifacts, missed during the despiking and cleaning tasks.

The rebinned maps are the telescope's dual-beam function convolved with the sky. We use "remdbm" to remove the dual-beam signature from the map. This package uses the Emerson2 (Emerson 1995; Emerson et al. 1979) technique to deconvolve the data and create the single-beam map of the source. We use no high-frequency filtering. We assess the RMS noise of the map with Starlink's "stats" package and create the maps in Figure 5.1-5.9. The contours begin at 2-σ and increase by 2-σ; greyscale begins at $-$2-σ and increases to the image maximum. Blue asterisks in Figures 5.1-5.9 represent the source positions in Table 5.6 while red crosses mark the position of IRAS sources, which were detected in any IRAS band.

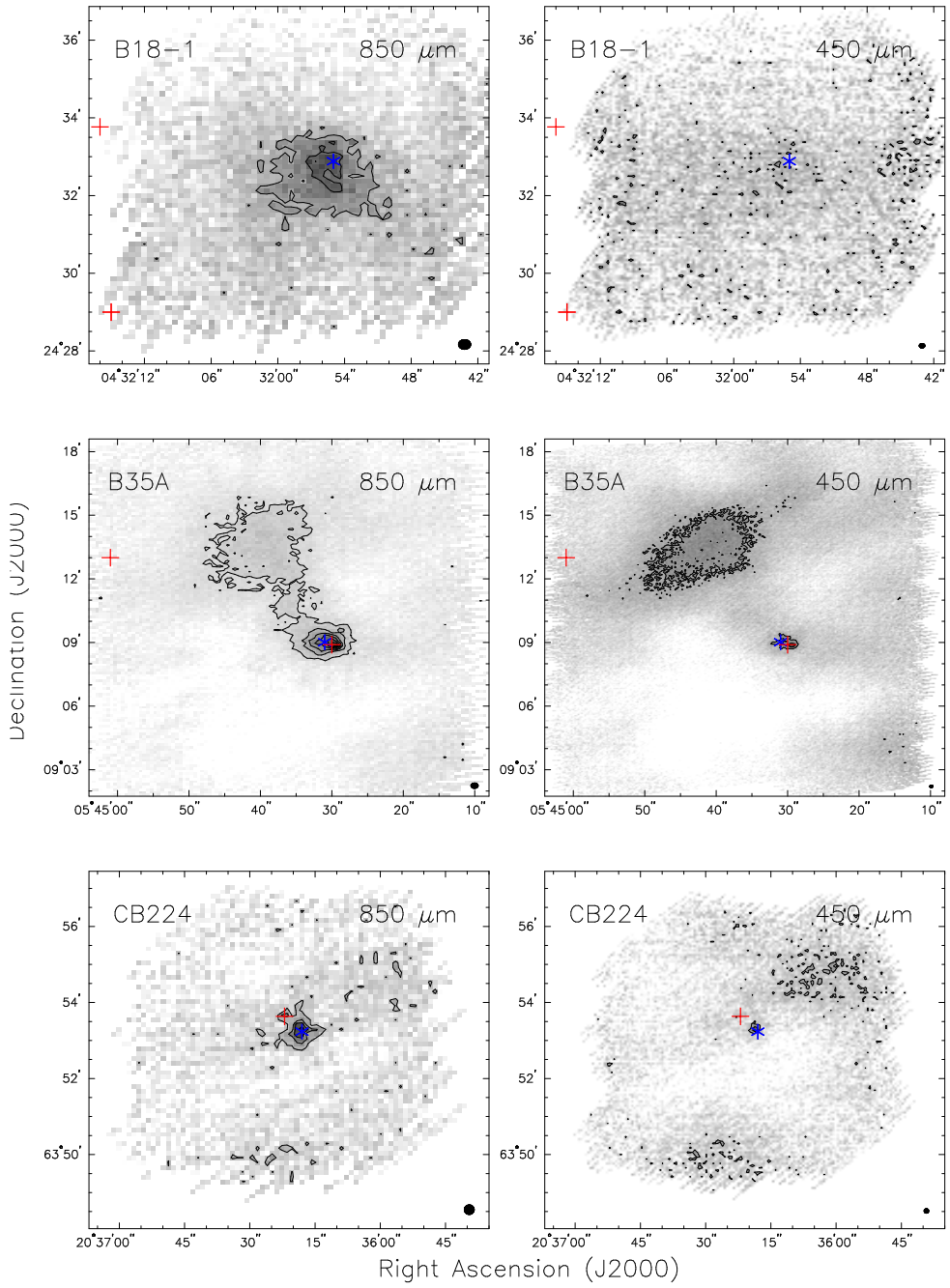

Figure 5.1: We show the 850 and 450 μm maps for the star-forming cores in Table 5.6. Contours begin at 2-σ and increase by 2-σ; greyscale begins at -2-σ and increases to the image maximum. Blue asterisks represent the source positions in Table 5.6 while red crosses mark the position of IRAS sources in the field.

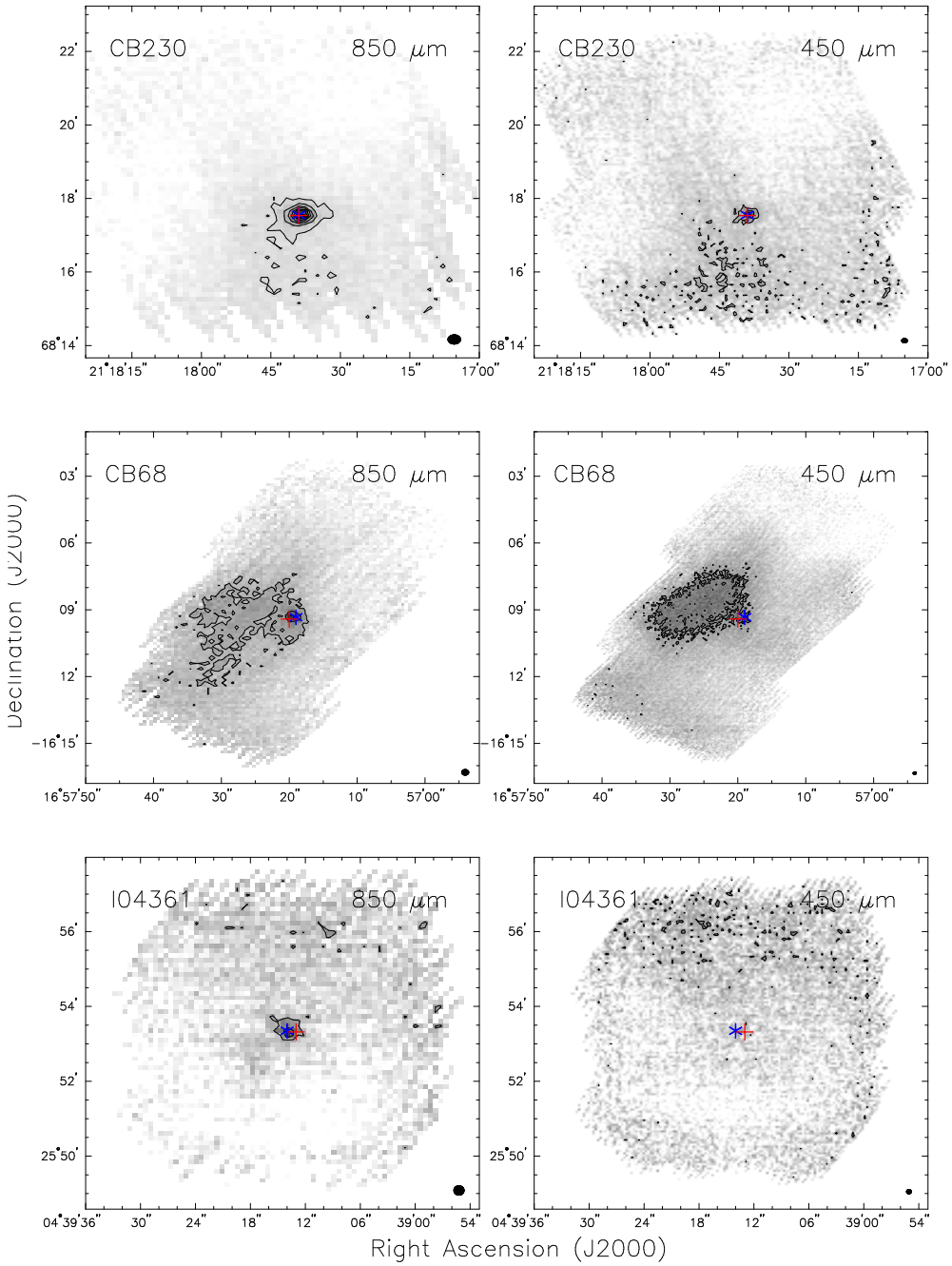

Figure 5.2: continued...

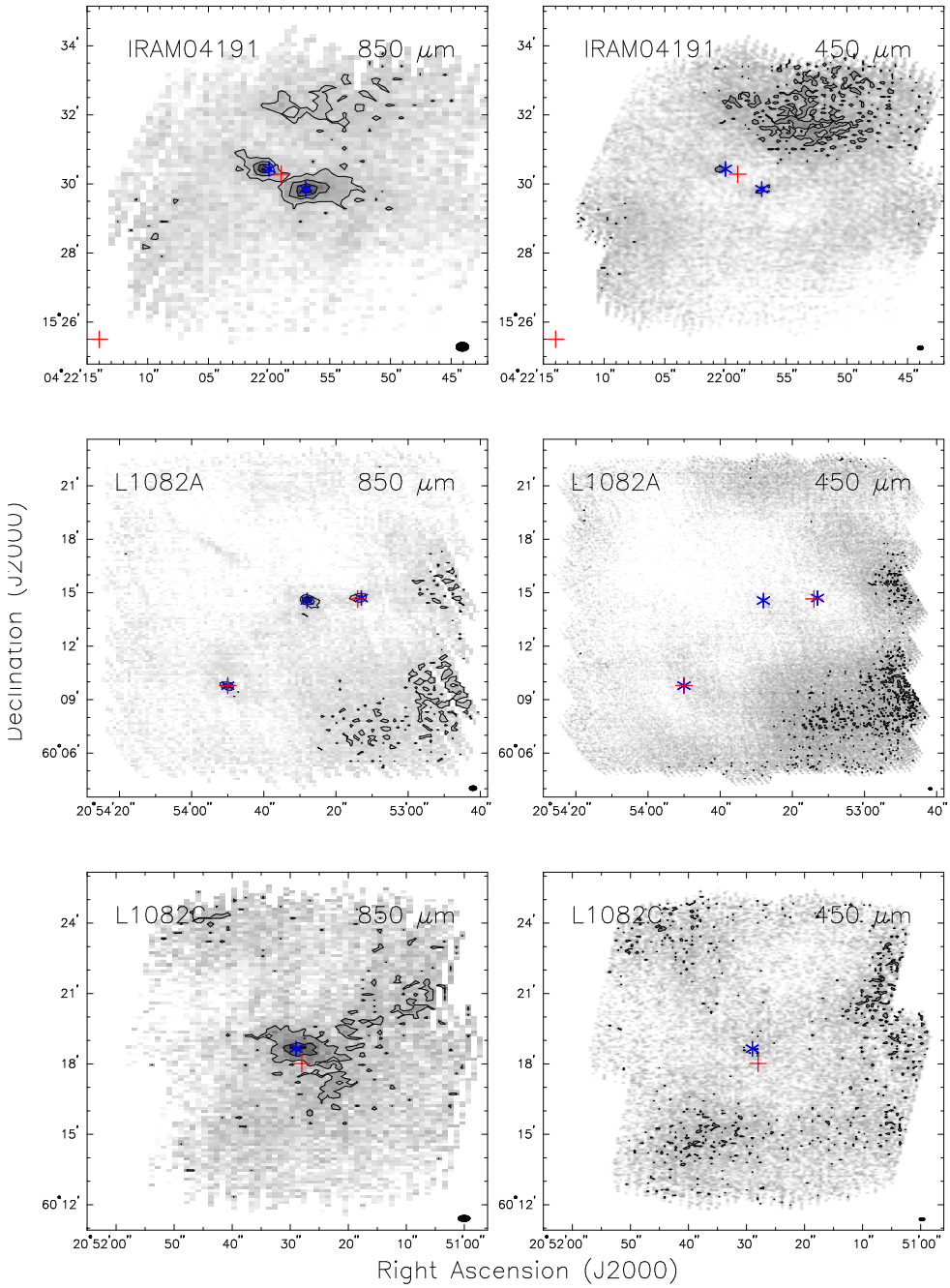

Figure 5.3: continued...

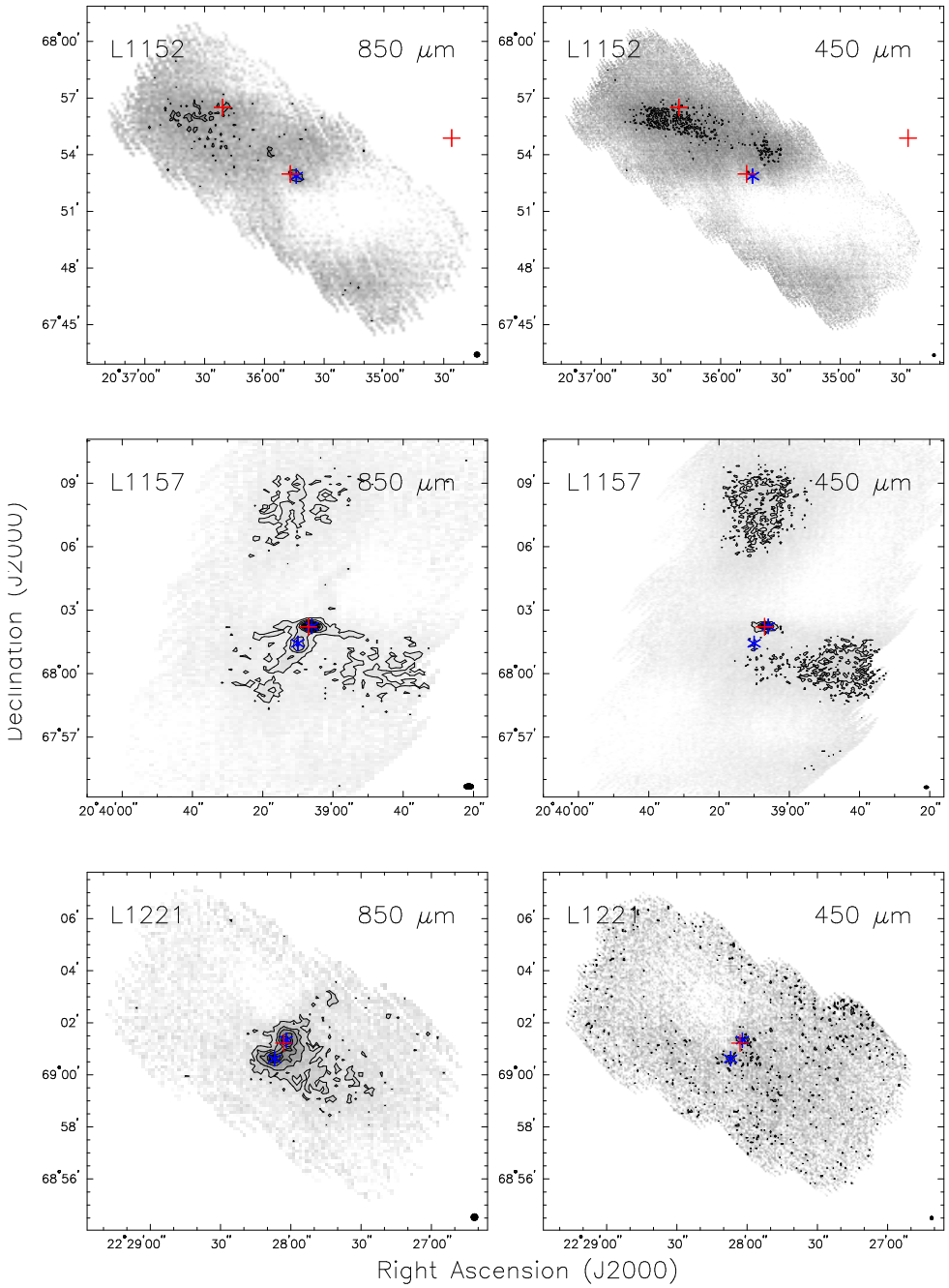

Figure 5.4: continued...

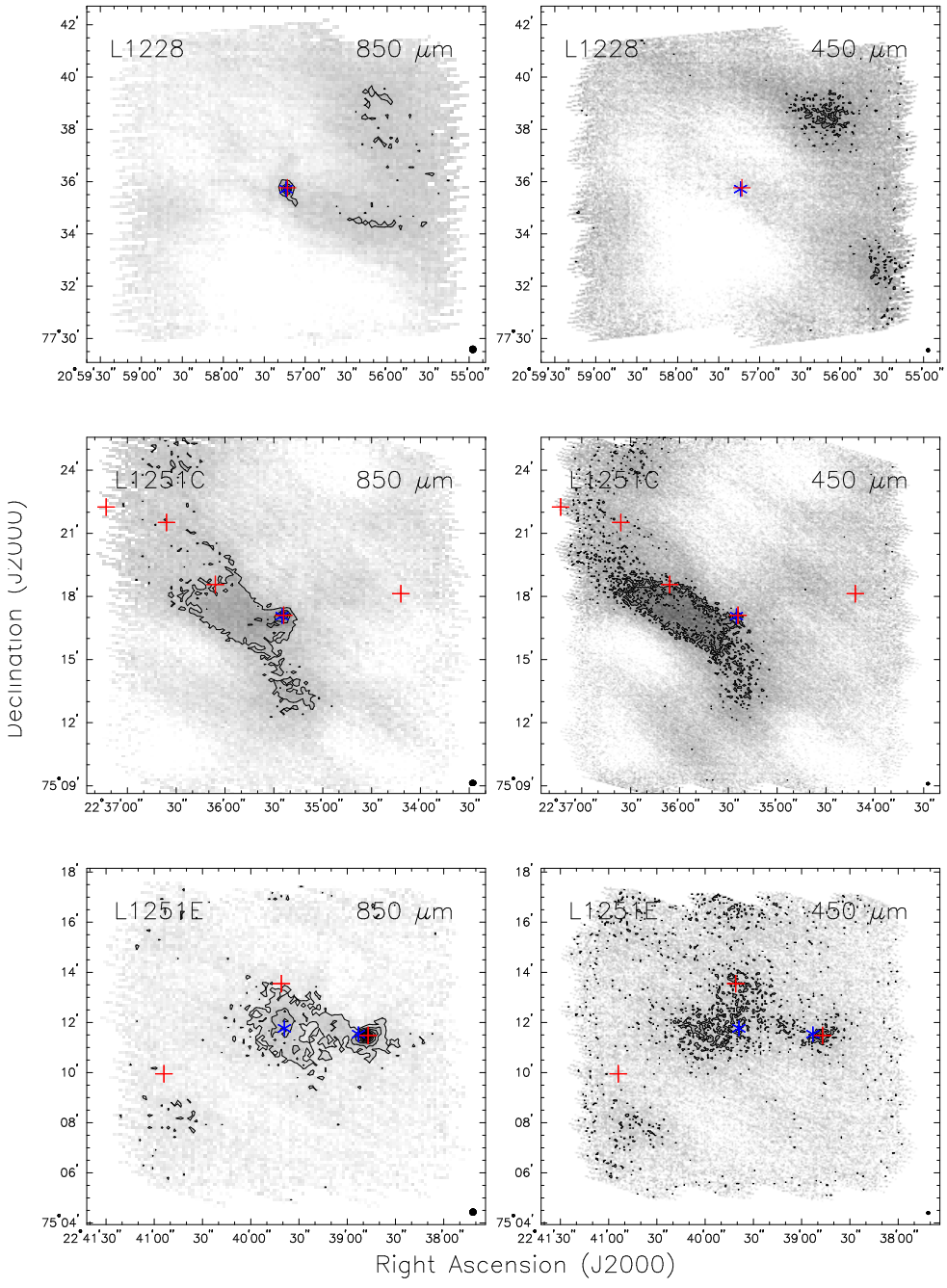

Figure 5.5: continued...

We have used Starlink's Extractor, which is based on SExtractor (Bertin 2003), to extract source positions for each of the maps in Figures 5.1-5.9 (Chipperfield & Draper 2004). This includes the source positions in Table 5.6.

5.3.4 Calibration

In Table 5.6, we list flux conversion factors (FCF) for all calibrators observed during the course of this project. In calculating the FCF, we simply average all values, except that for Jupiter and IRC 10216, and give this average and standard deviation in Table 5.6. As suggested on the SCUBA webpage, we do not use Jupiter and IRC10216 for flux calibration. We do not use FCFs when the uncertainty approaches 100%, as for the 450 μm FCFs for 80″ and 120″ apertures, but we list them in Table 5.6 along with all of the average calibration factors.

5.4 Results

5.4.1 Mass

In Table 5.6, we give the isothermal mass of each core from the 850μm emission, assuming a temperature of 15 K (Young et al. 2003;see Equation 2). We also give the virial mass, based on Δv of the N_2H^+ line, for those cores from Table 4 of Caselli et al. (2002).

We compare the isothermal dust mass and the virial mass in Figure 5.10. In general, the virial mass for a given source is larger than the mass derived from the 850 μm flux. This trend was also noticed in Young et al. (2003), who claimed this discrepancy was because N_2H^+ does not effectively trace the gas around more evolved, hotter protostars. This was also found in the work of Lee et al. (2004), who modeled the chemical evolution of a forming protostar and concluded that N_2H^+ is no longer abundant beyond the Class 0 stage.

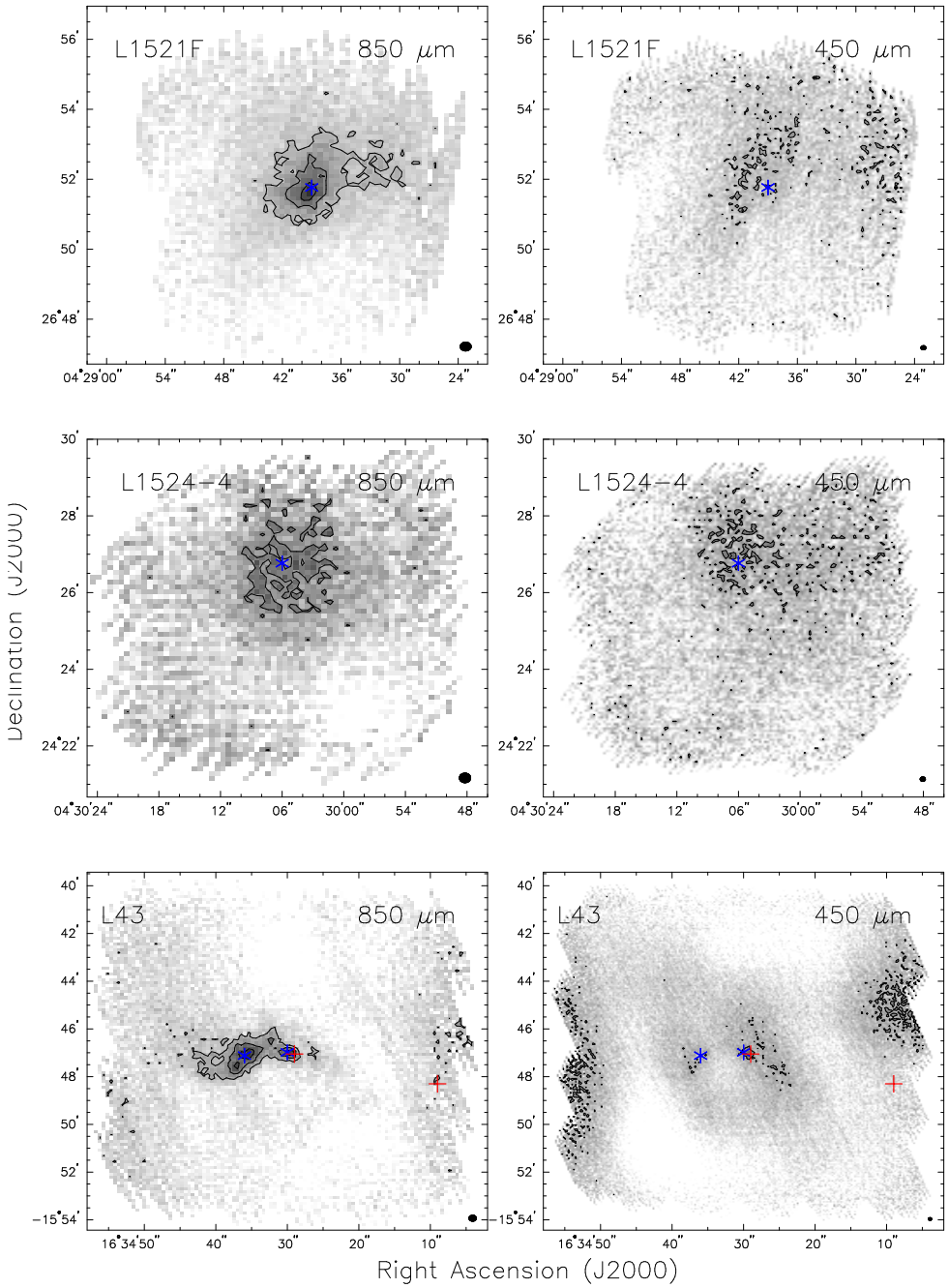

Figure 5.6: continued...

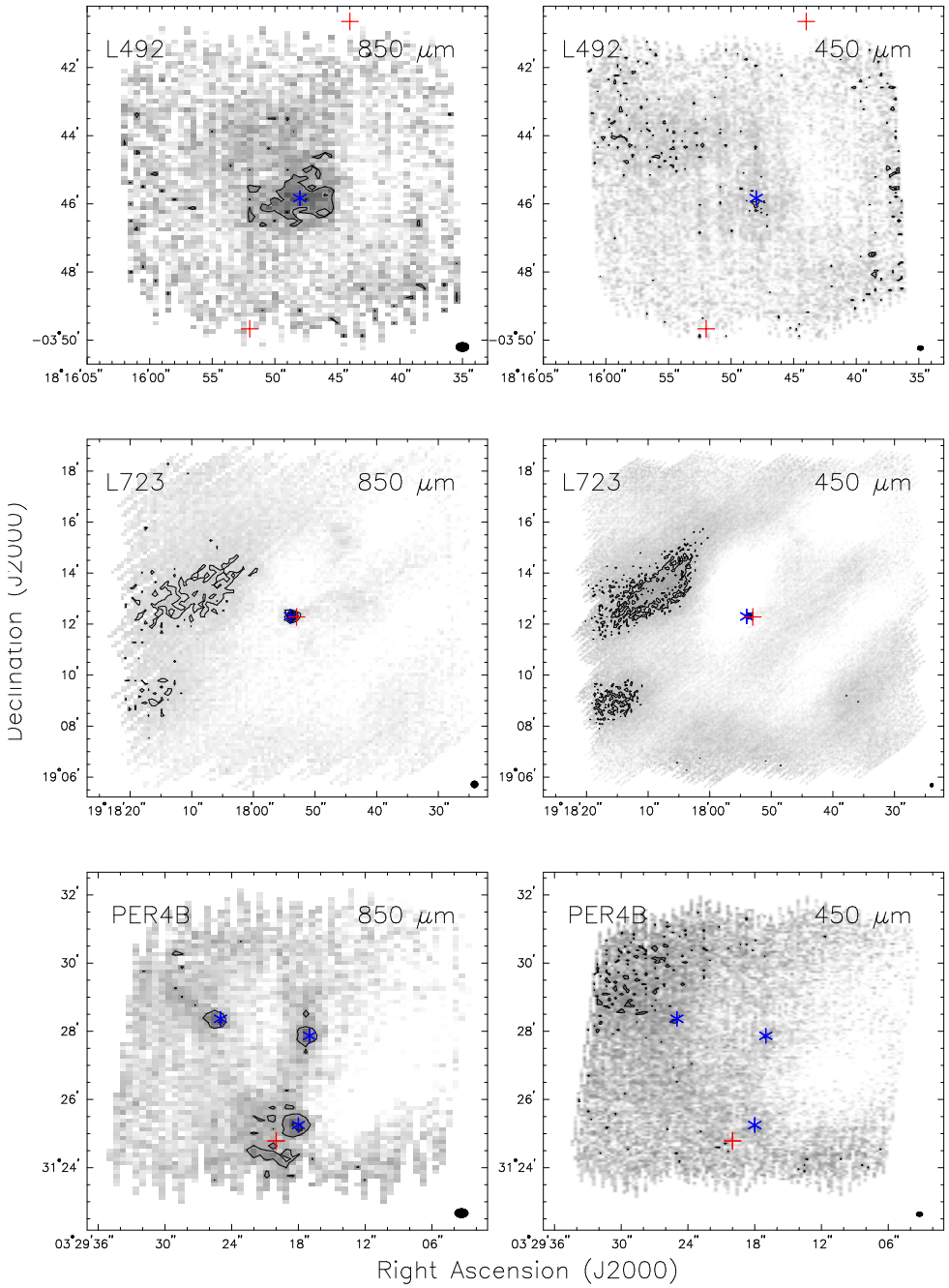

Figure 5.7: continued...

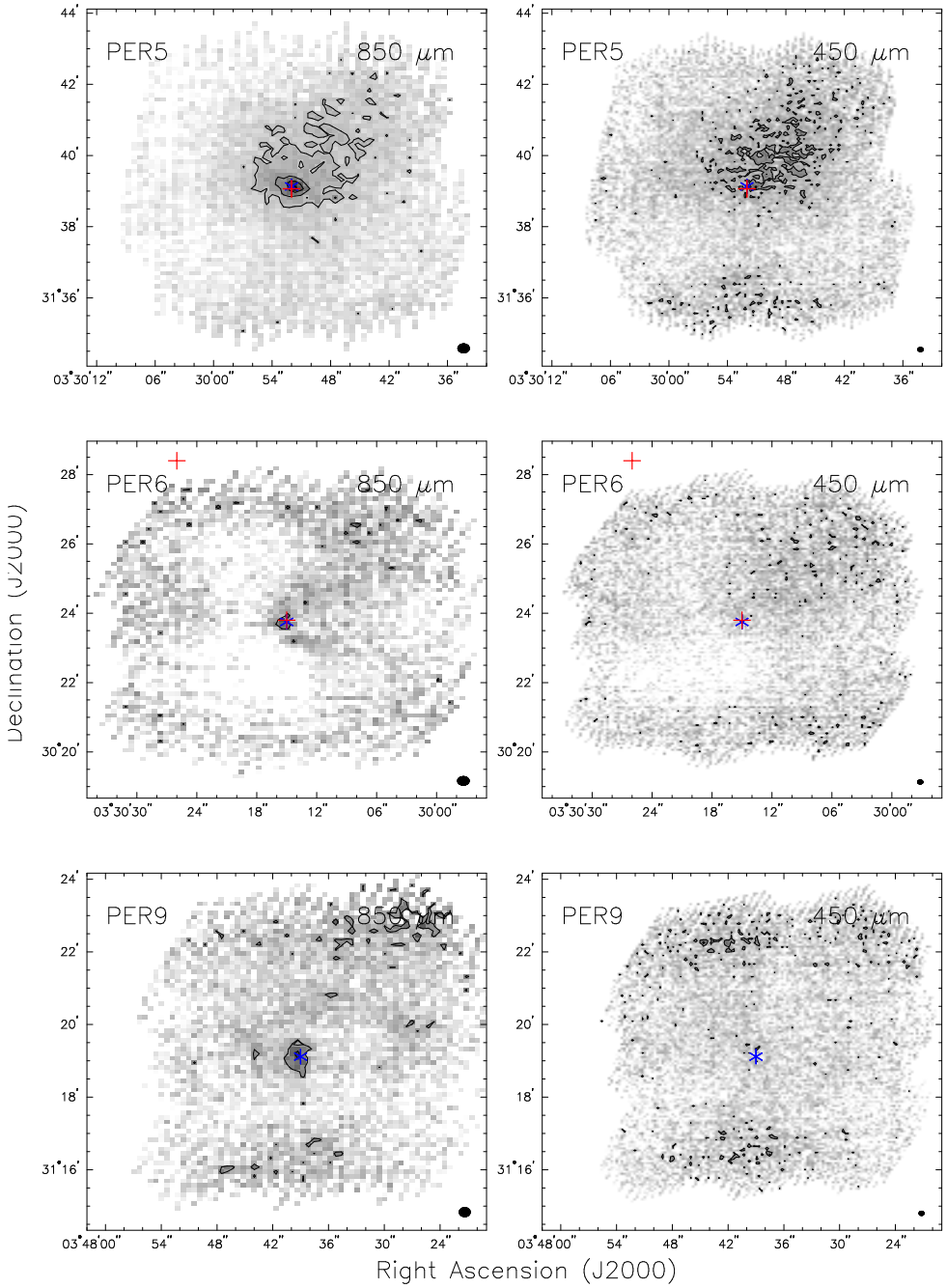

Figure 5.8: continued...

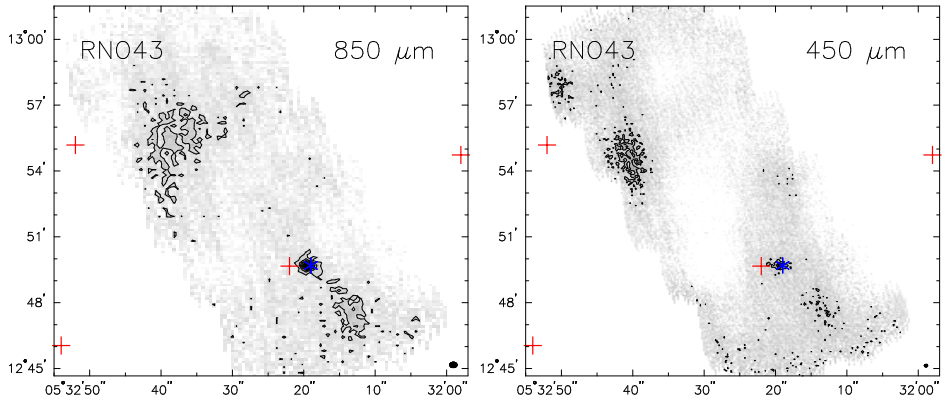

Figure 5.9: continued...

5.4.2 Multiplicity

Several of the dark clouds we mapped contained more than one dense core: IRAM 04191, L1082A, L1157, L1221, L1251E, L43, and Per4. Three other objects have some extended emission, which is either real or an artifact of the double-beam deconvolution (Pierce-Price 2001): B35A, CB68, and L1251C. For B35A, at least, the emission does appear to be real because the N_2H^+ map shows similar structure. The N_2H^+ map of L1251C is also similar to the 850 μm continuum image. CB68 was mapped by Huard et al. (1999), and their map, while much smaller than ours, does not appear to have this extended emission.

In all but one case, only one object in each of the multiple core systems was detected by IRAS. This implies that either these multiple cores are at different stages of evolution or that some of the cores are forming objects with lower luminosities than their companion and hence are not detected by IRAS.

5.4.3 Comparison with Spitzer Observations

Our intention in collecting this SCUBA data was that it would act as a complement to the Spitzer c2d observations. The submillimeter emission from star-forming cores gives a good census of the material surrounding the central, luminous object, and a measure of this emission is also needed to more adequately model the processes of star formation. Here we give two examples of how the SCUBA data are used in

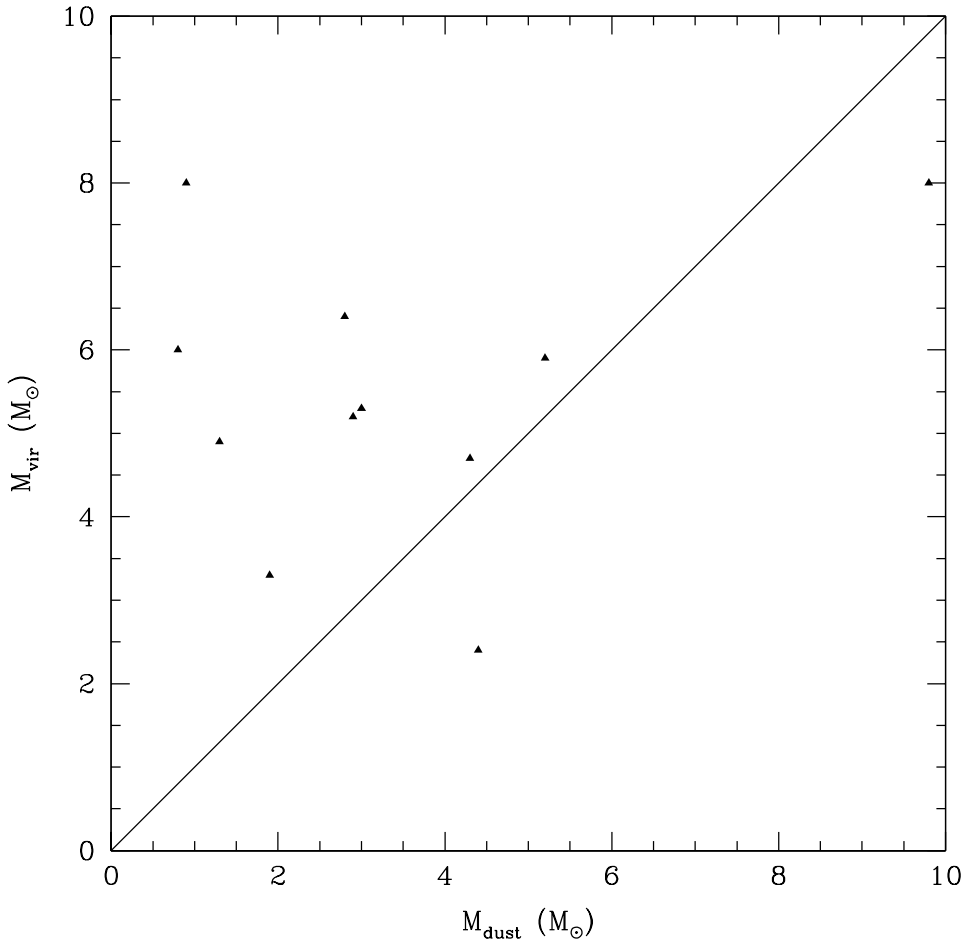

Figure 5.10: We compare the virial mass from Caselli et al. (2002) to the mass derived from the 850 μm flux. We find that M_{vir} is generally larger than M_{dust}.

concert with the c2d observations. More complete analysis of the c2d star-forming core observations will be presented in Huard et al. (2005).

L1221

The discovery of a star in L1014 was a suprise (Young et al. 2004). However, we are finding more and more "starless cores" that are, in fact, not starless. L1221 is an object with two distinct cores, one of which was clearly detected by IRAS and 2MASS. However, the second core has been considered to be starless. With the Spitzer observations, we see that both cores are harboring a central source. In Figure 5.11, we show the SCUBA 850 μm contours overlaid on 2MASS, IRAC, and MIPS images. The IRAS source is in the northern core, while the previously starless core is the southern one.

In Figure 5.12, we plot the SEDs for these two cores, including data from the near-infrared to submillimeter wavelengths. We use the 450 and 850 μm fluxes for a 40$''$ aperture; the two cores are distinct at this level ($\sim$6-σ). At submillimeter wavelengths, these two cores look very similar; both have 850 μm flux (in a 40$''$ aperture) that renders an isothermal mass of about 0.7 $M_\odot$ (2.0 and 1.9 Jy). However, at infrared wavelengths, these objects are very different. Perhaps, the southern core is in some quiescent stage during which there is no accretion from the envelope or disk, or, maybe, this core is forming a very low-mass object. Many explanations can be constructed to explain these SEDs, but the truly interesting point is more obvious. At some point in time, these two cores, which share very similar physical conditions, entered drastically different evolutionary roads.

B35A

Sometimes, the combination of submillimeter and IRAC data can reveal hidden information about the environs of a star-forming core. In Figure 5.13, we show the

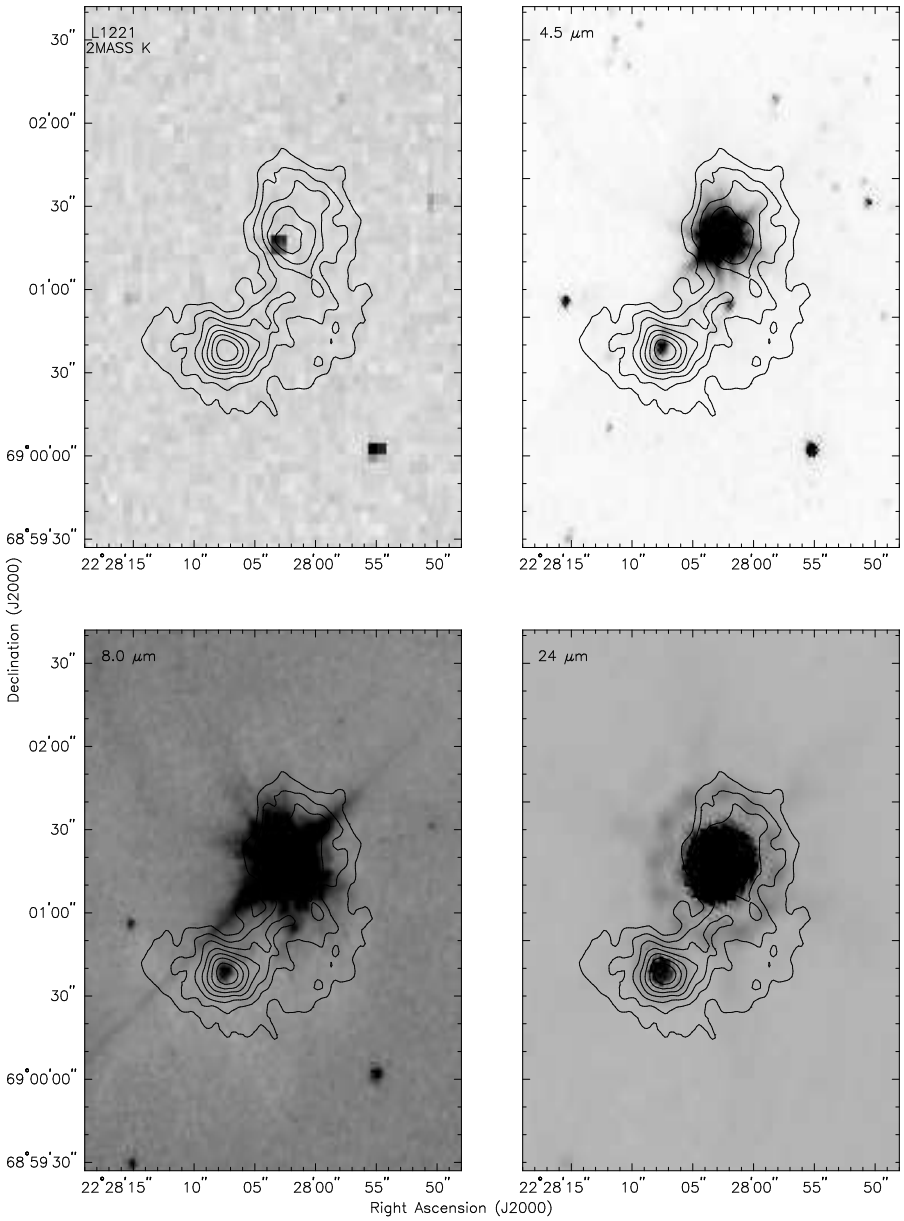

Figure 5.11: We show 850 μm data overlaid on 2MASS, IRAC, and MIPS images of L1221. The southern core was previously thought to be starless, and the northern core was detected by IRAS.

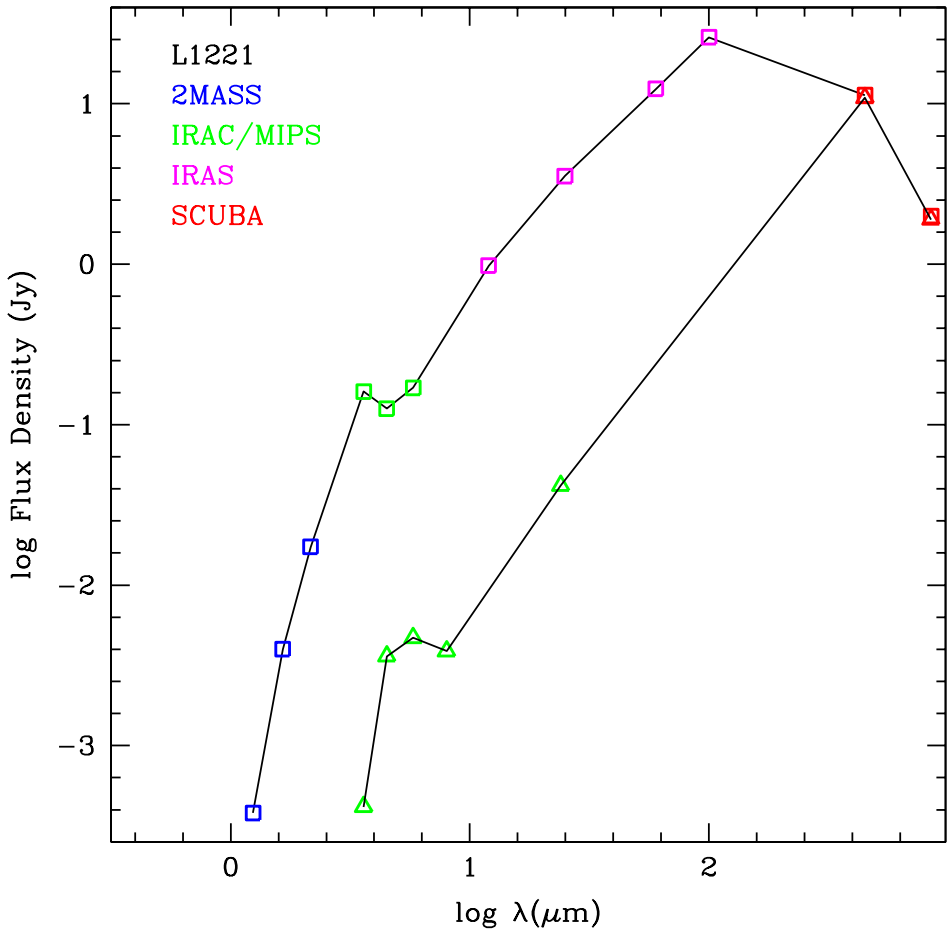

Figure 5.12: Triangles represent the data for the southern source, and squares are for the northern, IRAS-detected source. The SEDs of the two L1221 cores are basically identical at submillimeter wavelengths, suggesting that their physical environments are similar. However, the infrared portion of the SED shows markedly different objects embedded within L1221.

three-color image (red=8.0 μm, green=4.5 μm, and blue=3.6 μm) along with 450 μm data in yellow contours. There appears to be a cluster of at least three protostars within the B35A core, and some nebulous emission, seen most prominently at 3.6 μm, is also evident at 450 μm.

One or more of these protostars appear to be driving an outflow. In Figure 5.14, we again show the three color image but expanded and with 850 μm contours. We have enhanced the green 4.5 μm data in order to show the ridge of emission extending from the main core to the southeast (inside the green lines on this figure). The 4.5 μm bandpass contains atomic and molecular emission lines that are excited in the environments of outflows (Noriega-Crespo et al. 2004). We suggest this "green jet" is the result of an outflow from B35A. In addition, the 850 μm data shows an elongation in the direction of the outflow, which is to be expected since the outflow opens a cavity and allows the dust to be heated more directly by the central star.

5.4.4 2MASS 0347392+311912

We inadverdently observed 2MASS 0347392+311912, having intended to observe a known star-forming core in Perseus instead. The source lies outside of the c2d observations for Perseus (see Figure 5.15), so we have no mid- or far-infrared data. The 2MASS source, however, did have detectable submillimeter emission at 850 μm (0.7 Jy).

In Figure 5.16, we show the 850 μm data overlaid on 2MASS K-band and DSS R-band images. In both the near-infrared and optical maps, the source appears pointlike and is clearly detected. In Figure 5.17, we plot the SED for this source, including the near-infrared data from 2MASS and B, R, and I measurements from the USNO B1.0 catalog. The SED peaks at 1.65 μm (H), but quickly rises in the submillimeter. We propose that this source is a previously unknown protostar,

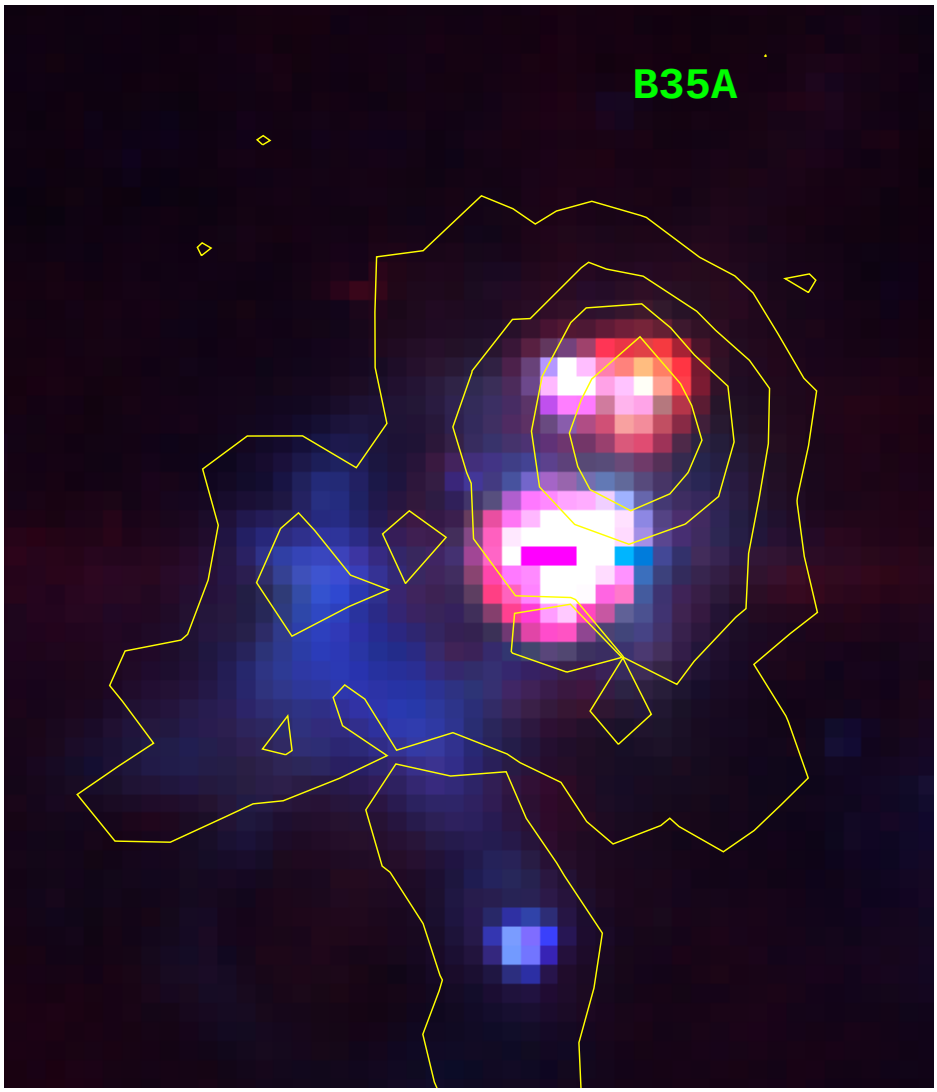

Figure 5.13: We show the three-color image for B35A (red=8.0 μm, green=4.5 μm, and blue=3.6 μm) with 450 μm contours overlaid; contours begin at 1.5-σ and increase by 1.5-σ. There is a cluster of objects in the center of this core that appears to be forming protostars. The blue ridge of emission to the southeast is also evident in the 450 μm data.

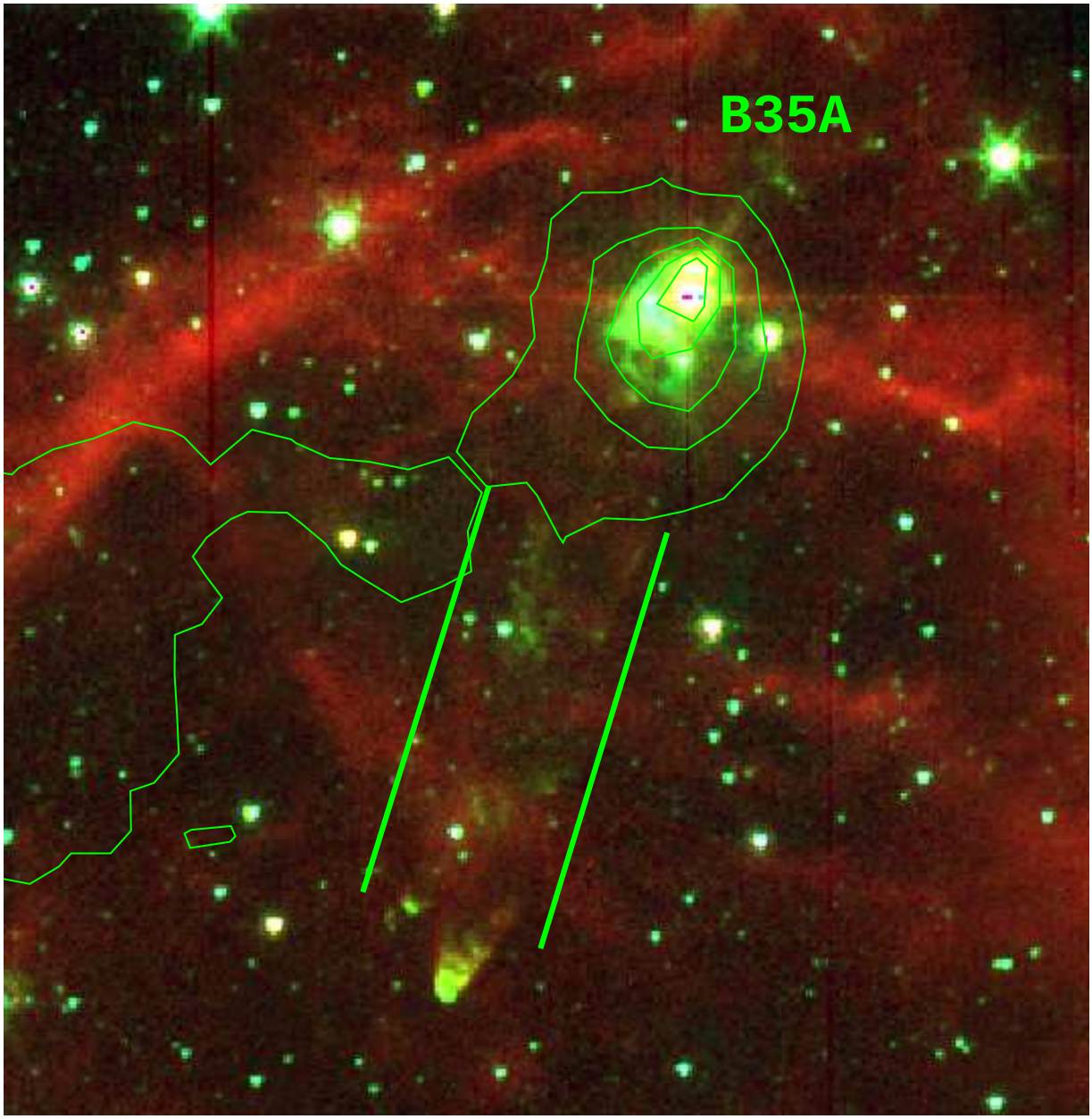

Figure 5.14: Green contours are 850 μm data of B35A beginning at 2-σ and increasing by 2-σ. The three-color image is the same as in Figure 5.13 but expanded and with the green, 4.5 μm enhanced. The green ridge of emission between the two green lines is likely due to an outflow from B35A. Possibly, this outflow also causes the elongation in the 850 μm data.

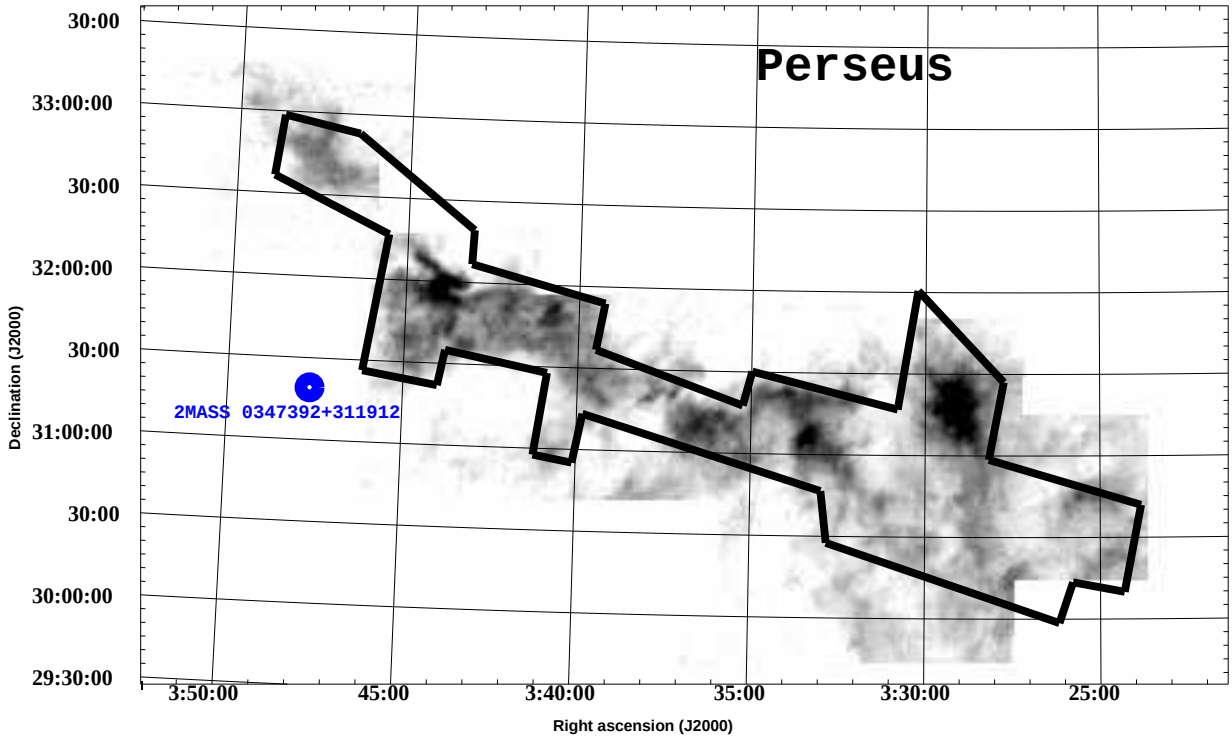

Figure 5.15: The possible protostar 2MASS 0347392+311912 lies just outside of the Perseus star-forming region and was not included in the c2d program.

which is possibly near the Perseus star-forming cloud.

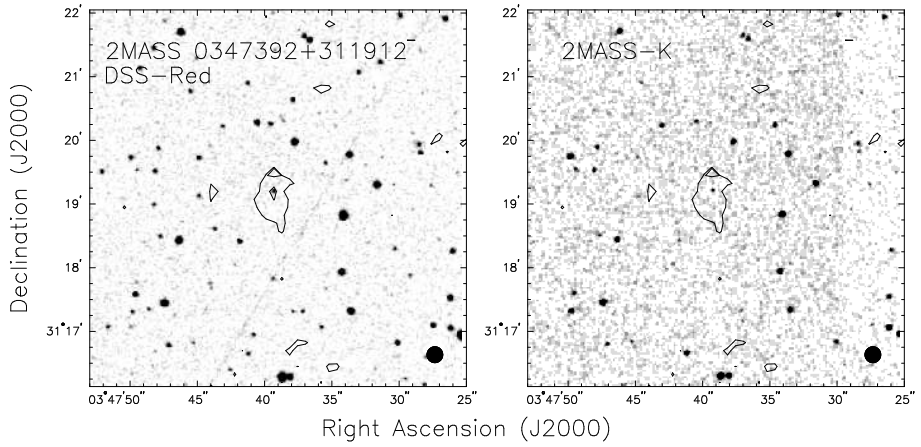

Figure 5.16: We show data for 2MASS 0347392+311912. The greyscale in the left panel is from the Digitized Sky Survey, and the right panel shows the 2MASS K-band image. The contours are from the SCUBA 850 μm observations. Contours begin at 2-σ and increase by 2-σ; we do not draw the 4-σ contour in the right panel because it obscures the 2MASS source, 2MASS 0347392+311912.

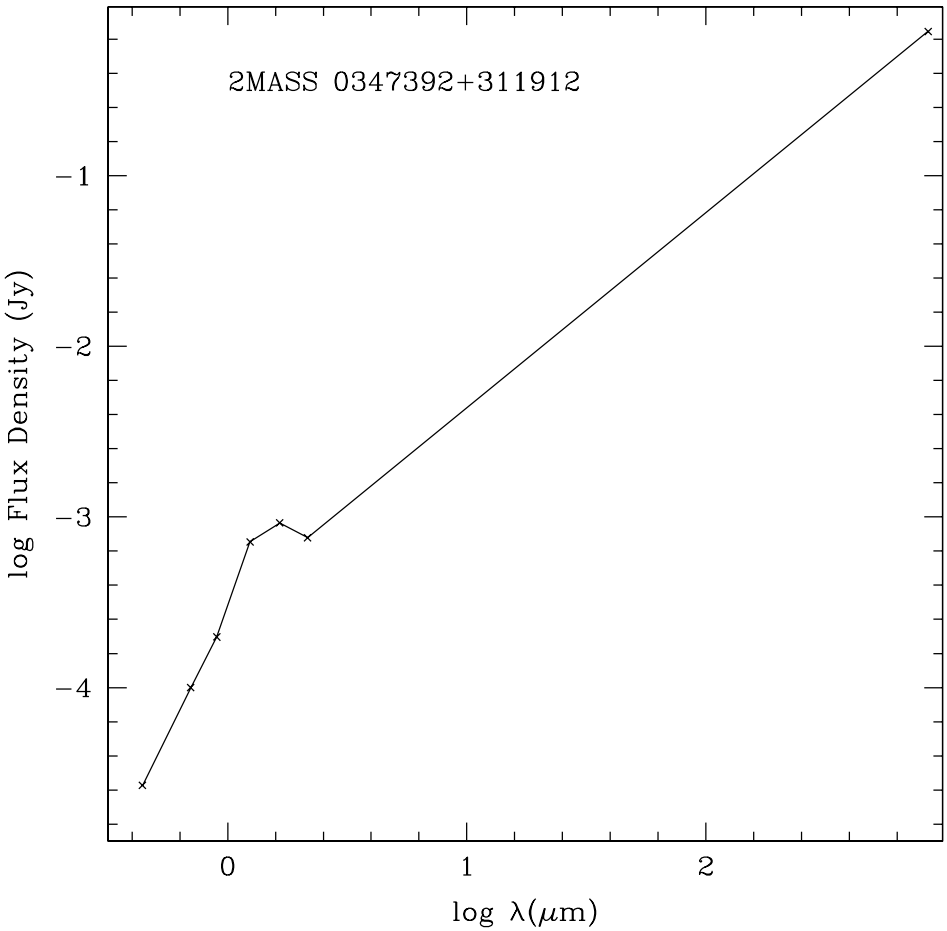

Figure 5.17: We show the SED for 2MASS 0347392+311912. The B, R, and I fluxes are from the USNO-B1.0 Catalog. J, H, and K data are from 2MASS. The 850 μm data is from this work.

5.5 Conclusion

I have presented basic data for a survey of star-forming cores completed with SCUBA on the JCMT. I give basic information for each source within the field: distance, position, fluxes for various apertures, and isothermal masses. This data will be further analyzed in a forthcoming paper (Young et al. 2005).

This data is complementary to Spitzer observations of the same areas, so I have also included Spitzer data for B35A and L1221. The submillimeter map of L1221 shows two distinct cores, only one of which was detected by IRAS. However, we have detected a luminous central object within the other core, which was previously considered "starless." These two cores appear almost identical in flux and morphology at submillimeter wavelengths. However, the infrared portion of the spectrum reveals two very different protostars. Somehow, these similar environments have produced starkly different protostars.

I have also shown the Spitzer data for B35A. The IRAC data shows an aggregate of candidate protostars that appear to be members of the core, which is traced by the submillimeter data. The 4.5 μm emission also reveals a shocked region of gas, presumably due to an outflow, that is consistent with the submillimeter emission.

5.6 Acknowledgements

The authors acknowledge the data analysis facilities provided by the Starlink Project which is run by CCLRC on behalf of PPARC. We are also grateful to the JCMT support scientists Remo Tilanus, Vicky Barnard, and Douglas Pierce-Price for much needed help in observing and data reduction. Support for this work, part of the Spitzer Legacy Science Program, was provided by NASA through contract 1224608 issued by the Jet Propulsion Laboratory, California Institute of Technology, under

NASA contract 1407. Astrochemistry in Leiden is supported by a NWO Spinoza grant and a NOVA grant. This work is supported by NASA grants NAG5-10488 and NNG04GG24G.

Table 5.1: Sources

Source Name	RA J2000	Dec J2000	Cloud	Distance pc	Reference[a]	IRAS[b] y/n	2MASS[b] y/n
B18-1	04 31 55.5	24 32 53	Taurus	140	1	N	N
B35A	05 44 30.7	09 09 01		400	2	Y	Y
CB224	20 36 18.3	63 53 14		450	3	Y	Y
CB230	21 17 38.6	68 17 33		450	3	Y	Y
CB68	16 57 19.5	-16 09 20		160	3	Y	Y
I04361	04 39 13.9	25 53 21	Taurus	140	1	Y	Y
IRAM04191	04 21 56.8	15 29 51	Taurus	140	1	N	N
IRAS04191	04 22 00.5	15 30 26	Taurus	140	....	Y	Y
L1082A	20 53 50.2	60 9 47		440	4	Y	N
	20 53 13.4	60 14 42		440	....	Y	Y
	20 53 27.5	60 14 34		440	....	N	Y
L1082C	20 51 28.6	60 18 39		440	4	Y	N
L1152	20 35 44.3	67 52 52		325	5	Y	Y
L1157	20 39 06.3	68 02 14		300		Y	N
	20 39 09.7	68 01 26		300		N	Y
L1221	22 28 01.6	69 01 20		200	7	Y	Y
	22 28 06.9	69 00 37		200	....	N	N
L1228	20 57 13.8	77 35 43		300	8	Y	Y
L1251C	22 35 24.6	75 17 04		300	9	Y	Y
L1251E	22 38 53.3	75 11 32		300	9	Y	Y
	22 39 38.6	75 11 46		300	....	N	N
L1521F	04 28 39.3	26 51 46	Taurus	140	1	N	N
L1524-4	04 30 06.2	24 26 46	Taurus	140	1	N	N
L43	16 34 30.1	-15 46 59		165	10	Y	Y
	16 34 35.9	-15 47 07		165	....	N	N
L492	18 15 47.9	-03 45 50		200	11	N	N
L723	19 17 53.7	19 12 18		300	12	Y	Y
PER4B	03 29 18.2	31 25 15	Perseus	320	13	Y	Y
	03 29 25.4	31 28 22	Perseus	320	....	N	Y
	03 29 17.3	31 27 52	Perseus	320	....	N	N
PER5	03 29 51.9	31 39 08	Perseus	320	13	Y	N
PER6	03 30 15.4	30 23 45	Perseus	320	13	Y	Y
PER9	03 47 39.4	31 19 07	Perseus	320	13	N	Y
RNO43	05 32 19.4	12 49 42	None	400		Y	N

[a] (1) Elias (1978), (2) Goodman et al. (1993), (3)Launhardt & Henning (1997), (4) Viotti (1969), (5) Straizys et al. (1992), (7) Felli et al. (1992), (8) Padgett et al. (2004), (9) Kun & Prusti (1993), (10) Dame & Thaddeus (1985), (11) Chini (1981) (12) Goldsmith et al. (1984), (13) de Zeeuw et al. (1999)

[b] We search a $1'$ radius for detections at any IRAS band. We search a $30''$ radius for any 2MASS detections.

Table 5.2: Calibrators

Date	Calibrator	τ_{850}	τ_{450}	$C_{20}^{850\,a}$	C_{40}^{850}	C_{80}^{850}	C_{120}^{850}	C_{20}^{450}	C_{40}^{450}	C_{80}^{450}	C_{120}^{450}
11 Jan 2002	CRL618	0.26	1.31	79.0	41.4	31.5	24.6	38.3	22.2	10.5	6.0
11 Jan 2002	Uranus	0.20	0.96	62.0	44.0	41.5	42.0	35.1	29.5	28.7	33.8
15 Jan 2002	CRL618	0.40	2.37	61.8	41.5	31.9	25.0	23.6	12.6	5.6	3.1
15 Jan 2002	Mars	0.35	2.14	62.8	47.3	43.6	42.9	34.2	25.9	21.5	19.8
15 Jan 2002	Uranus	0.37	2.17	68.1	47.7	45.3	46.6	31.9	32.0	119.2	-21.5
17 Jan 2002	CRL618	0.51	3.84	57.5	43.8	41.9	43.3	12.4	10.7	10.0	9.8
17 Jan 2002	CRL618	0.44	3.03	76.9	47.8	43.6	42.5	24.4	15.9	7.8	5.5
17 Jan 2002	Mars	0.52	3.24	80.6	49.6	45.1	43.9	29.5	21.8	17.1	15.3
18 Jan 2002	CRL618	0.60	4.28	76.6	38.9	27.1	19.8	5.8	2.3	0.9	0.4
18 Jan 2002	CRL618	0.60	4.28	67.0	48.0	47.9	55.5	16.6	17.7	-8.4	-2.6
18 Jan 2002	Mars	0.55	2.69	72.0	49.3	43.1	41.0	66.3	46.5	36.0	31.4
29 Oct 2002	Jupiter[b]	0.25	1.34	155.8	68.3	50.4	48.8	198.6	68.7	49.6	47.0
29 Oct 2002	Uranus	0.28	1.50	71.2	55.1	52.6	53.5	74.4	64.8	89.2	917.1
23 Mar 2003	IRC10216[b]	0.18	0.97	54.6	30.9	25.4	26.2	....	....	....	....
23 Mar 2003	IRC10216	0.17	0.88	52.6	29.4	24.0	24.6	....	....	....	....
25 Mar 2003	IRC10216	0.33	1.94	48.5	25.6	16.6	12.8	....	....	....	....
26 Mar 2003	IRC10216	0.35	2.11	50.9	28.8	26.2	27.8	....	....	....	....
26 Mar 2003	Mars	0.25	1.45	61.7	42.3	39.0	38.7	54.6	40.9	36.4	36.5
27 Mar 2003	IRC10216	0.30	1.57	54.0	29.8	23.6	22.5	....	....	....	....
28 Mar 2003	IRC10216	0.20	0.87	45.1	24.6	17.7	15.0	....	....	....	....
20 May 2003	Uranus	0.19	0.96	48.4	37.8	35.4	35.4	35.7	28.6	26.0	26.1
20 May 2003	Uranus	0.16	0.72	56.2	39.8	37.8	37.5	50.2	38.7	33.8	34.3
22 May 2003	Uranus	0.22	1.07	56.8	38.9	34.6	34.1	41.7	28.4	24.7	23.8
23 May 2003	Uranus	0.24	1.22	52.4	40.0	37.3	36.8	51.0	41.6	37.1	35.6
27 May 2003	Uranus	0.37	2.55	53.0	40.4	37.7	37.1	25.2	20.0	17.6	17.3
28 May 2003	Uranus	0.33	1.91	91.0	54.8	37.5	34.3	107.9	43.9	21.5	14.0
Average Values (Standard Deviation)				66(11)	45(5)	40(6)	39(9)	40(24)	29(15)	28(30)	....

[a] The calibration factor, in Jy/V, for a 40″ aperture. Also, we show the 80″ and 120″ calibration factors.
[b] We do not include Jupiter or IRC10216 in the average calibration factor.

Table 5.3: Source Fluxes

Source Name	S_{20}^{850a}	S_{40}^{850}	S_{80}^{850}	S_{120}^{850}	S_{20}^{450}	S_{40}^{450}
B18-1	0.5(0.1)	1.2(0.1)	3.5(0.6)	6.0(1.4)	7.6(4.7)	20.4(10.8)
B35A	0.7(0.1)	3.0(0.4)	6.8(1.1)	10.2(2.4)	5.3(3.2)	15.3(8.0)
CB224	0.4(0.1)	0.9(0.1)	1.5(0.3)	2.0(0.5)	2.4(1.5)	2.8(1.5)
CB230	1.7(0.3)	2.5(0.4)	4.1(0.7)	5.8(1.4)	7.0(4.3)	11.4(6.0)
CB68	1.3(0.2)	2.7(0.3)	6.0(1.0)	10.2(2.4)	11.6(7.0)	28.9(15.1)
I04361	0.4(0.1)	0.8(0.1)	1.3(0.2)	1.5(0.4)	7.1(4.4)	9.8(5.5)
IRAM04191	0.6(0.1)	1.0(0.1)	2.0(0.3)	3.1(0.7)	1.8(1.1)	1.4(0.8)
IRAS04191	0.5(0.1)	0.7(0.1)	1.3(0.2)	2.2(0.5)	1.7(1.0)	1.7(0.9)
L1082A	0.4(0.1)	0.6(0.1)	0.8(0.2)	1.0(0.3)	1.1(0.7)	....
	0.4(0.1)	0.7(0.1)	0.8(0.2)	0.5(0.2)	....	....
	0.8(0.2)	1.1(0.2)	1.4(0.3)	1.4(0.4)	0.9(0.6)	....
L1082C	0.5(0.1)	1.1(0.1)	2.5(0.4)	3.9(0.9)	2.5(1.6)	5.5(3.0)
L1152	0.5(0.1)	1.3(0.2)	2.2(0.4)	2.9(0.7)	3.2(1.9)	8.6(4.5)
L1157	0.7(0.1)	1.3(0.2)	2.6(0.4)	5.9(1.5)	2.0(1.2)	5.2(2.7)
	2.3(0.4)	2.6(0.5)	3.8(0.8)	5.2(1.3)	10.8(6.6)	13.7(7.3)
L1221	1.0(0.2)	2.0(0.3)	4.6(0.8)	8.0(1.9)	7.3(4.4)	11.3(5.9)
	0.9(0.2)	1.9(0.2)	4.8(0.8)	7.9(1.9)	5.0(3.0)	10.9(5.7)
L1228	1.6(0.3)	2.1(0.4)	3.5(0.7)	4.4(1.1)	4.4(2.9)	0.8(1.4)
L1251C	1.0(0.2)	2.4(0.3)	5.5(0.9)	9.2(2.2)	14.9(9.0)	29.4(15.4)
L1251E	1.0(0.3)	2.7(0.5)	6.3(1.2)	9.5(2.3)	12.8(7.9)	36.8(19.4)
	0.7(0.1)	1.7(0.2)	5.2(0.8)	9.3(2.2)	11.0(6.7)	27.8(14.6)
L1521F	0.7(0.1)	1.7(0.2)	4.4(0.7)	7.2(1.7)	4.2(2.6)	14.4(7.5)
L1524-4	0.2(0.0)	0.6(0.1)	2.3(0.4)	4.5(1.1)	2.8(1.7)	8.7(4.5)
L43	0.6(0.1)	1.4(0.2)	2.8(0.5)	4.6(1.1)	6.5(3.9)	15.4(8.1)
	0.9(0.2)	2.0(0.2)	5.1(0.8)	7.9(1.9)	3.5(2.1)	9.9(5.2)
L492	0.2(0.0)	0.5(0.1)	1.5(0.2)	2.3(0.6)	0.8(0.5)	1.7(0.9)
L723	1.3(0.3)	1.4(0.3)	1.1(0.4)	0.1(0.4)	4.4(2.8)	0.8(1.0)
PER4B	0.5(0.1)	0.9(0.1)	1.4(0.3)	2.0(0.5)	1.9(1.2)	3.8(2.1)
	0.5(0.1)	0.7(0.1)	1.0(0.2)	1.1(0.3)	4.8(2.9)	9.4(4.9)
	0.4(0.1)	0.7(0.1)	0.8(0.2)	0.4(0.2)	1.6(1.1)	2.2(1.3)
PER5	0.6(0.1)	1.5(0.2)	3.3(0.5)	5.7(1.4)	8.6(5.3)	22.8(11.9)
PER6	0.2(0.0)	0.3(0.1)	0.3(0.1)	....	1.8(1.3)	4.0(2.6)
PER9	0.2(0.0)	0.4(0.1)	0.7(0.1)	0.9(0.2)	2.0(1.5)	6.4(3.5)
RNO43	1.2(0.2)	1.7(0.3)	2.4(0.5)	3.0(0.8)	10.1(6.1)	13.9(7.3)

[a]The flux, in Jy, for a 20″ aperture. The remaining columns are fluxes in 40″, 80″, and 120″ apertures. We also give the 450 μm fluxes as measured in 20″ and 40″ apertures.

Table 5.4: Source Masses

Source Name	Dust Mass[a]	Virial Mass[b]
B18-1	0.6(0.1)	....
B35A	9.8(1.6)	8.0(1.0)
CB224	2.8(0.5)	....
CB230	7.4(1.4)	....
CB68	1.2(0.2)	....
I04361	0.2(0.0)	....
IRAM04191	0.3(0.1)	....
IRAM04191	0.2(0.0)	....
L1082A	1.4(0.0)	5.9(0.5)
L1082A	1.4(0.0)	5.9(0.5)
L1082A	2.4(0.0)	5.9(0.5)
L1082C	4.3(0.7)	4.7(0.4)
L1152	2.1(0.4)	....
L1157	2.1(0.4)	....
L1157	3.1(0.6)	....
L1221	1.7(0.3)	5.2(0.6)
L1221	1.7(0.3)	5.2(0.6)
L1228	2.8(0.5)	6.4(0.6)
L1251C	4.4(0.7)	2.4(0.2)
L1251E	5.1(0.9)	37.0(4.0)
L1251E	4.2(0.7)	37.0(4.0)
L1521F	0.8(0.1)	....
L1524-4	0.4(0.1)	....
L43	0.7(0.1)	3.3(0.2)
L43	1.3(0.2)	3.3(0.2)
L492	0.5(0.1)	....
L723	0.9(0.3)	....
PER4-C	1.3(0.3)	4.9(0.5)
PER4-A	0.9(0.2)	8.0(1.0)
PER4-B	0.8(0.2)	6.0(0.5)
PER5	3.0(0.5)	5.3(0.2)
PER6	0.3(0.1)	....
PER9	0.7(0.1)	....
RNO43	3.5(0.7)	....

[a]The mass of the core is derived from the 850 μm flux (for the 80$''$ aperture) assuming anisothermal temperature of 15 K.
[b] From Table 4 of Caselli et al. 2002.

Chapter 6

Summary

In this dissertation, I have presented four bodies of work that focus on the formation of low-mass stars. Three of these have been mostly observational (Chapters 2, 3, & 5), while the remaining chapter offers tools by which we can compare the Shu inside-out collapse model with future and ongoing observations. Here, I summarize the most relevant conclusions for each chapter.

6.1 Chapter 2

In chapter 2, "Tracing the Mass during Low-Mass Star Formation: Observations and Modeling of the Submillimeter Continuum Emission from Class I Protostars," my conclusions are based on analysis of a large survey of Class I protostars completed with SCUBA. This work has been completed with the collaboration of Yancy Shirley, Neal Evans, and Jonathan Rawlings; it is also in Young et al. (2003, ApJS, 145, 111). We find that 3/16 (20%) of the sources in this sample have distinct, neighboring condensations (IRAS 03256+3055, 04016+2610 and 04361+2547). These condensations could be the result of complex structure (03256+3055), neighboring preprotostellar cores (04016+2610), or the heating due to outflows (04361+2547).

Also for this sample, we have fit power law models for the density distribution in the outer envelopes of nine Class I cores and find $\langle p \rangle = 1.6 \pm 0.4$ and a median of $p = 1.8$. The existence of a disk or point-like component could cause p to be much *shallower*—by about 0.5. We also test the Shu inside-out collapse model and find that, in most cases, this model provides a good fit for the intensity profile but with an infall radius that is within the central resolution element of our observations. Most sources in this sample exhibit no evidence for a break in the power law density distribution on the scales we can probe with SCUBA ($\sim 1000 - 8000$ AU).

For the modeled sources in chapter 2, we have calculated the mass of the envelope surrounding the protostar: $\langle M_{env} \rangle = 6.6 \pm 2.4$ $M_\odot$ for the two most luminous sources and $\langle M_{env} \rangle = 0.2 \pm 0.1$ $M_\odot$ for those modeled sources in Taurus. We find that these masses are clearly less than those found for Class 0 cores (Paper III) and, further, contradict the virial masses predicted by N_2H^+ linewidths. Molecular line tracers such as N_2H^+ simply do not trace the mass in these Class I cores (Lee et al. 2004).

Finally, we find that the standard classification criteria, T_{bol} and L_{obs}/L_{smm}, are sometimes inconsistent for Class 0 and I cores. I analyze this inconsistency more in Chapter 5.

6.2 Chapter 3

In Chapter 3, I presented the discovery of a very low luminosity protostar within a "starless" core. This work was completed in collaboration with the c2d team and is also in Young et al. (2004, ApJS, 154, 396). Our observations span wavelengths from 2.17 to 1200 μm and include spatially resolved maps of the millimeter emission from L1014-IRS. Assuming a distance of 200 pc, we have created a model for this object that includes a 1.7 $M_\odot$ envelope heated externally by the ISRF. This core contains a central object with very low luminosity (~ 0.09 $L_\odot$). This central source must have

"stellar" and disk-like components in order to match the 3.6 to 70 μm photometry. This object appears to be substellar, though there is enough envelope mass to grow a star if a substantial fraction accretes. We have considered an alternate scenario, in which a distant, more luminous, but less embedded, protostar lies behind the core of the L1014 dark cloud. This scenario is unlikely but cannot be ruled out conclusively without further observations.

Assuming that the infrared source lies in the L1014 cloud, there are two significant conclusions. First, cores thought to be starless may harbor central objects. If this phenomenon is common, estimates for timescales for the evolution of starless cores will need revision. Second, for plausible distances, this source has a very low luminosity. The usual assumptions about accretion rates and pre-main-sequence masses and radii produce far more luminosity than is seen. This object currently appears to be substellar, though it is likely to accrete more mass.

6.3 Chapter 4

In Chapter 4, I have presented the results from modeling the evolution of protostars with 3 different masses: 0.3, 1.0, and 3.0 $M_{\odot}$. This work is also presented in Young & Evans (2005, ApJ, 627; astro-ph/0503456).

We note that the evolution of the modeled protostars is significantly affected by the existence and lifetime of the first hydrostatic core. The work done heretofore is useful (Boss & Yorke 1995; Masunaga et al. 1998), but more detailed theoretical work is needed. As we begin to observe earlier stages of star formation (Young et al. 2004a), the role of the FHC must be ascertained.

We find that the Class 0 stage, when determined by T_{bol}, should be short-lived, lasting only about 1/10 to 1/4 of the protostar's life. This result is somewhat model dependent, but it should also extend to other models of star formation. Therefore, the surveys being conducted with the Spitzer Space Telescope and 2MASS

should reveal a small fraction of Class 0 to Class I objects. However, we suggest not using the T_{bol} criterion for classification.

We find that the bolometric temperature is a poor discriminator for protostars at early evolutionary stages. Instead, we suggest using the L_{bol}/L_{smm} signature proposed by André et al. (1993). Based on physical grounds, we suggest these boundaries for classifying protostars: $L_{bol}/L_{smm} = 35$ for PPC/Class 0, $L_{bol}/L_{smm} = 175$ for Class 0/I, and $L_{bol}/L_{smm} \sim 2000$ for the Class I/II transition. The latter is largely dependent on the adopted disk model. Also, L_{bol}/L_{smm} is not relevant after all envelope mass has been accreted (beyond the Class I stage) since it is a measure of the stellar to envelope mass ratio (André et al. 1993).

We have presented several observational tools by which the inside-out collapse model can be effectively tested: infrared color-magnitude diagrams, plots of the bolometric luminosity and temperature, and a plot of T_{bol} and L_{bol}/L_{smm}. Large surveys will produce these observable quantities for hundreds of young protostars and test the theory of inside-out collapse.

6.4 Chapter 5

In Chapter 5, I have presented basic data for a survey of star-forming cores completed with SCUBA on the JCMT. I give basic information for each source within the field: distance, position, fluxes for various apertures, and isothermal masses. This data will be further analyzed in a forthcoming paper (Young et al. 2005).

This data is complementary to Spitzer observations of the same areas, so I have also included Spitzer data for B35A and L1221. The submillimeter map of L1221 shows two distinct cores, only one of which was detected by IRAS. However, we have detected a luminous central object within the other core, which was previously considered "starless." I have also shown the Spitzer data for B35A. The IRAC data shows an aggregate of candidate protostars that appear to be members of the

core, which is traced by the submillimeter data. The 4.5 μm emission also reveals a shocked region of gas, presumably due to an outflow, that is consistent with the submillimeter emission.

Bibliography

[1] Adams, F.C.& Shu, F.H., 1986, ApJ, 308, 836

[2] Adams, F.C., Lada, C.J., & Shu, F.H., 1987, ApJ, 312, 788.

[3] Adams, F.C., Shu, F.H., Lada, C.J. 1988, ApJ, 326, 865

[4] Alexander, D.R., Augason, G.C., & Johnson, H.R., 1989, ApJ, 345, 1014

[5] Allen, L. E., et al. 2004, ApJS

[6] André P., & Montmerle, T., 1994, ApJ, 420, 837

[7] Andre, P., Ward-Thompson, D., & Barsony, M., 1993, ApJ, 406, 122.

[8] Arce, H.G. & Goodman A.A., 2001, ApJ, 554, 132.

[9] Beichman, C.A., Myers, P.C., Emerson, J.P., Harris, S., Mathieu, R., Benson, P.J., & Jennings, R.E., 1986, ApJ, 307, 337.

[10] Beckwith, S.V.W., Sargent, A.I., Chini, R.S., & Güsten, R., 1990, AJ, 99, 3.

[11] Benjamin, R.A., et al. 2003, PASP, 115, 953

[12] Benson, P.J. & Myers, P.C., 1989, ApJS, 71, 89

[13] Bertin, E., SExtractor v2.3 User's Manual (Paris: Insitut d'Astrophysique)

[14] Black, J.H. 1994, ASP Conf. Ser. 58, *The First Symposium on the Infrared Cirrus and Diffuse Interstellar Clouds* , 355.

[15] Boss, A.P. & Yorke, H.W., 1995, ApJ, 439, L55

[16] Boyd, D.F.A. & Whitworth, A.P., 2005, A&A, 430, 1059

[17] Brand, J. & Blitz, L. 1993, A&A, 275, 67

[18] Butner, H.M., Natta, A., & Evans, N.J. II, 1994, 420, 326.

[19] Calvet, N., 1998, in AIP Conf. 431, ed. S.S. Holt and T.R. Kallman (Woodbury, NY:AIP Press), pp. 495-504

[20] Casselli, P., Benson, P.J., Myers, P.C., & Tafalla, M., 2002, ApJ, in press (astro-ph/0202173).

[21] Chandler, C.J. & Richer, J.S., 2000, 530, 851.

[22] Chandler, C.J., Richer, J.S., & Visser, A.E., 2002, BAAS.

[23] Chen, H., Myers, P.C., Ladd, E.F., & Wood, D.O.S., 1995, ApJ, 445, 377.

[24] Chen, H., Grenfell, T.G., Myers, P.C., & Hughes, J.D., ApJ, 478, 295

[25] Chiang, E.I. & Goldreich, P., 1997, ApJ, 490, 368

[26] Chini, R., 1981, A&A, 99, 346

[27] Chipperfield, A.J. & Draper P.W., Starlink User Note 226.8

[28] Clark, F.O. 1991,ApJ, 75, 611.

[29] Dame, T.M. & Thaddeus, P., 1985, ApJ, 297, 751

[30] D'Antona, F. & Mazzitelli, I., 1994, ApJS, 90, 467 (DM)

[31] Dent, W.R.F., Matthews, H.E., & Ward-Thompson, D., 1998, MNRAS, 301, 1049.

[32] Doty, S.D. & Palotti, M., 2002, submitted MNRAS.

[33] Doty, S.D., Everett, S.E., Shirley, Y.L., Evans, N.J. II, & Palotti, M.L., 2005, MNRAS, accepted, astro-ph/0501676

[34] Draine, B.T. 1978, ApJS, 36, 595.

[35] Draine, B.T. & Lee, H.M. 1984, ApJ, 285, 89

[36] Dullemond, C.P. & Dominik, C. 2004, A&A, 417, 159

[37] Egan, M.P., Leung, C.M., & Spagna, G.R. 1988, Comput. Phys. Comm., 48, 271

[38] Elias, J.H. 1978, ApJ, 224, 857.

[39] Emerson, D. T. 1995, in ASP Conf. Ser. 75, Multi-feed Systems for Radio Telescopes, ed. D. T. Emerson & J. M. Payne (San Francisco: ASP)

[40] Emerson, D. T., Klein, U., & C.G.T. Haslam, 1979, A&A, 76, 92

[41] Evans, N.J. II, Rawlings, J.M.C., Shirley, Y.L., & Mundy, L.G., 2001, ApJ, 557, 193.

[42] Evans, N.J. II, et al. 2003, PASP, 115, 965

[43] Fazio, G.G., et al. 2004, ApJS, this volume

[44] Felli, M., Palagi, F., & Tofani, G., 1992, A&A, 225, 293

[45] Foster, P.N. & Chevalier, R.A., 1993, ApJ, 416, 303.

[46] Froebrich, D., 2005, ApJS, 156, 169

[47] Galli, D. & Shu, F.H., 1993, ApJ, 417, 220.

[48] Gregersen, E.M., Evans, N.J. II, Mardones, D., Myers, P.C., 2000, ApJ, 533, 440.

[49] Goldsmith, P.F., Snell, R.L., Hemeon-Heyer, M., & Langer, W.D., 1984, ApJ, 286, 599

[50] Goodman, A.A., Benson, P.J., Fuller, G.A., & Myers, P.C., 1993, ApJ, 406, 528

[51] Harris, S., Clegg, P., & Hughes, J., 1988, MNRAS, 235, 441.

[52] Henning, Th. & Launhardt, R., 1998, A&A, 338, 223.

[53] Henriksen, R., André, P. & Bontemps, S., 1997, A&A, 323, 549.

[54] Heyer, M.H., Snell, R.L., & Goldsmith, P.F., 1987, ApJ, 321, 370.

[55] Hildebrand, R.D., 1983, *Quarterly Journal of the Royal Astronomical Society* , 24, 267-282.

[56] Hogerheijde, M. R., 2001, accepted by ApJ(astro-ph/0101569).

[57] Hogerheijde, M. R. & Sandell, G., 2000, ApJ, 534, 880.

[58] Hogerheijde, M. R., van Dishoeck, E.F., Blake, G.A., & van Langevelde, H.J., 1997, ApJ, 489, 293.

[59] Holland, W.S., et al., 1999, MNRAS, 303, 659

[60] Huard, T.L., Sandell, G., & Weintraub, D.A., 1999, ApJ, 526, 833.

[61] Huard, T.L., et al., 2005, in prep.

[62] Hunter, C., 1977, ApJ, 218, 834.

[63] Ivezić, Ž., Nenkova, M., & Elitzur, M. 1999, User Manual For *Dusty*, University of Kentucky Internal Report, astro-ph/9910475

[64] Ivezić, Ž. & Elitzur, M., 1997, MNRAS, 287, 799

[65] Jenness, T. & Lightfoot, J.F., 1997, SURF, SCUBA User Reduction Facility ver. 1.5-1 User's Manual.

[66] Jijina, J., Myers, P.C., & Adams, F.C., 1999, ApJS, 125, 161

[67] Kenyon, S.J., Hartman, L.W., Strom, K.M., & Strom, S.E., 1990, AJ, 99, 869.

[68] Kenyon, S.J. & Hartmann, L.W. 1995, ApJS, 101, 117

[69] Kenyon, S.J. & Hartmann, L., 1987, ApJ, 323, 714

[70] Kitamura, Y., Momose, M., Yokogawa, S., Kawabe, R., Tamura, M., & Ida, S., 2002, ApJ, 581, 357

[71] Koo, B.-C., et al. 2003, JKAS, 36, 43

[72] Koornneef, J., 1983, A&A, 128, 84.

[73] Kreysa, E., et al. 1999, SPIE, 3357, 319

[74] Kun, M. & Prusti, T., 1993, A&A, 272, 235

[75] Ladd, E.F., Myers, P.C., & Goodman, A.A. , 1994, ApJ, 433, 117L.

[76] Larson, R.B., 1969, MNRAS, 145, 271.

[77] Launhardt, R. & Henning, Th., 1997, A&A, 326, 329.

[78] Launhardt, R., Ward-Thompson, D., & Henning, Th., 1997, MNRAS, 288, L45.

[79] Launhardt, R., Evans, N.J., II, Wang, Y., Clemens, D.P., Henning, Th., & Yun, J.L. , 1998, ApJS, 119,59.

[80] Lee, C.W. & Myers, P.C., 1999, ApJS, 123, 233

[81] Lee, C.W., Myers, P.C., & Tafalla, 2001, ApJS, 136, 703

[82] Lee, J-E., Bergin, E.A., & Evans, N.J. II, 2004, ApJ, 617, 360

[83] Li, Z-Y., 2002, ApJ, 574, L159

[84] Lucas, P.W., Blundell, K.M., & Roche, P.F., 2001, MNRAS, 318,526.

[85] Lynds, B.T. 1962, ApJS, 7, 1

[86] Mardones,D., Myers, P.C., Tafalla, M., Wilner, D.J., Bachiller, R., & Garay, G., 1997, ApJ, 489, 719.

[87] Masunaga, H. & Inutsuka, S-I., 1999, ApJ, 510, 822

[88] Masunaga, H., Miyama, S.M., & Inutsuka, S-I., 1998, ApJ, 495, 346

[89] McLaughlin, D.E. & Pudritz, R.E., 1996, 469, 194.

[90] Monet, D.G., et al., 2003, AJ, 125, 984

[91] Moore, M. & Doty, S.D., 2002, BAAS.

[92] Moreira, M.C., Yun, J.L., Vazquez, R., & Torrelles, J.M., 1997, AJ, 113, 4

[93] Moriarty-Schieven, G.H., Wannier, P.G., Tamura, M., & Keene, J., 1992, ApJ, 400, 260.

[94] Moriarty-Schieven, G.H., Wannier, P.G., Keene, J., & Tamura, M., 1994, ApJ, 436, 800.

[95] Moriarty-Schieven, G.H., Wannier, P.G., Mangum, J.G., Tamura, M., & Olmsted, V.K. 1995, ApJ, 455, 190.

[96] Motte, F. & André, P., 2001, A&A, 365,440.

[97] Motte, F., André, P., & Neri, R., 1998, A&A, 336, 150

[98] Mundy, L.G., Looney, L.W., Erickson, W., Grossman, A., Welch, W.J., Forster, J.R., Wright, M.C.H., Plambeck, R.L., Lugten, J., & Thornton, D.D., 1996, ApJ, 464, L169.

[99] Myers, P.C., Adams, F.C., Chen, H., & Schaff, E., 1998, ApJ, 492, 703 (M98)

[100] Myers, P.C. & Benson, P.J. 1983, ApJ, 266, 309

[101] Myers, P.C., Fuller, G.A., Mathieu, R.D., Beichman, C.A., Benson, P.J., Schild, R.E., & Emerson, J.P., 1987, ApJ, 319, 340.

[102] Myers, P.C., Heyer, M., Snell, R.L., & Goldsmith, P.F., 1988, ApJ, 324, 907.

[103] Myers, P.C. & Ladd, E.F., 1993, ApJ, 413, L47

[104] Noriega-Crespo, A., et al., 2004, ApJS, 154, 352

[105] Onishi,T., Mizuno, A., Kawamura, A., Ogawa, H., & Fukui, Y., 1998, ApJ, 502, 296.

[106] Ossenkopf, V. & Henning, T. 1994, A&A, 291, 943

[107] Osterloh, M. & Beckwith, V.W., 1995, ApJ, 439, 288.

[108] Padgett, D.L., Brandner, W., Stapelfeldt, K.R., Strom, S.E., Terebey, S., & Koerner, D., 1999, AJ, 117, 1490.

[109] Padgett, D.L., et al., 2004, ApJS, 154, 433

[110] Palla, F. & Stahler, S.W., 1991, ApJ, 375, 288

[111] Park, S. & Kenyon, S.J., 2002, accepted ApJ, astro-ph/0203016.

[112] Pendleton, Y. J., Tielens, A. G. G. M., & Werner, M. W., 1990, ApJ, 349,107

[113] Penston, M.V., 1969, MNRAS, 144, 425.

[114] Pierce-Price, D.P.I., 2001, Ph.D. dissertation

[115] Pollack, J.B., Hollenbach, D., Beckwith, S., Simonelli, D.P., Roush, T., & Fong, W., 1994, ApJ, 421, 615

[116] Rieke, G.H. , et al. 2004, ApJS, 154

[117] Saito, M., Kawabe, R., Kitamura, Y., & Sunada, K., 2001, ApJ, 547, 840.

[118] Sato, F., Mizuno, A., Nagahama, T., Onishi, T., Yonekura, Y., & Fukui, Y., 1994, ApJ, 435, 279.

[119] Schechter, P.L., Mateo, M., & Saha, A. 1993, PASP, 105, 693

[120] Shirley, Y.L., Evans, N.J., II, Rawlings, J.M.C., & Gregersen, E.M., 2000, ApJ, 131,249.

[121] Shirley, Y.L., Evans, N.J., II, & Rawlings, J.M.C. 2002, ApJ, 575, 337

[122] Shirley, Y.L., Nordhaus, M.K., Grcevich, J.M., Evans, N.J. II, Rawlings, J.M.C., & Tatematsu, K., 2004, ApJ, submitted

[123] Straizys, V., Cernis, K., Kazlauskas, A., & Meistas, E., 1992, Baltic Astron., 1, 149

[124] Tafalla, M., Myers, P.C., Caselli, P., Walmsley, C.M., & Comito, C. 2002, ApJ, 569, 815

[125] Shu, F.H., 1977, ApJ, 214, 488.

[126] Shu, F.H., Adams, F.C., & Lizano, S. 1987, ARA&A, 25, 23

[127] Stahler, S.W., 1983, ApJ, 274, 822

[128] Tafalla, M., Mardones, D., Myers, P.C., Caselli, P., Bachiller, R., & Benson, P.J., 1998, ApJ, 504, 900

[129] Tamura, M., Gatley, I., Waller, W., & Werner, M.W., 1991, ApJ, 374, L25.

[130] Terebey, S., Beichman, C.A., Gautier, T.N., & Hester, J.J., 1990, ApJ, 362, L63.

[131] Terebey, S., Chandler, C.J., & André, P., 1993, ApJ, 414, 759.

[132] Terebey, S., Shu, F.H., & Cassen, P., 1984, ApJ, 286, 529.

[133] Terebey, S., Vogel, S.N., & Myers, P.C., 1989, ApJ, 340, 472.

[134] Ulrich, R.K., 1976, ApJ, 210, 377

[135] Ungerechts, H. & Thaddeus, P. 1987, 63, 645.

[136] Viotti, N.R., 1969, Mem. Soc. Astron. Italiana, 40, 75

[137] Visser, A.E., Richer, J.S., & Chandler, C.J. 2002, AJ, 124, 2756

[138] Visser, A.E., Richer, J.S., & Chandler, C.J.,2001, MNRAS, 323, 257.

[139] Wang, Y., Evans, N.J. II, Zhou, S., & Clemens, D.P. 1995, ApJ, 454, 217.

[140] Ward-Thompson, D., André, P., & Kirk, J.M. 2002, MNRAS, 329, 257

[141] Ward-Thompson, D., Scott, P.F., Hills, R.E., & André, P., 1994, MNRAS, 268, 276

[142] Werner, M., et al. 2004, ApJS, this volume

[143] White, R. & Hillenbrand, L., 2004, ApJ, 616, 998

[144] Whitney, B.A., Wood, K., Bjorkman, J. E., Cohen, M. 2003, ApJ, 598, 1079

[145] Whitworth, A.P. & Ward-Thompson, D. 2001, ApJ, 547, 317

[146] Whitworth, A.P. & Ward-Thompson, D., 2001, ApJ, 547, 317.

[147] Young, C.H., Shirley, Y.L., Evans, N.J. II, & Rawlings, J.M.C. 2003, ApJS, 145, 111

[148] Young, K.E., et al., 2005, accepted ApJ

[149] Young, K.E., Lee, J-E., Evans, N.J. II, Goldsmith, P.F., & Doty, S.D., 2004b, ApJ, 614, 252

[150] Young, C.H., et al., 2004a, ApJS, 154, 396

[151] Young, C.H., et al., 2005, in preparation

[152] Yun, J.L., 1996, AJ, 111, 2.

[153] Yun, J.L. & Clemens, D.P., 1994, ApJS, 92, 145.

[154] de Zeeuw, P.T., Hoogewerf, R., de Bruijne, J.H.J., Brown, A.G.A., & Blaauw, A. 1999, AJ, 117, 354.

[155] Zhou, S., Evans, N.J. II, Koempe, C., & Walmsley, C. M., 1993, ApJ, 404, 232

Vita

Chadwick Hayward Young was born in Jackson, Mississippi on 27 May 1976, the son of Odie Hayward and Teresa Diane Young. He attended the Mississippi School for Mathematics and Science (MSMS) in Columbus, Mississippi from 1992 to 1994. Upon graduation, he was inducted into the United States Naval Academy in Annapolis, Maryland where he studied physics along with the standard curriculum. In Fall 1996, Chadwick left the Academy and returned to MSMS as a resident assistant. Then, in Spring, 1997, he enrolled at Mississippi State University in Starkville, Mississippi. While pursuing his undergraduate degree, he was employed by the Los Alamos National Laboratory from January to August 1998, for work on Milagro, a TeV gamma-ray observatory. From May to August 1999, Chadwick worked at the Very Large Array as an REU (Research Experience for Undergraduates) student on the radio afterglow emission from gamma-ray bursts. From August 1999 to May 2000, he worked at Mississippi State University's Diagnostics Laboratory (DIAL) on spectroscopic methods to detect environmental toxins. In May 2000, he received the Bachelor of Science degree in physics with minors in English and mathematics. Then, in June 2000, he began work on this thesis under the employment and advisement of Neal J. Evans, II. Chadwick finished his Master of Arts degree in May 2002. In January 2003, Kaisa Mueller and Chadwick were married in Austin, Texas, where they both continued to work on their PhDs in astronomy. They are expecting their first child, Micah James Young, in June 2005.

Permanent Address: UT Department of Astronomy
1 University Station, C1400
Austin, Texas 78712

This dissertation was typeset with LaTeX 2_ε[1] by the author.

[1] LaTeX 2_ε is an extension of LaTeX. LaTeX is a collection of macros for TeX. TeX is a trademark of the American Mathematical Society. The macros used in formatting this dissertation were written by Dinesh Das, Department of Computer Sciences, The University of Texas at Austin, and extended by Bert Kay and James A. Bednar.